EVALUATION OF YTTRIUM-DOPED $SrTiO_3$ AS A SOLID OXIDE FUEL CELL ANODE

BY

SHIQIANG HUI, M.S.

A Thesis

Submitted to the School of Graduate Studies

In Partial Fulfillment of the Requirements

For the Degree

Doctor of Philosophy

McMaster University

DOCTOR OF PHOLOSOPHY (2000) McMaster University

(Materials Science and Engineering) Hamilton, Ontario

TITLE: Evaluation of Yttrium-Doped $SrTiO_3$ as a Solid Oxide Fuel Cell Anode

AUTHOR: Shiqiang Hui, M.S. (Auburn University)

SUPERVISOR: Professor Anthony Petric

NUMBER OF PAGES: xviii, 225

ABSTRACT

A number of perovskite oxides, typically, heavily doped $SrTiO_3$ samples, were synthesized and characterized with a view to establishing their potential as anode materials for solid oxide fuel cells (SOFCs). The structure, microstructure, electrical conductivity, reduction-oxidation behavior, phase stability, compatibility with electrolytes, and performance in SOFC operation were assessed.

Ceramic samples were prepared with the formula $(Sr_{1-x}R_x)(Ti_{1-y}T_y)O_3$ (R = rare earth elements, T = transition metals) and with charge balance achieved by A-site deficiency. Electrical conductivities were examined by the dc four-probe method and impedance spectroscopy. It was found that yttrium is soluble in $SrTiO_3$ (SYT) up to 8 mol% and has marked effects on conductivity. Electrical conductivities were observed to increase with increasing donor-doping level, on reduction in low oxygen partial pressures. Electrical conductivity with values as high as 82 S/cm was achieved at 800°C and $P(O_2) = 10^{-19}$ atm. Electrical conductivities were reversible upon reduction and oxidation. The thermal expansion coefficient is compatible with electrolyte materials such as yttria-stabilized ZrO_2 and doped $LaGaO_3$. Cobalt-doped SYT, which showed a relatively high resistance to oxidation, was tested as the anode material in a fuel cell. Yttrium-doped $SrTiO_3$ meets the requirements for the anode in SOFCs to a substantial degree, and is a promising alternative anode material.

ACKNOWLEDGEMENTS

I wish to express my sincere gratitude to Prof. Anthony Petric for his time, encouragement, advice, and assistance throughout this work. Many thanks are also due to Prof. John Greedan and Prof. Adrian Kitai for their fruitful suggestions and discussions.

Thanks are also due to many fellow students and technical staff who have shared with me their knowledge and experience, especially Craig Bridges, Anna Skowron, Xiaohua Deng, Kyle Wu, Ales Horky, Medy Shahideh, Yahui Bao, Taras Kolodiazhnyi, Luis Yamarte, George Tsintzilonis, Igor Zhitomirsky, Hanna Dabkowska, Anton Dabkowksi, Connie Barry, Jim Garrett, Bruce Collier, Frank Gibbs and Wenho Gong in the Departments of Chemistry, the Department of Materials Science and Engineering, and the Brockhouse Institute for Materials Research. Without their help, the completion of this work would not have been possible.

I am grateful for the financial support of an OGSST graduate scholarship. Support by the NSERC and Global Thermoelectric is also gratefully appreciated.

I especially wish to thank my wife, Judy, and our parents for all their years of support and encouragement. Finally, I would like to thank Jenny and Eric for coming into our lives during this difficult time, bringing much joy and happiness.

TABLE OF CONTENTS

ABSTRACT iii

ACKNOWLEDGEMENTS iv

TABLE OF CONTENTS v

LIST OF FIGURES xi

LIST OF TABLES xxi

CHAPTER 1. INTRODUCTION 1

1.1. Background 1

1.2. Objectives 3

PART I. LITERATURE REVIEW

CHAPTER 2. ANODE FOR SOLID OXIDE FUEL CELL 5

2.1. Solid Oxide Fuel Cell 5

2.1.1. Principles of Operation 5

2.1.2. SOFC Materials 9

2.1.3. SOFC Design 12

2.2. Anode Materials 13

2.2.1. Requirements for Anode 13

2.2.2. Anode Materials 18

CHAPTER 3. ELECTRICAL CONDUCTION IN OXIDES 25

3.1. Electrical Conductivity 25

3.1.1. Electronic Conductor: te >> ti 27

3.1.2. Ionic Conductors: te << ti 30

3.1.3. Mixed Ionic and Electronic Conductors: te » ti 32

3.2. Some Factors Affecting Electrical Conductivity 33

3.2.1. Effects of Electronic Structure on Conductivity 35

3.2.2. Effects of Temperature on Conductivity 40

3.2.3. Effects of Defects on Conductivity 45

3.3. Conduction Characterization 56

3.3.1.Conduction Behavior and Types of Charge Carriers 56

3.3.2. Separation of Electronic and Ionic Conductivity 60

CHAPTER 4. PHYSICAL AND CHEMICAL PROPERTIES OF SrTiO361 61

4.1. Structure and Synthesis of SrTiO3 61

4.2. Electrical Properties of SrTiO3 64

4.3. Defects in SrTiO3 71

PART II. EXPERIMENTAL WORK

CHAPTER 5. EXPERIMENTAL PROCEDURES 74

5.1. Sample Preparation 74

5.2. X-ray Diffraction 76

5.3. Thermogravimetric Analysis (TGA) 76

5.4. Atmosphere and Temperature Control 76

5.5. Electrical Conductivity Measurement 79

5.5.1. Four-Probe Measurement 79

5.5.2. Impedance Measurement 82

5.6. Seebeck Coefficient Measurement 87

5.7. Magnetic Susceptibility Measurement 90

5.8. Scanning Electron Microscopy (SEM) 90

CHAPTER 6. INITIAL MATERIALS INVESTIGATION 91

6.1. Selection of Materials 91

6.2. Stability 93

6.3. Electrical Properties 96

CHAPTER 7. DONOR-DOPED STRONTIUM TITANATES 104

7.1. Synthesis of Doped SrTiO3 104

7.2. Dependence of Electrical Conductivity on Donors 106

7.3. Yttrium-Doped SrTiO3 (SYT) 114

7.3.1. Solubility of Yttrium in SrTiO3 114

7.3.2. Dependence of Electrical Conductivity on Yttrium-Content 117

7.4. Electrical Properties of Sr0.88Y0.08TiO3-d 137

7.4.1. Effects of Temperature 137

7.4.2. Effects of Grain and Grain Boundary 143

7.4.3. Dependence of Electrical Conductivity on Cation-Cation Ratio 151

CHAPTER 8. ACCEPTOR-DOPED STRONTIUM TITANATES 155

8.1. Acceptor-Doped SrTiO3 155

8.2. Acceptor and Donor Co-doped SrTiO3 159

CHAPTER 9. OXIDATION-REDUCTION BEHAVIOR 177

9.1. Redox Behavior of Sr0.88Y0.08TiO3-d 177

9.2. Redox Behavior of Acceptor and Donor Co-doped SrTiO3 180

9.3. Effects of Materials Processing on Redox Behavior 186

9.3.1. Effects of Atmosphere and Temperature 186

9.3.2. Effects of Porosity 189

9.4. Compatibility with Electrolytes 192

9.5. Fuel Cell Performance 194

CHAPTER 10. SUMMARY AND CONCLUSIONS 199

10.1. Summary 199

10.2. Conclusions 202

REFERENCES 205

LIST OF FIGURES

Figure		Page No.
2.1	Operating principle of SOFC.	7
2.2	Schematic representation of SOFC: (a) planar configuration, (b) tubular configuration (Minh, 1993).	14
2.3	Illustration of the anode reaction zone (hatched parts) for three different types of anodes (a) electronic conductor, (b) cermet, (c) mixed ionic and electronic conductor (MIEC).	17
3.1	Typical applications for electrical conductors as a function of increasing magnitude of conductivity (Tuller, 1994).	27
3.2	Electrical conductivity of oxygen ionic conductors (Steele, 1989).	31
3.3	The major sources of electronic and ionic carriers in oxides and their respective mobilities. Broken arrows indicate that large numbers of carriers generated via deviation from stoichiometry or doping may alter the carrier mobilities (Tuller, 1981; Tallan, 1974).	36
3.4	(a) Cubic perovskite ABO_3 (Raccah and Goodenough, 1967), (b) Corresponding energy band structure and levels (Tamura, et al., 1980).	38

3.5 Electrical character of perovskite oxides classified by their electronic structures (Goodenough, 1968; 1971; 1974) 40

3.6 (a) Small polaron showing the distortion of the lattice around an electron trapped at a metal ion; (b) electron distribution of a large polaron of radius R, formed in a metal oxide MO. (Cox, 1987). 43

3.7 Some electronic consequences of defects in non-metallic solids: (a) and (b) extra electrons or holes in conduction or valence band; (c) and (d) defect levels providing free electrons or holes by thermal excitation; (e) and (f) defect levels acting as traps for electrons or holes; (g) levels giving optical absorption at energies below the band gap (Cox, 1987). 49

3.8 (a) Defect diagram of undoped MO_2 with anti-Frenkel disorder. (b) Corresponding conductivity diagram (Gao and Sammes, 1999). 55

4.1 Calculated total and partial densities of states for $SrTiO_3$. Dotted lines indicate the energy gap at the Fermi level (Takegahara, 1994). 63

4.2 SrO-TiO_2 phase diagram. 63

5.1 Calculated oxygen partial pressure as a function of CO/CO_2 ratio at different temperatures. 78

5.2 System used for the four-probe conductivity measurement. 80

5.3 Electrical conductivities versus oxygen partial pressures for CeO_2 at 800^oC. 81

5.4 Schematic impedance diagrams for some simple RC circuits. 84

5.5 Equivalent circuit (a) and impedance diagram (b) for a solid placed between two-plane parallel electrodes (Macdonald, 1976). 86

5.6 Sample holder for thermopower measurement. 89

6.1 Powder x-ray diffraction patterns for (a) $LaNi_{0.67}Nb_{0.33}O_3$, (b) $LaNi_{0.75}Mo_{0.25}O_3$ (c) $LaNi_{0.75}W_{0.25}O_3$, (d) $LaNi_{0.5}V_{0.5}O_3$, and (e) $LaNi_{0.5}V_{0.25}Ti_{0.25}O_3$. 95

6.2 Powder x-ray diffraction patterns for (a) $La_{0.7}Sr_{0.3}VO_{3-\delta}$, (b) $La_{0.8}Sr_{0.2}VO_{3-\delta}$, (c) $La_{0.9}VO_{3-\delta}$. 95

6.3 Powder x-ray diffraction patterns for $SrVO_{3-\delta}$ (a) as-prepared, (b) oxidized during conductivity measurement; and $SrV_{0.5}Ti_{0.5}O_{3-\delta}$ (c) as prepared, (d) oxidized during conductivity measurement. 97

6.4 The dependence of conductivity on oxygen pressure at 800^oC for: (a) $LaNi_{0.5}V_{0.5}O_3$, (b) $LaNi_{0.75}Mo_{0.25}O_3$, (c) $LaNi_{0.5}V_{0.25}Ti_{0.25}O_3$, (d) $LaNi_{0.75}W_{0.25}O_3$, (e) $LaNi_{0.67}Nb_{0.33}O_3$. 98

6.5 Periodic table of transition metals forming oxides with n-type (shadow) 100

or p-type (bold) behavior. Other elements shown do not change valence state in the fuel cell environment (suitable as electrolytes).

6.6 Phase stability and oxygen partial pressure of selected oxides at 800°C. 101

6.7 The dependence of conductivity on oxygen pressure at 800°C: (a) $La_{0.7}Sr_{0.3}VO_{3-\delta}$, (b) $La_{0.8}Sr_{0.2}VO_{3-\delta}$, (c) $La_{0.9}VO_{3-\delta}$. 103

6.8 Variation of conductivity versus temperature in forming gas (H_2 : Ar = 7 : 93) for (a) $La_{0.7}Sr_{0.3}VO_{3-\delta}$ and (b) $La_{0.8}Sr_{0.2}VO_{3-\delta}$. 103

7.1 Electrical conductivity as a function of oxygen partial pressures at 800°C for donor-doped titanates (a) $Sr_{0.88}Y_{0.08}TiO_{3-\delta}$, (b) $Sr_{0.25}La_{0.50}TiO_{3-\delta}$, (c) $Sr_{0.88}Yb_{0.08}TiO_{3-\delta}$, (d) $Sr_{0.88}Gd_{0.08}TiO_{3-\delta}$, (e)$Sr_{0.88}Sm_{0.08}TiO_{3-\delta}$, (f) $Sr_{0.85}La_{0.10}TiO_{3-\delta}$, (g) $Ca_{0.88}Y_{0.08}TiO_{3-\delta}$. 108

7.2 Reproducibility of electrical conductivity for the same composition of $Sr_{0.88}Y_{0.08}TiO_{2.97}$ at 800°C. 108

7.3 Electrical conductivity as a function of dopant radius at 800°C and oxygen partial pressure of 10^{-19} atm. 111

7.4 Effects of donor doping on conductivity at 800°C. 114

7.5 X-ray diffraction patterns for Y-doped $SrTiO_3$. 116

7.6 Variation of lattice parameter with yttrium content for $Sr_{1-x}Y_xTiO_{3-\delta}$. 117

7.7 Conductivity of undoped $SrTiO_3$ and Y-doped $SrTiO_3$ at 800°C as a function of oxygen partial pressure. 118

7.8 Effects of impurities on conductivity for $Sr_{0.88}Y_{0.08}TiO_{3-\delta}$ at 800°C: a) grades of starting materials were greater than 99.5%, b) grades of starting materials were greater than 98%. 120

7.9 Conductivity of $Sr_{0.88}Y_{0.08}TiO_{3-\delta}$ versus oxygen partial pressure at different temperatures. 123

7.10 Temperature dependence of minima of conductivities extracted from Fig. 7.9. 123

7.11 Seebeck coefficient of $Sr_{0.88}Y_{0.08}TiO_{3-\delta}$ as a function of temperature. 126

7.12 Conductivity of Y-doped $SrTiO_3$ as a function of oxygen partial pressure at 800°C (Region IV in Fig. 7.9). 127

7.13 Conductivity as a function of Y-doping level at 800°C and oxygen partial pressure of 10^{-19} atm. 128

7.14 Oxygen loss as a function of Y-doping level. 130

7.15 Magnetic susceptibility plots for (a) $Sr_{0.97}Y_{0.02}TiO_{3-\delta}$, (b) $Sr_{0.88}Y_{0.08}TiO_{3-\delta}$. 134

7.16 Comparison of the electrical conductivity for SYT: (a) calculated 135

according to the Y-doping level, (b) calculated from thermogravimetric measurements, (c) experimentally determined.

7.17 Conductivity versus temperature under different atmospheres. 138

7.18 Conductivity versus oxygen partial pressure at different temperatures. 138

7.19 Conductivity versus temperature for $Sr_{0.88}Y_{0.08}TiO_{3-\delta}$ in forming gas. 140

7.20 Thermodynamic calculation of oxygen partial pressure as a function of temperature in forming gas. 141

7.21 SEM micrographs of fracture surfaces of Y-doped $SrTiO_3$: (a) $Sr_{0.97}Y_{0.02}TiO_{2.989}$ 1400°C 10h, (b) $Sr_{0.94}Y_{0.04}TiO_{2.980}$ 1400°C 10h, (c) $Sr_{0.91}Y_{0.06}TiO_{2.970}$ 1400°C 10h, (d) $Sr_{0.88}Y_{0.08}TiO_{2.968}$ 1400°C 20h. 144

7.22 (a) The ac complex impedance plot for $Sr_{0.88}Y_{0.08}TiO_{2.968}$ at 650°C, (b) The equivalent circuit that gives rise to the complex impedance plot. 147

7.23 Conductance contribution from grains and grain boundaries as a function of temperature for $Sr_{0.88}Y_{0.08}TiO_{2.968}$. 148

7.24 (a) Illustration of band bending in grain boundary, and (b) corresponding conductance. 150

7.25 Dependence of conductivity on composition $Sr_xY_{0.08}TiO_{3-\delta}$ ($0.80 \leq x \leq 0.92$) over a range of oxygen partial pressures at 800°C. 152

7.26 Variation of conductivity with composition for $Sr_xY_{0.08}TiO_{3-\delta}$ at 800^oC and oxygen partial pressure of 10^{-19} atm. 153

8.1 Dependence of conductivity on oxygen partial pressure at 800^oC for (a) $SrTi_{0.95}Co_{0.05}O_{3-\delta}$, (b) $SrTi_{0.95}Ga_{0.05}O_{3-\delta}$, (c) $SrTiO_{3-\delta}$. 157

8.2 Effects of temperatures on plots of conductivity versus oxygen partial pressure for Ga-doped $SrTiO_3$. 160

8.3 Dependence of conductivity on oxygen partial pressure for yttrium and cobalt co-doped $SrTiO_3$ at 800^oC. 162

8.4 Comparison of conductivity as a function of yttrium content between (a) $Sr_{1-1.5x}Y_xTiO_{3-\delta}$ and (b) $Sr_{1-1.5x}Y_xTi_{0.95}Co_{0.05}O_{3-\delta}$ at 800^oC at oxygen partial pressure of 10^{-19} atm. 163

8.5 Effects of acceptor doping level on conductivity for $Sr_{0.85}Y_{0.10}TiO_{3-\delta}$ at 800^oC. 166

8.6 X-ray diffraction spectrums for (a) $Sr_{0.85}Y_{0.10}TiO_{3-\delta}$ and (b) $Sr_{0.85}Y_{0.10}Ti_{0.95}Co_{0.05}O_{3-\delta}$. 166

8.7 Semiconductor to metal transition with changing oxygen partial pressure for Co-doped SYT. 168

8.8 (a) semiconducting behavior in the region of high oxygen partial 169

pressure, (b) metallic behavior in the region of low oxygen partial pressure.

8.9 Metallic behavior for cobalt and yttrium co-doped $SrTiO_3$ under strongly reducing atmospheres. 170

8.10 Effects of acceptor doping on conductivity at 800°C in a range of oxygen partial pressures for (a) $Sr_{0.85}Y_{0.10}Ti_{0.95}M_{0.05}O_{3-\delta}$, (b) $Sr_{0.88}Y_{0.08}Ti_{0.95}M_{0.05}O_{3-\delta}$. 173

8.11 Trend of conductivity versus acceptor dopants with 3d transition series for (a) $Sr_{0.85}Y_{0.10}Ti_{0.95}M_{0.05}O_{3-\delta}$ (b) $Sr_{0.88}Y_{0.08}Ti_{0.95}M_{0.05}O_{3-\delta}$. 175

8.12 Comparison between conductivity of $Sr_{0.85}Y_{0.10}Ti_{0.95}M_{0.05}O_{3-\delta}$ and M-O bond strength for V_2O_5, Cr_2O_3, Mn_2O_3, Fe_2O_3, CoO, NiO, and CuO. 175

9.1 Change of electrical conductivity for $Sr_{0.88}Y_{0.08}TiO_{3-\delta}$ at 800°C after a sudden oxygen partial pressure change. 178

9.2 Plots of thermogravimetric analysis during (a) oxidation process and (b) reduction process for (1) $Sr_{0.85}Y_{0.10}Ti_{0.95}Co_{0.05}O_{3-\delta}$, (2) $Sr_{0.85}Y_{0.10}Ti_{0.95}Cu_{0.05}O_{3-\delta}$, (3) $Sr_{0.85}Y_{0.10}Ti_{0.95}Ga_{0.05}O_{3-\delta}$, (4) $Sr_{0.88}Y_{0.08}TiO_{3-\delta}$. 181

9.3 Electrical conductivity as a function of time during reduction in 7% H_2 at 800°C. 184

9.4 Change of conductivity at 800°C after a sudden oxygen partial pressure change: (a) oxidation in air, (b) reduction in 7% H_2. 185

9.5 Change of conductivity versus time in 7% H_2 at 950°C for $Sr_{0.85}Y_{0.10}Ti_{0.95}Co_{0.05}O_{3-\delta}$ at 1400°C fired (a) in Ar, (b) in air. 187

9.6 Comparison of conductivity change in (a) H_2 and (b) 7% H_2 at 950°C for $Sr_{0.88}Y_{0.08}Ti_{0.95}Mn_{0.05}O_{3-\delta}$ fired in air at 1400°C. 188

9.7 Effects of firing temperatures on the reduction of $Sr_{0.85}Y_{0.10}Ti_{0.95}Mn_{0.05}O_{3-\delta}$ in 7% H_2 at 800°C. 189

9.8 Influence of porosity on electrical conductivity for $Sr_{0.85}Y_{0.10}Ti_{0.95}Co_{0.05}O_{3-\delta}$ at 800°C. 191

9.9 Comparison of conductivity between dense and porous samples of $Sr_{0.88}Y_{0.08}TiO_{3-\delta}$ during oxidation-reduction processes at 800°C. 191

9.10 Thermal expansion plots for (1) $Sr_{0.88}Y_{0.08}TiO_{3-\delta}$, (2) $Sr_{0.85}Y_{0.10}Ti_{0.95}Co_{0.05}O_{3-\delta}$, (3) $Sr_{0.85}Y_{0.10}Ti_{0.95}Al_{0.05}O_{3-\delta}$, (4) $La_{0.8}Sr_{0.2}Ga_{0.8}Mg_{0.2}O_{3-\delta}$, (5) $Zr_{0.84}Y_{0.16}O_{2-\delta}$. 193

9.11 X-ray spectrums for the sintered mixtures (a) $Sr_{0.88}Y_{0.08}TiO_{3-\delta}$ + $Zr_{0.84}Y_{0.16}O_{2-\delta}$, (b) $Sr_{0.88}Y_{0.08}TiO_{3-\delta}$ + $La_{0.8}Sr_{0.2}Ga_{0.8}Mg_{0.2}O_{3-\delta}$. 193

9.12 Effect of component elements in electrolytes on conductivity of 195

$Sr_{0.85}Y_{0.10}TiO_{3-\delta}$ at 800°C, containing 5% (a) Ga, (b) Zr, (c) Mg on the B-site.

9.13 Schematic of fuel cell test apparatus. 196

9.14 Voltage and power density versus current for anodes with composition (a) $Sr_{0.85}Y_{0.10}Ti_{0.95}Ga_{0.05}O_{3-\delta}$, (b) $Sr_{0.85}Y_{0.10}Ti_{0.95}Co_{0.05}O_{3-\delta}$. 197

LIST OF TABLES

Table		Page No.
2.1	Advantages and disadvantages of the planar and tubular SOFC designs (Gao and Sammes, 1999)	15
2.2	Properties of nickel/YSZ cermet (in reducing atmosphere) (30 vol% nickel, 30% porosity)	20
2.3	Problems associated with Ni-YSZ anode and some possible solutions	23
3.1	Electronically conductive oxides	28
3.2	Conductivities measured in air at 800^{o}C for mixed conducting oxides	34
3.3	Fermi energy in semiconductors	44
3.4	Defect classification	47
3.5	Kröger-Vink notation for point defects in oxide MO	52
3.6	Comparison of different techniques for measuring partial conductivity	59
4.1	Selected properties for SrTiO3	65

4.2 Available transition-metal ions to substitute for Ti^{4+} in $SrTiO_3$ where n is the number of d electrons (Hayes and Stoneham, 1985) 69

5.1 List of starting materials for studies 75

6.1 Preparation conditions and conductivity of selected perovskite compositions studied 94

7.1 Properties of host and donor cations 107

7.2 Compositions of donor-doped titanates studied 107

7.3 Comparison of lattice parameters of $SrTiO_3$ and related oxides 112

7.4 Parameters for yttrium-doped $SrTiO_3$ 115

7.5 Experimentally determined values for C and θ 133

7.6 Activation energy for conduction in $Sr_{0.88}Y_{0.08}TiO_{3-\delta}$ 139

9.1 Results of thermogravimetric analysis (Oxidation was carried out at a constant heating rate of 5oC/min up to 1500oC. Reduction was carried out at 800oC in 7% H2 for 5 h.) 183

9.2 Average thermal expansion coefficients of doped $SrTiO_3$ and electrolyte materials from 25 to 1100^oC 194

CHAPTER 1

INTRODUCTION

1.1. Background

Solid oxide fuel cells (SOFCs) are currently at the forefront of research into new generations of energy conservation systems, owing to their high efficiency and environmentally friendly nature. The development of the fuel cell has included a major investigation of component materials, their fabrication techniques, and cell design. SOFC materials used at present are yttria-stabilized zirconia (YSZ) as the electrolyte, strontium-doped lanthanum manganite ($La_{1-x}Sr_xMnO_3$) as cathode, nickel/zirconia cermet as anode, and calcium-doped lanthanum chromite ($La_{1-x}Ca_xCrO_3$) as interconnect (Brugnoni et al., 1995). Searching for new SOFC materials with improved properties is still an active endeavor due to the different requirements arising from the range of operating temperatures (500-1000^oC), various design configurations and market opportunities.

The low oxygen ion conductivity of ceramics such as yttria-stabilized zirconia (YSZ) restricts the operating temperature of SOFC to high temperatures near 1000^oC. In order to reduce the ohmic loss of the SOFC for medium temperature operation, it is necessary to fabricate thin film zirconia electrolytes (Minh, 1999) or synthesize novel solid electrolytes with higher ionic conductivity. Present-day thick-film ceramic technology

can provide reliable membranes of less than 10 μm, which restricts the use of YSZ to temperatures above approximately 700°C (Steele, 1996). Recently, $LaGaO_3$-based perovskite oxides such as $La_{0.8}Sr_{0.2}Ga_{0.8}Mg_{0.2}O_{2.8}$ (LSGM) have been reported as new oxide ion conductors (Ishihara et al., 1994; Nomura et al., 1997). These compounds have 4-5 times higher ionic conductivity than 8 mol% Y_2O_3 stabilized ZrO_2 (8YSZ) and exhibit almost pure oxide ion conduction in the range of oxygen partial pressures from 10^5 to 10^{-16} Pa (Nomura et al., 1997). Thus, these compounds may find application in SOFCs operating at lower temperatures. CeO_2-based electrolytes are alternative materials for SOFC operation at still lower temperatures (450-700°C) (Visco et al., 1999; Honegger et al., 1999).

Ni/ZrO_2 cermets have been operated successfully as fuel cell anodes. However, these materials do present some problems. Firstly, the Ni metal sinters on prolonged operation, reducing contact area and, increasing resistance loses. Secondly, the cermet suffers from thermal mismatch with the YSZ, giving rise to stresses that may lead to failure. When utilizing more practical fuels such as natural gas, the Ni/ZrO_2 shows additional problems. Ni is known to be susceptible to sulfur poisoning resulting from surface adsorption at levels far below that is necessary to produce NiS, and to inducing carbon formation (coking) from catalytic cracking during internal reforming (Minh, 1992). Finally, the anode reaction occurs only at the triple points between oxygen ions /fuel gas/electrons, which may result in polarization losses. This is also true for cathode reactions since the standard cathode material ($La_{1-x}Sr_xMnO_3$) is known to have a negligible oxygen ion conductivity (Carter, 1992). There is therefore a need for the development of new anode and cathode materials for SOFCs.

1.2 Objectives

The goal of this thesis is to investigate new materials to overcome some of the present problems. Mixed electronic-ionic conductivity is required in order to extend the reaction zone away from the three-phase boundary (TPB), namely, gas-electrode-electrolyte over the entire electrode surface. Materials used as electrodes in such cells are believed to catalyze the redox reactions at the gas-solid interface when they exhibit substantial mixed ionic and electronic conduction (MIEC) (Voorhoeve et al., 1975). The specific objectives are as follows:

1. Search for alternative anode materials, e.g., mixed ionic and electronic oxide conductors that meet the requirements of SOFC anodes. A particular emphasis is given to oxides of perovskite structure.

2. Evaluate the properties of candidate materials in terms of structure, electrical conductivity, redox behavior, stability, and thermal expansion.

3. Study the effect of processing on electrical conductivity.

4. Use defect chemistry to understand the relationship between structure and properties.

Perovskites are good candidate materials because they are known to possess properties such as high electronic conductivity, high oxide ion conductivity and good catalytic activity. It was found in this work that yttrium doped $SrTiO_3$ perovskites meet all three of these properties to a degree which enables their use as a new class of metal-free anodes.

In order to present a critical, concise, and systematic development of new anode materials, the thesis is divided into two parts with ten chapters. In Part I, state-of-the-art anode research (Chapter 2), the mechanisms of electrical transport in solid oxides (Chapter 3), and previous studies on electrical properties of $SrTiO_3$ (Chapter 4) are briefly reviewed. The experimental methods employed in this research, the results, and discussions are presented in Part II, including Chapters 5 to 9. In the final chapter, the results and the significance of this study are summarized and some general recommendations for future work are listed.

CHAPTER 2

ANODE MATERIALS FOR SOLID OXIDE FUEL CELLS

2.1. Solid Oxide Fuel Cells (SOFC)

2.1.1. Principles of Operation

A solid oxide fuel cell is a solid-state electrochemical device producing dc electricity directly from the electrochemical oxidation of a fuel. Sir William Robert Grove invented the original fuel cell in 1839. A fuel cell operates like a battery, but does not need to be recharged, and continuously produces power, when supplied with fuel and oxidant. It remained only a scientific curiosity until the United States National Aeronautics and Space Administration (NASA) developed it for use in the space program in the mid-1960's.

The SOFC offers a number of advantages over existing power generation technologies, including high efficiency (up to 70%), low emission, quiet operation, more flexibility in siting, fuel flexibility, modular (scalable) construction, useful heat for integrated fuel conversion, cogeneration, or combined cycle. However, the cost per kilowatt of an SOFC system is at present far greater than that of conventional systems.

The fuel cell generally consists of a porous fuel electrode (anode) and a porous oxidant electrode (cathode) separated by a dense ion conducting membrane (electrolyte)

as shown in Fig. 2.1. The principle of operation of an SOFC involves reduction of molecular O_2 and acceptance of electrons at the cathode, diffusion of the O^{2-} through an oxygen electrolyte, and oxidation of the fuel by O^{2-} and release of electrons at the anode. At the same time, electrons flow from the anode to the cathode through an external circuit to generate direct current. If the fuel is hydrogen, the only waste product is water. Other fuels such as natural gas, gasoline, methanol, propane and diesel can be used, but they need to be at least partially reformed to avoid coking before entering cell.

At the cathode, the reaction of oxygen occurs according to Eq. (2.1):

$$O_{2(cathode)} + 4e' = 2O^{2-}_{(electrolyte)} \tag{2.1}$$

At the anode, the reverse reaction takes place:

$$2O^{2-}_{(electrolyte)} = O_{2(anode)} + 4e' \tag{2.2}$$

The overall cell reaction is then given as

$$O_{2(cathode)} = O_{2(anode)} \tag{2.3}$$

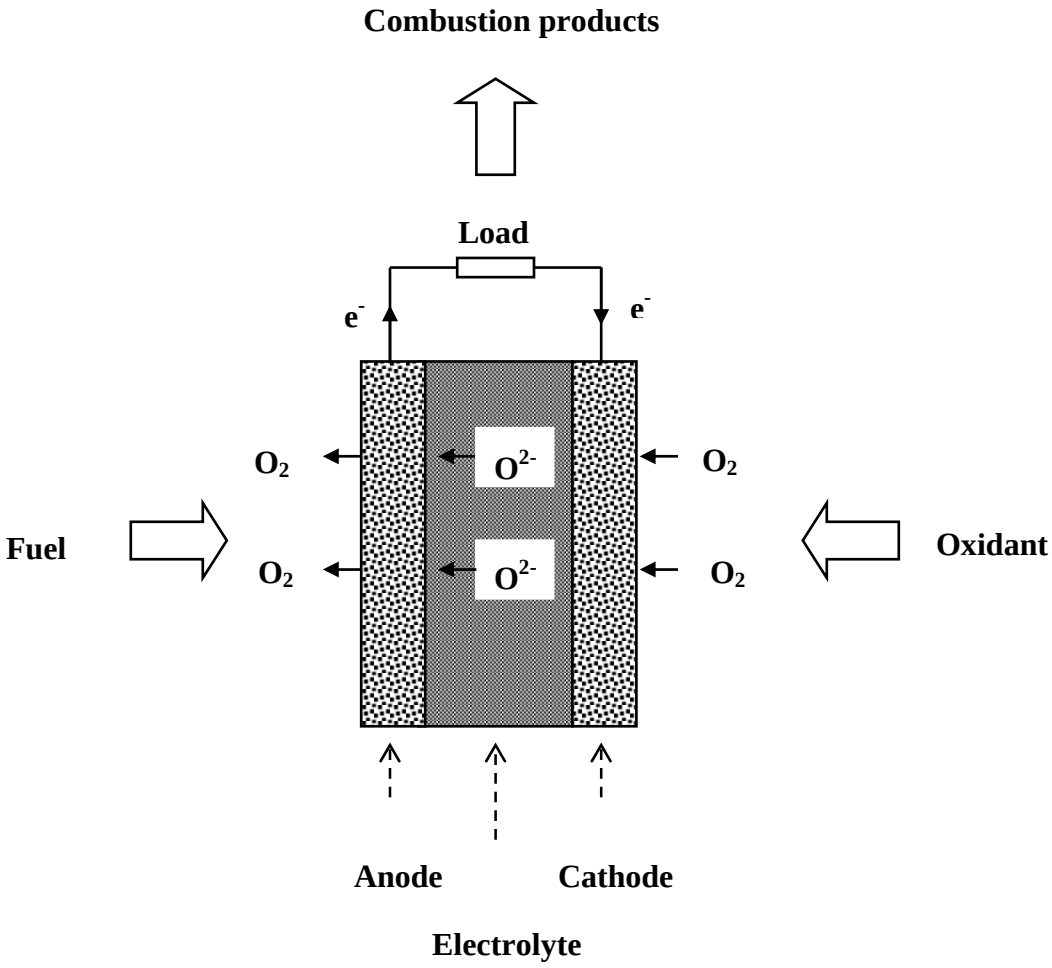

Fig. 2.1 Operating principle of SOFC

Thus, an SOFC can be regarded as an oxygen concentration cell. The electromotive force (EMF) or thermodynamically reversible voltage, E_r, is represented by the Nernst equation when the ionic transport number t_i is close to unity:

$$E_r = \frac{RT}{4F} \ln \frac{P_{O_2(cathode)}}{P_{O_2(anode)}} \tag{2.4}$$

where R is the gas constant, T the temperature, F the Faraday constant, and P_{O_2} the oxygen partial pressure at the electrode. For a specific oxygen partial pressure at the cathode, the magnitude of E_r is dependent on the anode oxygen partial pressure, which in turn is dependent on the type of fuel and its respective composition. For example, when H_2 is introduced to the anode, the reaction is

$$H_{2(anode)} + \frac{1}{2} O_{2(cathode)} = H_2O_{(anode)} \tag{2.5}$$

and the reversible cell voltage is then given as

$$E_r = E^o + \frac{RT}{4F} \ln P_{O_2(cathode)} + \frac{RT}{2F} \ln \frac{P_{H_2(anode)}}{P_{H_2O(anode)}} \tag{2.6}$$

where E^o is the reversible voltage at the standard state given by:

$$E^o = -\frac{\Delta G^o}{4F} = -\frac{\Delta H^o - T\Delta S^o}{4F} \tag{2.7}$$

where ΔG^o is the Gibbs free energy of the reaction given in Eq. (2.5), ΔH^o is the standard enthalpy change, ΔS^o is the standard entropy. The maximum energy is given as

$-\Delta G^o$, where the ideal thermodynamic efficiency is represented by $\Delta G^o / \Delta H^o$. This value varies with different anode gases such as H_2, CO, CH_4 and CH_3OH.

The effect of temperature and partial pressure on the reversible voltage of a fuel cell can be expressed in terms of the change in free energy with temperature (Eq. 2.8), and pressure (Eq. 2.9), where ΔV is the change in volume.

$$\left(\frac{\partial E_r}{\partial T}\right)_P = \frac{\Delta S}{4F} \tag{2.8}$$

$$\left(\frac{\partial E_r}{\partial P}\right)_T = -\frac{\Delta V}{4F} \tag{2.9}$$

For the reaction between hydrogen and oxygen, the entropy is negative, and thus the thermodynamic voltage of the cell decreases with increasing temperature. However, increased operational temperature can improve cell performance, as it increases mass transfer, enhances reaction rates and can lower resistance associated with electrodes and electrolyte. The volume change is negative so the voltage increases with increasing pressure. For this reason, both atmospheric pressure and pressurized SOFCs are under development (Singhal, 1999; Mori, 1999).

2.1. 2. SOFC Materials

A high operating temperature is required for SOFCs mainly due to the slow oxygen transfer rate through the electrolyte at low temperatures. This combined with the multi-component nature of the fuel cell and the required lifetime of 5-10 years severely restricts the choice of materials for cell components. Each material not only has to function

optimally in its own right but has to be viewed in conjunction with other cell components. For practical reasons, single cells with an output potential of 1 volt or less are connected in series using interconnects to form a stack. The components of the fuel cell stack are the anode, cathode, electrolyte, interconnect and seal. Common requirements of all cell components include:

(1) chemical stability in the fuel cell environment ($P_{O_2} \sim 1$ atm on the cathode side and approximately 10^{-19} atm on the anode side) and compatibility with other cell components;

(2) phase and microstructural stability;

(3) thermal expansion matching between various cell components;

(4) for structural components such as electrolyte or electrode, reasonable strength and toughness at the cell operating temperature, as well as reasonable thermal shock resistance;

(5) low vapor pressure at operating temperature;

(6) competitive component fabrication and materials costs.

Minh and Takahashi (1995) give an excellent overview of ceramic fuel cell materials. A brief discussion of SOFC materials is given below, with detailed discussion of the anode in Section 2.2.

Electrolyte: High efficiency fuel cells require electrolytes which, in addition to

the general properties outlined above, must have sufficient oxygen ion conductivity (> 0.05 S/cm) at the operating temperature and remain ionic conductors in oxidizing and reducing atmospheres. Doped zirconia-based materials offer the best possible choice at this stage. Dopants are selected from a large number of divalent and trivalent metal oxides (Y_2O_3, Yb_2O_3, Sc_2O_3, CaO, MgO, etc.), which stabilize the high temperature tetragonal or cubic phase to room temperature. In the ZrO_2-Y_2O_3 system, 2.5 mol% Y_2O_3 stabilizes the tetragonal and 8.5 mol% Y_2O_3 the cubic phase at 1000°C. The tetragonal phase with small grain (0.5 μm) has high mechanical strength, toughness and thermal shock resistance, and an ionic conductivity of 0.055 S/cm at 1000°C. In comparison, the large grained cubic phase has lower strength but a conductivity of around 0.15 S/cm at 1000°C. CeO_2 doped with CaO, Y_2O_3, Sm_2O_3, Gd_2O_3 and a number of other rare earth oxides develops high oxygen-ion conductivity (Azad, 1994). However, the ionic conductivity regime is rather narrow, and in reducing environments, ceria based systems lose oxygen and develop electronic conductivity (P_{O_2} limit at 800°C of about 10^{-3}–10^{-5} atm). The best oxygen ion-conducting electrolyte is doped bismuth oxide with about an order of magnitude higher conductivity than zirconia (Fig. 3.2), but has the disadvantages of easy reduction, high reactivity, a melting temperature < 900°C, and very low strength and toughness.

Cathode: The most common cathode material used in the SOFCs is doped lanthanum manganite, a p-type semiconductor. Substituting part of the lanthanum by lower valent cations enhances the electronic conductivity by increasing the Mn^{4+} content in $LaMnO_3$. Strontium doped lanthanum manganite (LSM) is the currently preferred composition. The extent of strontium doping determines the electronic conductivity and

the thermal expansion coefficient. A change of morphology of the cathode layer with time (decreasing three-phase contact area and limiting gas diffusion) and interfacial reaction between cathode and electrolyte during operation limit the life of SOFCs. A number of other cathode materials have been considered, such as Sr-doped lanthanum-cobaltite, a material with much higher electronic conductivity, and high ionic conductivity, but with the disadvantages (compared to LSM) of a high thermal expansion mismatch and lower stability due to reaction with the electrolyte.

Interconnect: In the Westinghouse tubular design (see page 14), the interconnects within the cell are made with $La_{1-x}Sr_xCr_{1-y}Mg_yO_3$ layers and cells are connected with nickel felt pads. Ceramic interconnect layers are also used in monolithic stacks. In the planar design, three interconnect options, i.e., ceramic, metallic (high temperature alloys) and cermet, are possible. Metals have the advantages of high electric and thermal conductivities that minimize the temperature gradient in the stack and easy fabrication, but are susceptible to rapid oxidation and thermal expansion mismatch is generally large. Cr-based alloys with matching thermal expansion to YSZ over a wide temperature range have been widely studied (Hou et al., 1999; Glatz et al., 1999).

Seal: In the planar SOFC design, seals between cells are essential. Melt type and gasket type seal options have been explored, and the most common seal materials used to date are glass or glass-ceramics.

2.1.3. SOFC Design

To achieve workable power outputs, single cells are combined into a multi-cell unit,

known as the fuel cell stack. Numerous configurations have been reported (Minh, 1993), differing in geometry, power density and method of sealing. There are two major designs of the ceramic fuel cell: planar and tubular (Fig.2.2.). Both rely on a laminate membrane with cathode, electrolyte and anode. The advantages and disadvantages of both designs are summarized in Table 2.1.

2.2 Anode Materials

2.2.1. Requirements for Anode

The requirements for the SOFC anode are determined by its function, the environment, and by its laminated structure. The main functions of the anode are to provide reaction sites for the electrochemical oxidation of the fuel and to provide a path for electrons to be transported from the reaction sites to the interconnect. Fuel oxidation at the anode in contact with the electrolyte contributes electrons to the external circuit and produces water and carbon dioxide according to the following reaction:

$$CO, H_2 + O^{2-} \rightarrow CO_2, H_2O + 2e^- \quad (2.10)$$

CO and H_2 are supplied either individually or simultaneously by reforming of hydrocarbon fuels according to the following reaction:

$$CH_4 + H_2O = CO + 3H_2 \quad (2.11)$$

The anode, therefore, must be a good electronic conductor with high surface area and catalytic activity towards this reaction in addition to the general properties discussed in Section 2.1.2. Porous anodes are used to allow the fuel and byproducts to be delivered

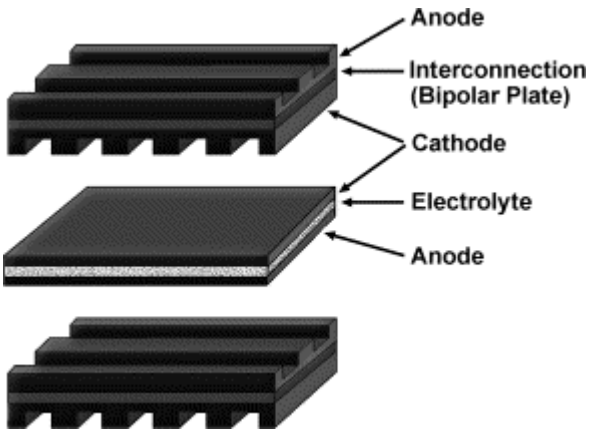

(a)

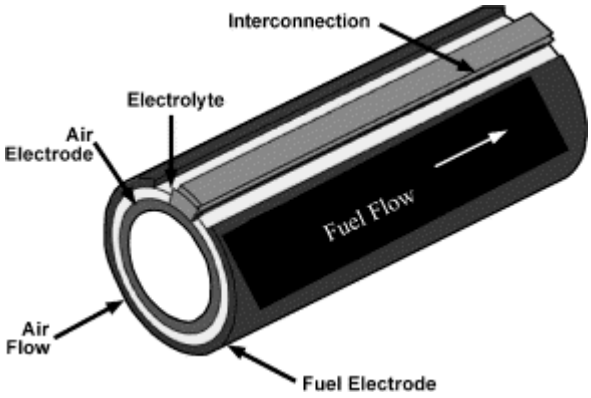

(b)

Fig. 2.2. Schematic representation of SOFC: (a) planar configuration, (b) tubular configuration (Minh, 1993)

Table 2.1. Advantages and disadvantages of the planar and tubular SOFC designs (Gao and Sammes, 1999).

Tubular Design		Planar Design	
Advantages	Disadvantages	Advantages	Disadvantages
No gas seals	Long current path, therefore high internal cell resistances	Improved performance and higher power densities	High temperature gas seals required which may react with the cell components
Very robust structure	EVD processes limit the use of suitable dopants	Cross-plane conduction means lower internal resistance losses	Seals may limit the height of the stack
Some freedom in thermal expansion	Cost is somewhat prohibitive at the moment	More flexibility in design	Contact resistance can be high
Easy cell connections		Easy to fabricate	Stacking thin plates can be difficult and may limit size
Integration of a high temperature heat exchanger		All components can be fabricated separately	
No gas-tight seals		Each component can be assessed separately	
No costly interconnect		Can incorporate different materials such as metallic interconnects	

and removed from the reaction sites without significant diffusion limitation. It is accepted that the reaction involving charge transfer occurs at the triple phase boundaries (TPB), the junction between electrolyte, electrode and gas phase. The limitation of the charge transfer to the TPB means that only part of the electrolyte and anode interface is active in contributing to the ion flux in the electrolyte. The current lines are constricted at the TPBs, which locally gives rise to higher current densities. Consequently a higher electrolyte resistance is observed compared to the situation where the complete electrolyte area contributes to the ion flux (van Berkel et al., 1993; Tedmon, 1969; van Heuveln et al., 1993). Overpotential loss is inversely proportional to the TPB length (Ogumi et al., 1995; Sridhar and Pal, 1996; Dees et al., 1987; Isenberg, 1982), and the reaction rate for electrochemical oxidation of hydrogen has been demonstrated to correlate with the length of the TPB on the model Ni anode (Mizusaki et al., 1994; Osberg and Norby, 1995). SOFCs with enhanced anode TPB have demonstrated improved fuel cell performance such as higher power density and low resistance loss (Wang et al., 1999). Anode materials could potentially be metals, cermets, or mixed ionic and electronic conductors (MIECs). The active area of the anode increases from the contact point between electrolyte and metal for metal anodes, to the whole surface area for MIECs as shown in Fig. 2.3. There is also evidence that efficient operation of certain catalytic oxide electrodes is believed to be a consequence of mixed conduction (Voorhoeve et al., 1975). Therefore, ionic conduction is also required for anode materials to achieve advanced fuel cell performance.

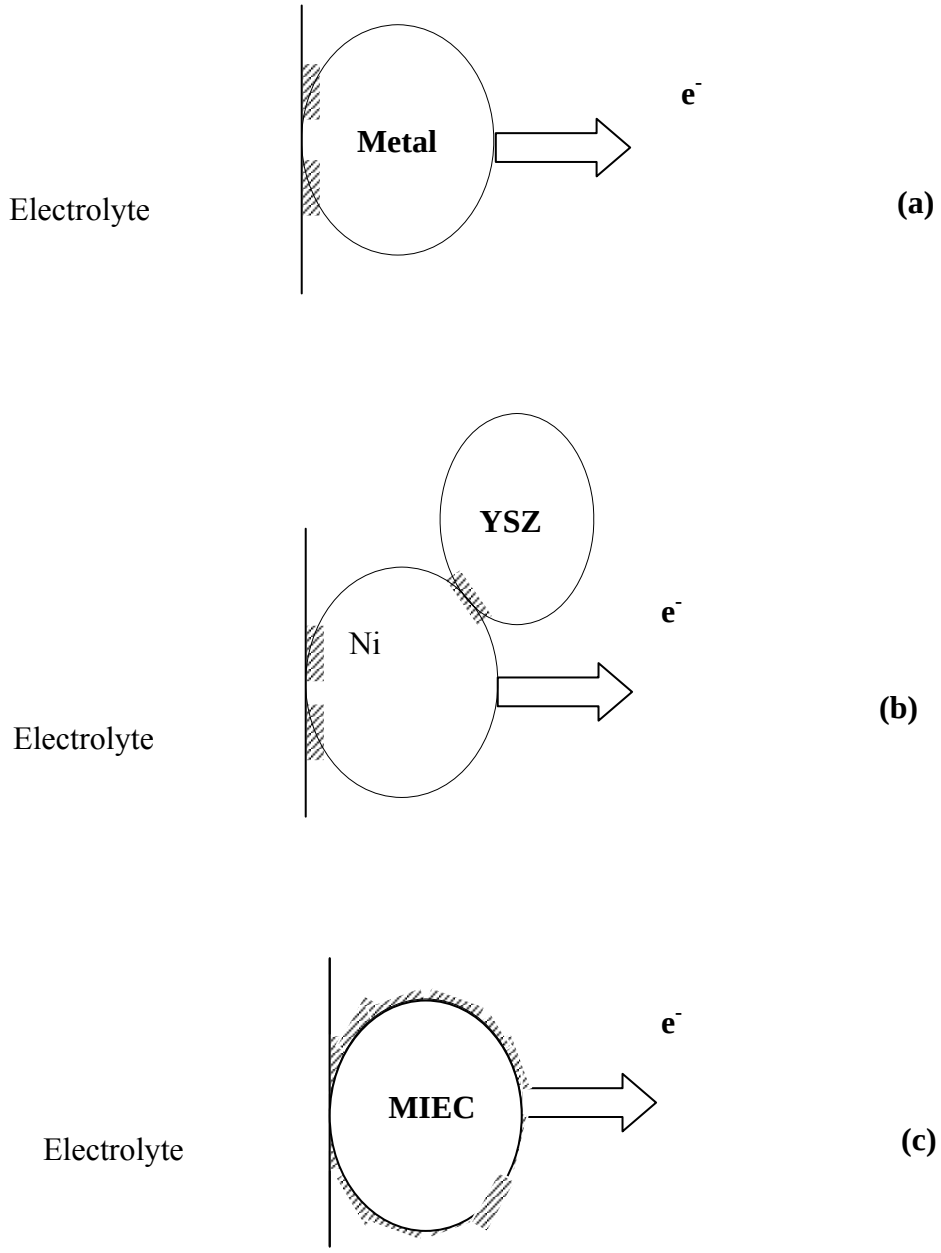

Fig. 2.3. Illustration of the anode reaction zone (hatched parts) for three different types of anodes (a) electronic conductor, (b) cermet, (c) mixed ionic and electronic conductor (MIEC)

2.2.2. Anode Materials

The first type: metals Because of the low oxygen partial pressure of the fuel, certain metals can be used as the anode in SOFCs. Suitable metals must be non-oxidizable not only at the fuel inlet but also at the less reducing fuel outlet (Minh, 1993). Various metals such as Ni, Pt, Co, Ti and Cu or their consequent oxides have been studied as anodes (Takahashi, 1972). Pure metallic anodes have high electronic conductivity. In this case, however, the reaction sites are limited to the interfaces between electrolyte and anode, which makes gas diffusion a limiting factor, particularly when SOFCs operate at low temperature and high current density. Thus, high overpotential loss is to be expected.

In addition, because of the thermal expansion mismatch between the metallic anode and electrolyte, induced stress can be a problem. Since there is no wetting at a solid-solid contact, the thermal stress can easily create cracks that deteriorate the contact further after several heating and cooling cycles. Furthermore, vapor loss, sintering and poisoning of metallic anodes over long duration of SOFC operation also cause serious degradation problems.

The second type: cermets In order to overcome the problems with pure metallic anodes, metal-ceramic (cermet) composite anodes such as Ni-YSZ have been widely studied (Minh, 1993). The ceramic component serves to maintain the porous structure of the anode for long periods at high temperatures; to support the Ni particles, and inhibit sintering during long term operation, which is a major cause of fuel cell degradation; to reduce the thermal expansion of pure Ni to values more compatible with

other cell components; and to increase the TPB by providing ionic conduction pathways (Minh, 1993; Mogensen, 1996). Compared with the first type of anode, the reaction sites in the cermet extend to the grain boundaries between metal and ceramic.

Among the combinations of metal and YSZ, Ni is the preferred choice due to low cost and high catalytic activity towards H_2 oxidation (Setoguchi et al., 1992). Both nickel and YSZ phases are known to be chemically stable in the reducing fuel environment. NiO has less than 5% solubility in ZrO_2 that limits the amount of interdiffusion during sintering. Compared to nickel, cobalt has the advantage of high sulfur tolerance (Markin et al., 1976; Suzuki et al., 1991) but is more easily oxidized and is more expensive. Ruthenium has a higher melting point (2310 ^{o}C) than nickel (1453 ^{o}C), thus providing better resistance to particle coarsening. Ru/YSZ cermets have been shown to have minimal sintering at fuel cell operating temperatures, high catalytic activity for steam reforming, and negligible carbon deposition under reforming conditions. The high cost of ruthenium is a major disadvantage.

Some properties of the Ni-YSZ cermet are given in Table 2.2. In most cases, the cermet is first made with NiO and YSZ. The NiO is then reduced *in situ* to nickel metal when exposed to the fuel in the fuel cell. The reduction of NiO to nickel increases the porosity of the anode. The electrical conductivity of the cermet is strongly dependent on its nickel content (Minh, 1993). The Ni loading is generally chosen to be slightly in excess of the percolation limit for electronic conduction. At higher Ni content, there are problems with thermal mismatch with the YSZ substrate (Dees et al., 1987).

Table 2.2. Properties of nickel/YSZ cermet in reducing atmosphere (30 vol% nickel, 30% porosity)

Melting point, ^{o}C (melting point of nickel)	1453
Density, g/cm^{3}	6.87
Conductivity at 1000 ^{o}C, S/cm	500
Thermal expansion coefficient, 10^{-6} ppm/K	12.5
Strength at 25 ^{o}C, MPa	100

Anode performance has been studied mainly in relation to the TPB, the electrical conductivity, the thermal expansion, the stability and reactivity with the electrolyte. It is commonly believed, however, that anode performance is attributable not only to the materials, but also the interfacial structure. One of the key factors in the preparation of the cermet anode is to tailor and control electrode morphology, because the characteristics and stability of the anode microstructure are known to significantly affect electrode electrochemical performance (Kawada et al., 1990a; Elangovan et al., 1991).Ionic path impedance through the ceramic phase and electronic path impedance through the metallic phase have been found to be dominant factors in determining anode characteristics (Kawada et al., 1990b). In order to provide a low sheet resistance anode, it is imperative that the metallic and ceramic phase have maximized continuous paths that allow ionic and electronic migration from the electrolyte and anode interface throughout the entire anode. In general, the smaller the particles at the electrolyte and anode interface, the larger the area that is involved in the reaction and the higher the currents

that can be drawn through the anode. Tannenberger and Siegert have already showed the necessity for a large number of small particles at the interface in 1969. An extension of the TPB can also be achieved by increasing the thickness of the cermet anode. In practice, however, both methods are limited by the requirement for low-resistivity percolation of active species. As the characteristic dimension of the structure decreases and as the anode thickness increases, the transport resistivities also increase. Meanwhile, the electrocatalytically effective thickness of Ni-YSZ cermet anodes has been shown to be only about 10 μm at 1000^{o}C (Primdahl et al., 1999). A great deal of work has been aimed at improving Ni-YSZ performance or solving the associated problems as summarized in Table 2.3.

The third type: MIEC Attention is increasingly turning to mixed conductors. This type of anode material is expected to replace the state of the art SOFC cermet anodes because MIECs promise considerable improvements over Ni-YSZ cermets in relation to most of the problems discussed above.

(i) In mixed conductors where both oxygen ions and electrons are mobile, the electrochemical reactions occur over the entire electrode/gas interfacial area. The usual requirements of a triple phase contact between electrode, electrolyte and gas, are replaced by a simple requirement of a two-phase boundary region between electrode and gas phase. The positive effect of mixed conductors at the interface has been well known for many years (Inoue et al., 1989; Eguchi et al., 1991, 1993; Setoguchi et al., 1992; Schäfer et al., 1996) and is illustrated in Fig. 2.3. Thus, polarization losses

with a mixed conducting electrode are expected to be significantly less than with electrodes exhibiting only electronic conductivity (Schouler, 1982; Liou and Worrell, 1989).

(ii) MIECs are much less susceptible to the problems associated with agglomeration and particle growth on prolonged annealing at operating temperatures (600^{o}C to 1000^{o}C).

(iii) Sulfur poisoning might not be so problematic because ceramics have a lower affinity for sulfur.

(iv) Ceramic anodes have advantages in producing direct electrochemical oxidation of dry methane without carbon deposition (Steele et al., 1988). Steele et al. has demonstrated that platinum anodes are very poor electrocatalysts for the oxidation of CH_4 at 800^{o}C. However Bi_2O_3-Pr_6O_{11} anodes could electrochemically oxidize 100% CH_4 to CO_2 and H_2O at reasonable efficiencies without producing carbon deposition.

Table 2.3. Problems associated with Ni-YSZ anode and some possible solutions

Problems	Reasons	Solutions	References
Resistance loses	Prolonged operation causes Ni grain coarsening hence reducing contact area	finer starting powders and equal proportion of Ni and YSZ; Metals with higher T_m (Ru); Pre-calcination	Lee et al., 1997; Wildenhöner et al., 1997; Minh, 1995; Huebner et al., 1999
NiS deposition	Sulfur poisoning	Co-YSZ	Jacobson and Worrell, 1983; Markin et al., 1976; Suzuki et al., 1991
Cracking	Thermal mismatch with electrolyte	Ni-TiO_2 cermet	Dees, et al., 1987; Stöver et al., 1999
Carbon deposition	Catalytic cracking occurs during internal reforming when utilizing natural gas as fuel gas	Cu-CeO_2 cermet; Cu-CeO_2-YSZ cermet; Ni-CeO_2 cermet;	Mogensen and Bentzen, 1989a; Steele, et al., 1988; Park et al., 2000; Wang et al., 1999; Murray and Barnett, 1999;
Polarization losses	Limited reaction sites	Surface modification by CeO_2; finer structure or thicker anode;	Thampi et al., 1995; Tsai and Barnett, 1997; Brown et al., 2000

CeO_2 based materials have been evaluated for SOFC anode applications under this category (Mogensen, 1991; Metcalfe et al., 1992; Mogesen et al., 1989b). Doped CeO_2 exhibiting mixed conduction in the fuel environment, has been studied both as anode material and as support, replacing the ZrO_2 in nickel/YSZ cermet. The material has shown considerable promise as an electrode material for direct oxidation of CH_4. However, anodes based on doped CeO_2 have not replaced nickel/YSZ anodes because of the relatively low levels of electronic conductivity and the relatively large lattice expansion (Mogesen et al., 1994) associated with the loss of oxygen under anodic conditions, which can eventually result in the anode spilling off the electrolyte.

Various oxides in addition to CeO_2 have also been investigated, including Y_2O_3-ZrO_2-TiO_2 solid solution (Worrell, 1992), doped $Gd_2Ti_2O_7$ (Porat et al., 1997), doped $SrTiO_3$ (Slater et al., 1997), and a number of titanate systems such as $Mg_{1-y}Ti_{2+y}O_5$ and $Mg_{1-y}Ti_{1+y}O_3$ (Fagg et al., 1994).

So far, however, it has not been possible to develop a single phase material that is stable over the oxygen partial pressure range associated with typical anode operation and exhibits sufficient electronic conductivity. Identifying anode materials that satisfy all requirements simultaneously is a significant challenge. Some of the required properties deteriorate when others are improved, as for example, electronic conductivity versus ionic conductivity or single-phase composition versus stability over a wide range of oxygen partial pressure. To optimize the anode materials requires a compromise in the chemical and physical properties.

CHAPTER 3

ELECTRICAL CONDUCTION IN OXIDES

3.1. Electrical Conductivity

Oxides cover the entire range of conductivity from insulators, through semiconductors and metallic conductors, to superconductors (Cox, 1992; Tsuda et al., 1991). Compared with a simple metal, the electronic properties of oxides show certain characteristic features. One is the metal-insulator transition (MIT), in which at a certain composition, or temperature, or pressure, an insulator becomes a metallic conductor (Imada et al., 1998). Another characteristic feature is that the electrical conductivity is a function of oxygen partial pressure. A change of oxygen partial pressure leads to the generation of electronic defects in oxides, which results in an increase or decrease in carrier concentration (Kofstad, 1983). Finally, ionic conduction in some oxides is an important feature in addition to their various electronic conduction properties (Tallan, 1974). Some fundamental electrical transport properties are reviewed in this chapter.

A general form of the electrical conduction theory for ionic crystals established by Wagner is based on the idea that every ionic crystal is a mixed conductor (Wagner, 1957). Electrical conductivity is the net transport of charge in the presence of an applied field. Electrical conductivity σ of a solid is simply the sum of the partial conductivity associated with each type of charge carrier and is given by

$$\sigma = \sum_j \sigma_j = \sigma_e + \sigma_i = \sigma_n + \sigma_p + \sigma_{m^-} + \sigma_{m^+} \tag{3.1}$$

where σ_e, σ_i, σ_n, σ_p, σ_{m^-}, and σ_{m^+} represents conductivity contribution from electronic charge carriers, ionic charge carriers, electrons, holes, anions, and cations, respectively. For oxides as discussed in Section 3.2, the electronic conductivity may be further expressed by the oxygen partial pressure dependence: $\sigma_e = \sigma_n^o P_{O_2}^{-1/n} + \sigma_p^o P_{O_2}^{1/n}$. Each partial conductivity σ_j, which may represent transport of either ionic or electronic carriers, is defined by

$$\sigma_j = n_j (z_j e) \mu_j \tag{3.2}$$

where n_j is the concentration of charge carrier j, $z_j e$ is its charge, and μ_j its mobility (drift velocity in unit potential gradient).

The fraction of the total conductivity contributed by each charge carrier is

$$t_j = \frac{\sigma_j}{\sigma} \tag{3.3}$$

where t_j is known as the transference number. The ionic transference number t_i includes cation and anion contributions, and the electronic transference number t_e represents the sum of the electron and hole transference numbers $t_n + t_p$. The transference number may vary as a function of oxygen partial pressures as in the case of CeO_2-based and $LaAlO_3$-based materials (Tuller and Nowick, 1975; Kilner et al., 1978). Since neither t_i nor t_e is ever truly zero, all solids are in principle mixed conductors. Generally, only one type of carrier dominates charge transport, and so contributions from minority carriers are often

ignored. Therefore, electrical conductors can be categorized in three cases as discussed below, and some corresponding applications are illustrated in Fig. 3.1.

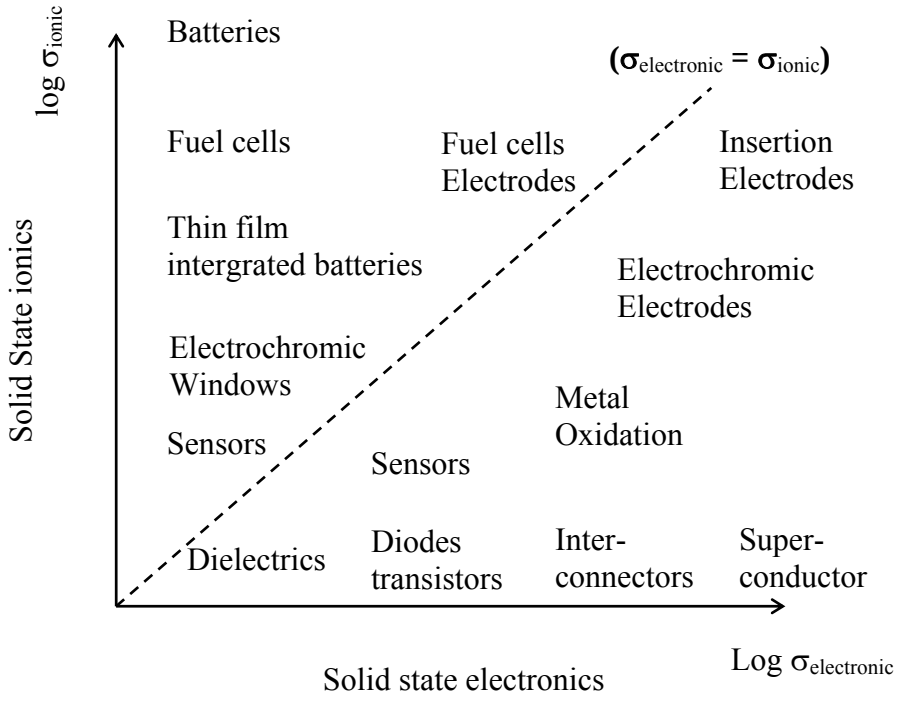

Fig. 3.1. Typical applications for electrical conductors as a function of increasing magnitude of conductivity (Tuller, 1994)

3.1.1. Electronic Conductor: $t_e >> t_i$

Some high conducting oxides are summarized in Table 3.1.

In insulating and semiconducting materials at low temperature the valence band is fully occupied by electrons and the conduction band is empty. Consequently, unless electrons are excited across the band gap there are no available energy states for electrons to occupy on application of a field. The field thus can have no effect on the electron

Table 3.1. Electronically conductive oxides

Oxides	Conductivity at 300 K (S/cm)	References
$LiTi_2O_4$	5×10^5	Inukai et al., 1982
LiV_2O_4	1.3×10^5	Rogers et al., 1967
Fe_3O_4	2.5×10^4	Adler, 1968
ReO_3	1×10^7	Sleight and Gillson, 1966
$LaTiO_3$	8.3×10^2	Greedan & Maclean, 1978
$YTiO_3$	1.3×10^{-3}	
$CaVO_3$	2.5×10^2	Chamberland et al., 1971
$SrVO_3$	3.3×10^6, single[1]	Dougier et al., 1975
$La_{1-x}Sr_xVO_3$	1×10^3 at x = 0.3, M-I	Sayer et al., 1975
$Gd_{1-x}Sr_xVO_3$	3.1×10^3	Dougier and Casalot, 1970
$CaCrO_3$	1.4×10^5, single	Weiher et al., 1971
$SrCrO_3$	2.5×10^5	Chamberland, 1967
$La_{1-x}Sr_xMnO_3$	1×10^4, M-I	Goodenough, 1971
$CaFeO_3$	3.3	Takeda et al., 1978
$SrFeO_3$	5×10^4	MacChesney et al., 1965
$SrCoO_3$	1×10^4	Takeda et al., 1972
$YCoO_3$	metal > 1200 K	Jadhao et al., 1975
$LaCoO_3$	metal > 700 K, M-I	Thornton et al., 1982
$La_{1-x}Sr_xCoO_3$	1×10^6 at x = 0.5, metal	Raccah et al., 1968
$La_{0.8}Sr_{0.2}Co_{1-x}Fe_xO_3$	2.5×10^2 s.c. at x = 0.3, M-I	Anderson et al., 1995
$LaNiO_3$	1×10^5, metal	Mohan Ram et al., 1986
$LaNi_{1-x}M_xO_3$	M = Cr, Mn, Fe, Co, M-I	Ganguly et al., 1984
$La_{0.8}Sr_{0.2}CrO_3$	1.2	Webb et a., 1977
$BaPbO_3$	3.3×10^5, s.c[2] , single	Bogatko et al., 1980
$SrMoO_3$	1×10^6	Hayashi et al., 1979
V_2O_3	1×10^5, M-I at 168 K	Honig and Reed, 1968
Ti_2O_3	1.1×10^4, M-I ~ 660 K	Leiva et al., 1982
VO_2	2×10^5, metal > 340 K	Bianconi et al., 1981
Ti_3O_5	1×10^4, metal > 460 K	Bartholomew et al., 1969
SnO_{2-x}	5×10^3, s.c.	Fonstad and Rediker, 1971

[1] single-single crystal [2] s.c.-semiconductor

or momenta and the crystal is nonconducting. Electronic charge carriers are provided by electrons in the conduction band or by missing electrons (electron holes) in the valence band; depending on the width of the band in which these carriers move, two conduction types can be distinguished. In the broad band the electrons are delocalized, move through the crystal as free electrons, and subjected to a small perturbing potential provided by the atoms on their sites. In narrow bands the electrons are localized around particular atoms and move by hopping from the potential well around one atom to that around another. This kind of conduction is more likely to occur in compounds where the metal ions can have more than one oxidation state, and is therefore likely to be observed in transition metal oxides (Weller, 1973).

For purposes of developing a good electrode material, a small-gap material would be of interest. It is also possible to select an oxide material in which the Fermi energy lies within the conduction band such as $SrVO_3$ (Cox, 1992). The same result can be achieved by doping. One must select temperature, oxygen partial pressure and dopant concentration to ensure electronic compensation. Selection of a cation with variable valence contributes to higher electronic conductivities due to the enhanced excursions from stoichiometry shown by the following equation:

$$O_O = \frac{1}{2}O_2 + V_O^{\bullet\bullet} + 2e' \tag{3.4}$$

Thus, CeO_2, in which Ce can readily take on +3 and +4 valences, shows much higher electronic conductivities at reduced oxygen partial pressure than does ThO_2 or ZrO_2 which have fixed +4 valences. It thereby follows that, if one wished to introduce electronic conductivity into solids with fixed-valence host cations, one should introduce

variable-valent cations into solid solution.

3.1.2. Ionic Conductors: te << ti

Ionic conductors involve mass (material) transport while the electronic conductors do not. Ionic conductors may have different conduction mechanisms. Some have large defect concentration extrinsically, for example YSZ. Others, including β–alumina, have channels, planes, or more complex open paths allowing rapid ion motion (Hayes and Stoneham, 1985). There are intriguing two-phase systems, like LiI/Al_2O_3, where two poor ionic conductors combine to produce a highly conducting composite (Maier, 1985). The ionic conductivity for some oxide electrolytes is plotted as a function of temperature in Fig. 3.2.

Any of the effectively charged defects (except electrons and holes) gives rise to ionic conductivity if the defect can diffuse. Such diffusion requires the existence of either vacancies or interstitials. It takes an activation energy of approximately 1-5 eV to create an interstitial-vacancy pair and an energy of equivalent magnitude to move the vacancy or interstitial ion through the material (Tallan, 1974). Like the diffusion coefficient, ionic mobility is an activated process, increasing strongly with temperature. The same process also applies for hopping electron conduction as described earlier. Only at high temperatures, where defect concentrations become quite large and ions have high thermal energy, does the conductivity become appreciable. Only oxides with high defect mobilities that are either sufficiently heavily doped or structurally disordered are likely to

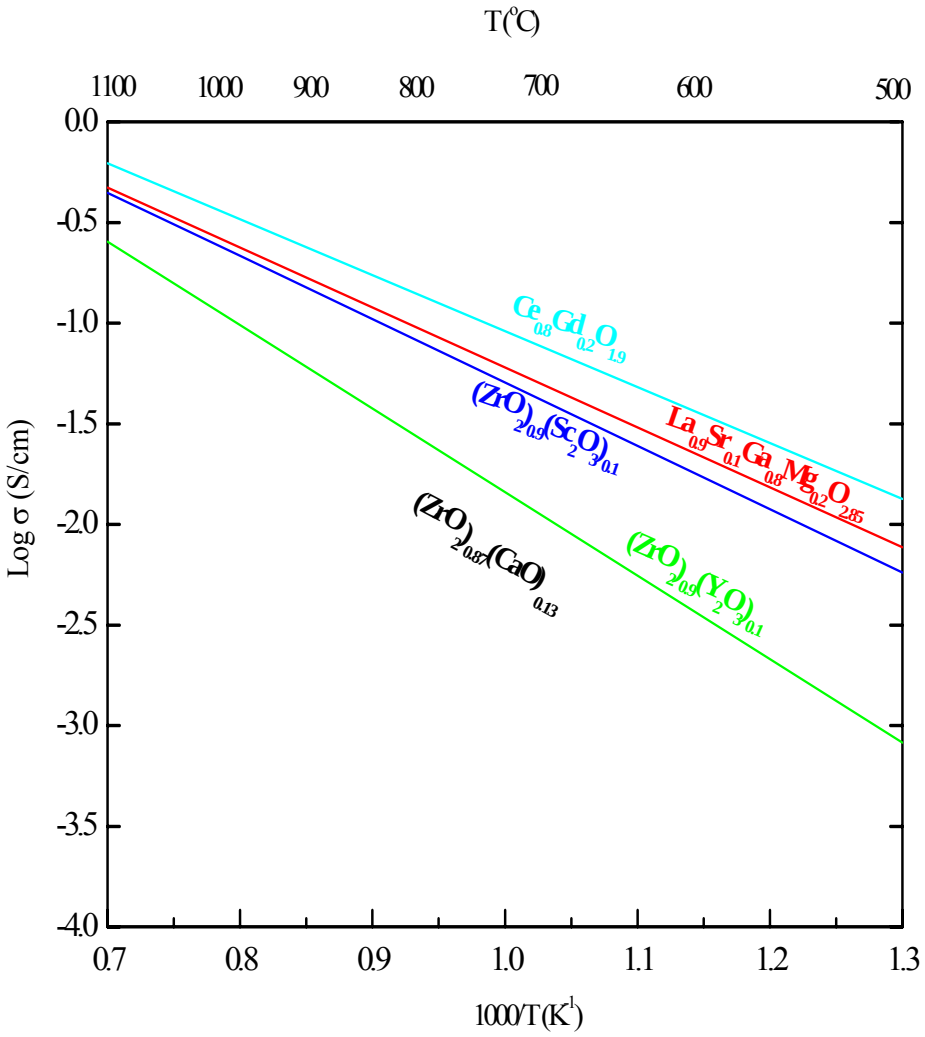

Fig. 3.2. Electrical conductivity of oxygen ionic conductors (Steele, 1989)

exhibit mixed conduction (Sorensen, 1981). One can achieve high ionic carrier densities in one or more of three ways (Tallan, 1974; Tuller, 1992). Due to entropy considerations, solids tend to disorder intrinsically. This may take the form of Schottky, Frenkel or anti-site disorder. For oxides, Frenkel disorder on the oxygen sublattice, given by

$$O_i'' + V_O^{\bullet\bullet} = \Phi \tag{3.5}$$

is of great relevance. In fluorite oxides, such as CeO_2, ThO_2, and monoclinically disordered ZrO_2, this mechanism supplies an inadequate number of ionic carriers to achieve high ionic conductivities. Ionic defects can also be introduced by equilibration of the solid with the gas. Thus, reduction may be described by Eq. (3.4). This mechanism obviously leads to mixed conduction. Finally, ionic defects may be introduced by doping with aliovalent impurities. To satisfy charge compensation, acceptor impurities are compensated by oxygen vacancies.

3.1.3. Mixed Ionic and Electronic Conductors: $t_e \approx t_i$

In general, the reasons for ionic and for electronic conduction are independent (Heyne, 1977). The first is mainly related to crystal structure; the latter is determined by the electronic band gap, which depends more on the individual properties of the constituent ions. Thus if a crystal structure is favorable for fast ionic movement, the high ionic mobility in it may well be accompanied by either a low or high electronic conductivity. The partial contribution to the total conductivity, i.e., the transference number, may change depending on the atmosphere (Tuller and Nowick, 1975; Kilner et al., 1978).

For most situations, only one type of ionic and electronic carrier predominates. Thereby, the condition, $t_e \approx t_i$, requires that

$$n_i \mu_i \approx n_e \mu_e \tag{3.6}$$

Because electronic mobilities are typically 10^4-10^8 times greater than ionic mobilities at high temperatures, this has the important consequence that all mixed conductors must possess 10^4-10^8 times greater concentrations of ionic carriers than electronic carriers. This condition is satisfied only in oxides in which high densities of mobile ions can be induced by doping or by crystallographic disorder and which simultaneously possess a relatively large energy band gap, thereby ensuring a low concentration of intrinsic electronic carriers. Table 3.2 summarizes some mixed conductors with significant ionic conductivity except $LaMnO_3$. More mixed conductors can be found in the literature (Steel, 1992; Tuller, 1981).

Simultaneous ionic and electronic conduction plays a critical role in a number of important processes occurring in oxides. For example, it accounts for the rate of formation of oxide layers on metals, their oxidation-reduction kinetics, and their gas permeation rates (Wagner, 1979; Smith et al., 1966). Efficient operation of certain catalytic oxide electrodes is believed to be a consequence of mixed conduction (Voorhoeve et al., 1975).

3.2. Some Factors Affecting Electrical Conductivity

The electrical conductivities are determined primarily by the nature of the atomic bonding and the crystal structure, and are related to the charge carrier concentration and

Table 3.2. Conductivities measured in air at 800°C for mixed conducting oxides

Compounds	Electronic σ_e (S/cm)	Ionic σ_i (S/cm)	References
$Ce_{0.8}Sm_{0.2}O_{1.9}$		0.1	Eguchi et al., 1992
ZrO_2-9%Y_2O_3		0.035	Feng and Goodenough, 1994
$SrTiO_3$	$6x10^{-4}$	$6x10^{-5}$	Chan et al., 1981
$SrTi_{0.9}Al_{0.1}O_3$	$3x10^{-3}$	$4x10^{-4}$	Takahashi, 1971
$SrTi_{0.8}Fe_{0.2}O_3$	0.3	$1.5x10^{-2}$	Steinsvik et al., 1994
$SrCo_{0.8}Fe_{0.2}O_3$	100	10	Teraoka et al., 1998
$CaTiO_3$	$3x10^{-4}$	$3x10^{-5}$	Iwahara et al., 1988
$CaTi_{0.8}Fe_{0.2}O_3$	0.09	0.04	Iwahara et al., 1988
$CaTi_{0.95}Mg_{0.05}O_3$	$6.4x10^{-3}$	$4x10^{-3}$	Takahashi 1971
$CaTi_{0.5}Al_{0.5}O_3$	$3x10^{-3}$	$2x10^{-3}$	Takahashi 1971
$La_{0.5}Sr_{0.5}CoO_3$	870	0.4	Kharton et al., 1995
$La_{0.8}Sr_{0.2}Co_{0.8}Fe_{0.2}O_3$	250	0.1	Teraoka et al., 1988
$La_{0.6}Sr_{0.4}Co_{0.8}Ni_{0.2}O_3$	500	~0.05	Carter et al., 1992
$La_{0.75}Sr_{0.25}FeO_3$	~50	0.03	Ishigaki et al., 1988
$La_{0.7}Ca_{0.3}AlO_3$	10^{-3}	$5x10^{-4}$	Takahashi, 1971
$La_{0.5}Sr_{0.5}MnO_3$	320	$\sim10^{-8}$	Carter et al., 1992

mobility by Eq. 3.2. A schematic diagram, which includes the most likely mechanisms controlling electronic and ionic carrier generation and their respective mobilities, is given in Fig. 3.3.

3.2.1. Effects of Electronic Structure on Conductivity

There are two limiting theories for the outer electrons in solids to correlate structure and physical properties with the chemical composition of crystalline compounds: crystal-field theory and band theory (Cox, 1987; Hoffmann, 1988). A metal has a partially filled band, with no energy gap above the top-occupied level (Fermi level). A semiconductor has no partially filled band, with an energy gap smaller than 3 eV. An insulator may be treated as a semiconductor with a greater energy gap. However, solids may have a metallic to non-metallic transition under certain conditions. More details regarding these matters are given in the literature (Cox, 1987; Tsuda, 1991; Goodenough, 1971; Imada, et. al., 1998).

For transition metal oxide insulators, in which the 3d electrons are localized due to strong electron-electron interaction, metallic conductivity can be achieved in two ways, namely, through band-gap closure and valence control or filling control (Imada, et. al., 1998). In the band-gap closure scheme, the splitting between energy bands which form the gap is somehow diminished or their band widths are increased. In the filling control process, the mean valence of the transition metal ions is intentionally modified from integral to intermediate values through chemical substitution or other stoichiometry

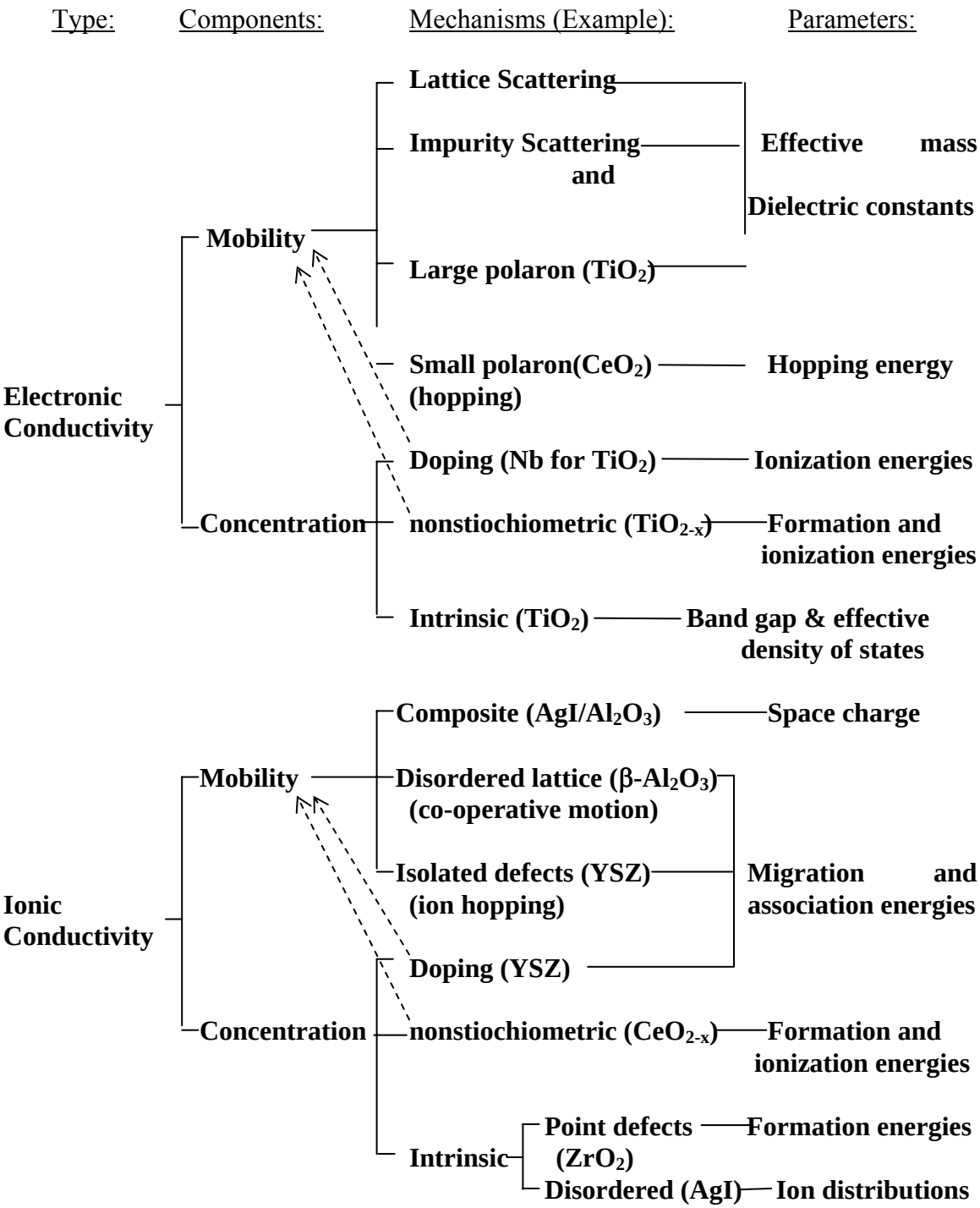

Fig. 3.3. The major sources of electronic and ionic carriers in oxides and their respective mobilities. Broken arrows indicate that large numbers of carriers generated via deviation from stoichiometry or doping may alter the carrier mobilities (Tuller, 1981; Tallan, 1974)

control; this leads to the generation of extra electron or hole carriers into an otherwise insulating system. In the case of either band-gap closure or filling control, the band gap of the parent insulator can be that of the *d-d* Mott-Hubbard type or the ligand *p*-to-metal *d* charge-transfer type depending on the relative magnitudes of the *d-d* Coulomb repulsion energy U and the *p*-to-*d* charge-transfer energy Δ (Zaanen, et. al., 1985; Hüfner, 1985). Most of the late 3d transition metal oxides beginning with Mn belong to the charge-transfer regime ($U_{eff} > \Delta_{eff}$) whereas early 3d transition compounds such as Ti and V oxides are believed to be in the Mott-Hubbard regime ($U_{eff} < \Delta_{eff}$).

According to the ionic framework, the transfer of electrons from the metal to the electronegative partner provides the bonding. The ionic model predicts the valence band, which forms the top-filled level in the solid, should be composed of the top-occupied orbitals of the non-metal anion; the bottom empty level, the conduction band, is correspondingly formed from the lowest empty orbitals of the metal cation. It is easy to see why simple ionic oxides are good insulators.

For perovskite oxides, the lattice constant is larger than 3.5 Å, so that the interaction of constituent ions in the oxide is important only in the B-O-B array of ABO_3 and not in the B-B, B-A-B, and A-O-A as shown in Fig. 3.4 (a) (Goodenough, 1967a; 1967b; 1971). Electronic and magnetic properties are determined mainly by the degree of interaction of the d-orbitals of the B cation with the p-orbitals of the neighboring oxygen anions. The d-orbitals are split by the octahedral crystal field into two degenerate e_g and t_{2g} orbitals. On the other hand, the p-orbitals of the oxygen anion are split into the p_π and p_σ orbitals.

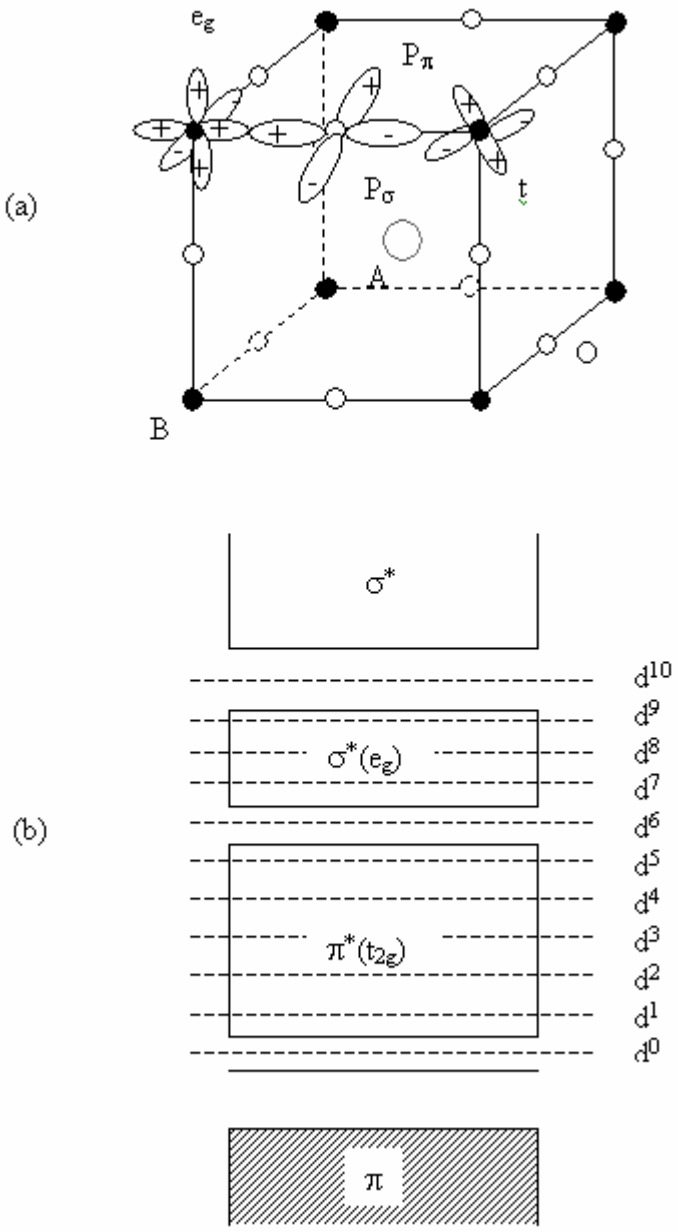

Fig. 3.4. (a) Cubic perovskite ABO_3 (Raccah and Goodenough, 1967), (b) Corresponding energy band structure and levels (Tamura, et al., 1980)

The most favorable conditions for the formation of B-O-B bond in perovskites are realized when the B-O-B angle is 180^{o} which is possible only in the case of an undistorted unit cell. Fig. 3.4 (b) shows the manner of band formation due to the B and oxygen ions.

Fig. 3.5 depicts a comprehensive set of perovskites, arranged in rows according to the oxidation state for species B, and arranged in columns according to the electronic configuration ($t_{2g}^{m}\ e_{g}^{n}$) or net spin S of species B. Goodenough distinguishes three possible regimes. Region I encompasses the "low-spin" and high-charge cases where cation-anion overlap remains sufficiently extensive that all electrons in d-like bands are collective; the band-structure scheme of Fig. 3.4 is qualitatively applicable. Region II includes compounds of intermediate spin and charge where exchange effects are sufficiently strong to result in a splitting of d states. All compounds having B-ion electronic configurations of d^{7}-d^{9} will have a partially filled σ^{*} band and exhibit metallic properties; all other electronic configurations should result in semiconducting properties. Region III encompasses materials of high spin and low charge; the configuration of orbitals is now sufficient to localize all d electrons, and compounds in this region should be semiconductors. Whether d electrons in transition metal compounds are localized or delocalized depends on many factors: on the outer electronic configuration and the size of cations, on their degree of oxidation, on the characteristics of the crystal structure, etc. (Cox, 1987) In order to assess the state of electrons, the phenomenological approach proposed by Goodenough is widely used (Goodenough, 1971).

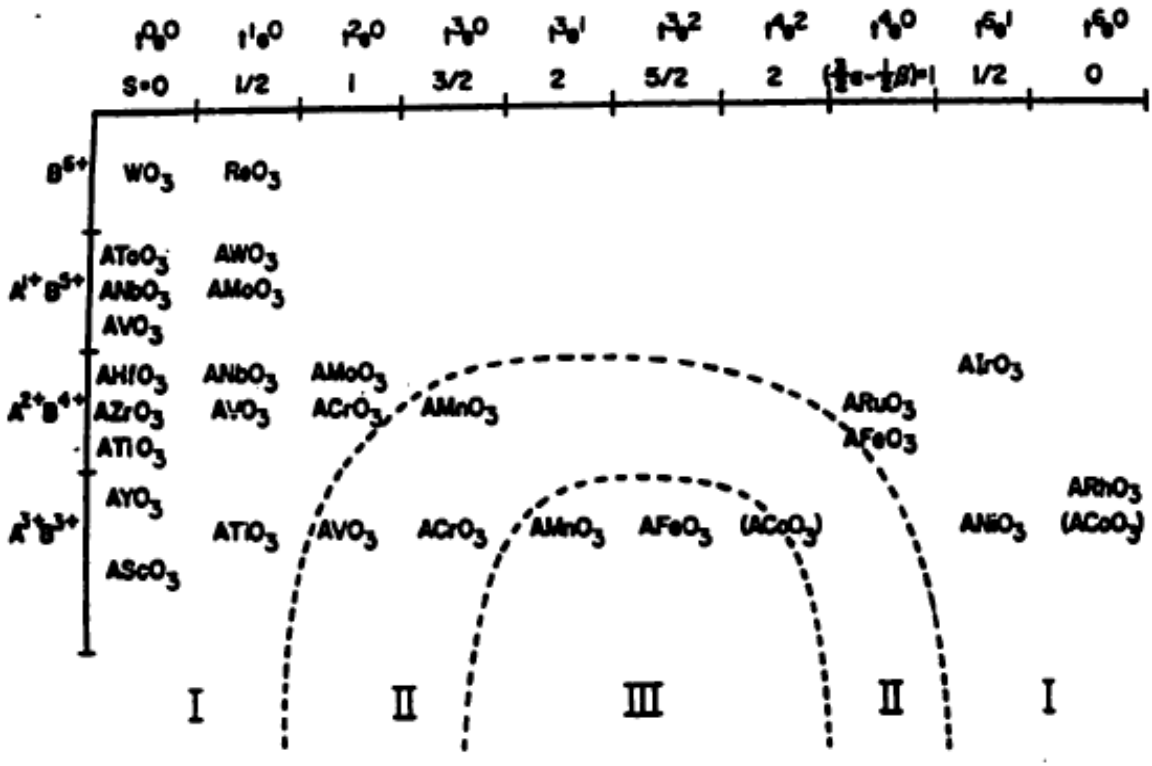

Fig. 3.5. Electrical character of perovskite oxides classified by their electronic structures (Goodenough, 1968; 1971; 1974)

3.2.2 Effects of Temperature on Conductivity

Charge carrier concentrations are controlled by temperature in intrinsic solids, and by dopants in extrinsic solids. The main source of the different behavior in metals, semiconductors and insulators lies in the charge carrier concentration and its temperature dependence. For metals, charge carrier concentration is large and essentially unchanged with temperature. The only variable in conductivity is mobility and since mobility decreases slightly with temperature, conductivity also decreases. For semiconductors and

insulators, electronic defects are generated intrinsically via the following equation

$$[n][p] = C \tag{3.7}$$

The equilibria between negative electrons, n, and positive holes, p, in semiconductors is analogous with the equilibria of ionic solutions (Phillips and Williams, 1965): $[H^+][OH^-] = K_\omega$. The equations are simplified in a pure solvent or in an intrinsic semiconductor respectively as $[H^+] = [OH^-]$ and $[n] = [p]$. The charge carrier concentration usually increases exponentially with temperature as shown by (Cox, 1992),

$$n = p = \sqrt{N_c N_v}\exp(-E_g/2kT) \tag{3.8}$$

where n and p are the intrinsic concentrations of electrons and holes and $N_{c,v}$, the effective density of states in the conduction and valence bands, is as follows (Kittel, 1976):

$$N_{c,v} = 2(2\pi m^*_{e,h} kT/h^2)^{3/2} \tag{3.9}$$

where $m^*_{e,h}$ represents the effective mass of electrons and holes. Changing the temperature in a semiconductor has a much greater effect on the carrier concentration than on the mobility, and the conductivity normally increases with temperature.

According to Matthiessen's rule, one can approximately separate the two contributions to the conductivity (Kittel, 1976):

$$1/\sigma = \rho = \rho_{dis} + \rho_{lat} \tag{3.10}$$

where ρ_{dis} is the residual resistance at low temperatures due to scattering by static disorder, and ρ_{lat} the lattice contribution from scattering by thermally excited vibrations. At higher temperatures, mobility is dominated by electron-phonon interactions and, for pure nonpolar broad-band semiconductors,

$$\mu = \mu_o T^{-3/2} \tag{3.11}$$

At lower temperatures, impurity scattering usually dominates and (Goodenough, 1971)

$$\mu = \mu_o T^{3/2} / \ln(\alpha T) \tag{3.12}$$

where α is a constant.

In ionic crystals, the electron-phonon interaction is stronger than in a metal. The electron state becomes more complex as a result of the interaction. The electron and its surrounding polarization cloud are referred to as a polaron. In broad bands, the lattice distortion extends over several lattice constants. In this case, the polaron is called a large polaron (Fig. 3.6b.). In narrow bands, the electron-lattice interaction is so strong that a local lattice deformation is induced. In this case, the electron no longer can move freely through the lattice and a small polaron (Fig. 3.6a.) model can be applied. For broad band conduction the mobility is relatively large (>1 cm^2/V-sec) and the mobility decreases with increasing temperature (Appel, 1968)

$$\mu = \mu_o T^{-1/2} \tag{3.13}$$

since carrier scattering caused by thermal vibrations of the lattice atoms is enhanced. For

narrow band conduction the mobility is small (< 1 cm^2/V-sec) . Above the Debye

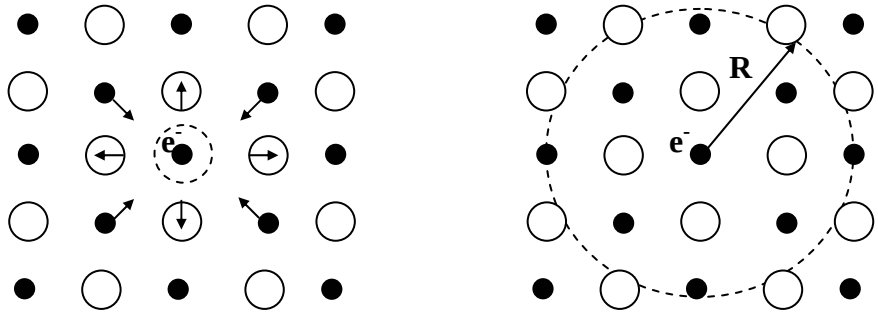

(a) (b)

Fig. 3.6. (a) Small polaron showing the distortion of the lattice around an electron trapped at a metal ion; (b) electron distribution of a large polaron of radius R, formed in a metal oxide MO. (Cox, 1987)

temperature, Θ, conductivity is an activated process, the carriers having to be excited from the localized sites where they were trapped by polarization of the lattice around them. The mobility increases with increasing temperature (Cox, 1987)

$$\mu_e = \mu_o \exp(-E_e^F / kT) \tag{3.14}$$

Thus, the two models of conduction can be distinguished by measuring the mobility as a function of temperature via the Hall effect. At low temperatures (T < Θ), where the hopping probability is small, mobility should decrease with increasing temperature as in a normal semiconductor. The transition between the two conduction modes should be continuous.

The electronic conductivity may be given in a general formula as Eq. 3.15.

$$\sigma_e = \sigma_o \exp[-(E_e^F + E_e^M)/kT] \tag{3.15}$$

where E_e^F and E_e^M is energy for carrier formation and migration, respectively. For non-activated migration such as delocalized electrons, $E_e^M = 0$, whereas for activated migration such as hopping, $E_e^M \neq 0$ (Cox, 1987). For a semiconductor, $E_e^F \neq 0$, and $E_e^F = E_g \approx 2E_F$, where E_g is the energy gap between valence and conduction bands and E_F is the Fermi energy. The approximate relationship among conduction band edge (E_c), valence band edge (E_v), donor energy (E_d), acceptor energy (E_a), E_g and Fermi energy is summarized in Table 3.3.

Table 3.3. Fermi energy in semiconductors

	Intrinsic semiconductors	n-type semiconductors	p-type semiconductors
Fermi energy (E_F)	$\sim E_g/2$	$\sim (E_c - E_d)/2$	$\sim (E_v + E_a)/2$

Electrons in localized states in a disordered solid can move between defect site by a phenomenon known as variable-range hopping (Cox, 1987). The conductivity is predicted to vary at low temperatures according to the $T^{1/4}$ law of Eq. 3.16.

$$\sigma = A\exp[-(T_o/T)^{1/4}] \tag{3.16}$$

Other factors that affect electron mobility are impurities, solid solution, and plastic deformation. All three disrupt the short-range uniformity of the structure and decrease the mean free path of the electron.

Defects in a solid may not only provide electronic carriers; they are themselves potentially mobile species, and are involved in both diffusion and ionic conduction processes. For ionic constituents the mobility is related to the diffusion coefficient according to the Nernst-Einstein relation (Hayes and Stoneham, 1985):

$$\mu_i = \frac{(ze)D}{kT} = \frac{A_i}{T}\exp(-\mathrm{E_i^F}/\mathrm{kT}) \tag{3.17}$$

and ionic conductivity is given by

$$\sigma_i = \frac{\sigma_o}{T}\exp[-(\mathrm{E_i^F} + E_i^M)/\mathrm{kT}] \tag{3.18}$$

where E_i^F and E_i^M are the energies for charge carrier generation and migration, respectively. They are never equal to zero because both processes are activated. Both the ionic and the electronic conductivities of any ionic compound exhibit Arrhenius-type temperature dependencies. At constant temperature, however, the electronic conductivity may vary considerably with minor deviations from stoichiometric composition, while the ionic conductivity remains substantially constant due to higher mobility of electrons over ions, such as in CeO_{2-x}.

3.2.3. Effects of Defects on Conductivity

(1) Defect Creation and Classification

The introduction of a defect into a crystal always increases the lattice energy. However, this effect is counter-balanced by the entropy change arising from the introduction of defects, so that a crystal in thermodynamic equilibrium at a finite temperature always contains a finite concentration of defects (West, 1987). The type of defect that predominates in a particular material is clearly the defect which is easiest to form, i.e., the defect with the smallest enthalpy change and for which the free energy minimum is associated with the highest defect concentration. Generally, Schottky defects are formed in stoichiometric crystals where the cations and anions are of comparable size, while Frenkel defects predominate when the size of the cations and anions are appreciably different (Kofstad, 1983). BaO and CeO_2 are well known examples of stoichiometric oxides with Schottky and Frenkel defects, respectively (Hayes and Stoneham, 1985).

Various schemes have been proposed for the classification of defects as summarized in Table 3.4. Each of the schemes has certain advantages. Atomic defects create electronic defects if they possess a charge different from the charge normally present at that lattice point. In addition to these atomic/electronic defects, the possibility of free electrons or holes also needs to be considered. Atomic defects are important in the discussion of ionic conductivity, mechanical strength, and diffusion while electronic defects are important for electronic and optical properties.

Table 3.4. Defect classification

Criteria	Defects		References
Structure	Atomic		Kröger and Vink, 1956; Swalin, 1972
	Electronic		
Source	Intrinsic		Swalin, 1972
	Extrinsic		
Dimensionality	Point	Vacancy, Interstitial, Substitutional Foreign atoms	Hench and Dove, 1971; Hayes and Stoneham, 1985; West, 1987; Dieckmann, 1998
	Line	Screw dislocation Edge dislocation	
	Planar	External surface Internal surface	
	Volume	Stacking faults, Multiple phases, Order-disorder, Phonons, Pores	
Priority	Primary	Point	Swalin, 1972
	Secondary (extended)	Clusters, Pairs, Shear planes	
Composition	Stoichiometric	Frenkel, Schottky	West, 1987
	Nonstoichiometric		
Electroneutrality	Neutral		Cox, 1992
	Positive		
	Negative		

(2) Electrical Consequences of Defects

All defects break the regular periodicity of the ideal crystal lattice, and this has the consequence that electrons travelling through the crystal are scattered. Thus defects and impurities in metals tend to decrease the electrical conductivity. The same is true in non-metallic solids such as oxides, where electrons or holes thermally excited into bands are also scattered by defects. However, in non-metallic solids, defects and impurities can have much more important effects, since they can introduce extra electronic levels into the energy gap. The impurities increase the concentration of structural defects, which either increases the number of electrons or holes available for conduction or provides a lower energy path for migration of ions.

The electronic consequences of these defects is mainly determined by (a) the energies of the extra levels; and (b) the number of electrons that occupy them. Some of the different possibilities are illustrated in Fig. 3.7. The study of electrical conduction in solids is, to some degree, the study of defects, their concentrations, and their mobilities in the solid host medium.

Intentionally introducing electronic defects into crystals (doping) is a common approach to adjusting and improving the electrical properties. Doping of transition metal oxides to tailor electrical properties is extensively exploited in ceramic technology (Moulson and Herbert, 1990). Composition deviation from stoichiometry can be considered as doping by vacancies or self-doping. Some general rules are summarized as follows.

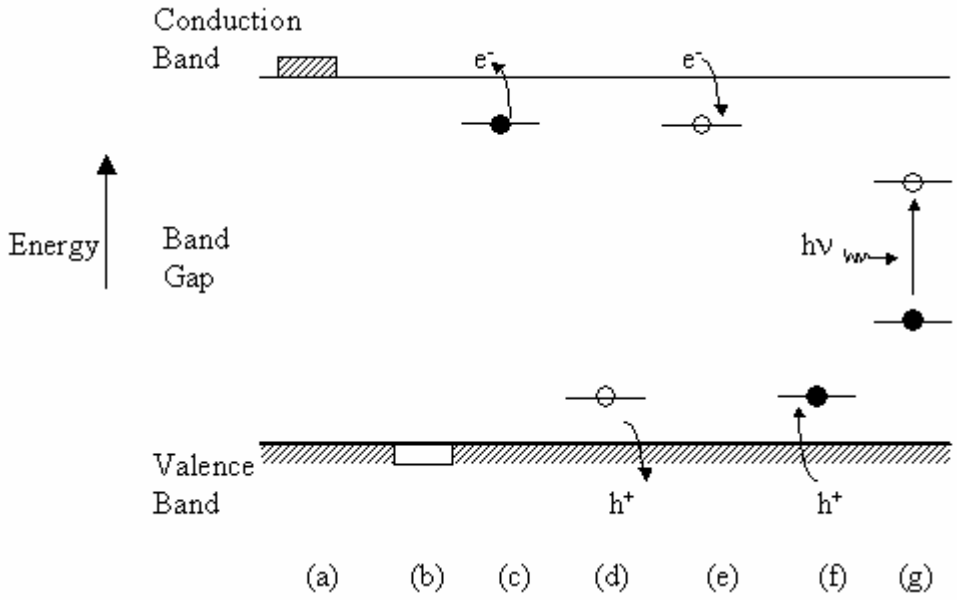

Fig. 3.7. Some electronic consequences of defects in non-metallic solids: (a) and (b) extra electrons or holes in conduction or valence band; (c) and (d) defect levels providing free electrons or holes by thermal excitation; (e) and (f) defect levels acting as traps for electrons or holes; (g) levels giving optical absorption at energies below the band gap (Cox, 1987)

(i) Not all dopants lead to an increase in electrical conductivity in the extrinsic region. Dopants of the same valence normally have no effect on electrical conductivity unless they are present in large concentration (West, 1987).

(ii) Dopants that lead to an increase in concentration of the mobile species result in an increase in electrical conductivity. Otherwise dopants cause a reduction in electrical conductivity. In both cases, dopants are usually of different valence from the normal atoms of the lattice (West, 1987; Tallan, 1974).

(iii) Introduction of equivalent quantities of donor and acceptor throughout the

crystal leads to electrical compensation, the electrons being replaced by the donor returning charge to the holes created by the acceptor (Hayes and Stoneham, 1985).

(iv) Doping level is limited by dopant solid solubility in the host solid oxide, which is controlled by (a) relative charge, (b) ionic radii, (c) coordination number or crystallographic structure, (d) electronegativity of the dopant as compared to the material being replaced, (e) the range of values of the oxygen partial pressure for which the oxide of the dopant is stable as compared to the range of stability of the host material (Kingery, 1976).

(v) Heavily doped semiconductors may become metallic (Hayes and Stoneham, 1985; Cox, 1992). The Mott criterion, or critical concentration for metallic conduction based essentially on the Hubbard condition W > U for hydrogenic orbitals, is (Mott, 1974)

$$n_c^{1/3} a_o > 0.25 \tag{3.19}$$

where n_c is the critical carrier concentration and a_o the radius of the dopant orbital given by $a_o = a_H \varepsilon_r / (m^*/m_o)$, where a_H the Bohr radius.

Many oxides containing transition elements may become, by doping, mixed-valence compounds according to the electroneutrality requirement. A number of oxides are known where mixed-valency is associated with high conductivity (Verwey et. al., 1950). However, mixed-valence compounds include not only the doped and nonstoichiometric (self-doped) compounds, but also many stoichiometric ones such as Fe_3O_4 and Ti_4O_7, which can be classified into three groups (Robin and Day, 1967; Day, 1979). The

interesting properties of mixed-valence compounds arise from the possibility of electron transfer between atoms with different oxidation states. The behavior can vary greatly, according to how easy such a transfer is, i.e., delocalized electrons, small polaron, and large polaron. In simple terms, if the interaction between the ionic centers is so strong that electrons can be transferred from site to site with no expenditure of energy we could have a metal. Electrons may be localized by the potential field of defects and by polaron formation. In this case, a large activation energy was needed, and the compound would be a semiconductor or insulator.

(3) Effects of Oxygen Partial Pressure on Conductivity

One of the most important features of conducting oxides is the effect on their behavior of the external oxygen pressure. It is assumed that the conductive behavior is controlled by the equilibrium between oxygen partial pressure, oxygen vacancies, oxygen interstitials, electrons and holes (Kofstad, 1983; Moulson, *et al.*, 1990). The effects of oxygen partial pressure on electrical conductivity can be discussed by using Kröger-Vink notation (Kröger and Vink, 1958). Table 3.5 gives various symbols and their meaning which are used in this discussion.

Table 3.5. Kröger-Vink notation for point defects in oxide MO

Symbol	Defect	Effective Charge
e'	Free electron	-1
$h^{\bullet}$	Free (electron) hole	+1
V_M''	M vacancy	-2
$V_O^{\bullet\bullet}$	O vacancy	+2
M_M	M at an M site	0
O_O	O at an O site	0
A_M'	A^+ dopant ion at M site (acceptor)	-1
$D_M^{\bullet}$	D^{3+} dopant ion at M site (donor)	+1
$M_i^{\bullet\bullet}$	M at an interstitial site	+2
O_i''	O at an interstitial site	-2

* normally $[e']$ = n, $[h^{\bullet}]$ = p

The effects of oxygen partial pressure on conductivity can be demonstrated by considering MO_2 with predominantly anti-Frenkel defects such as ZrO_2. Then the reaction of the oxide with the surrounding oxygen partial could be written as either Eq. (3.20) or (3.21):

$$\frac{1}{2}O_2 + V_O^{\bullet\bullet} + 2e' = O_O \tag{3.20}$$

$$\frac{1}{2}O_2(g) = O_i'' + 2h^{\bullet} \tag{3.21}$$

The equilibrium constant, K, can be obtained for both reactions, K_1 for Eq. (3.20) and K_2 for Eq. (3.21), respectively.

$$K_1 = (P_{O_2}^{-1/2}) / [V_O^{\bullet\bullet}][e']^2 \tag{3.22}$$

$$K_2 = (P_{O_2}^{-1/2})[h^{\bullet}]^2 [O_i''] \tag{3.23}$$

The intrinsic Frenkel defect equilibrium in ZrO_2 is given by the following reaction:

$$nil = O_i'' + V_O^{\bullet\bullet} \tag{3.24}$$

The intrinsic electronic equilibrium can be written by the following reaction:

$$nil = e' + h^{\bullet} \tag{3.25}$$

(i) In regions of intermediate partial pressure or near stoichiometric composition, $[O_i''] \approx [V_O^{\bullet\bullet}]$ and is independent of the oxygen partial pressure. Hence when the number of electrons is greater than the number of electron holes (n-type), the relationship becomes

$$[e'] \propto P_{O_2}^{-1/4} \tag{3.26}$$

and when the number of electron holes is greater than the number of electrons (p-type), we find that

$$[h^{\bullet}] \propto P_{O_2}^{1/4} \tag{3.27}$$

For oxides with a large band gap energy such as ZrO_2, ionic defects are predominant over the electronic defects (Heyne, 1973; Kofstad, 1983). Therefore, the oxide may exhibit appreciable ionic conductivities at or close to stoichiometry.

(ii) At low oxygen partial pressure, oxygen vacancies ($V_O^{\bullet\bullet}$) are the predominant defects. By considering the electroneutrality requirement,

$$2[V_O^{\bullet\bullet}] \approx [e'] \tag{3.28}$$

and combining with Eq. (3.22), we have:

$$[V_O^{\bullet\bullet}] \propto P_{O_2}^{-1/6} \tag{3.29}$$

$$[e'] \propto P_{O_2}^{-1/6} \tag{3.30}$$

(iii) At high oxygen partial pressure, oxygen interstitials (O_i'') predominate. Using the same argument as shown for low oxygen partial pressure with Eq. (3.23), we get

$$[O_i''] \propto P_{O_2}^{1/6} \tag{3.31}$$

$$[h^{\bullet}] \propto P_{O_2}^{1/6} \tag{3.32}$$

The approximation used above to describe the effect of oxygen partial pressure on the defect equilibria can be graphically presented in Fig. 3.8, which is known as a Brouwer diagram (Brouwer, 1954).

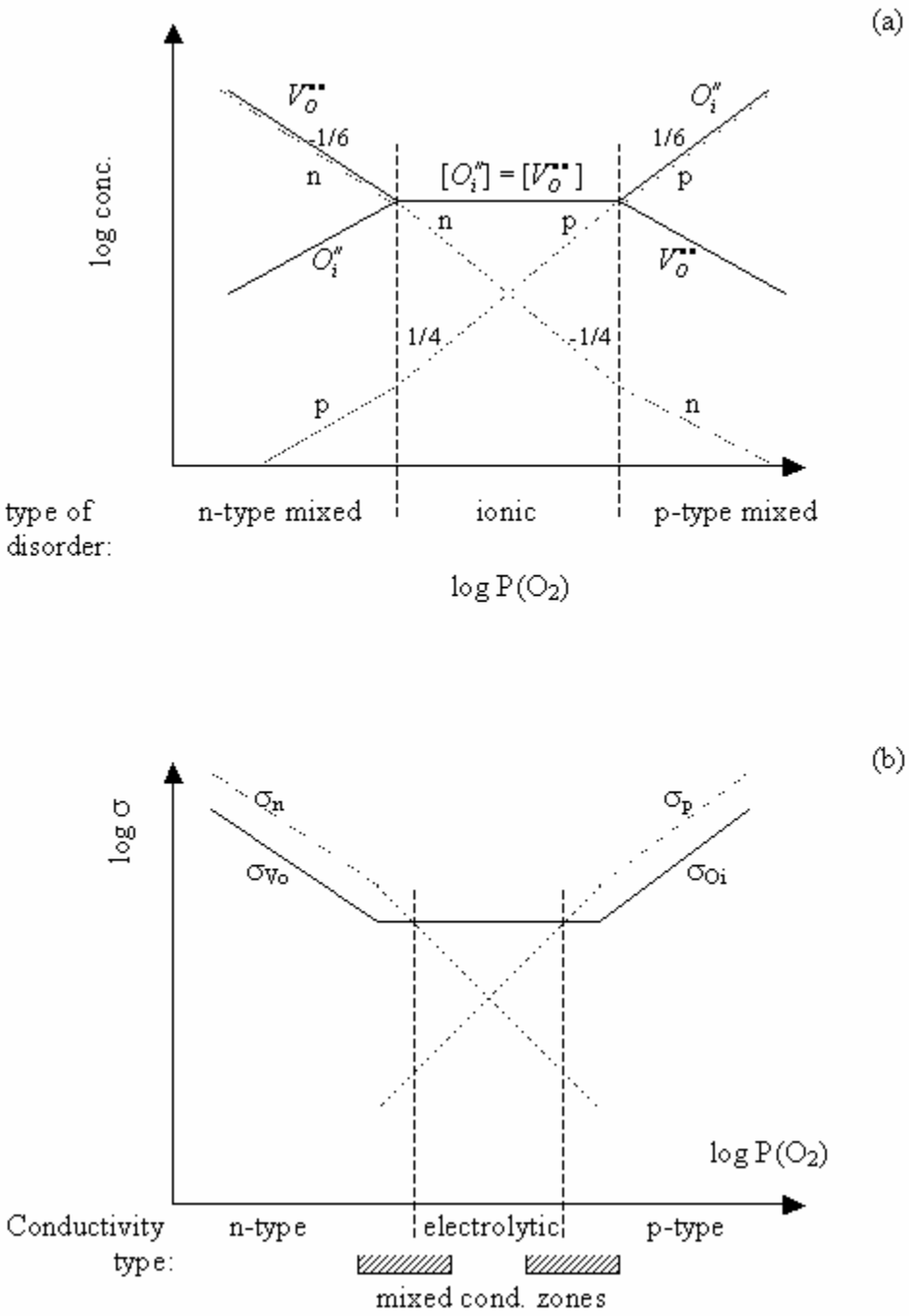

Fig. 3.8. (a) Defect diagram of undoped MO_2 with anti-Frenkel disorder. (b) Corresponding conductivity diagram (Gao and Sammes, 1999)

The process described above can be repeated for other defect equilibria such as in ternary compounds, where a similar diagram is observed (Smyth, 1977; Schmalzried, 1965). In addition, a three dimensional log σ versus log P_{O_2} and 1/T plot outlining the domain boundaries can also be considered based on the same principles (Patterson, 1971; Heyne, 1973). In this model, it is assumed that defects are isolated point defects, and interaction between defects can be neglected. However, since electronic defects all carry a net charge, they must interact through long-range Coulomb forces. The defect interaction may be significant as the defect concentration increases.

3.3. Conduction Characterization

3.3.1. Conduction Behavior and Types of Charge Carriers

The conduction behavior can be effected in different ways. N-type behavior, where n >> p, can be a produced by slight reduction of an insulator (such as TiO_{2-x}), by substitutional doping (for example of Ti by Nb in TiO_2), or by insertion (interstitial doping) of an electropositive element (such as Li in $Li_xV_2O_5$). In all these cases, the lattice defects present must carry a net positive charge to provide overall electroneutrality in the presence of the extra negative charge carriers. A natural consequence of this charge is to produce a bound impurity state for each electron. The energy required to excite the electron from the impurity state into the conduction band is known as the donor ionization energy E_d (Table 3.3.). Typical values of E_d in oxides are in the range of 0.1-0.5 eV (Cox, 1992). A similar consideration applies to p-type semiconductors, where electrons are removed by oxidation of a stoichiometric compound

($Ni_{1-x}O$) or by appropriate doping ($Li_xNi_{1-x}O$). The defect forms an acceptor center, having a net negative charge with respect to the perfect lattice, and traps the hole in an impurity state similar to that found with donors. In some cases metallic oxides are formed at high doping levels for either n-type or p-type semiconductors. The simple chemical picture of semiconducting properties suggests that n-type behavior should only be found in compounds where the metal can have an oxidation state lower than that in the pure solid. Conversely, p-type oxides are those where the metal can increase its oxidation state (Kingery, 1976). However, an n-type semiconductor may transfer to a p-type one depending on the predominant defects that are controlled by oxygen partial pressures as discussed in Section 3.2.3. (3).

Metallic or semiconducting behavior is usually determined by the opposite temperature dependence of electrical conductivity as discussed in Section 3.2.2. Under constant oxygen partial pressure, conductivity decreases for a metallic oxide and increases for a semiconducting one with increasing temperatures. The carrier type (n or p) in a semiconducting oxide was investigated by a number of different techniques and shown to give consistent results (Choi and Tuller, 1988).

(i) One way is to study the influence of oxygen partial pressure on the carrier concentration as discussed in Section 3.2.3. (3) (Kofstad, 1983). In the n-type case, carriers arise from reduction of the oxide, which should be favored by equilibrating the solid with low oxygen partial pressures. Thus the conductivities of the n-type oxides mentioned above are all found to fall with increasing oxygen partial pressure, as the temperature is kept constant. On the other hand, in p-type oxides, the conductivity depends

on oxidation of the solid, and rises with oxygen pressure.

(ii) The second is by the Hall effect (West, 1987). The Hall mobility, $\mu_H = R\sigma$, where R is the Hall coefficient and σ is the conductivity, is equal to the drift mobility, $\mu_D = \sigma/ne$, for crystals with non-localized electronic defects. However, for polar compounds where the electrons are trapped or localized at specific sites (polarons), the drift and Hall mobilities may have significantly different values (Emin, 1982; Emin, 1980).

(iii) The Seebeck effect is often more useful, as it is difficult to interpret Hall measurements on magnetic oxides with localized electrons (Heikes and Ure, 1961; Nowotny, 1997). Seebeck coefficients of semiconductors are generally much larger than those of metals, and often easier to interpret. Studies of the Seebeck effect, combined with conductivity measurement, give information about the concentration and sign of the majority carriers (Cox, 1992).

(iv) The other way of investigating a semiconducting oxide is by photoelectron spectroscopy. Binding energies of electrons in solids are usually measured from the Fermi level, and the position of the bands with respect to this level depends on the carrier type (Cox, 1992).

In addition to methods (ii) and (iii) above, charge carrier concentration may also be estimated by thermogravimetric analysis (TGA) (Gong et. al., 1991).

Table 3.6. Comparison of different techniques for measuring partial conductivity

Techniques	Principles	Advantages	Disadvantages	References
EMF Technique	$E_m = \frac{RT}{4F} t_i \ln \frac{P'_{O_2}}{P''_{O_2}}$ Measure E_m Calculate t_i	Relatively easier assembly	For $t_i > 0.1$	Kharton et. al., 1996
Polarized Cell Technique	Blocking I_i to measure σ_e, or blocking I_e to measure σ_i	Detection of deviations from ideal behaviors	Negligible or blocked oxygen transfer across free surface	Riess, 1997
Oxygen Permeation	Static ambipolar diffusion rate: $j = \left\| \frac{\sigma_e \sigma_i}{q(\sigma_e + \sigma_i)} \nabla \mu_M \right\|$	When $\sigma_e << \sigma_i$ or $\sigma_i << \sigma_e$, very smaller σ obtained	High temperature sealings required	Park and Blumenthal, 1989; Patrakeev et al., 1993
Non-stoichiometry Analysis	Brouwer diagram	Measure total conductivity using ac or dc method	Ionic σ may not occur in the range of controllable P_{O_2}	Riess, 1994

3.3.2. Separation of Electronic and Ionic Conductivity

Some techniques for measuring partial conductivity are summarized in Table 3.6. More details are available in the references listed.

CHAPTER 4

PHYSICAL AND CHEMICAL PROPERTIES OF SrTiO3

4.1. Structure and Synthesis of $SrTiO_3$

Strontium titanate has been studied extensively for technological applications as well as for basic science due to its electronic properties, chemical stability, and structural behavior. Most work on $SrTiO_3$ has been related to ambient or low temperature applications such as capacitors, photoelectrolysis of water, and superconductor substrate but the transport properties of $SrTiO_3$ may also be suitable for high temperature applications such as oxygen sensors. In addition, $SrTiO_3$ is thought to have an important role for immobilization of high-level radioactive waste.

$SrTiO_3$ was first reported in 1935 (Hoffman, 1935), but it was not until 1946 that its structure was determined from X-ray powder diffraction studies to be of the ideal perovskite type belonging to the cubic space group Pm3m (Megaw, 1946). This structure was verified (Swanson, 1954) and the refinement improved at room temperature from Rietveld analysis of high-resolution neutron powder diffraction data (Meyer et al., 1978). At room temperature, $SrTiO_3$ has the cubic perovskite structure, but at low temperatures it undergoes phase transitions to tetragonal (108K), orthorhombic (65K), and rhombohedral (35K) phase (Landolt-Börnstein, 1976).

Most electronic structure calculations for $SrTiO_3$ predict direct band gaps as shown in Fig. 4.1. The Sr 5s orbital contributes to empty orbitals at considerably higher energy than the Ti 3d, but not to the lower part of the conduction band. The octahedral surroundings of the corner Ti ions cause their 3d levels to split into t_{2g} and e_g sublevels while the O_{2p} orbitals split ($2p_\pi$, $2p_\sigma$) with the $2p_\sigma$ orbital lying lower in energy as its lobes point directly towards its electropositive neighbors. Due to their s-type overlap (Fig. 3.5a), bonding and antibonding–like bonds are formed where the antibonding bands have predominantly $3e_g$ ($\sigma^*(e_g)$) and 4σ (σ^*) character as illustrated in Fig. 3.5b. Also shown in the figure are the π–like bands resulting from the weaker $3t_{2g}$ and $2p_\pi$ interactions. The bands associated with Sr lie well above the other bands and no valence electrons associated with it, fall to the lower empty states. One establishes the position of the Fermi energy by filling the levels sequentially with the total number of valence electrons available per formula unit. Thus for $SrTiO_3$ there are 24 valence electrons which are accommodated totally by filling the lower bands of anionic character. Indeed Ti^{4+} has $3d^0$ character which places the Fermi energy midway between the highest occupied level (P_π) and the lowest empty band $\pi^*(t_{2g})$ as illustrated in Fig. 3.4b. Experimentally, the gap is measured to be 3.26 eV (Choi, 1986), resulting in the insulating nature of undoped, stoichiometric $SrTiO_3$.

The existing phase information for $SrTiO_3$ gives no indication of any solubility for excess TiO_2 as shown in Fig. 4.2 (Levin et al., 1969). When the strontium content of $SrTiO_3$ is increased it forms a series of compounds having the generic formula SrO-

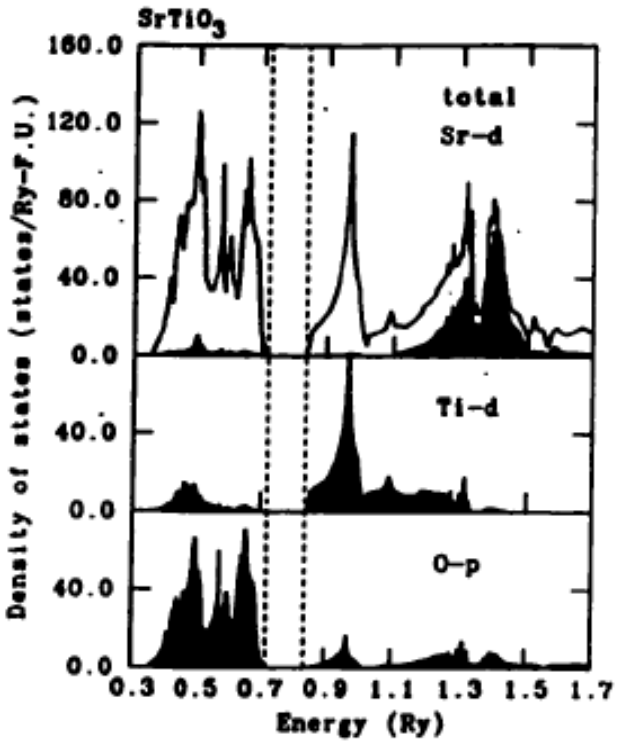

Fig. 4.1. Calculated total and partial densities of states for $SrTiO_3$. Dotted lines indicate the energy gap at the Fermi level (Takegahara, 1994)

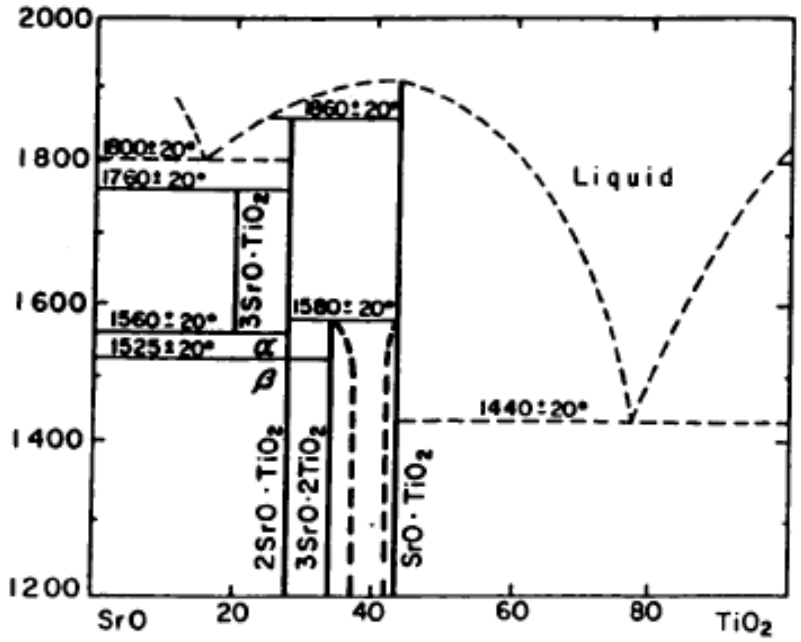

Fig. 4.2. SrO-TiO_2 phase diagram

$nSrTiO_3$ (Ruddlesden and Popper, 1958). The structures consist of two-dimensional perovskite slabs, n unit cells thick, separated by single layers of excess SrO in a NaCl structure sequence. This behavior is a demonstration of the high degree of energetic stability characteristic of the perovskite pattern. The systems try to retain as much of this pattern as possible, even when the composition deviates grossly from the ideal. It has been shown that most of the known high temperature superconducting oxides can be described in terms of an expanded Ruddlesden-Popper series with the generic formula $mAO\text{-}nABO_3$ (Smyth, 1988).

Many techniques have been employed to synthesize $SrTiO_3$, including solid state reaction, a liquid solution technique known as the Pechini method (Eror and Balachandran, 1981), and a wide variety of crystal growth techniques (Nassau and Miller, 1988). The Pechini method provides multi-component oxides with as high purity as the starting materials (no subsequent milling is required), homogeneity on the atomic scale, and a very small particle size of a few hundred angstroms. Strontium carbonate, lanthanum carbonate and tetra isopropyl titanate solution can be dissolved in an ethylene glycol-citric acid solution to prepare lanthanum-doped $SrTiO_3$. The rigid transparent polymeric glassy samples obtained by slow evaporation of the solution are then calcined at 1350^oC in air for a period of 8 to 12 hours. Ferric nitrate and aluminum nitrate dissolved in ethylene glycol-citric acid complex form the source for acceptor doping.

4.2. Electrical Properties of $SrTiO_3$

The important electronic properties include semiconductivity (Weise and Lesk, 1953; Frederikse et al., 1964; Balachandran and Eror, 1982), transition to metallic

state (Lee et al., 1975), superconductivity (Schooley et al., 1964; Hulm et al., 1970), and ferroelectricity (Bednorz and Muller, 1984; Gervais et al., 1987). $SrTiO_3$ was the first ternary oxide found to be superconducting, and perovskite-related structures are dominant in oxide superconductivity (Sleight, 1988). Selected data for $SrTiO_3$ are summarized in Table 4.1.

Table 4.1. Selected properties for $SrTiO_3$

Properties		Reference
Band gap (eV)	~ 3.3	Steinsvik et al., 1994
Mobilities (cm^2/V.sec)	$\mu_p = 8.9x10^5(T)^{-2.36}$ $\mu_n = 4.5x10^5(T)^{-2.2}$ $\mu_v = 10^4(T)^{-1}\exp(-0.86/kT)$	Denk et al., 1995
Lattice parameter, Å	3.905	Nassau and Miller, 1988
Density (g/cm^3)	5.12	
Thermal expansion Coefficient (K^{-1})	$10.4x10^{-6}$	
Thermal conductivity (mW/cm.K)	~52	
Young's modulus (Pa)	$2.65x10^9$	
Shear modulus (Pa)	$1.22x10^9$	
Dielectric constant at R.T.	~310	
Curie-Weiss law	χ=78300/(T-28)	

Weise and Lesk first studied the electrical transport properties of $SrTiO_3$ at different levels of reduction, and reported a semiconducting behavior (Weise and Lesk, 1953). The electrical conductivities increased with increasing degree of reduction of $SrTiO_3$. Similar results were achieved for other alkaline earth titanates such as $MgTiO_3$, $CaTiO_3$, and $BaTiO_3$. Upon reduction, the presence of some Ti^{3+} enables conduction by electron transfer from one ion to the other via an oxygen ion (double exchange). Based on the Hall mobility and Seebeck coefficient measurements in reduced and doped $SrTiO_3$ single crystals, the conduction was confirmed to be a band-type conduction process with an electron effective mass much greater than the free electron mass and low temperature Hall mobilities greater than 1000 $cm^2/V.sec$. (Frederikse et al., 1964). This implies that electron mobility is proportional to $T^{-3/2}$. This was supported by the observation that $SrTiO_3$ became superconducting at sufficiently high carrier concentrations and low temperatures (Schooley et al., 1964). The electron mobility of reduced and/or slightly donor doped single crystals shows a T^{-M} behavior, which is typical for a lattice scattering mechanism. M varies from approximately 2.7 at room temperature to 1.6 - 2 at 1000 K (Uematsu et al., 1984; Moos & Härdtl, 1996). In addition, the activation energy of carriers is zero (Cox, 1992), indicating that electron transport by a large polaron process is possible (Choi et al., 1986).

From the optical transmission studies on single crystal $SrTiO_3$ which was heated in vacuum, an energy gap of 3.15 eV was determined (Gandy, 1959). Yamada and Miller have determined the carrier concentration by Hall effect measurements for single-crystal $SrTiO_3$ quenched from equilibrium at various oxygen partial pressures (Yamada and Miller, 1973). Balachandran and Eror have reported a series of electrical conductivities

as a function of oxygen partial pressure for La-doped polycrystalline $SrTiO_3$ (Balachandran and Eror, 80; 81; 82). All of the reported studies on $SrTiO_3$ indicate that there is an extensive range at low oxygen partial pressures where the conductivity increases with decreasing oxygen partial pressure, characteristic of n-type conduction related to oxygen deficiency. In the range near one atmosphere, the conductivity increases with increasing oxygen partial pressure, characteristic of p-type conduction, related to a stoichiometric excess of oxygen. Similar results have been reported for the structural analog $BaTiO_3$ both in the polycrystalline and single crystal states (Long and Blumenthal, 1971; Chan and Smyth, 1976; Daniels and Härdtl, 1976).

$SrTiO_3$ can be converted into a highly semiconducting n-type material either by reduction as mentioned above or by doping with donors such as La^{3+}, Y^{3+}, and Gd^{3+} on the Sr-site and Nb^{5+} on the Ti-site. Frederikse et al. investigated the electrical conductivity and the Hall and Seebeck coefficients of Nb doped single crystal $SrTiO_3$ over the temperature range 4.2-300 K. Tufte and Chapman studied Nb doped $SrTiO_3$ and measured the Hall mobility over the temperature range from 1.6 to 550 K (Tufte and Chapman, 1967). They concluded that Nb donor centers remain fully ionized down to 1.6 K. The Hall mobility of Nb and La doped single crystal $SrTiO_3$ was also studied at high temperature up to 1000 K in air (Frederikse and Hostler, 1967). The transport properties of highly La doped $SrTiO_3$ has been reported recently (Moos and Härdtl, 1996). No data on the conductivity of heavily doped $SrTiO_3$ with yttrium at high temperatures and in equilibrium with different oxygen partial pressures has been found in the literature.

Electrical conductivity of acceptor-doped $SrTiO_3$ also has been studied in the past. When $SrTiO_3$ crystals are doped with Ni (Müller et al., 1969; Mohapatra and Wagner,

1979), Fe (Carter and Okaya, 1960; Faughnan and Kiss, 1968), Al (Chan et al., 1981) Ni and Mo (Staebler, 1975), their EPR spectra show the positions occupied by these impurities. According to the EPR spectra the doped impurities are substituted on the cubic Ti^{4+} sites and axial sites. Electrical conductivity of Fe-doped and Ni-doped $SrTiO_3$ has been studied over a wide range of oxygen partial pressures at elevated temperatures (Steinsvik et al., 1994; Kim et al., 1985). Partial electronic and ionic conductivities have been determined for Fe-doped $SrTiO_3$ by means of concentration cell measurements and from the slope of the total conductivity versus oxygen partial pressure. All the samples are predominantly p-type electronic conductors at high oxygen partial pressures, n-type conductors at low, and mixed electronic/ionic conductors at intermediate oxygen partial pressures. All conductivities increase strongly with increasing Fe content, reflecting decreased activation energies for both electrons and oxygen vacancies.

Many transition metals have been used as dopants to study the electrical properties in $SrTiO_3$. Transition metal ions have multiple charge states giving a range of levels in the band gap separated by a few tenths of an eV, and this deep-level spectrum may be complex for electrical conductivity (Hayes and Stoneham, 1985). Some of the transition ions, substituting Ti^{4+} in $SrTiO_3$, are listed in Table 4.2. The charge states are listed in columns according to n, the number of 3d electrons. Highly positive states are limited by capture of electrons from the valance band; low positive charges are limited by loss of electrons to the conduction band.

Table 4.2. Available transition-metal ions to substitute for Ti^{4+} in $SrTiO_3$ where n is the number of d electrons (Hayes and Stoneham, 1985)

Host	n = 1	2	3	4	5	6	7	8	9
Substitute	Cr^{5+}		Fe^{5+}						
Ti^{4+} in	V^{4+}		Mn^{4+}	Fe^{4+}	Co^{4+}	Ni^{4+}			
$SrTiO_3$			Cr^{3+}		Fe^{3+}	Co^{3+}	Ni^{3+}		
					Mn^{2+}	Fe^{2+}		Ni^{2+}	

The existence of a perovskite phase of composition $Sr_{1-1.5x}La_xTiO_3$ in the ternary system $SrO\text{-}TiO_2\text{-}La_2O_3$ has been reported (Tien and Hummel, 1967). Although pure $La_{2/3}TiO_3$ could not be prepared in air, small amount of $SrTiO_3$ suffice for stabilization of this phase (Hennings, 1971). Similar relationships are found in $PbTiO_3$, in which a perovskite phase of the composition $Pb_{1-1.5x}La_xTiO_3$ can be produced (Hennings and Hardtl, 1970). Ordering phenomena have been observed at compositions containing more than 70 mol% $La_{2/3}TiO_3$ in $SrTiO_3$. These had been cooled slowly from 1400°C to room temperature. In all of these examples the large cation to small cation radius ratio was less than unity. Bouwma et al. reported that their sample of composition $Sr_{0.65}La_{0.35}TiO_3$ with radius ratio equal to unity consisted of two or more phases, one of which was a perovskite phase (Bouwma et al., 1976). They concluded that this composition lies outside the perovskite homogeneity range. Tofield and Scott reported that they were not able to obtain single phase materials of composition $Sr_{0.8}La_{0.2}TiO_3$ (Tofield and Scott, 1974). After firing in oxygen at 1500°C, reducing in hydrogen

at 1100°C and reoxidizing in air at 800°C, they found La_2O_3 lines were always present in their compound. The reduced and oxidized samples had no significant difference in lattice parameters (3.9084 Å and 3.9080 Å respectively). From this they concluded that La is only slightly soluble in $SrTiO_3$. In the structural analog $BaTiO_3$, up to 20 at% Ba may be substituted by La to maintain a single phase in fully oxidized materials (Eror and Smyth, 1970). No second phase was observed by either optical or x-ray diffraction studies. However, many metal-insulator transition studies for the system $Sr_{1-x}La_xTiO_3$ have indicated that $LaTiO_3$ can form a complete solid solution with $SrTiO_3$ for the whole composition range (Sunstrom et al., 1992; Maeno et al., 1990)

In an early explanation of the conduction mechanism, a hopping model was proposed for limited La doping in an assumed composition $Sr_{1-x}^{2+}La_x^{3+}Ti_{1-x}^{4+}Ti_x^{3+}O_3$. The disorder created by La^{3+} as a donor in $SrTiO_3$ should lend itself to description by Verwey's controlled valency model (Verwey, 1950). By this model, there would be compensation for the La^{3+} at Ba^{2+} sites by the creation of equal number of Ti^{3+} ions. The Ti^{3+} ions are then responsible for the increase in electrical conductivity. In this case the donor-dopant dominates the positive side of the electroneutrality equation and as a consequence the negative defect concentration would be independent of equilibrium oxygen activity. Similarly, the donor-dopant may be compensated by the formation of charged point defects that would also be independent of equilibrium oxygen activity. The controlled valency model is appropriate only for dopant concentration of a few tenths percent. Some other researchers have reported that carriers in the doped materials essentially originated from the donor rare earth ion replacing Sr^{2+} (Balachandran and Eror, 1982). In both models, no account was taken of the variation in oxygen vacancy

level caused by La doping.

$SrTiO_3$ may have a transition from the semiconducting to metallic state. The extremely high dielectric constants leads to very weak carrier binding and large donor radii (Cox, 1987). From the Mott criterion (Eq. 3.16) with the carrier effective mass $m^* = 12\ m_o$ and the static dielectric constant $\varepsilon_r = 220$ appropriate to $SrTiO_3$, one predicts an effective Bohr radius $a_o = 10$ Å and $n_c \sim 5 \times 10^{18}$ carriers per cm^3, not far from the observed 3×10^{18} (Schooley et al., 1964). The system $Sr_{1-x}La_xTiO_3$ has been widely studied for its metal-insulator transition (Sunstrom et al., 1992; Maeno et al., 1990). $LaTiO_3$ has an electrical resistivity of approximately 10^{-2} Ω-cm (Greedan and MacLean, 1978), which can be classified as a poor metal while $SrTiO_3$ is an insulator. The solid solution $Sr_{1-x}La_xTiO_3$ with $x = 0.2$ goes through a semiconductor-metal transition at approximately 190 K (Sunstrom et al., 1992).

4.3. Defects in $SrTiO_3$

The defect chemistry of $SrTiO_3$ is well established, and the relevant equilibrium constants for pure and doped $SrTiO_3$ are available as a function of temperature, oxygen partial pressure, and doping level as well as of the mobilities of ionic and electronic charge carriers.

The self-diffusion of ions has been studied in single crystal $SrTiO_3$. Walters and Grace investigated the diffusion of point defects in $SrTiO_3$ (Walters and Grace, 1967a). Paladino studied the oxidation kinetics of single crystal $SrTiO_3$ (Paladino, 1965). On the basis of oxygen self-diffusion and oxidation measurements, Paladino et al. concluded that

an oxygen vacancy defect model was applicable to $SrTiO_3$ at elevated temperatures. Walters and Grace examined the electrical conductivity and Seebeck coefficient of $SrTiO_3$ in water-hydrogen atmospheres for a narrow range of oxygen partial pressure (Walters and Grace, 1967b). They also concluded that an oxygen vacancy model was applicable to their results. A relatively high oxygen ion conductivity may be expected based on the mobile oxygen vacancies in $SrTiO_3$. From this point of view, $SrTiO_3$ has been studied as a mixed electronic and oxygen ion conductor (Noll et al., 1996). The pronounced mixed conductivity allows oxygen to be incorporated in the material and to change the intrinsic electronic properties significantly. Owing to the sensitive dependence of the electrical conductivity on the oxygen partial pressure, $SrTiO_3$ is used as an oxygen sensor withstanding high temperatures (Gerblinger and Meixner, 1991). The significant ionic conductivity together with the sluggish surface kinetics limits the stability of perovskite capacitor or actuator materials under voltage stress (Waser et al., 1990). Attempts have been made to detect the degree of ionic conductivity in $SrTiO_3$. Electrochromic experiments point to a substantial concentration and mobility of oxygen vacancies (Blanc and Staebler, 1971; Mohapatra and Wagner, 1979). Smyth et al. used the indication of the flattening in the $\log \sigma$ vs $\log P_{O_2}$ curve close to the intrinsic point to derive ionic conductivity data (Chan et al., 1981). Waser refined this procedure by deliberately freezing-in the ionic defect concentration of the samples and was able to extend the conductivity analysis to lower temperatures (Waser, 1991). In heavily Fe-doped $SrTiO_3$, electrical conductivities were measured as a function of oxygen partial pressure at elevated temperatures (Steinsvik et al., 1994).

The defect structure of $SrTiO_3$ when the Sr to Ti ratio is at variance from 1:1 was

also studied (Eror and Balachandran, 1982). The deviation from the ideal Sr to Ti ratio was found to be accommodated by the formation of neutral vacancy pairs ($V''_{Sr}V^{\bullet\bullet}_{O}$) in $SrTiO_3$, which is similar to the case in $BaTiO_3$ (Eror and Smyth, 1978; Chan and Smyth, 1976). The results indicate that the single-phase field of $SrTiO_3$ extends beyond 50.505 mol% TiO_2 at elevated temperatures.

A defect model has been proposed for doped $SrTiO_3$, assuming that it can be treated as a mixture of SrO and TiO_2 (Chan et al., 1981). Dopant reacts with the individual binary oxide according to the dopant-site in the perovskite. Therefore, the defects in a ternary system can be treated as those in the binary case. Theoretical calculations have been reported very recently for defect energies, solubility and mobilities of dopants in $SrTiO_3$ (Crawford and Jacobs, 1999). These results indicate that in undoped $SrTiO_3$, transport proceeds via the migration of oxygen vacancies formed from Schottky defects, as concluded by Paladino et al. (1965) from their studies of oxygen diffusion in single crystal $SrTiO_3$. The calculated activation energies for diffusion are 0.76, 4.27, 14.33eV for $V^{\bullet\bullet}_{O}$, V''_{Sr}, and V''''_{Ti}, respectively.

CHAPTER 5

EXPERIMENTAL PROCEDURES

5.1. Sample Preparation

In achieving the objective of finding a single-phase fuel cell anode material, a large number of oxide compounds, mainly complex perovskites, were synthesized and characterized. High temperature solid state reaction was used for synthesis. The techniques for analysis of material properties including electrical conductivity are described in this chapter. The starting materials are listed in Table 5.1. To eliminate hydration effects, some starting powders were heated beforehand in air ($SrCO_3$ at 200^oC, La_2O_3 at 800^oC). Complex perovskite compositions were balanced for charge by choosing an appropriate ratio of higher and lower valent cations or by balancing higher valent cations with cation vacancies.

Mixtures of the starting materials were ground and pressed into 6 mm tablets at 5000 psi, and sintered on Al_2O_3 substrates in air or controlled atmospheres at 1400^oC for 10 - 20 h. The controlled atmospheres were either high purity argon or forming gas (7% H_2 + Ar). The synthesis was carried out with intermediate regrinding. Additional pellets were made for X-ray analysis. The samples for four-point conductivity measurement were formed into cylinders of about 6 mm diameter and 1.5 cm long.

Table 5.1. List of starting materials for studies

Compound	Purity %	Particle Size (mesh)	Supplier
$SrCO_3$	99.999	-325	Cerac
$SrTiO_3$	99	-200	Tam Ceramic
TiO_2 (rutile)	99.5	-325	Cerac
Y_2O_3	99.99	-200	Johnson Matthey
La_2O_3	99.99	-200	Johnson Matthey
CeO_2	99.9	-200	Cerac
Pr_6O_{11}	99.9	-325	Cerac
Sm_2O_3	99.9	Powder	Alfa Inorganics
Nd_2O_3	99.9	-200	Johnson Matthey
Gd_2O_3	99.9	-200	Cerac
Yb_2O_3	99.9	Powder	NUCOR Corp.
Sc_2O_3	99.99	Powder	Johnson Matthey
MgO	99.95	-325	Cerac
Al_2O_3	99.99	1-15 μm	Alfa Inorganics
V_2O_5	99.9	-200	Aldrich Chemicals
Cr_2O_3	Analytical reagent	-200	British Drug Houses
MnO	99.9	-100	Cerac
Co_3O_4	99.5	-325	Cerac
Fe_2O_3	99.9	1-15 μm	Alfa Inorganics
NiO	99.995	-100	Cerac
Cu_2O	99.9	-200	Cerac
ZnO	99.99	Powder	Johnson Matthey
Ga_2O_3	99.995	-325	Johnson Matthey
ZrO_2	99.9	-200	BDH Chemicals
Mo_2O_3	99.9	-200	Cerac
W_2O_3	99.7	-40	Johnson Matthey
SnO_2	99	Powder	Cerac

5.2. X-ray Diffraction

Phase identification of synthesized samples was performed by X-ray diffraction on a Nicolet 12 automated diffractometer using Cu Kα radiation. X-ray analysis was also done following conductivity measurements in reducing atmospheres to determine the stability of a sample.

A Guinier-Hägg camera (IRDAB Model XDC700) with Cu $K\alpha_1$ radiation was used for cell parameter determination of selected samples of Y-doped $SrTiO_3$. High purity silicon powder was used as internal standard to correct for film shrinkage or stretching during processing. The films were measured with a KEJ Instruments Model LS20 laser line scanner interfaced with a PC which produces directly a digitized data file. The data were converted to accurate d-spacings with the program SCANPI. The lattice parameters were extracted from this data using the least squares refinement program LSUDF.

5.3. Thermogravimetric Analysis (TGA)

The oxygen vacancy concentration was determined by thermogravimetric analysis in a Netzsch STA 409 thermal balance under an atmosphere of flowing air at 1000^{o}C. The method is based on the weight change observed as a function of temperature or time. The error in the experimental weight gain is estimated to be ±0.05 percent.

5.4. Atmosphere and Temperature Control

A gas mixture of carbon monoxide and carbon dioxide, controlled by an MKS mass-

flow controller, type 1159B and an MKS readout, type 247C, was used to fix different oxygen partial pressures. The effective oxygen pressures can be adjusted by adjusting the ratio of CO and CO_2 gases according to the equilibrium:

$$CO_2 = CO + \frac{1}{2}O_2 \tag{5.1}$$

The resulting oxygen partial pressure of a CO/CO_2 mixture is a function of the Gibbs energy of reaction (5.1):

$$\Delta G^o = -RT \ln K = -RT \ln \frac{P_{CO} P_{O_2}^{1/2}}{P_{CO_2}} \tag{5.2}$$

Kinetics may become a limiting factor as the temperature is decreased. Furthermore, the control of the oxygen partial pressure with the aid of reaction (5.1) is no longer possible if the oxygen pressure is equal to or falls below the equilibrium oxygen partial pressure of the reaction:

$$2CO = C + O_2 \tag{5.3}$$

If this is the case, carbon precipitation will occur.

Fig. 5.1 shows the oxygen partial pressure as a function of CO/CO_2 ratio at different temperatures (Gaskell, 1981). As can be seen from Fig. 5.1, the effective range of control, which can be achieved at 800°C, is 10^{-14} to 10^{-20} atm of oxygen partial pressure.

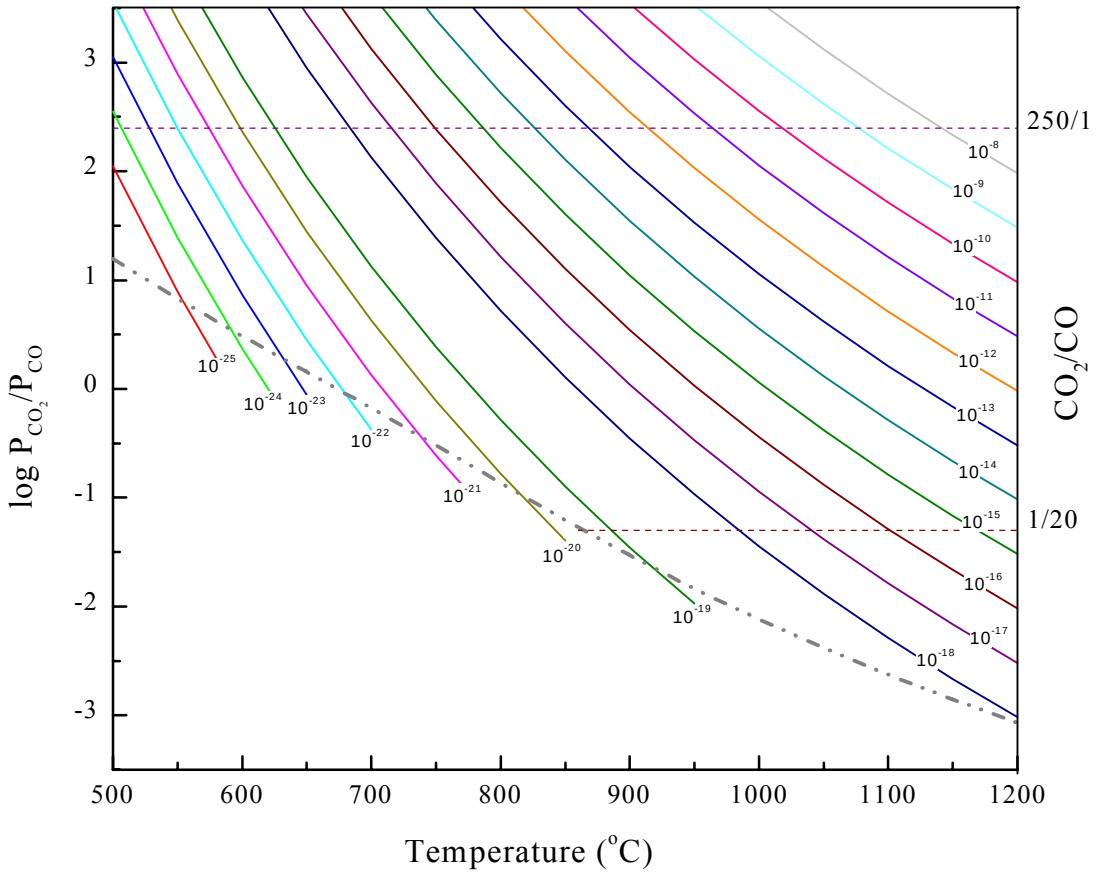

Fig. 5.1. Calculated oxygen partial pressure as a function of CO/CO_2 ratio at different temperatures

After the gases have been metered, they are passed through a mixing chamber of glass beads to ensure complete homogeneity before entering the furnace. The gases enter at the bottom of the vertical-reaction tube assembly and exit via a water bubbler to the fume hood.

5.5. Electrical Conductivity Measurement

5.5.1. Four-Probe Measurement

The conductivity was measured by a standard four-probe dc method (van der Pauw, 1958). The four-probe method is best suited to materials having moderate to high conductivities. With this method the effect of non-ohmic contacts or barrier layers can be overcome. The basic system used is shown in Fig. 5.2. The sample was placed in a holder, and external platinum leads were attached to both ends. The external leads were connected to a Keithley 225 current source providing a current of 0.1 A. Wires were wrapped around the samples approximately 2 mm from either end, and connected to an HP 34401A multimeter. The internal leads were used to measure the voltage drop across the sample, and consisted of chromel wire for measurement in air, and copper for measurement under reducing conditions. Gold and platinum wires were also used, and could be employed for all oxygen pressures. The input impedance of the multimeter is 10^{10} ohms which is much higher than the specimen resistance (<10 ohms). It assured that no significant current flowed in the voltage-measuring leads. Therefore, there is no voltage drop across the resistance associated with the voltage contacts and this resistance will not influence the conductivity measurement. If the current *I* through the specimen

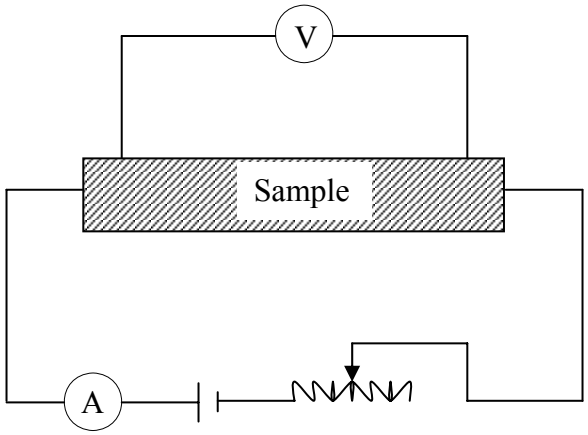

Fig. 5.2. System used for the four-probe conductivity measurement.

and the voltage across two inner probes are measured, the specimen conductivity is given by

$$\sigma = \frac{Il}{VA} \tag{5.4}$$

where A is the cross-sectional area of the specimen and l is the separation of the two inner probes. In order to eliminate the polarization effects due to the electrode and grain boundaries, the voltage was measured with the current in both forward and reverse directions, and the conductivity was calculated from the average values. The conductivity was measured as a function of oxygen partial pressure in the temperature range 600-900^{o}C. All the measurements were taken after the gas mixture had been allowed to equilibrate for at least one hour, and no significant change in conductivity was

observed.

To confirm the system reliability, the conductivities of CeO_2 were measured at 800°C over a range of oxygen partial pressures. An excellent agreement can be seen in Fig. 5.3 for these results and the data reported earlier (Tuller et al., 1979; Blumenthal et al., 1971). A zirconia-based oxygen sensor was used to monitor the oxygen partial pressure by Blumenthal's group.

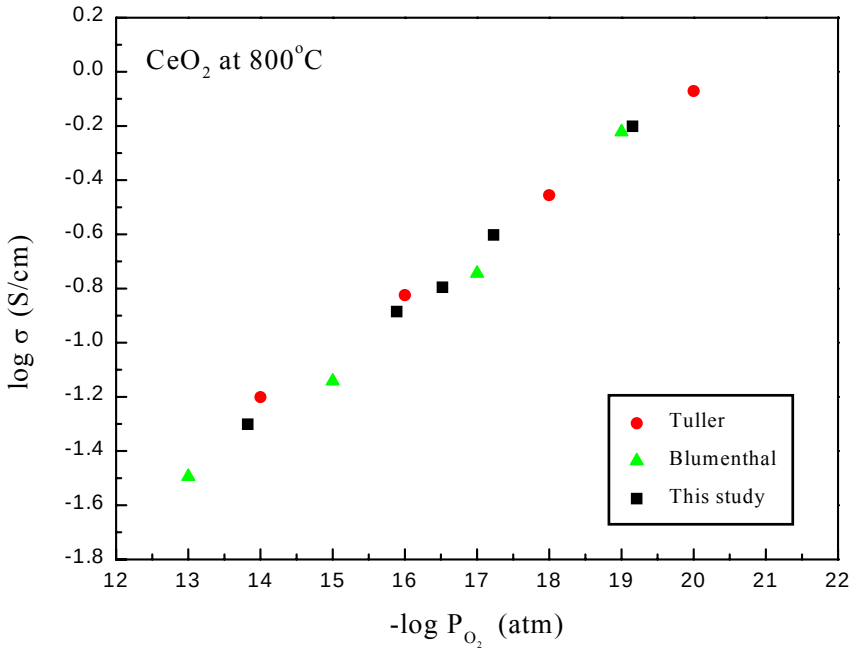

Fig. 5.3. Electrical conductivities versus oxygen partial pressures for CeO_2 at 800°C

5.5.2. Impedance Spectroscopy

A computerized impedance analysis system, a Frequency Response Analyzer (Solartron 1260), was used to determine the bulk, the grain, and the grain boundary resistance. The impedance measurements were performed in the frequency range from 10 MHz to 1 mHz at temperatures ranging from 300 to 900^{o}C in air or controlled atmospheres.

Impedance spectroscopy (IS) is a technique commonly used to measure the bulk and both the electrode and the grain boundary characteristics (Macdonald, 1987). Analysis of small-amplitude ($V<kT/q$) ac impedance data can yield estimates of bulk conductivity of new materials free from the electrode polarization effects that plague steady-state dc measurements. Under favorable conditions, detailed analysis of impedance data for homogeneous materials can also yield accurate estimates of microscopic parameters such as mobility, dielectric constant and electrode reaction rate constants (Duncan, 1956). The disadvantages of IS are primarily associated with possible ambiguities in interpretation. The requirements for the IS to be successful are a homogeneous sample and minimum effect of noise such as induction from long lead wire and coiled heating element. For bulk property measurements, electrode effects should be minimized as far as possible.

The impedance spectroscopy of a material is compared to an equivalent circuit in order to assign values to its electrical processes. Charge transfer processes for grain, grain boundary, and electrode under a small signal exhibit a response that can be described as a capacitor and a resistor in parallel. The impedance, defined as the response of capacitors and resistors to an ac signal, is

$$Z(\omega) = \frac{R}{1 + i\omega RC}, \quad i = \sqrt{-1} \tag{5.5}$$

where $\omega = 2\pi f$, f is the signal frequency, $0 \leq \mathrm{Re}Z \leq R$, and $0 \leq -\mathrm{Im}Z \leq R/2$, with

$$(\mathrm{Re}\, Z - R/2)^2 + (\mathrm{Im}\, Z)^2 = (R/2)^2 \tag{5.6}$$

Eq. (5.6) shows that plotting –ImZ versus ReZ, known as a Cole-Cole plot, forms a semicircle with a radius R/2, centered around R/2 on the real axis. In combination with other elements that contribute to the impedance, the center may be shifted from that point. In general, each semicircular arc corresponds to a lumped RC combination: a point on the real axis represents a lone resistor, a vertical line represents a lone capacitor, and a quarter circle with a 45^o line represents a Warburg impedance which is the electrical analog of a diffusion process (Fig. 5.4). The resistance values can be gotten from the intercepts on the real axis, and the capacitance values can be calculated by:

$$C = \frac{1}{R\omega} \tag{5.7}$$

where R and ω correspond respectively to the values of resistance and frequency at the highest point in the semicircle.

Impedance measurement has been successful in qualitative as well as quantitative determination of equivalent circuits and therefore provides much better insight into the transport mechanism. In principle any such equivalent circuit may be represented by a Voigt model. Although a three layer Voigt model is very often used to describe a measurement, the actual circuit may be quite complicated and depend on the exact nature

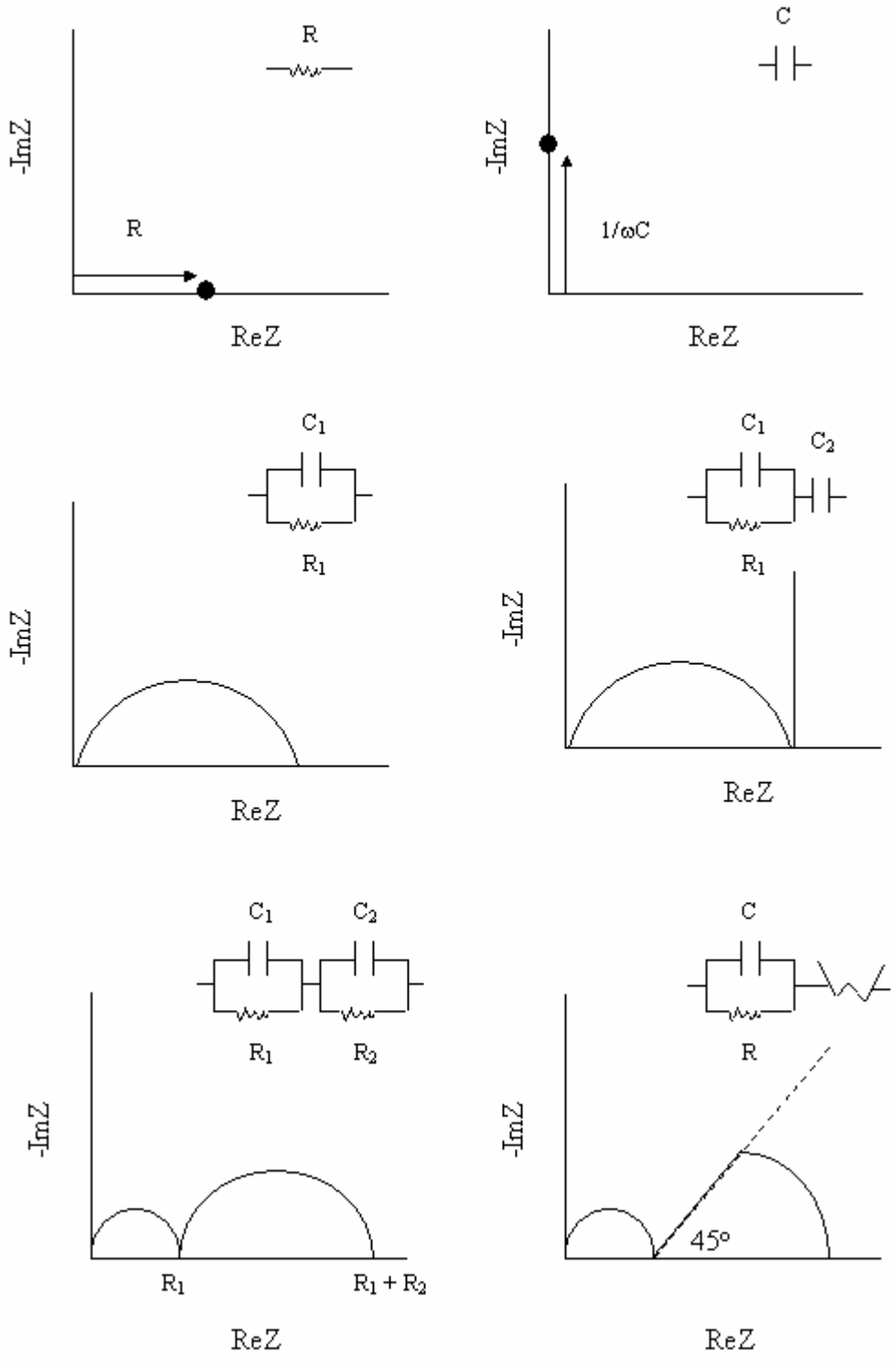

Fig. 5.4. Schematic impedance diagrams for some simple RC circuits

the transport mechanism. McDonald has proposed a five-layer Voigt model (Fig. 5.5. a) in which each of the RC sections corresponds to one of the following five impedances: (1) bulk or intragrain impedance (B), (ii) intergrain impedance (G), (iii) electronic impedance of the electrode (E), (iv) absorption reaction impedance (A), and (v) Warburg diffusion impedance (D). An impedance diagram for such a system will result in a series of connected arcs (Fig. 5.5.b). Each arc is associated with a single impedance provided the relaxation time ($\tau = RC$) of these processes differs at least by two orders of magnitude. Since each of these relaxation processes follows Arrhenius behavior, impedance measured as a function of frequency and temperature enables a determination of activation energy for each. In practice, however, it is quite common that all five arcs may not be observable at the same time. The relative sizes will also vary greatly depending on the experimental conditions. In general, the absorption impedance and the electronic impedance are too small to be observed for a pure solid electrolyte.

When the impedance plot is sufficiently detailed and the various contributions resolved, one can determine the various resistances, capacitance, and diffusion process parameters. Care must be taken in analyzing the data as different equivalent circuits can yield the same or very similar impedance plots (Macdonald, 1987). It may therefore be meaningless to use sophisticated programs for fitting complicated equivalent circuits comprising many elements and to look for best fit if the data are not sufficiently accurate, which is usually the case. It is then advisable to guess at as simple an equivalent circuit as possible that can be justified electrochemically for describing the supposed processes in the cell and fit its parameters.

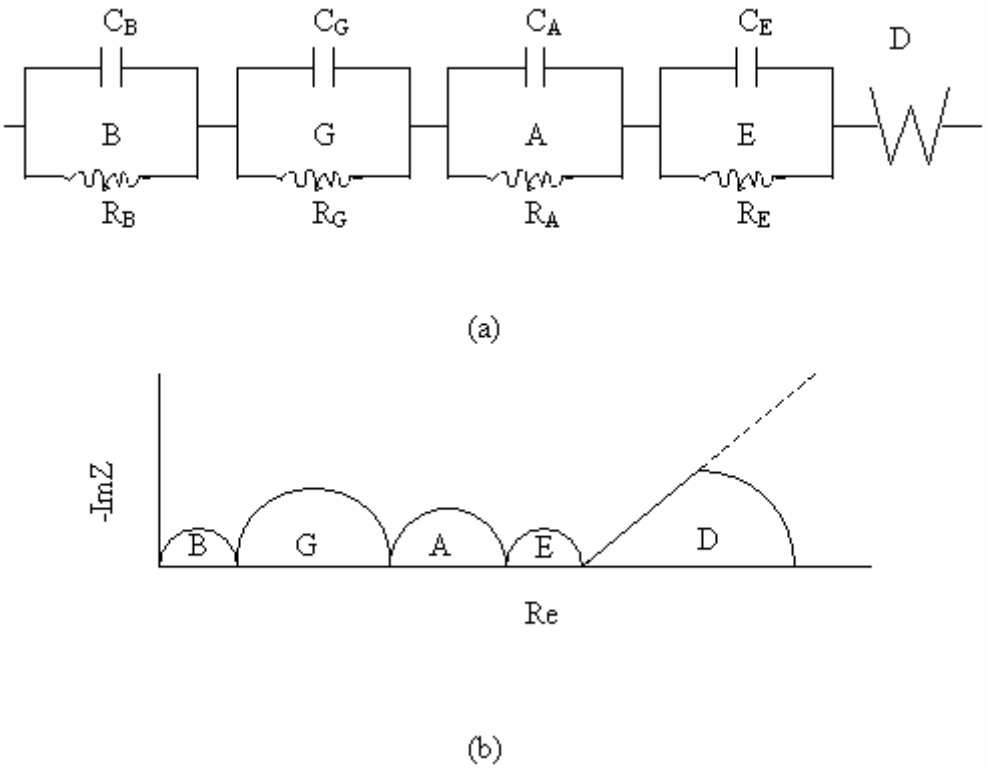

Fig. 5.5. Equivalent circuit (a) and impedance diagram (b) for a solid placed between two-plane parallel electrodes (Macdonald, 1976)

To assist in identifying the phenomena that determine the ac impedance spectrum one can vary parameters that affect the relaxation processes differently. The typical parameters are temperature, oxygen partial pressure, dc voltage superimposed on the ac, length of sample, and grain size. Raising the temperature will enhance the contribution of the process with the higher activation energy. Lowering the oxygen partial pressure will magnify the oxygen diffusion limitation and the corresponding impedance. Applying a dc voltage does not affect the impedance of components that are ohmic, but changes the impedance of the non-ohmic components. For a diffusion-limited process, the dc bias increases the ac impedance. Increasing the length of the sample and keeping

the nature of the electrodes the same should increase the bulk impedance linearly with length, but should not change the electrode impedance. Increasing the grain size reduces the total grain boundary area per unit volume and should therefore reduce the impedance associated with the grain boundaries.

The shape of the impedance plots may deviate from that expected for the simple RC and Warburg elements. There are different reasons for deviations (Macdonald, 1987). Typical reasons are rough surfaces, constriction resistance, and distribution of elements with different characteristic parameters, mainly in the bulk. The constriction resistance is due to a smaller contact area of the electrode than the nominal electrode area. At low frequencies the capacitance reflects the actual contact area, while at high frequencies the capacitance reflects the area of the electrode material which may be larger. Thus the contact can not be described by a single capacitance (Fleig and Maier, 1995).

5.6. Seebeck Coefficient Measurement

The Seebeck coefficient (or so-called thermopower) of doped $SrTiO_3$ was measured between 50 and 300 K. The sample was a rod 6 mm in diameter and 6 mm in length, which was sintered in a gas mixture of 7% H_2 in Ar at 1400^{o}C for 10 h. In the determination of Seebeck coefficients, two fundamental quantities must be measured, the temperature gradient across the sample, ΔT, and the corresponding voltage, V, that results. The instrument and the data extraction process are described below.

The instrument used for this measurement was built at the Brockhouse Institute for Materials Research at McMaster University. A schematic diagram of the sample holder is shown in Fig. 5.6. The sample is sandwiched between two copper heads A

and B that are in thermal contact (but electrically isolated) with base stage C. The holder is placed in a sealed chamber with a CTI Inc. Model 21C closed cycle refrigerator. The copper heads A and B consist of a 6 Ω ceramic resistor that serves as heater, respectively, while C has a wire wound Ni-Cr 25 W cartridge heater. The temperature gradient across the sample can be controlled by varying the power to the heaters in heads A and B while keeping the temperature of the base C constant. The chromel versus Au-0.07%Fe thermocouples and the two copper wires for voltage measurement are attached to the sample with silver paste.

In order to determine the Seebeck coefficients at various temperatures, the sample is allowed to equilibrate at each temperature setting. One end of the sample is held at a constant temperature, T_1, while the other end T_2 is allowed to vary in the range of $T_1 \pm 5$ K in δT (2 K) steps. At each δT step in the temperature profile, the sample is allowed to reach equilibrium at which point the temperature difference, ΔT, and the voltage, V, are measured several times for statistical averaging. Once the temperature profile ($T_1 \pm 5K$, δT) has been swept, the sample is heated to the next temperature and the measurement is repeated. The data collection is computer controlled via a standard RS232 serial interface. The Seebeck coefficient, S, at each temperature, is then extracted from the gradient of the average voltage (V) versus the temperature difference (ΔT) obtained at each δT step.

Thermocouple

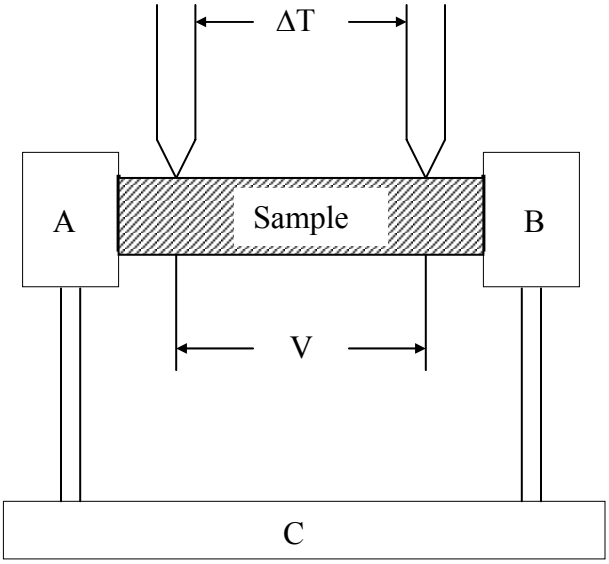

Fig. 5.6. Sample holder for thermopower measurement

5.7. Magnetic Susceptibility Measurement

Magnetic susceptibility measurements were carried out on a Quantum Design superconducting quantum interference device (SQUID) magnetometer. All of the samples were sintered pellets with a typical sample size of 300 mg. Susceptibility measurements were taken in the temperature range 5-300 K with an applied magnetic field strength of 1000 Oe.

5.8. Scanning Electron Microscope (SEM)

The fracture microstructures of yttrium-doped $SrTiO_3$, as prepared under reducing condition, were examined using a Philips 515 scanning electron microscope. No coating was applied to the sample surface.

CHAPTER 6

INITIAL MATERIALS INVESTIGATION

6.1. Selection of Materials

Compound oxides have been targeted as the most likely SOFC anode materials because they can simultaneously transport oxygen ions and electrons, thus being less prone to the problems of coking (Metcalfe et al., 1992) and sulfur poisoning (Katz et al., 1975). In particular, the perovskite structure with a host of possible B-site cations including Ti, V, Nb, Mo, and W offers many useful features for potential anode materials, including mixed valence states, the mobility of oxygen ions, and the stabilization of noble metal oxides in high dispersion (Galasso, 1969).

The perovskite structure has been central to many of the recent developments in solid state chemistry, including fuel cell cathodes, colossal magnetoresistance, and high-temperature superconductivity. Specific compositions with optimized properties have been developed for applications in SOFCs and as potential catalysts for environmental applications. The progress in these research areas has relied on the ability of the ABO_3 composition to be varied extensively by atomic substitution or by non-stoichiometry on either cation or anion sublattices. One can vary the interaction between the metal and oxygen orbitals in this structure by substituting the large A-site cation and/or the transition metal ion to obtain a wide variation in properties. Electronic and ionic

conductivities, sintering behavior, and catalytic performance are all modified by such substitutions. The combination of an inactive A-site ion (such as La^{3+} or Sr^{2+}) with an active B-site ion (such as Co^{3+}, Mn^{3+}, Ti^{3+}, Ru^{4+}) in the perovskite structure provides *a priori* choice of the active site contributing to catalysis (Voorhoeve et al., 1977). Moreover, the properties of the B-site ion and its neighbor oxygen ions can be modified by the choice of the A ion. Generally perovskite oxides are electronic conductors. Ionic conduction is not favored because of the close-packed nature of the perovskite structure. However, substitution by lower valence ions of fixed valence at the B site in ABO_3 oxides creates oxygen vacancies for charge neutrality. This increase in the oxygen ion mobility and conductivity has been observed by many researchers (Browall et al., 1976; Steinsvik et al., 1994; Takahashi, 1971).

In this work, the preliminary criteria for materials selection are the formation of a single phase, electrical conductivity under anodic conditions, and stability upon reduction and oxidation at high temperatures. Based on these considerations, mixed perovskites such as $LaNi_{1-x}M_xO_3$ (M = Ti, V, Nb, Mo, W), $La_{1-x}Sr_xVO_{3-\delta}$ (x = 0.2, 0.3), $SrV_{1-x}Ti_xO_{3-\delta}$ (x = 0, 0.5), and doped $SrTiO_3$ have been studied. Under reducing conditions, these compounds are capable of sustaining one or two d-electrons in the transition metal ions that enables electronic conduction. Nickel was included in all initial compositions because of its superior catalytic properties. Subsequent studies focussed on vanadium containing perovskites since $SrVO_3$ is known to be a good electronic conductor in reducing atmospheres. These two groups of oxides (the nickel compounds and vanadates) were evaluated according to the material selection scheme in this chapter, while doped $SrTiO_3$ is discussed in detail in the following chapters.

6.2. Stability

Out of a total of approximate 100 attempted perovskite compounds, only the ones listed in Table 6.1 were determined by XRD to be single phases, and their electrical conductivities were further examined.

$LaNi_{1-x}M_xO_3$ can be regarded as a solid solution of $LaNiO_3$ or as a compound containing enough M to ensure charge balance when all nickel is in the Ni^{2+} state. Although $LaNiO_3$ becomes unstable at an oxygen partial pressure of 10^{-2} atm and 1000°C, $LaNi_{1-x}M_xO_3$ mixed perovskites (M = Ti, V, Nb, Mo, W) were stable under typical fuel cell anode conditions (oxygen partial pressure range of 10^{-20} – 10^{-14} atm at 800°C). This was confirmed by x-ray diffraction (Fig. 6.1). No change in the x-ray diffraction pattern was observed after the materials had undergone conductivity measurements under reducing conditions.

Powder x-ray diffraction patterns for samples of $La_{1-x}Sr_xVO_{3-\delta}$ (Fig. 6.2) showed no change before and after conductivity measurement. $LaVO_3$, one end member of $La_{1-x}Sr_xVO_{3-\delta}$ solid solution, was determined by TGA to be stable to an oxygen partial pressure of less than 10^{-12} atm at 1000°C (Nakamura et al., 1979). $SrVO_{3-\delta}$, as the other end member of $La_{1-x}Sr_xVO_{3-\delta}$, could be formed from the reduction of $Sr_2V_2O_7$ at 1250°C in forming gas ($Ar:H_2$ = 93:7). This was confirmed by XRD as shown in Fig. 6.3 (a).

Table 6.1. Preparation conditions and conductivity of selected perovskite compositions studied

Composition	Preparation	Conductivity (S/cm)		
		Air at 25°C	Air at 800°C	7%H_2 at 800°C
$LaNi_{0.67}Nb_{0.33}O_3$	1450°C 9h in air	1.2×10^{-2}	9.5×10^{-2}	2.1×10^{-3}
$LaNi_{0.5}V_{0.5}O_3$	1500°C 9h in air	5.4×10^{-2}	8.82	0.79
$LaNi_{0.5}V_{0.25}Ti_{0.25}O_3$	1400°C 9h in air	8.4×10^{-3}	5.8×10^{-1}	3.2×10^{-2}
$LaNi_{0.75}Mo_{0.25}O_3$	1400°C 8h in air	2.7×10^{-1}	5.98	1.2×10^{-2}
$LaNi_{0.75}W_{0.25}O_3$	1400°C 9h in air	5.4×10^{-2}	4.8×10^{-1}	9.4×10^{-3}
$La_{.9}Ce_{.1}Ti_{.5}Ni_{.5}O_3$	1500°C 5h in Ar			3.0×10^{-4}
$La_{.9}Ce_{.1}Ti_{.55}Ni_{.45}O_3$	1500°C 5h in vaccum			0.12
$La_{.7}Ca_{.3}Ti_{.6}Ni_{.4}O_{3-\delta}$	1550°C 8h in Air			7.4×10^{-4}
$SrVO_{3-\delta}$	1400°C 6h in 7%H_2	3.2×10^{3}		1.0×10^{3}
$SrV_{0.5}Ti_{0.5}O_{3-\delta}$	1450°C 8h in 7%H_2	7.1×10^{3}		9.7×10^{-1}
$La_{0.8}Sr_{0.2}VO_{3-\delta}$	1450°C 6h in 7%H_2	1.2×10^{2}		4.5 x 10
$La_{0.7}Sr_{0.3}VO_{3-\delta}$	1450°C 6h in 7%H_2	3.0×10^{2}		1.2×10^{2}
$La_{0.9}VO_{3-\delta}$	1450°C 6h in 7%H_2	3.3		2.9

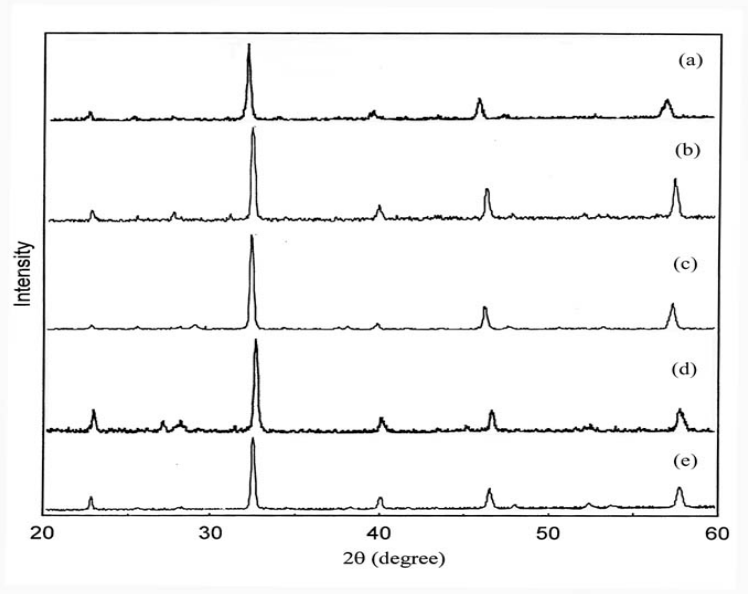

Fig. 6.1. Powder x-ray diffraction patterns for (a) $LaNi_{0.67}Nb_{0.33}O_3$, (b) $LaNi_{0.75}Mo_{0.25}O_3$ (c) $LaNi_{0.75}W_{0.25}O_3$, (d) $LaNi_{0.5}V_{0.5}O_3$, and (e) $LaNi_{0.5}V_{0.25}Ti_{0.25}O_3$

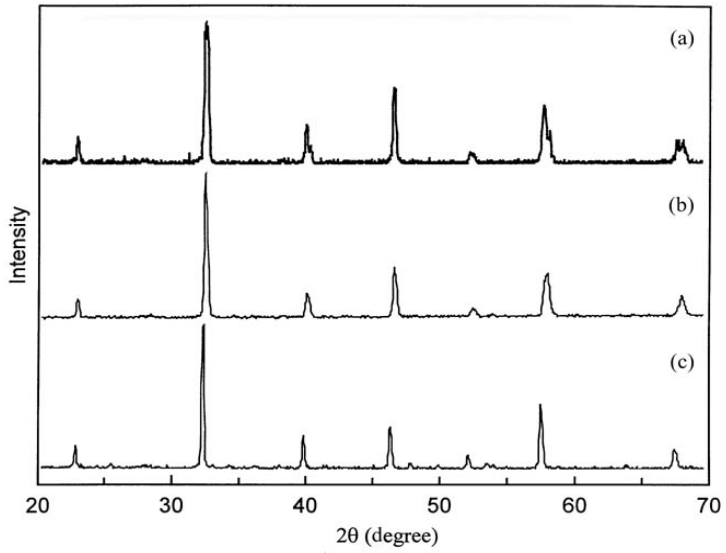

Fig. 6.2. Powder x-ray diffraction patterns for (a) $La_{0.7}Sr_{0.3}VO_{3-\delta}$, (b) $La_{0.8}Sr_{0.2}VO_{3-\delta}$, (c) $La_{0.9}VO_{3-\delta}$

However, $SrVO_{3-\delta}$ is stable only when the oxygen partial pressure is less than 10^{-17} atm at 800°C as indicated by the appearance of second phases when the oxygen partial pressure exceeded this limit. Additional phases shown in Fig. 6.3(d) were also found in doped $SrVO_{3-\delta}$, *i.e.,* $SrV_{0.5}Ti_{0.5}O_{3-\delta}$ and $SrV_{0.5}Zr_{0.5}O_{3-\delta}$, at higher oxygen pressure. The x-ray analysis for oxidized $SrVO_{3-\delta}$ is shown in Fig. 3(b). The major peaks correspond to $Sr_3V_2O_8$, an apatite phase isostructural with $Sr_3P_2O_8$. Liu and Greedan (1994) observed similar results for the Ba-V-O system. Based on their earlier studies, the phases in oxidized $SrVO_{3-\delta}$ are likely to be $Sr_3V_2O_8$ as the major phase and a vanadium-rich minor phase with the formula Sr_xVO_n ($x < 1$). Meanwhile, $SrVO_3$ has a high conductivity of $3x10^3$ S/cm at 25°C, but $Sr_3V_2O_8$ is an insulating compound wherein the vanadium ions are isolated in tetrahedral coordination.

6.3. Electrical Properties

Since addition of suitable ions may force part of the transition ion content into a lower oxidation state so as to maintain charge neutrality, thereby greatly modifying the conductivity behavior, a number of nominal perovskite oxide compositions were prepared as summarized in Table 6.1. Four-probe dc conductivity results of dense pellets obtained at 800°C over a range of oxygen partial pressures of 10^{-20} – 10^{-14} atm are shown in Fig. 6.4 for the $LaNi_{1-x}M_xO_3$ (M = Ti, V, Nb, Mo, W) samples. The conductivity in all the cases decreased with decreasing oxygen partial pressure, indicating p-type behavior.

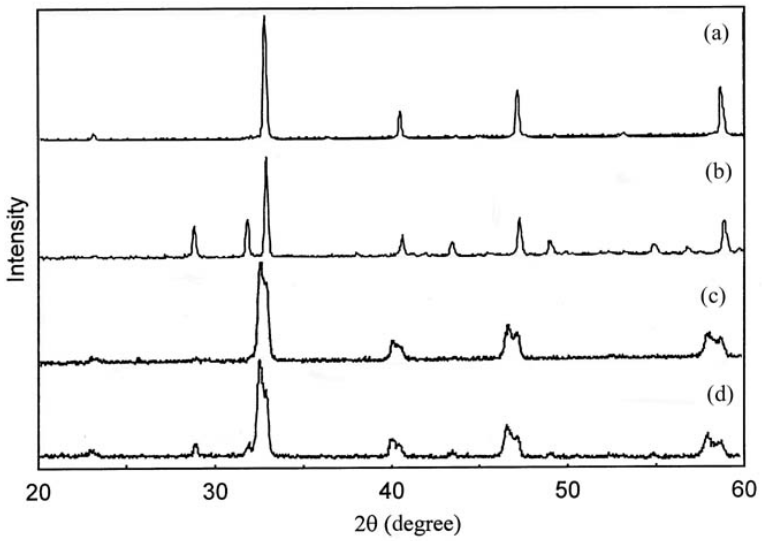

Fig. 6.3. Powder x-ray diffraction patterns for $SrVO_{3-\delta}$ (a) as-prepared, (b) oxidized during conductivity measurement; and $SrV_{0.5}Ti_{0.5}O_{3-\delta}$ (c) as prepared, (d) oxidized during conductivity measurement

In the case of transition metal compounds with residual d-electrons in the outer shell, higher oxidation states are more easily accommodated by the removal of one electron, thereby forming electron holes. For example, NiO reacts with oxygen to form cation vacancies.

$$2Ni_{Ni}^{x} + \frac{1}{2}O_2(g) = 2Ni_{Ni}^{\bullet} + O_O + V_{Ni}'' \tag{6.1}$$

$$\frac{1}{2}O_2(g) = O_O + V_{Ni}'' + 2h^{\bullet} \tag{6.2}$$

Assuming that nickel vacancies are doubly ionized, the equilibrium constant is given by

$$K = \frac{[O_O][V_{Ni}''][h]^2}{P_{O_2}^{1/2}} \tag{6.3}$$

Since the concentration of oxygen ions in the crystal is not significantly changed ($[O_O] \approx 1$) and the concentration of electron holes equals twice the concentration of vacancies, $2[V_{Ni}''] = [h^\bullet]$,

$$[h^\bullet] \propto P_{O_2}^{1/6} \tag{6.4}$$

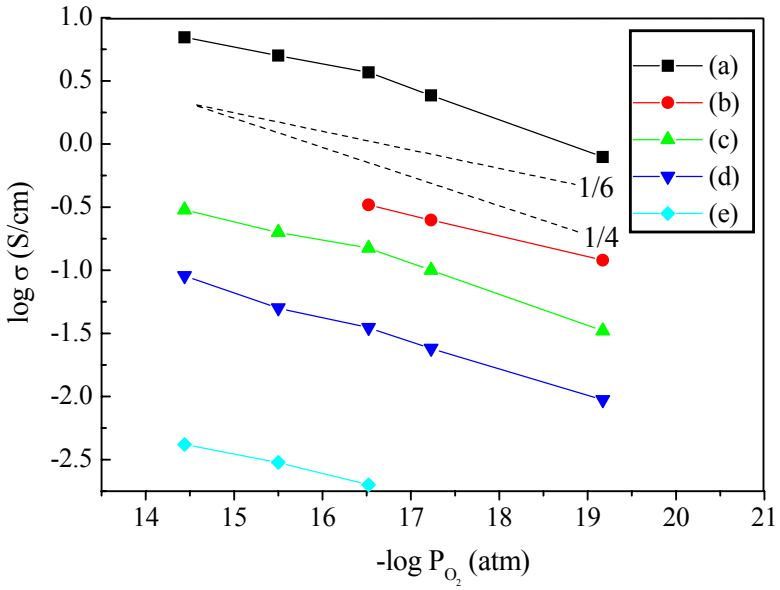

Fig. 6.4. The dependence of conductivity on oxygen pressure at 800°C for: (a) $LaNi_{0.5}V_{0.5}O_3$, (b) $LaNi_{0.75}Mo_{0.25}O_3$, (c) $LaNi_{0.5}V_{0.25}Ti_{0.25}O_3$, (d) $LaNi_{0.75}W_{0.25}O_3$, (e) $LaNi_{0.67}Nb_{0.33}O_3$

Alternatively, if nickel vacancies are singly ionized, we can obtain

$$[h^{\bullet}] \propto P_{O_2}^{1/4} \tag{6.5}$$

since the electrical conductivity is proportional to the concentration of free charge carriers and therefore to the oxygen partial pressure in the surrounding atmosphere. The same results are obtained if we assume oxygen vacancies dominate at low oxygen partial pressure and are filled by oxygen at high oxygen partial pressure, a situation more common with perovskites. In Fig. 6.4, we observe that the electrical conductivity is related to the oxygen partial pressure by a fourth to sixth root dependence, which indicates that both singly and doubly ionized nickel vacancies are present as the actual defect mechanism. This is consistent with the hypothesis that a mixed valence state of Ni^{3+} and Ni^{2+} might dominate the conduction process. In comparison with the oxide systems in Fig. 6.4, the highest electrical conductivity was observed for $LaNi_{0.5}V_{0.5}O_3$. The conductivity of $LaNi_{0.75}Mo_{0.25}O_3$ was found to have the second highest conductivity whose value was consistent with previous work (Subramanian, 1980).

In general, p-type behavior is observed for compounds containing transition metal ions with non-zero d-electron occupancy. Otherwise, the behavior is n-type (Kingery et al., 1976; Anderson, 1992). This division is shown on the periodic table (Fig. 6.5). When the outer valence shell of the ion has no d-electrons, the metal has reached its maximum oxidation state. However, under a reducing atmosphere, d-electrons could be recovered in the outer valence shell. For example,

$$Ti^{4+} + e' \xrightarrow{reduction} Ti^{3+} \tag{6.6}$$

The extra electrons may contribute to conductivity either by hopping between titanium ions of mixed valence, or by occupying the conduction band, giving rise to n-type behavior. This requires high concentrations of both tetravalent and trivalent titanium ions in the lattice (Mott, 1968).

Sc	Ti	V	Cr	Mn	Fe	Co	Ni	Cu
Y	**Zr**	Nb	Mo					
La	**Hf**	**Ta**	W	Re				

Fig. 6.5. Periodic table of transition metals forming oxides with n-type (shadow) or p-type (bold) behavior. Other elements shown do not change valence state in the fuel cell environment (suitable as electrolytes)

The equilibrium oxygen partial pressure and temperature determine the oxidation states of transition metals. The phase stability of selected oxides at 800^{o}C was calculated using FACT thermodynamic software (Bale et al., 1996) and is shown in Fig. 6.6. The phase boundaries in Fig. 6.6 shift towards the right when temperature is higher than 800^{o}C because lower oxidation states are more stable. The oxidation states of transition metals may be also influenced by crystal structure, especially in the case of pentavalent species when the coordination is difficult to accommodate such as $LaNi_{0.5}V_{0.5}O_3$. Note that the formation of $LaNi_{0.5}V_{0.5}O_3$ is possible in air. One explanation is that the perovskite structure might constrain the valence of vanadium to 4+, even in an oxidizing

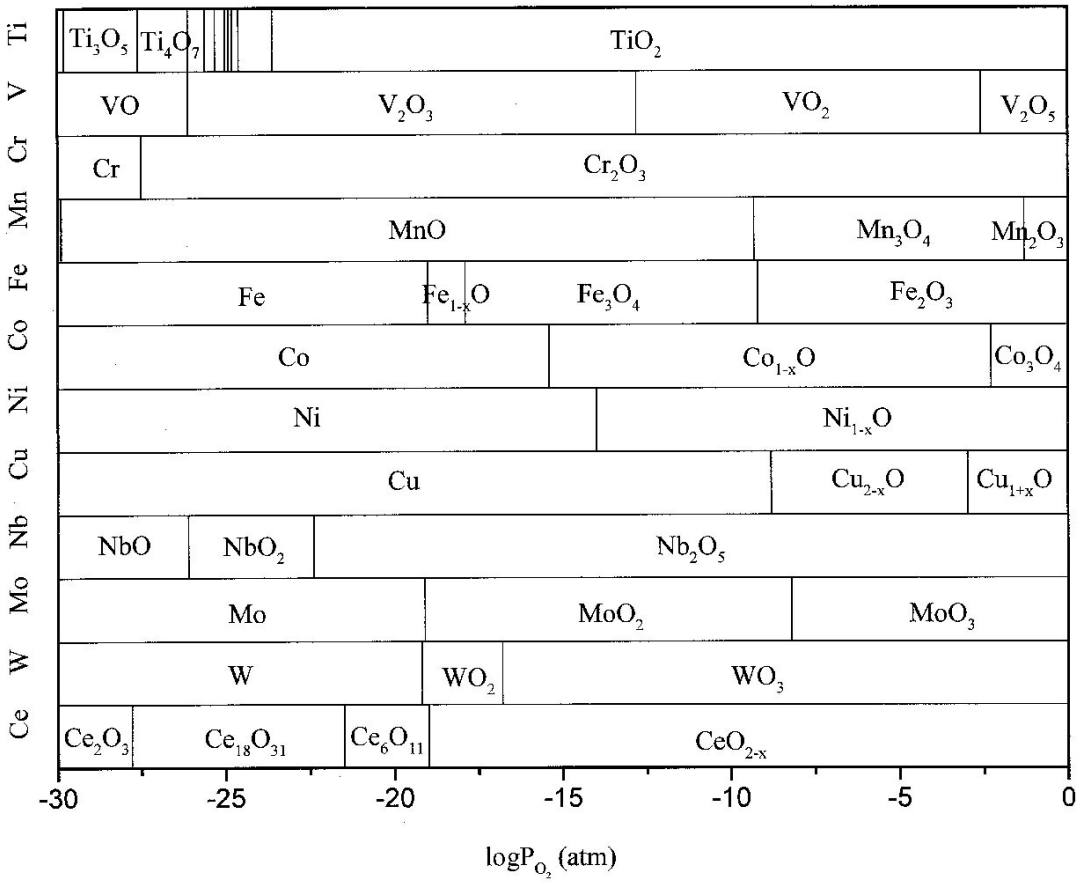

Fig. 6.6. Phase stability and oxygen partial pressure of selected oxides at 800°C

atmosphere. As is evident from Fig. 6.1, there exist two faint diffraction lines near 27° and 28° (2θ) that may indicate the presence of an impurity or second phase.

A comparison of the electrical conductivities at 25°C with those at 800°C in Table 6.1 shows that all of the single-phase samples prepared in air are semiconductors. In the case of $LaNi_{0.75}W_{0.25}O_3$ the results are in accord with earlier electrical conductivity studies (Alvarez, 1996).

The variation of electrical conductivity as a function of oxygen partial pressure at

800°C for $La_{1-x}Sr_xVO_{3-\delta}$ is shown in Fig. 6.7. The experimental data show that the conductivity of $La_{0.8}Sr_{0.2}VO_{3-\delta}$ and $La_{0.7}Sr_{0.3}VO_{3-\delta}$ increase slightly with decreasing oxygen partial pressure, indicating a weak n-type behavior. It is reported that the $La_{1-x}Sr_xVO_{3-\delta}$ system exhibits a composition controlled metal-insulator (M-I) transition in a temperature range of –196°C ~ 527°C (Dougier and Casalot, 1970). The metal-insulator transition occurs at $x \approx 0.2$. It is suggested that the incorporation of Sr^{2+} ions onto La^{3+} site leads to the formation of V^{4+} ions in place of V^{3+} that enhances conductivity in the system. However, no conductivity data are available for high temperature or over a range of oxygen partial pressures.

Since the $La_{1-x}Sr_xVO_{3-\delta}$ samples are unstable under more oxidizing conditions, and their electrical conductivities are not strongly dependent on the oxygen partial pressure, the variation of conductivity of $La_{0.8}Sr_{0.2}VO_{3-\delta}$ and $La_{0.7}Sr_{0.3}VO_{3-\delta}$ with temperature was measured in forming gas ($Ar:H_2 = 93:7$, $P_{O2} = 10^{-19}$ atm at 800°C) as shown in Fig. 6.8. The plots of conductivity versus temperature show a linear decrease with increasing temperature, consistent with semiconductor behavior and with Dougier's previous study (Dougier and Casalot, 1970).

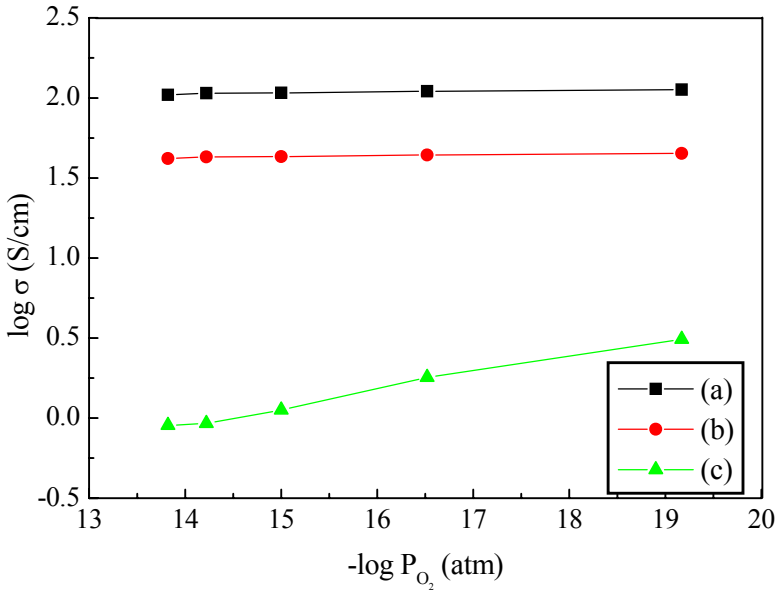

Fig. 6.7. The dependence of conductivity on oxygen pressure at 800°C: (a) $La_{0.7}Sr_{0.3}VO_{3-\delta}$, (b) $La_{0.8}Sr_{0.2}VO_{3-\delta}$, (c) $La_{0.9}VO_{3-\delta}$

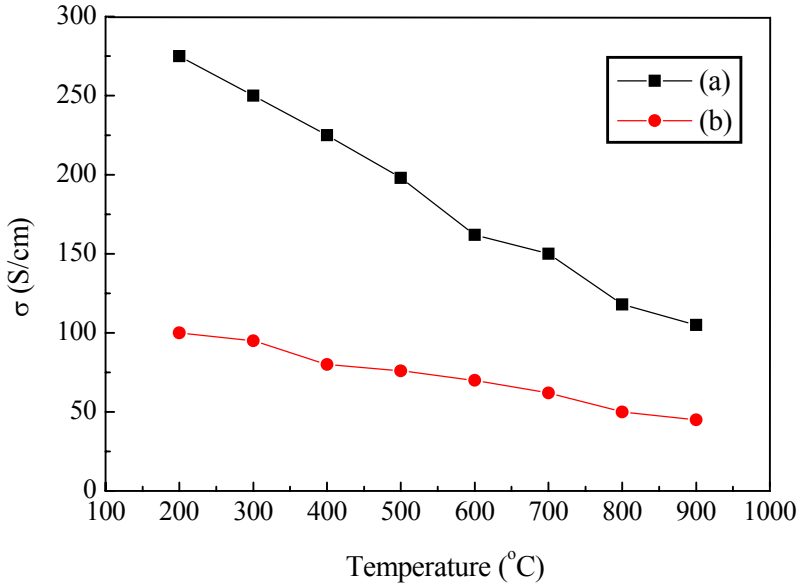

Fig. 6.8. Variation of conductivity versus temperature in forming gas (H_2 : Ar = 7 : 93) for (a) $La_{0.7}Sr_{0.3}VO_{3-\delta}$ and (b) $La_{0.8}Sr_{0.2}VO_{3-\delta}$

CHAPTER 7

DONOR-DOPED STRONTIUM TITANATES

7.1. Synthesis of Doped $SrTiO_3$

$SrTiO_3$ is commonly produced by the solid-state reaction of $SrCO_3$ with TiO_2 at temperatures of 1000°C – 1600°C by:

$$SrCO_3 + TiO_2 = SrTiO_3 + CO_2 \tag{7.1}$$

and ΔG^o is approximately –140 kJ with a weak temperature dependence.

Normally, pure $SrTiO_3$ has a low level of p-type conductivity in air at 800°C (about 10^{-4} S/cm) and an equivalent ionic conductivity. Doping on either the strontium or titanium site can increase the electronic conductivity of $SrTiO_3$. Appropriate dopants must have sufficient solubility, determined mainly by their size, i.e., large donor such as La on Sr-sites and small donor such as Nb on Ti-sites. Large donors were employed in this study, and two schemes have been reported to synthesize large donor doped $SrTiO_3$, given by Eq. (7.2) (Moos, et al., 1996; Balachandran and Eror, 1982) and (7.3) (Battle et al., 2000, Shirasaki et al, 1980; Tien and Hummel, 1967):

$$(1-x)SrCO_3 + \frac{x}{2}R_2O_3 + TiO_2 \rightarrow Sr_{1-x}R_xTiO_3 \tag{7.2}$$

$$(1-1.5x)SrCO_3 + \frac{x}{2}R_2O_3 + TiO_2 \rightarrow Sr_{1-1.5x}V''_{0.5x}R_xTiO_3 \qquad (7.3)$$

where R represents rare earth elements. The excess charge introduced by substitution of the rare earth can be compensated either by an increase in oxygen content, $Sr_{1-x}R_xTiO_{3+1/2x}$, or by electronic charge compensation through a change in valence, $Sr_{1-x}R_xTi^{4+}_{1-x}Ti^{3+}_xO_3$. Eror and Balachandran proposed that the rare earth dopant is accompanied by excess oxygen absorption (1981), that is accommodated by the formation of SrO layers in the perovskite. Eventually, the formation of SrO layers in perovskite results in rare earth compensation by Sr vacancies. However, the charge compensation in this formula may have other mechanisms such as segregation or second phase formation on the grain boundaries and bulk surface. After being reduced in moist hydrogen, the resistivity of $SrTiO_3$ with 1 mol% excess SrO at room temperature was 10^{10} Ω.cm or about three orders of magnitude higher than that of pure $SrTiO_3$. From the ESCA spectra, Aksenova et al. (1986) concluded that the protection from reduction is related to the formation of surface microphases that are close to Sr_2TiO_4 in composition (viz., $SrO.SrTiO_3$). The surface microphases shifted the reduction equilibrium toward lower partial pressure of oxygen at high temperature. The effect of the composition change on conductivity was also observed in this study and is discussed in Section 7.4.3. To eliminate the possible effect of extra SrO and therefore maximize the conductivity, Eq. (7.3) was used in this study, where *R* = La, Pr, Sm, Gd, Yb, Y, and the rare earth dopant is accompanied by Sr vacancies. Vacancies on the Sr-site in $SrTiO_3$ are preferred over Ti-site vacancies due to the low electrostatic potential of the Sr-site as demonstrated by Akhtar et al. (1995) Based on computer simulation studies, they concluded that the

intrinsic defect energy of V_{Sr}'', V_{Ti}'''', and $V_O^{\bullet\bullet}$ is 20.51, 82.23, and 18.16 eV, respectively. Interstitial defects are negligible in perovskites due to their close-packed structure.

7.2. Dependence of Electrical Conductivity on Donors

The donor dopants used in this study are listed in Table 7.1 together with the corresponding ionic radii in twelve coordination (Shannon, 1976) and Pauling electronegativity (www.webelements.com). Twelve-coordinate radii for Y^{3+} and Pr^{3+} were estimated based on the 11% increase from nine-coordinate radii for other rare-earth ions (Eylem et al., 1992). Rare earth doped titanates were prepared in forming gas (7%H_2 + 93%Ar) at 1400°C for 10 h according to the formula $Sr_{1-1.5x}R_xTiO_3$, and are listed in Table 7.2. All the samples were identified by XRD to be cubic perovskites, and all were black-blue in color, an indication of the presence of Ti^{3+}. The introduction of carriers on doping an oxide generally gives rise to strong absorption bands (Cox, 1992). If the absorption is strongest in the IR, a blue coloration is found, which frequently occurred with reduced or doped d^o oxides.

The electrical conductivity of 8 mol% rare-earth-doped titanates was measured by the dc four-probe method as a function oxygen partial pressures at 800°C (Fig. 7.1.). For comparison, the conductivity of 50 mol% La-doped $SrTiO_3$ is also given. Two separate batches with the same composition $Sr_{0.88}Y_{0.08}TiO_{2.97}$ were prepared with different processing. Their conductivities were consistent under the same test conditions, showing a high degree of reproducibility that can be obtained. (Fig. 7.2.). However, as discussed

Table 7.1. Properties of host and donor cations

Host and donors	Ionic radius (Å) (12-fold coordination)	Pauling Electronegativity (Pauling units)
Sr^{2+}	1.44	0.95
La^{3+}	1.36	1.10
Pr^{3+}	1.31	1.13
Sm^{3+}	1.24	1.17
Gd^{3+}	1.23	1.20
Y^{3+}	1.19	1.22
Yb^{3+}	1.16	

Table 7.2. Compositions of donor-doped titanates studied

Composition	Tolerance factor
$Sr_{0.85}La_{0.1}TiO_{3-\delta}$	0.998
$Sr_{0.25}La_{0.5}TiO_{3-\delta}$	0.997
$Sr_{0.88}Pr_{0.08}TiO_{3-\delta}$	0.998
$Sr_{0.88}Sm_{0.08}TiO_{3-\delta}$	0.996
$Sr_{0.88}Gd_{0.08}TiO_{3-\delta}$	0.995
$Sr_{0.88}Y_{0.08}TiO_{3-\delta}$	0.994
$Sr_{0.88}Yb_{0.08}TiO_{3-\delta}$	0.993

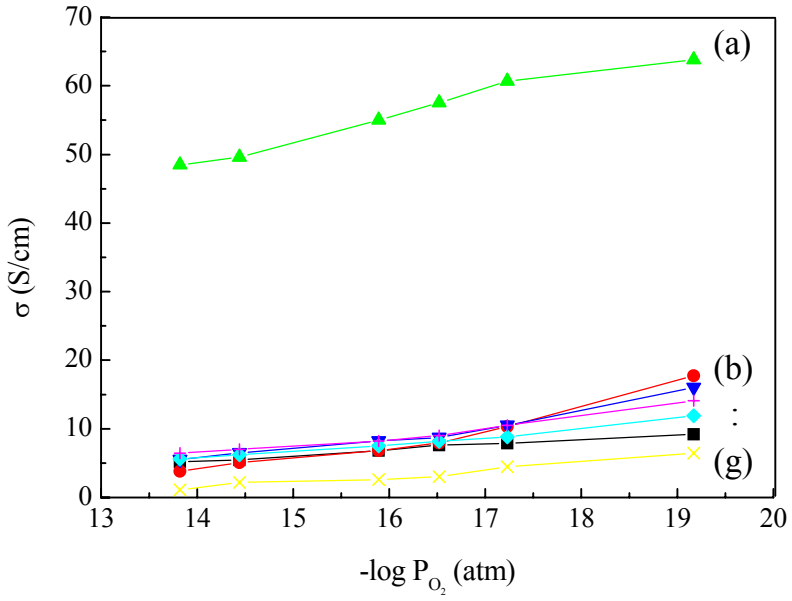

Fig. 7.1. Electrical conductivity as a function of oxygen partial pressures at 800°C for donor-doped titanates (a) $Sr_{0.88}Y_{0.08}TiO_{3-\delta}$, (b) $Sr_{0.25}La_{0.50}TiO_{3-\delta}$, (c) $Sr_{0.88}Yb_{0.08}TiO_{3-\delta}$, (d) $Sr_{0.88}Gd_{0.08}TiO_{3-\delta}$, (e)$Sr_{0.88}Sm_{0.08}TiO_{3-\delta}$, (f) $Sr_{0.85}La_{0.10}TiO_{3-\delta}$, (g) $Ca_{0.88}Y_{0.08}TiO_{3-\delta}$

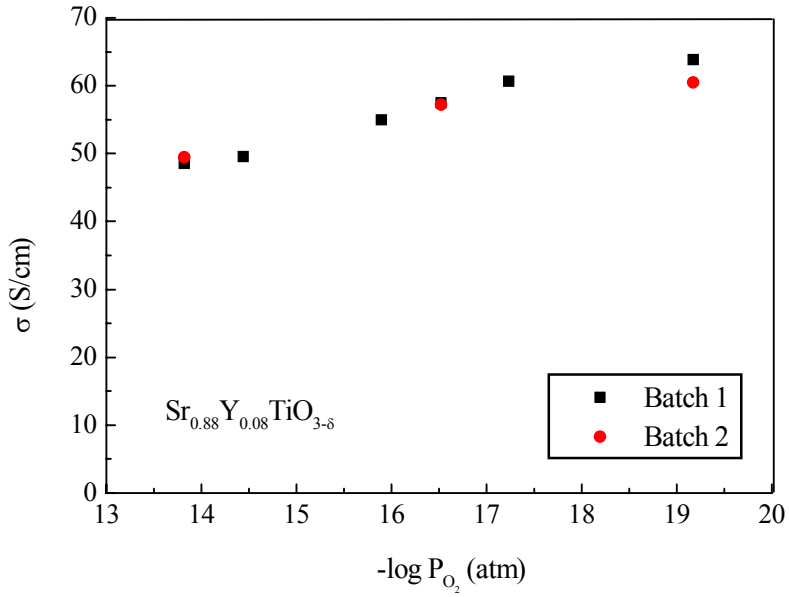

Fig. 7.2. Reproducibility of electrical conductivity for the same composition of $Sr_{0.88}Y_{0.08}TiO_{3-\delta}$ at 800°C

in Section 7.3.2, the reproducibility of conductivity is strongly related to the impurity level and degree of reduction. As we can see, Y-doped $SrTiO_3$ has much higher conductivity that the other rare-earth-doped titanates at 800°C in the range of oxygen partial pressures of 10^{-14} to 10^{-19} atm. The conductivity of all donor-doped titanates increase slightly when decreasing oxygen partial pressures, indicating an n-type conductivity predominated.

Electrical conductivity of donor-doped $SrTiO_3$ with Sr-site deficiency such as $Sr_{1-1.5x}R_xTiO_3$ may be influenced by factors such as excess strontium vacancies and properties of the rare-earth dopants, while reduction makes the case more complicated. It is well known that electron migration in the given compounds is strongly influenced by the differences in structure. As already mentioned in Chapter 3, the electrical properties in perovskite are mainly determined by the B-O interaction while the A-O interaction modifies the effect of the B-O interaction. The optimum conditions for the formation of a π-bond in ABO_3 perovskites are obtained for a B-O-B bond angle of 180°, which occurs only for the ideal perovskite. For example, the rare-earth titanates, $RTiO_3$, have the orthorhombic structure. Their physical properties are influenced by two factors: the chemical nature of the rare earth, such as electronegativity, and the degree of distortion of the perovskite unit cell that is related to the size of rare earth (Greedan, 1985; Bazuev and Shveikin, 1980). Since the covalence of the R-O bond increases with increasing atomic number of the rare earth owing to an increase in the electronegativity of R^{3+} (Table 7.1.), the Ti-O bond regularly weakens. On the other hand, the observed increase in the deformation of the perovskite unit cell along the series $RTiO_3$ also causes weakening of the Ti-O bond. Consequently, metallic conductivity is observed for R = La and Ce, and

all other *R* are semiconducting with activation energies increasing from 10^{-2} eV (Pr, Nd) to 10^{-1} eV (Gd, Y).

The Ti-O-Ti bond angle distortion, which affects the transfer energy of the 3d electrons or the one-electron bandwidth, depends critically on the ionic radius of the A-site ions or the Goldschmidt tolerance factor that is defined as

$$t = (r_A + r_O)/\sqrt{2}(r_B + r_O) \tag{7.4}$$

where r_i represents the ionic size of each element. The Goldschmidt tolerance factors for donor-doped $SrTiO_3$ were calculated using the equation above and are listed in Table 7.2. The values of r_A were calculated from the weighted average for the corresponding composition. By geometry, the ideal cubic structure should have t = 1. The perovskite structure occurs only within the range $0.75 < t < 1.00$ (Goodenough and Longo, 1970). As t decreases from 1, the perovskite structure deforms towards structures with lower coordination for A. When it is slightly less than unity a rhombohedral distortion usually results (Goodenough and Longo, 1970). Although the usual x-ray patterns in these cases can be indexed on a pseudo-cell with rhombohedral angle $\alpha \approx 90^o$, faint lines are observed in careful x-ray studies (Geller, 1957). From this point of view, a decrease of conductivity is expected for rare earth doped $SrTiO_3$ with decreasing tolerance factors. However, the opposite effect was observed as shown in Fig. 7.3. This suggests that the effect of possible lattice distortion is less important than changing oxidation state on the electrical conductivity.

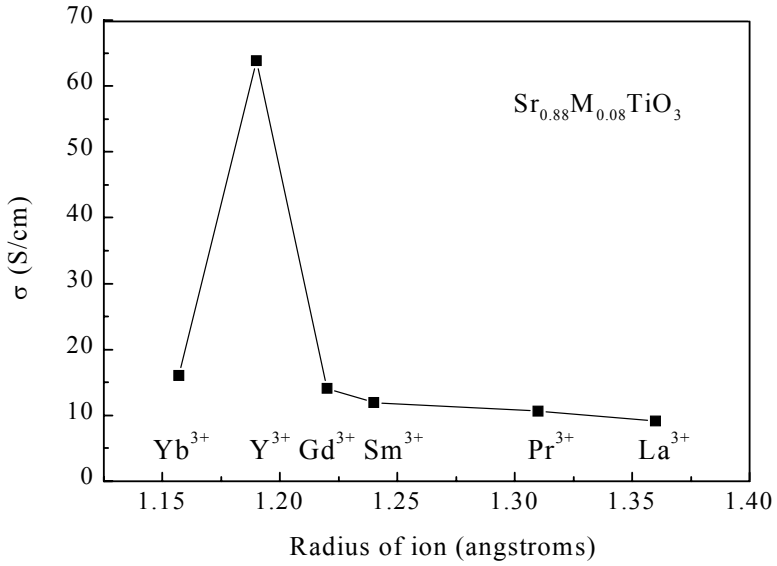

Fig. 7.3. Electrical conductivity as a function of dopant radius at 800°C and oxygen partial pressure of 10^{-19} atm

The conductivity of donor-doped $SrTiO_3$ may be affected not only by the size of donor but also by the existence of Ti^{3+} which is produced under reducing conditions. Kilner has suggested that a better means of evaluating the relative ion mismatch of dopant and host would be to compare the cubic lattice parameter of the host oxide and that of the pseudocubic lattice parameter of the corresponding dopant oxide. In this way, it has been successfully explained why Gd and Sc are excellent dopants in CeO_2 and ZrO_2, respectively (Kilner, 1983). Such a comparison was applied to rare-earth-doped titanates here, assuming $RTiO_3$ and $SrTiO_3$ are the end members of $Sr_{1-1.5x}R_xTiO_3$. Table 7.3 shows a comparison of lattice parameters between $SrTiO_3$ and related oxides. Note that the best match is between $SrTiO_3$ and $EuTiO_3$ rather than $YTiO_3$.

Table 7.3 Comparison of lattice parameters of $SrTiO_3$ and related oxides.

Alkaline earth titanates	Pseudocubic lattice parameter (Å)	Rare-earth titanates	Pseudocubic lattice parameter (Å)
$BaTiO_3$	4.02	$LaTiO_3$	3.956
$SrTiO_3$	3.905	$PrTiO_3$	3.940
$CaTiO_3$	3.823	$NdTiO_3$	3.909
		$SmTiO_3$	3.907
		$EuTiO_3$	3.904
		$GdTiO_3$	3.890
		$YTiO_3$	3.860
		$YbTiO_3$	
		$LuTiO_3$	3.837

*** Pseudocubic lattice parameter was estimated by** $a_c = \frac{1}{3}(\frac{a}{\sqrt{2}} + \frac{b}{\sqrt{2}} + \frac{c}{2})$ **, here, a, b, or c represents the lattice parameters of orthorhombic structure.**

On the basis of observations, the decrease of dopant radius may allow the lattice to contract, thus decreasing the distance between metal atoms and allowing greater overlap between them in a cubic cell. Meanwhile, since the ionic radius of Ti^{3+} is greater than that of Ti^{4+}, the Ti^{3+} induced by reduction would increase the strain of the lattice. The addition of rare earth of small ionic radius may relieve the strain, and make the reduction easy as experimentally observed. It appears that these interactions lead to the increase of conductivity with decreasing radius of donor dopant. However, the marked effect of yttrium on electrical conductivity of $SrTiO_3$ can not be explained in a straightforward manner. Other researchers also observed the unusual behavior of Y as

dopant in titanates. In a previous study, a comparison of resistivity was also reported for rare-earth-doped $SrTiO_3$ sintered in air. In the case of $SrTiO_3$ doped with 0.4 mol% Y, the resistivity at room temperature was about 10^{11} Ωcm, while the resistivity of $SrTiO_3$ doped with 1 mol% La was about 10^{12} Ωcm (Burn and Neirman, 1982). Xue et al. (1988) reported that Y^{3+} can occupy either A or B site in $BaTiO_3$, while Dy^{3+}, having the same ionic radius as Y^{3+}, and Ho^{3+}, with a smaller ionic radius, can only occupy the Ba site in $BaTiO_3$. According to a study of phase assemblage and lattice parameter by XRD, Zhi et al. (1999) found a slight solubility (~1.5 mol%) of Y at the Ba site at 1440°C but a high solubility (~12.2 mol%) of Y at the Ti site at 1515°C. The difference between Y and the rare earths may be due to not only the ionic radius, but also other factors such as the f-shell electronic structure, bonding character, and polarizability.

An interesting effect has been observed in donor-doped $SrTiO_3$ containing both yttrium and lanthanum simultaneously. X-ray diffraction indicates the presence of a single-phase perovskite for $Sr_{0.7}Y_{0.1}La_{0.1}TiO_{3-\delta}$. However, the conductivities of $Sr_{0.7}Y_{0.1}La_{0.1}TiO_{3-\delta}$ in the range of oxygen partial pressures of 10^{-14} to 10^{-19} atm at 800°C were much lower than that of $Sr_{0.85}Y_{0.1}TiO_{3-\delta}$ or $Sr_{0.85}La_{0.1}TiO_{3-\delta}$ (Fig. 7.4). Similarly, although the conductivity of $SrTiO_3$ can be improved by doping either La^{3+} at strontium sites or Nb^{5+} at titanium sites, further increase of conductivity was not observed for $SrTiO_3$ co-doped with La^{3+} and Nb^{5+}. This effect, together with other observed phenomena in this study, shows how diverse the electrical transport is, and how difficult it is to understand the nature of the forces that control electrical conduction.

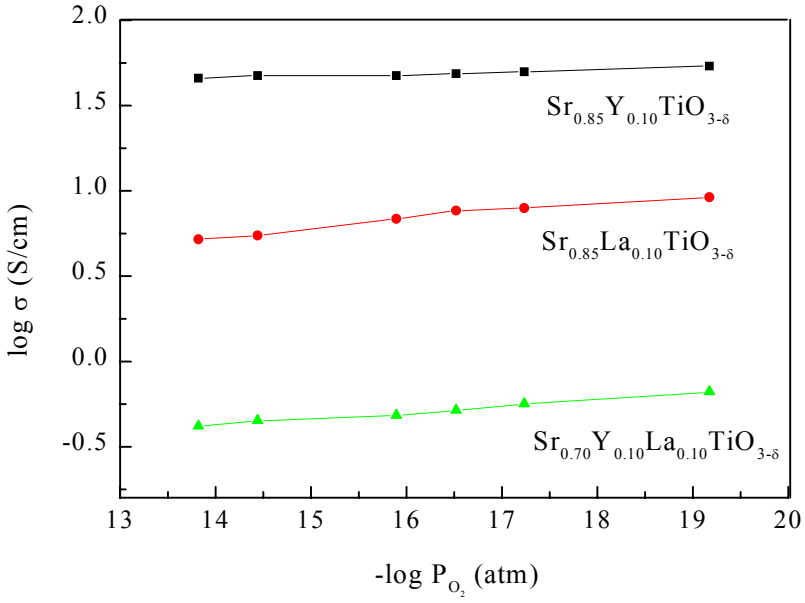

Fig. 7.4. Effects of donor-doping on conductivity at 800°C

7.3. Yttrium-Doped $SrTiO_3$ (SYT)

7.3.1. Solubility of Yttrium in $SrTiO_3$

Y-doped $SrTiO_3$ ceramics with the composition $Sr_{1-1.5x}Y_xTiO_3$ ($0 \leq x \leq 0.14$) were synthesized in forming gas (7% H_2 + 93% Ar) at 1400°C, and the densities relative to the theoretical density of $SrTiO_3$ are reported in Table 7.4. To the limit of detection by x-ray diffraction, single-phase cubic perovskite-type solid solutions were observed for all compositions containing up to 8 mol% of $YO_{1.5}$ for samples heated at 1400°C in air or forming gas. A pyrochlore phase $Y_2Ti_2O_7$ was observed in compositions with $YO_{1.5}$ greater than 8 mol%, and the amount of $Y_2Ti_2O_7$ phase increased as the yttrium content increased (Fig. 7.5).

Table 7.4. Lattice parameters (±0.0005 Å) for yttrium-doped $SrTiO_3$.

Composition	Lattice parameter (Å) (in reducing conditions)	Relative density (%)
$Sr_{0.97}Y_{0.02}TiO_{3-\delta}$		89.3
$Sr_{0.94}Y_{0.04}TiO_{3-\delta}$	3.9035	95.3
$Sr_{0.91}Y_{0.06}TiO_{3-\delta}$	3.9022	90.2
$Sr_{0.88}Y_{0.08}TiO_{3-\delta}$	3.9013	93.1
$Sr_{0.85}Y_{0.10}TiO_{3-\delta}$	3.9012	92.4
$Sr_{0.79}Y_{0.14}TiO_{3-\delta}$	3.9010	91.2

The lattice parameter decreased with increasing $YO_{1.5}$ content up to about 8 mol% as shown in Fig. 7.6, which is consistent with a previous lattice parameter study (Zhang et al., 1998). The linear dependence of the cubic lattice parameter simply follows Vegard's law. The increase of lattice parameters for reduced $Sr_{1-1.5x}Y_xTiO_{3-\delta}$ is most likely due to the existence of Ti^{3+}. The small changes in the lattice parameter upon reduction and oxidation suggest that the structural integrity of SYT is tolerant to oxidation-reduction cycling or to the variation in oxygen partial pressure between fuel inlet and outlet in fuel cell operation.

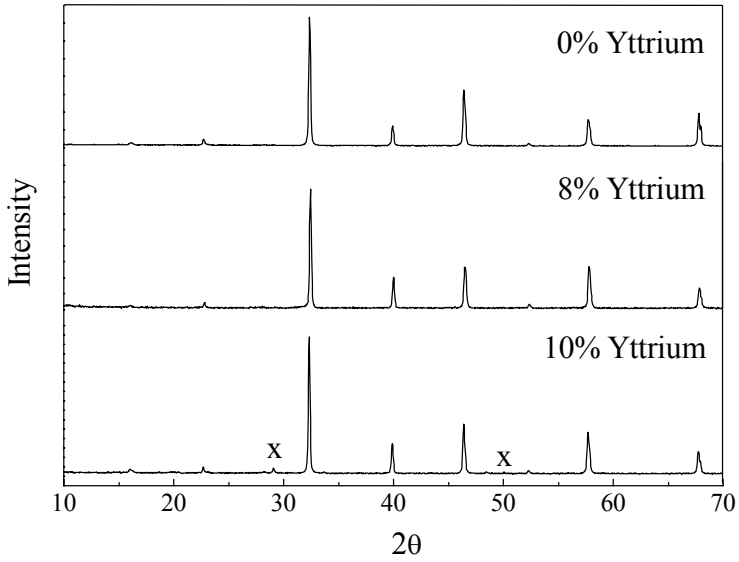

Fig. 7.5. X-ray diffraction patterns for Y-doped $SrTiO_3$ (x – impurity)

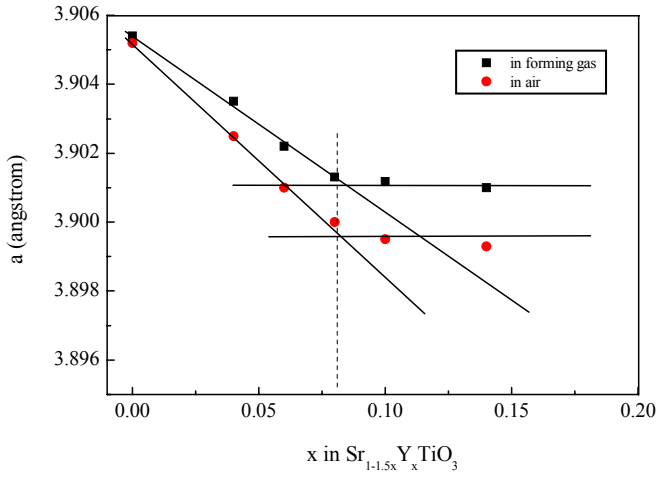

Fig. 7.6. Variation of lattice parameter with yttrium content for $Sr_{1-x}Y_xTiO_{3-\delta}$

For the structural analog, La-doped $SrTiO_3$, the measured variation of lattice parameter showed a significant difference from previous studies. Howard et al. (1989) found that the lattice parameter of $Sr_{1-x}La_xTiO_3$ increases as a function of La content regardless of the atmosphere in which the samples were sintered. The increase in lattice parameter was reported to be linear between the two end members $SrTiO_3$ and $LaTiO_3$ from 3.905 Å to pseudocubic 3.957 Å. Other researchers have observed the opposite result (Tien and Hummel, 1967; Johnson et al., 1970; Eror and Balachandran, 1981). According to x-ray diffraction measurements, Johnson et al. (1970) have showed that the rare earth titanates $La_{2/3}TiO_3$ to $Lu_{2/3}TiO_3$ form solid solutions of perovskite structure with $SrTiO_3$. The limit of solubility decreased rapidly with atomic number (decreasing ionic size) from roughly 70 mol% in $La_{2/3}TiO_3$ solution to less than 5 mol% in $Lu_{2/3}TiO_3$. Lattice parameter measurements showed that the unit size decreased linearly with the concentration of rare earth, and as would be expected, decreased more rapidly for the smaller ions.

7.3.2. Dependence of Electrical Conductivity on Yttrium Content

In order to obtain constant conductivity measurement at a temperature, the samples were equilibrated in the same atmosphere at 1400^{o}C for 5 h in advance. Fig. 7.7 shows a plot of the logarithm of the electrical conductivity versus the logarithm of the oxygen partial pressure at 800^{o}C, and four featured regions can be identified.

(1) Region I

As explained by earlier investigators (Choi and Tuller, 1988; Eror and Smyth,

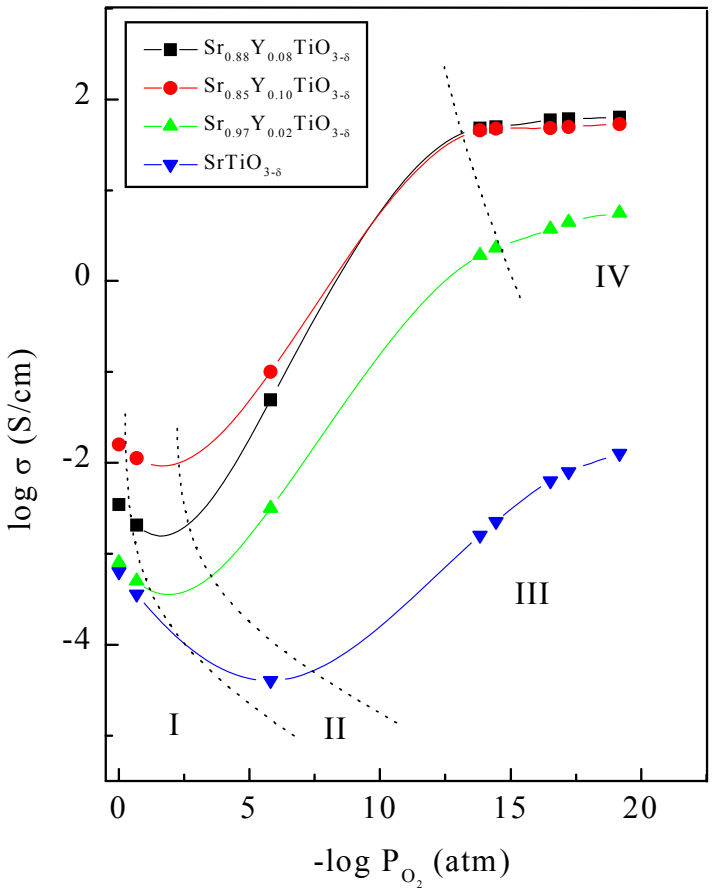

Fig. 7.7. Conductivity of undoped $SrTiO_3$ and Y-doped $SrTiO_3$ at 800°C as a function of oxygen partial pressure

1978), the p-type behavior of undoped $SrTiO_3$ is due to the presence of acceptor impurities such as Al^{3+} that were charge compensated by oxygen vacancies, $Sr(TiAl^{3+})O_{3-\delta}$. These impurities are often present in the starting materials or are picked up from the processing media. Chan and Smyth pointed out that acceptor impurities, such as Na^+, K^+, Fe^{2+}, Mg^{2+}, and Al^{3+}, are much more likely to be present than donor impurities, such as La^{3+} and other rare-earths or Th^{4+}, Nb^{5+}, Ta^{5+}, W^{6+} etc., because of their greater natural abundance (1976). The natural acceptors in starting materials may influence the electrical conductivity of the system under study, and result in a lack of reproducibility. As an example of the effect of these acceptor ions, Fig. 7.8 depicts the decrease in conductivity by impurities in $Sr_{0.88}Y_{0.08}TiO_{3-\delta}$. The importance of the purity of raw materials is especially noticeable in studies of positive temperature coefficient of resistivity in $BaTiO_3$ (Peng and Lu, 1988).

In this region, oxygen sites are likely occupied at high oxygen partial pressures, and generate the holes responsible for p-type behavior as shown by Eq. (7.4)

$$\frac{1}{2}O_2 + V_O^{\bullet\bullet} = O_o + 2h^{\bullet} \tag{7.4}$$

The conductivity in this region increases with increasing oxygen partial pressure, as seen in Fig. 7.7. At equilibrium, charge neutrality in Eq. (7.4) is given by:

$$[h^{\bullet}] = 2[V_O^{\bullet\bullet}] \tag{7.5}$$

Combining the law of mass action expression in Eq. (7.4) with Eq. (7.5) gives

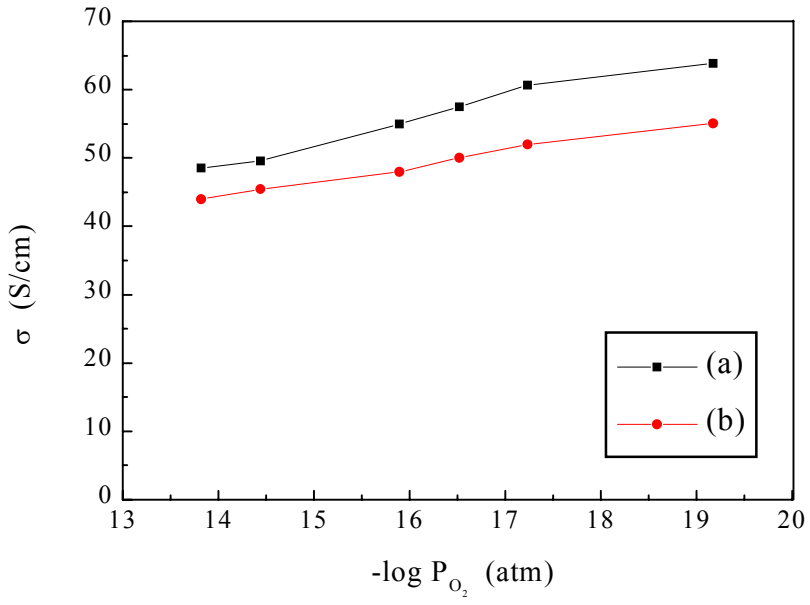

Fig. 7.8. Effects of impurities on conductivity for $Sr_{0.88}Y_{0.08}TiO_{3-\delta}$ at 800°C: a) grades of starting materials were greater than 99.5%, b) grades of starting materials were greater than 99%

$$\sigma \propto P_{O_2}^{1/4} \tag{7.6}$$

as observed in Fig. 7.7. Such an argument has also been suggested to account for the behavior of $BaTiO_3$ (Daniels and Härdtl, 1976). The p-type behavior as well as the n-type behavior in Region III were confirmed by thermopower measurements (Choi and Tuller, 1988; Daniels and Härdtl, 1976).

For Y-doped $SrTiO_3$, the reasons for p-type behavior are different. In this region, the oxygen partial pressures were high, and the electrical conductivities were poor even for

donor-doped $SrTiO_3$. It appears that substitution of the strontium by higher charge ions such as Y do not produce an increase in the number of conduction electrons in the usual sense of doping. However, the increase of conductivity is still proportional to the Y doping level as shown in Fig. 7.7, indicating the existence of Ti^{3+} in SYT. By using x-ray photoelectron spectroscopy, Yang confirmed the existence of Ti^{3+} in La-doped $SrTiO_3$ sintered in air (1999). In contrast, air oxidized $SrTiO_3$ contained no detectable amount of Ti^{3+}. Therefore, $Sr_{1-1.5x}Y_xTiO_3$ may be best understood as $Sr_{1-1.5x}Y_xTi^{4+}_{1-2y}Ti^{3+}_{2y}O_{3-y}$ even in air-sintered samples. However, the magnitude of this oxygen deficiency is expected to be very small, which may have a value on the order of 10^{-3} which is the same as for δ in undoped $SrTiO_{3-\delta}$ near 800°C (Eror and Balachandran, 1981). Assuming the Kröger-Vink notation, the positively charged defects, $2Y_{Sr}^{\bullet} + V_O^{\bullet\bullet}$, are neutralized by negatively charged ones, $2e' + V_{Sr}''$.

Since the generation of holes in this region requires the existence of oxygen vacancies, one can expect that no p-type behavior appears without intrinsic oxygen vacancies. Therefore, p-type behavior is observed normally for undoped and acceptor-doped $SrTiO_3$ and $BaTiO_3$ (Choi and Tuller, 1988; Daniels and Härdtl, 1976). The p-type behavior was not found for donor-doped titanates with stoichiometric composition such as $Sr_{1-x}La_xTiO_3$ (Balachandran and Eror, 1982) and $Ba_{1-x}La_xTiO_3$ (Daniels and Härdtl, 1976). However, Chan et al. (1976) found that donor-doped $SrTiO_3$ also showed p-type behavior with increasing Sr-site deficiency, which is consistent with the observation in this study. The difference in behavior between the stoichiometric and nonstoichiometric compound such as $Sr_{1-1.5x}La_xTiO_3$ in the high oxygen partial pressure region suggests the existence of oxygen vacancies in the latter compound but not in the former one.

(2) Region II

As concluded in earlier studies and summarized in Chapter 3, region II is the p-type to n-type transition region. At the n/p transition point the electronic conductivity is at a minimum, σ_{min}, and $\sigma_n = \sigma_p$. As pointed out earlier, there is no p-type behavior without intrinsic oxygen vacancies. If the oxygen vacancy concentration increases by increasing the acceptor-doping level, the minimum of the conductivity is shifted on the oxygen partial pressure scale to lower partial pressures. Conversely, the minima of the conductivities of SYT were shifted by two to three orders of magnitude to higher partial pressures in comparison with undoped $SrTiO_3$.

The band-gap energy (extrapolated to zero temperature) of a semiconductor that exhibits a p-to-n transition may be determined from the Arrhenius plots of the conductivity minima (Choi and Tuller, 1988; Eror and Smyth, 1978). Assuming band-conduction for both electrons and holes with equal mobility, the expression for the Arrhenius plot is

$$\log \sigma_{\min} = C - \frac{E_g^o}{2kT} \tag{7.7}$$

where C is a constant, and k is Boltzmann's constant, 8.617 x 10^{-5} eV/K. Fig. 7.9 shows a plot of the logarithm of the electrical conductivity versus the logarithm of the oxygen partial pressure for $Sr_{0.88}Y_{0.08}TiO_{3-\delta}$ in the temperature range of 600 to 900°C. The log σ_{min} versus 1/T data in Fig. 7.10 indicates a value of $E_g^o = 2.6$ eV as the band-gap energy for $Sr_{0.88}Y_{0.08}TiO_{3-\delta}$ extrapolated to 0 K. The decrease of band-gap energy causes the minimum of conductivity to shift upward in Fig. 7.7.

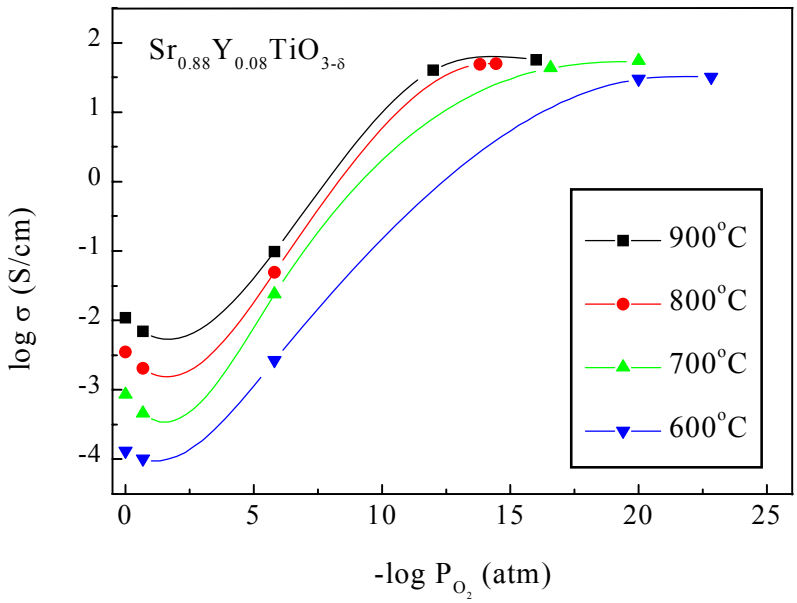

Fig. 7.9. Conductivity of $Sr_{0.88}Y_{0.08}TiO_{3-\delta}$ versus oxygen partial pressure at different temperatures

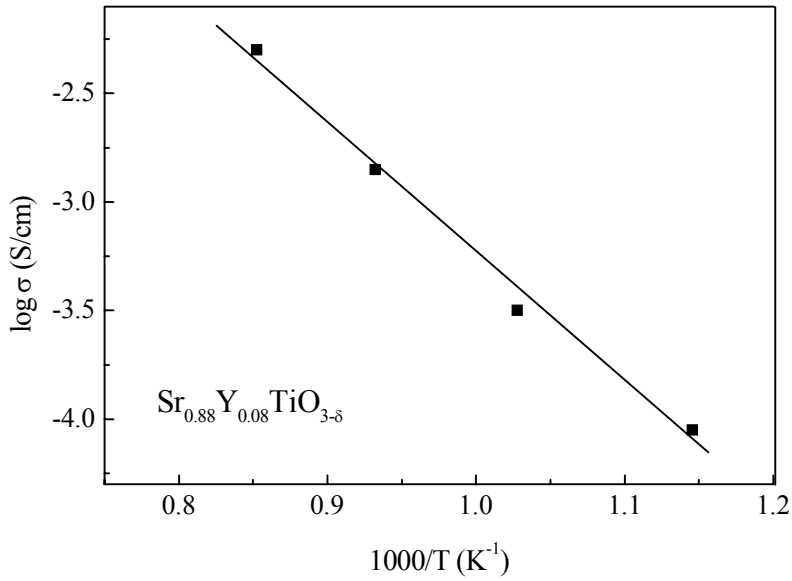

Fig. 7.10. Temperature dependence of minima of conductivities extracted from Fig. 7.9

Since the electronic conductivity is minimum at the n/p transition point, the minimum of conductivity is dominated by ionic conductivity for materials with large band-gap energy and consequently negligible electronic conductivity. The ionic conductivity is independent of oxygen partial pressure for compounds such as YSZ in which extrinsic oxygen vacancies dominate. In such cases, a broad conductivity plateau is expected in this region. However, a narrow plateau is expected for mixed conductors such as CeO_{2-x} because the ionic transference number is a function of oxygen partial

The minima of conductivity of $Sr_{0.88}Y_{0.08}TiO_{3-\delta}$ and $Sr_{0.97}Y_{0.02}TiO_{3-\delta}$ were 1.5 x 10^{-3} and 3.5 x 10^{-4}, respectively. These data may be considered as a rough indication of ionic conductivity at 800^{o}C. Since the band-gap energy for $Sr_{0.88}Y_{0.08}TiO_{3-\delta}$ is only 2.6 eV, equating the ionic conductivity to the total conductivity at the minimum may not be accurate. The accuracy of this estimate needs to be confirmed by other means such as permeation measurements (Park and Blumenthal, 1989; Patrakeev et al., 1993).

(3) Region III

For undoped $SrTiO_3$, a slope of approximately –1/6 was observed (Fig. 7.7) consistent with earlier investigators (Eror and Smyth, 1978). Yamada and Miller (1973) have shown that the oxygen vacancies formed upon reduction can be quenched in upon cooling to room temperature and they remain doubly ionized to very low temperatures. The reduction reaction can be written as

$$O_O = \frac{1}{2}O_2 + V_O^{\bullet\bullet} + 2e' \qquad (7.9)$$

$$K = [V_O^{\bullet\bullet}][n]^2 P_{O_2}^{1/2} \tag{7.10}$$

Reaction (7.9) represents the formation of a doubly ionized oxygen vacancy and two electrons available for conduction by the removal of oxygen from a normal lattice site into the gas phase. Therefore, the charge carriers in this region are n-type, which was confirmed for yttrium-doped $SrTiO_3$ by thermopower measurement. Considering that two electrons result from each oxygen vacancy, $[n] = 2[V_O^{\bullet\bullet}]$, and combining Eq. (7.10), we get

$$[n] \propto P_{O_2}^{-1/6} \tag{7.11}$$

At constant temperature, assuming that mobility is independent of the change in concentration of oxygen vacancies, a plot of the logarithm of the conductivity versus the logarithm of the oxygen partial pressure should result in a straight line with a slope of –1/6.

Measurements of Seebeck coefficient, S, were performed for $Sr_{0.88}Y_{0.08}TiO_{3-\delta}$ as a function temperature (Fig. 7.11). Seebeck coefficient is sensitive to the carrier types associated with the transport properties of materials. For a non-degenerate broad band semiconductor, the Seebeck coefficient, S, can be expressed as

$$S_e = -\frac{k_B}{e}\left(\ln\left[\frac{N_c}{n}\right] + A_e\right) \tag{7.12}$$

$$S_h = \frac{k_B}{e}\left(\ln\left[\frac{N_v}{p}\right] + A_h\right) \tag{7.13}$$

where N_c and N_v are the density of states in the conduction and valence band, n and p the concentrations of electrons and holes, A_e and A_h the transport constants depending on scattering mechanism. The observed negative value of S is a good indication of electrons as carriers in $Sr_{0.88}Y_{0.08}TiO_{3-\delta}$.

In contrast with undoped $SrTiO_3$, electron concentration in Y-doped $SrTiO_3$ was not only related to the degree of reduction, but also to Y-doping levels as observed in Fig. 7.7. In this case, it may not necessarily be a linear plot of the logarithm of the conductivity versus the logarithm of the oxygen partial pressure for SYT. Unfortunately, the data in this region were insufficient to resolve this variation clearly.

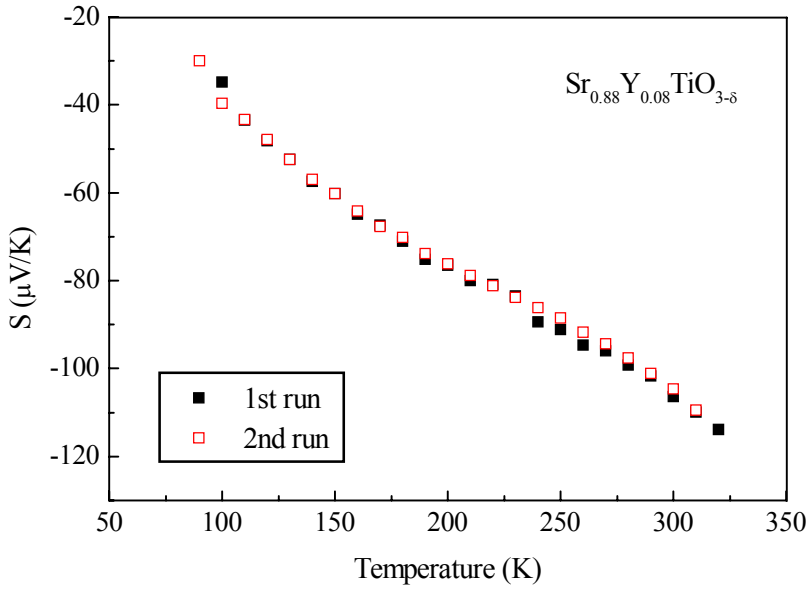

Fig. 7.11. Seebeck coefficient of $Sr_{0.88}Y_{0.08}TiO_{3-\delta}$ as a function of temperature

(4) Region IV

Region IV applies only to SYT, and is an extension of the n-type region. The electron concentration, or Ti^{3+} concentration is saturated by the Y-doping level, and the conductivities were only a weak function of oxygen partial pressure as seen in Fig. 7.7. More data in this region are shown in Fig. 7.12. The conductivities in this oxygen partial pressure range increase with increasing Y-doping level up to 8 mol%, indicating a maximum conductivity corresponding to the Y content under measurement conditions. The variation of conductivity as a function of Y-doping level can be more clearly seen when all other parameters are fixed. Fig. 7.13 shows the conductivity versus Y-doping level at 800°C and oxygen partial pressure of 10^{-19} atm, and a peak value of conductivity of 64 S/cm was observed for the composition $Sr_{0.88}Y_{0.08}TiO_{3-\delta}$.

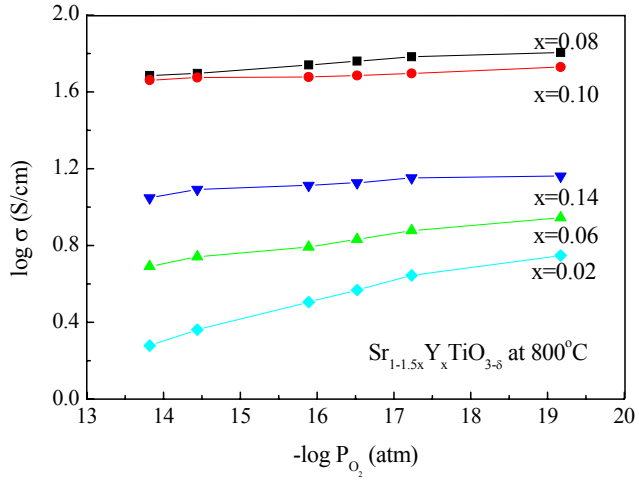

Fig. 7.12. Conductivity of Y-doped $SrTiO_3$ as a function of oxygen partial pressure at 800°C (Region IV in Fig. 7.9)

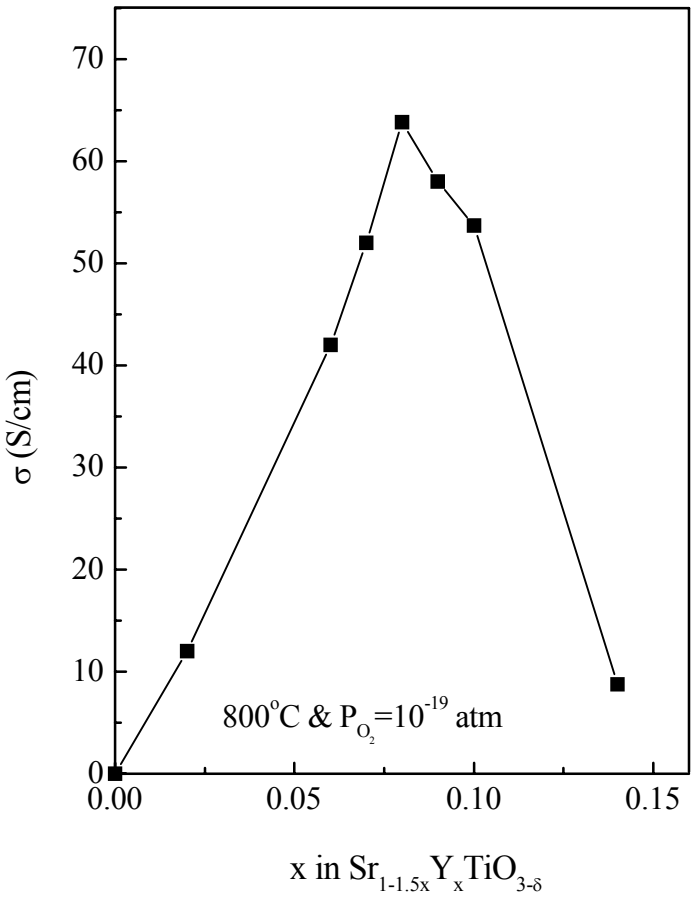

Fig. 7.13. Conductivity as a function of Y-doping level at 800^{o}C and oxygen partial pressure of 10^{-19} atm

Thermogravimetric measurements were performed on the $Sr_{1-1.5x}Y_xTiO_{3-\delta}$ composition (x = 0, 2, 6, 8, 10, 12, 14) as prepared under reducing conditions. The samples were heated under flowing air at 1000°C so that complete oxidation was obtained. The weight change associated with this oxidation was used to determine the amount of oxygen present per formula unit. The oxygen loss, δ, can be expressed in terms of the percent of observed weight loss, ΔW, and weight per mole, W, assuming the normal cation and anion content:

$$\frac{16\delta}{W-16\delta} = \Delta W\% \tag{7.14}$$

or

$$\delta = \frac{W \times \Delta W\%}{16(1+\Delta W\%)} \tag{7.15}$$

The calculated oxygen loss by thermogravimetric measurement was plotted in Fig. 7.14 for different compositions. A similar profile can be seen in Fig. 7.13, and the maximum of oxygen loss occurs for the composition $Sr_{0.88}Y_{0.08}TiO_{3-\delta}$. The decrease of conductivity and oxygen vacancies at high Y-doping levels may be understood in terms of defect interaction as discussed below.

According to the defect model proposed by Chan et al. (1981), $SrTiO_3$ can be treated as a mixture of SrO and TiO_2 where they do not enter into reactions. Dopant reacts with the individual binary oxides according to the dopant-site in the perovskite lattice. Therefore, the defects in a ternary system can be treated as that in a binary one. However, all the defects in $SrTiO_3$ may interact with each other rather than being limited to a binary system. For SYT, the extra positive charge from Y^{3+} substitution of Sr^{2+}

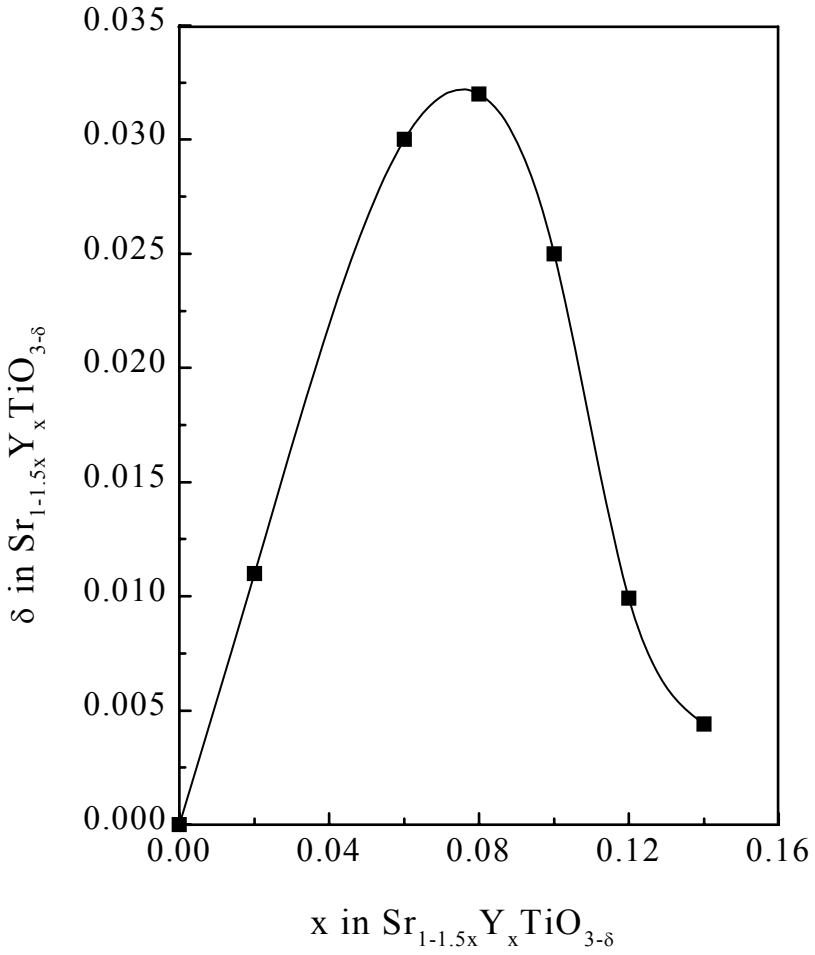

Fig. 7.14. Oxygen loss as a function of Y-doping level

could be compensated by a negatively charged strontium vacancy, V_{Sr}'' . This compensation mechanism is supported by the work of Odekirk et al. (1982) who found evidence for V_{Sr}'' in La-doped $SrTiO_3$ using low temperature conductivity measurements. Most recently, Battle et al. (2000) have observed V_{Sr}'' ordering in $Sr_{1-1.5x}La_xTiO_3$ when x > 0.30 by high-resolution transmission electron microscopy (HRTEM) and electron diffraction (ED). The incorporation of Y in $SrTiO_3$ can be described by Kröger-Vink notation as

$$Y_2O_3 \xrightarrow{SrTiO_3} 2Y_{Sr}^{\bullet} + V_{Sr}'' + 3O_O \tag{7.16}$$

or fully expressed according to balanced charge, mass, and site as

$$SrO + Y_2O_3 + 4TiO_2 = 2Y_{Sr}^{\bullet} + V_{Sr}'' + Sr_{Sr} + 4Ti_{Ti} + 12O_O \tag{7.17}$$

Upon reduction of SYT, the reduction reaction is given by

$$O_O = \frac{1}{2}O_2(g) + V_O^{\bullet\bullet} + 2e' \tag{7.9}$$

As pointed out in Chapter 4, the energy level of Sr-sites is greater than that of Ti-sites in a band structure. The electrons generated by reduction are trapped at Ti-sites

$$Ti^{4+} + e' = Ti^{3+} \tag{7.18}$$

Combining Eqs (7.9) and (7.18), the reduction reaction in SYT can be represented by

$$2\,TiO_2 \xrightarrow{SrTiO_3} 2Ti_{Ti}' + V_O^{\bullet\bullet} + \frac{1}{2}O_2(g) + 3O_O \tag{7.19}$$

Thus, Y-doped $SrTiO_3$ contains mixed-valent titanium ions, and the concentration of Ti^{3+}, and consequently the conductivity, depends on the degree of reduction or oxidation:

$$Sr^{2+}_{1-1.5x}Y^{3+}_{x}Ti^{4+}O_3 \xrightarrow{reduction} Sr^{2+}_{1-1.5x}Y^{3+}_{x}Ti^{4+}_{1-2y}Ti^{3+}_{2y}O_{3-y} \tag{7.20}$$

The dependence of electrical conductivity of mixed-valence oxides on oxygen partial pressure is also found for p-type perovskites such as $La_{1-x}Sr_xMnO_{3-\delta}$ and $La_{1-x}Sr_xCoO_{3-\delta}$ (Mizusaki, 1992; Anderson, 1992).

The extra electrons at Ti-sites may enter into the conduction band, and a transition from semiconducting to metallic behavior may occur if the concentration of Ti^{3+} exceeds a critical value predicted by Mott (1974). This transition has been reported for reduced or donor-doped $SrTiO_3$ (Fujimori et al., 1996; Tokura et al., 1993; Sunstrom et al., 1992). The presence of Ti^{3+} has been analyzed quantitatively by chemical titration through a redox reaction between Ti^{3+} and Fe^{3+} (Moos et al., 1995). The Ti^{3+} also can be detected qualitatively by physical methods such as magnetic susceptibility measurement and electron magnetic resonance (EPR). The temperature dependence of the magnetic susceptibilities for the composition $Sr_{1-1.5x}Y_xTiO_{3-\delta}$ (x = 0, 0.02, 0.08) as prepared in forming gas can be seen in Fig. 7.15. A good fit to the Curie-Weiss law can be seen,

$$\chi = \frac{C}{T-\theta} \tag{7.21}$$

where C is the Curie constant, T the temperature, and θ the Weiss constant. The experimentally determined values of the Curie and Weiss constants are found in Table 7.5. The Curie constant is directly proportional to the number of magnetic ions present,

or the concentration, N, of Ti^{3+} in $Sr_{1-1.5x}Y_xTiO_{3-\delta}$, as expressed by:

Table 7.5. Experimentally determined values for the Curie constant C and the Weiss constant θ

Composition	C (emu·K·mol^{-1})	θ (K)
$SrTiO_{3-\delta}$	0.0005	-1.02
$Sr_{0.97}Y_{0.02}TiO_{3-\delta}$	0.0036	-13.40
$Sr_{0.88}Y_{0.08}TiO_{3-\delta}$	0.0015	-1.51

$$C = \frac{N\mu_o\mu_{eff}^2}{3k_B} \tag{7.22}$$

where μ_o is permeability of free space, and μ_{eff} the effective magnetic moment. As we expected, the Curie constant of yttrium-doped $SrTiO_3$ is greater than that of undoped $SrTiO_3$. However, the Curie constant decreases with increasing yttrium content.

As seen in Fig. 7.7, the conductivities in region IV were relatively constant, indicating that the conductivities or electron concentration were saturated by yttrium doping, i.e., $[n] = [Y_{Sr}^{\bullet}]$. Therefore, one can expect that the conductivity calculated from the Y-doping level as electron concentration should match the measured conductivities. Such a comparison can be seen in Fig. 7.16. A conductivity calculation from thermogravimetric measurements, supposing one oxygen vacancy to provide two electrons is also shown in Fig. 7.16. The electron mobility at 800°C was taken as 0.3 cm^2/V-s from Tufte and Chapman (1967). The conductivity calculated from thermogravimetric analysis (TGA) shows a good agreement with that measured directly

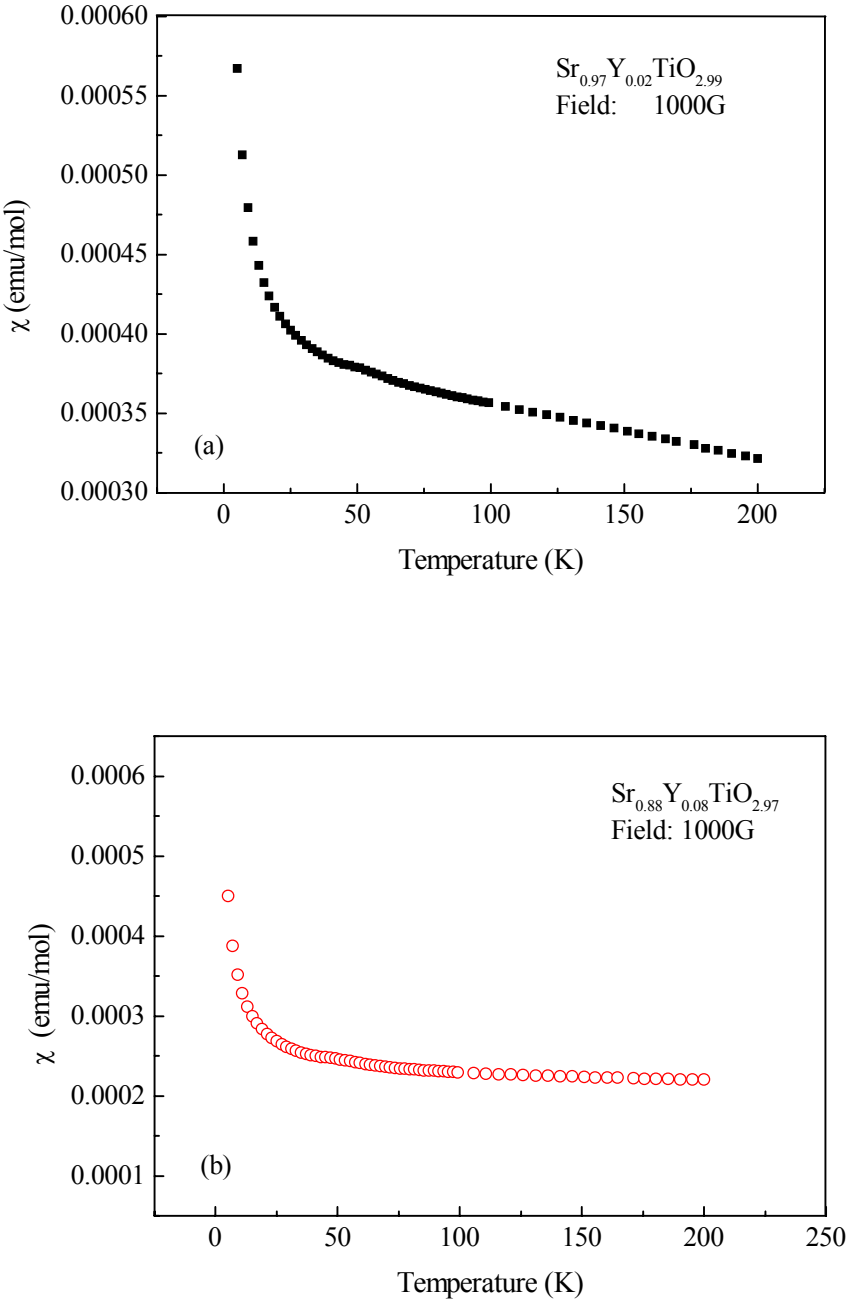

Fig. 7.15. Magnetic susceptibility plots for (a) $Sr_{0.97}Y_{0.02}TiO_{3-\delta}$, (b) $Sr_{0.88}Y_{0.08}TiO_{3-\delta}$

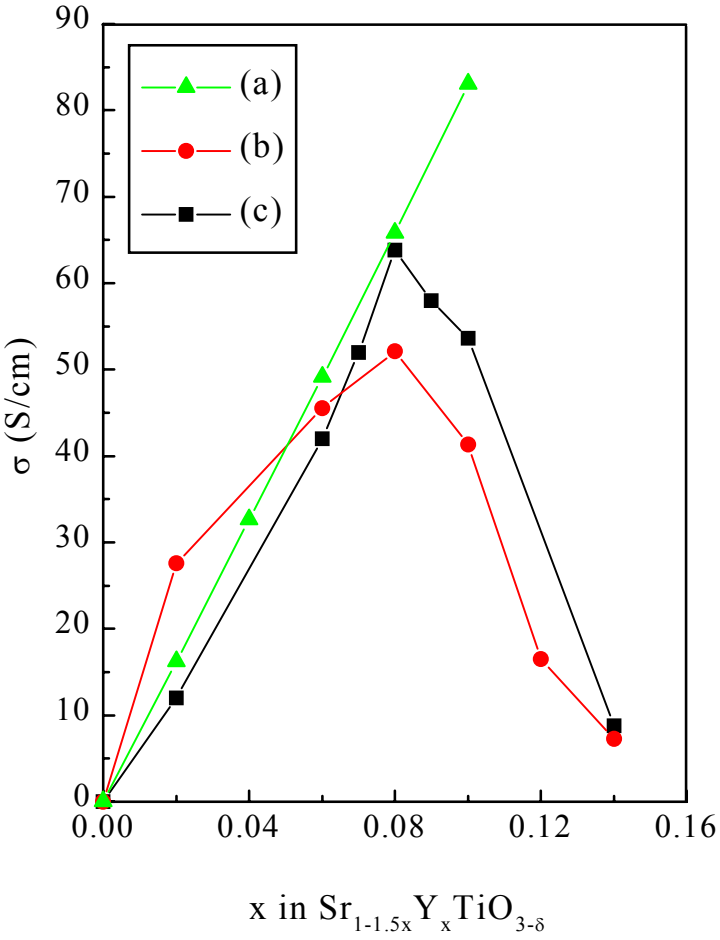

Fig. 7.16. Comparison of the electrical conductivity for SYT: (a) calculated according to the Y-doping level, (b) calculated from thermogravimetric measurements, (c) experimentally determined

by the four-probe method. In contrast to the calculation from TGA, the conductivity calculated from the donor-doping level is only in agreement with that of four-probe measurement until the peak value of conductivity. This indicates that the loss of oxygen is somehow decreased at high donor-doping levels, and results in decreased conductivity. It seems that conductivity is controlled by reduction rather than by the donor-doping level. The true donors in doped or undoped SrTiO3, therefore, appear to be oxygen vacancies produced by loss of oxygen from the materials at high temperatures.

From Eqs. (7.16) and (7.19), the defects present in SYT include $Y_{Sr}^{\bullet}$, V_{Sr}'', Ti_{Ti}', and $V_O^{\bullet\bullet}$. It is well known that interactions between ions and their charge-compensation defects can lead to the formation of distinct clusters that can trap the migrating species. For example, oxides that crystallize in the fluorite structure, e.g. stabilized ZrO_2, CeO_2, and ThO_2, accommodate a large fraction of lower valence cations, such as Ca, Y, and trivalent rare-earths into solid solution, resulting in oxygen deficiencies as high as 10-15%. A key feature observed by many researchers is the maximum ion conductivity which occurs at doping levels corresponding to 5-10% anion vacancies while the decrease in conductivity and increase in activation energy at higher doping levels are generally attributed to the onset of substantial defect association and ordering (Khan and Islam, 1998). For $SrTiO_3$, strontium vacancies, V_{Sr}'', and oxygen vacancies, $V_O^{\bullet\bullet}$, may be associated into neutral vacancy pairs as

$$V_{Sr}'' + V_O^{\bullet\bullet} = (V_{Sr}'' V_O^{\bullet\bullet}) \tag{7.23}$$

where the parentheses indicate that the enclosed species are electrostatically bound to

adjacent lattice sites. Balachandran and Eror (1982) have found that the defect association energy for V_{Sr}'' and $V_O^{\bullet\bullet}$ is 1.78 eV at 850°C for a sample with Sr/Ti = 0.99. Smyth (1976) and Eror and Smyth (1978) have discussed both the extreme cases of defect association and negligible defect association. These defect pairs may grow when the concentration of defects V_{Sr}'' and $V_O^{\bullet\bullet}$ increases. Eventually, the pairing of V_{Sr}'' and $V_O^{\bullet\bullet}$ may lead to the formation of TiO_2 precipitation:

$$V_{Sr}'' + Ti_{Ti} + V_O^{\bullet\bullet} + 2O_O \xrightarrow{SrTiO_3} TiO_2 \qquad (7.24)$$

Chiang et al. (1997) have discussed a similar process observed in MgO containing alumina. When the solid solution limit is exceeded upon cooling, precipitation of $MgAl_2O_4$ spinel occurs. Since the Y in $SrTiO_3$ is compensated by V_{Sr}'', the consumption of V_{Sr}'' by formation of precipitate may decrease the effective doping of Y in $SrTiO_3$. This will result in the formation of a Y-containing phase such as $Y_2Ti_2O_7$ as observed by XRD in Fig. 7.5. Meanwhile, the consumption of $V_O^{\bullet\bullet}$ by formation of precipitates and the decrease of effective Y-doping lead to a decrease of oxygen loss as shown by thermogravimetric measurements in Fig. 7.14.

7.4. Electrical Properties of $Sr_{0.88}Y_{0.08}TiO_{3-\delta}$

7.4.1 Effects of Temperature

$Sr_{0.88}Y_{0.08}TiO_{3-\delta}$ has the highest conductivity for yttrium concentration in the range $0 \leq x \leq 0.14$ under anodic conditions. Subsequent work has been focused on this composition, and the effects of temperature, bulk and grain boundaries,

and composition deviation on conductivity.

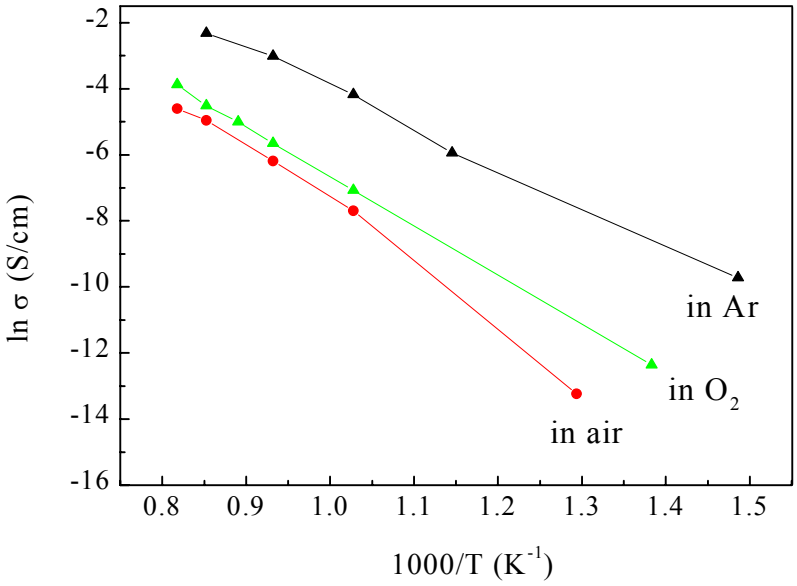

Fig. 7.17. Conductivity versus temperature under different atmospheres

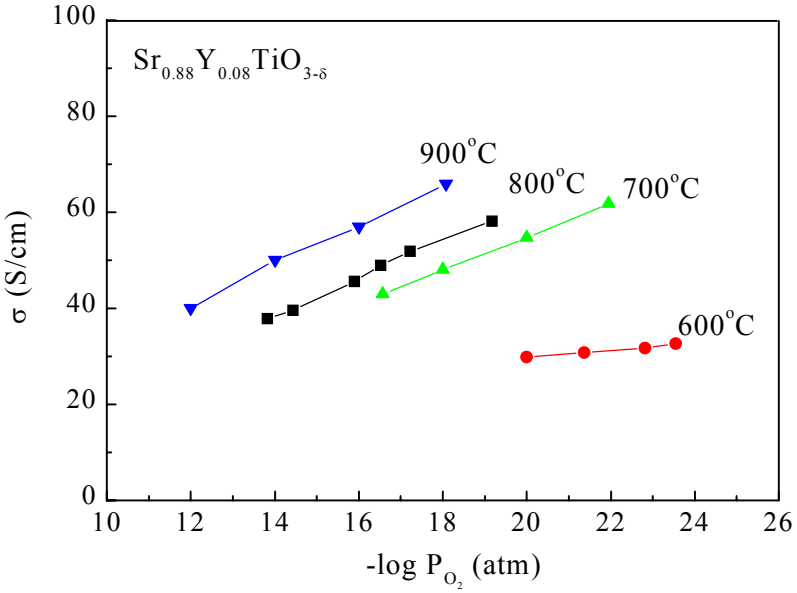

Fig.7.18. Conductivity versus oxygen partial pressure at different temperatures

The conductivity of $Sr_{0.88}Y_{0.08}TiO_{3-\delta}$ was measured as a function of temperature under different atmospheres as shown in Fig. 7.9, Fig. 7.17, and Fig. 7.18. In all cases, the conductivity increased with increasing temperature, indicating a semiconducting behavior. As pointed out in Section 7.3.2, the charge carriers in region I in Fig. 7.7 are p-type, and in region III n-type. Therefore, $Sr_{0.88}Y_{0.08}TiO_{3-\delta}$ is a p-type semiconductor when oxygen partial pressure is high, and an n-type semiconductor when oxygen partial pressure is low. For a semiconductor, the conductivity can be expressed by

$$\sigma = \frac{\sigma_o}{T}\exp(-\frac{E_a}{kT}) \tag{7.25}$$

where σ_o is a constant, and E_a is the activation energy for conduction. Table 7.6 summarizes the activation energy for $Sr_{0.88}Y_{0.08}TiO_{3-\delta}$ calculated by plotting ln σ versus 1/T at different oxygen partial pressures. As expected, the activation energy decreases with decreasing oxygen partial pressure because of the pressure dependence of electron concentration.

Table 7.6. Activation energy for conduction in $Sr_{0.88}Y_{0.08}TiO_{3-\delta}$

Oxygen partial pressure (atm)	Activation energy for conduction (eV)
10^{-18}	0.43
10^{-6}	2.45
1	2.57

It is interesting to note the variation of conductivity of $Sr_{0.88}Y_{0.08}TiO_{3-\delta}$ in forming

gas as a function of temperature. Fig. 7.19 shows the conductivity measured from high temperature to low temperature. It might seem that a metal-semiconductor transition occurs at about 425°C but this is not the case. The oxygen partial pressure in forming gas

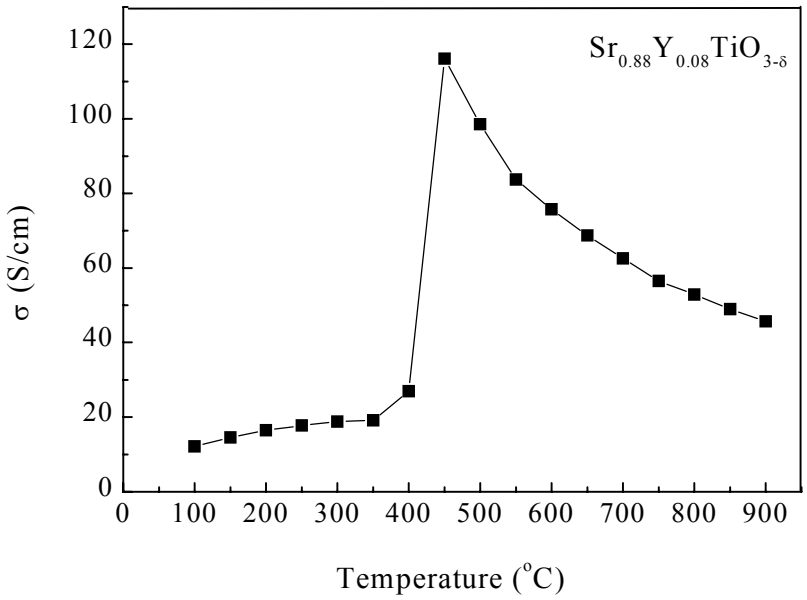

Fig. 7.19. Conductivity versus temperature for $Sr_{0.88}Y_{0.08}TiO_{3-\delta}$ in forming gas

is determined by

$$H_2(g) + \frac{1}{2}O_2(g) = H_2O(g) \tag{7.26}$$

$$\Delta G^o = -\frac{RT}{2F}\ln\left(\frac{P_{H_2O}}{P_{H_2}P_{O_2}^{1/2}}\right) \tag{7.27}$$

The oxygen partial pressure depends on the content of H_2O and H_2 in the gas as well as on the temperature. For 7% H_2 saturated with H_2O at room temperature, taking

$\Delta G^o = -246000 + 54.8T$ J and P_{H2O} = 0.0313 atm (Bale et al., 1996), the oxygen partial pressure in forming gas significantly decreases with decreasing temperature (Fig. 7.20).

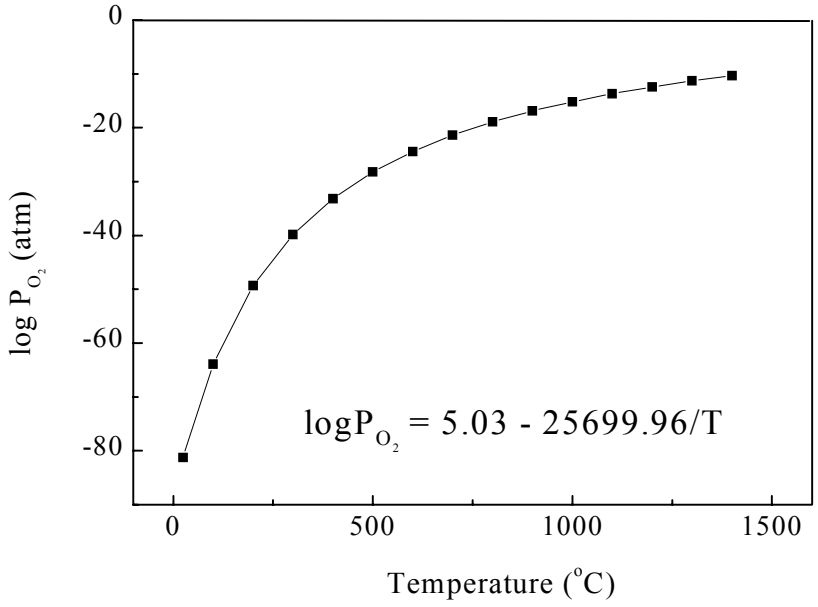

Fig. 7.20. Thermodynamic calculation of oxygen partial pressure as a function of temperature in forming gas

Assuming a constant oxygen partial pressure in forming gas over a range of temperatures is a common source of error. Similarly, when CO/CO_2 is used to control oxygen partial pressure, a constant CO/CO_2 ratio does not provide a constant oxygen partial pressure for a range of temperature as shown in Fig. 5.1. Therefore, the increase of conductivity with decreasing temperature is most likely due to the decrease of oxygen partial pressure. However, when the temperature is below a kinetic limit (about 425°C in this case), Eq. (7.26) may not be in thermodynamic equilibrium. The temperature

thereby controls the electron generation rather than the reduction or oxygen partial pressure. The true conduction behavior was observed in the low temperature range while the conductivities in the high temperature range were controlled not only by temperature but also by changing oxygen partial pressure.

Note that the semiconducting behavior is not mandatory in Y-doped $SrTiO_3$ because of the possibility of a metal-insulator transition controlled by filling. The system $Sr_{1-1.5x}Y_xTiO_{3-\delta}$ ($0 < x < 1$) is a mixed-valent oxide which has a d^1 electronic configuration or a fraction of an electron in the d shell. The electron concentration can be varied through control of the titanium valence by changing the Y-doping level and loss of oxygen in $Sr_{1-1.5x}Y_xTiO_{3-\delta}$. $YTiO_3$ has an electrical resistivity of approximately 77 Ω at room temperature (Greedan and MacLean, 1978) which can be classified as a semiconductor like $SrTiO_3$. This is significantly different from the solid solution $Sr_{1-x}La_xTiO_3$ wherein $LaTiO_3$ is classified as a poor metal. $YTiO_3$ shows stronger electron correlation than $LaTiO_3$ because of a reduced bandwidth due to Ti-O-Ti bending in the distorted perovskite structure. $LaTiO_3$ obeys the prediction of band theory, but not $YTiO_3$. The system $Sr_{1-x}La_xTiO_3$ undergoes a semiconductor-metal transition within a range of x from 0.05 to 0.2 (Fujimori et al., 1996; Tokura et al., 1993; Sunstrom et al., 1992). Therefore, as the end members in $Sr_{1-1.5x}Y_xTiO_{3-\delta}$ are both insulators, two metal-insulator transitions are anticipated as a function of doping level. Meanwhile, increasing the Sr-site doping levels increases disorder in the material, which may cause a localization of electrons, known as Anderson localization (Cox, 1987). Since critical doping concentrations for a metal-insulator transition are determined by an interplay between the tendency toward delocalization of extra charge carriers and their Anderson localization by disordered

potential, metallic conductivity may not be observed in $Sr_{1-1.5x}Y_xTiO_{3-\delta}$ with significant Sr-site deficiency. In a structural analog, $Ca_{1-x}Y_xTiO_3$, two metal-insulator transitions have been found at x = 0.1 and 0.7 (Taguchi et al., 1993).

7.4.2. Effects of Grain and Grain Boundary

Fractured surfaces of $Sr_{1-1.5x}Y_xTiO_{3-\delta}$ (x = 0.02, 0.04, 0.06, 0.08) sintered at 1400°C for either 10 or 20 h were examined by scanning electron microscopy (SEM) as shown in Fig. 7.21. In all cases, the grain size varied only slightly from 3 to 6 μm. Grain growth in $SrTiO_3$ and $BaTiO_3$ have been reported to be highly sensitive to donor-doping (Burn and Neirman, 1982; Yan, 1981; Kahn, 1971). At low donor concentrations, grain growth may become pronounced during high temperature sintering, often resulting in 50-100 μm grains, but at high donor concentrations grain growth is suppressed, with resulting grains of a few microns in size as we observed. Burn and Neirman found that the threshold in Y-doped $SrTiO_3$ was close to 1%, depending on the overall lattice cation stoichiometry (1982). While this so-called donor-anomaly has been the subject of much research, to date a clear mechanistic interpretation has not been proposed.

While the small grain structure may provide good mechanical properties, the accompanying large grain boundary area may impede electrical conductivity. Grain boundaries play an important role in the electrical properties of a variety of ceramic materials and components. In a broad range of ceramics that show ionic conduction, mixed ionic-electronic conduction, or electronic conduction, grain boundaries act as barriers for the cross-transport of the charge carriers. In donor-doped $SrTiO_3$ and $BaTiO_3$, it is well known that electrons trapped at grain boundaries are screened by the

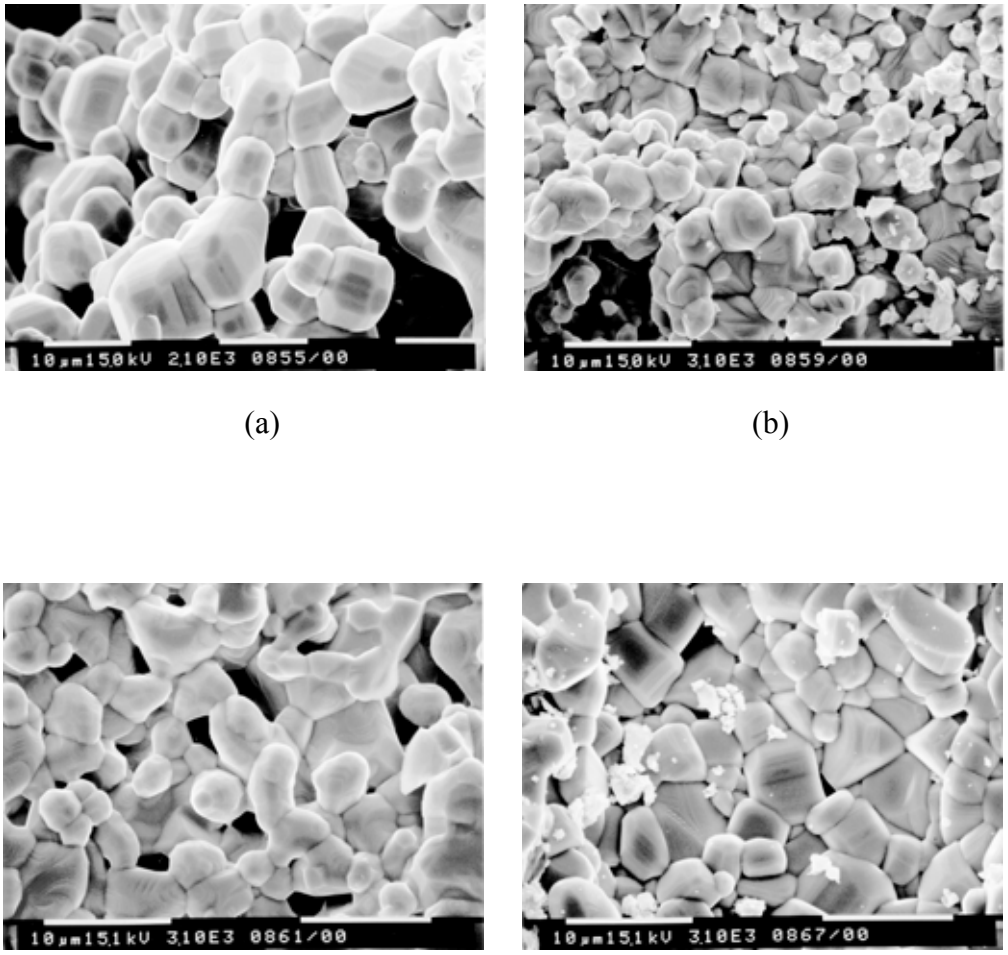

(a) (b)

(c) (d)

Fig. 7.21. SEM micrographs of fracture surfaces of Y-doped $SrTiO_3$: (a) $Sr_{0.97}Y_{0.02}TiO_{2.989}$ 1400°C 10h, (b) $Sr_{0.94}Y_{0.04}TiO_{2.980}$ 1400°C 10h, (c) $Sr_{0.91}Y_{0.06}TiO_{2.970}$ 1400°C 10h, (d) $Sr_{0.88}Y_{0.08}TiO_{2.968}$ 1400°C 20h

ionized defect states forming a depletion space charge layer. From an electronic view, that grain boundary can be described as a back-to-back double Schottky barrier (Chiang and Takagi, 1990). The electric field generated by the charged interface gives rise to a band bending in the adjacent grains. Grain boundaries represent inhomogeneities in structure and composition. Compositional inhomogeneities can be marked due to processes such as impurity segregation and/or kinetically limited reactions in the vicinity of the boundaries. These grain boundary defects and impurities give rise to a distribution in energy of a planar array of localized interface states (Kingery, 1974). Fujimoto et al. (1985) used HRTEM and SEM to reveal Ti_nO_{2n-1} Magneli phase (Ti_4O_7, Ti_5O_9 and others). The Magneli phases exist at multiple grain junctions in $SrTiO_3$. Based on a study by HRTEM, Battle et al. (2000) also concluded that the surface contains relatively more Ti^{3+} than the inner material that is rich in TiO_2. Magneli phases were formed by complexes of TiO_2 and Ti_2O_3 at the grain boundaries inside the bulk. The increased permittivity and dielectric relaxation found on donor-doped $SrTiO_3$ sintered in air was explained as a boundary-layer effect resulting from semiconducting grains and weakly insulating grain boundaries (Burn, 1982). Often, the barrier character of the grain boundaries is especially pronounced in the low-temperature region. Since $SrTiO_3$ consists of semiconducting grains which are separated by an insulating material (Magneli phases), the "brick-wall"-like microstructure of the Magneli phases surrounds the $SrTiO_3$ grains, resulting in a high dielectric constant (Kingery et al., 1976).

The conduction of a polycrystalline material is a complex superposition of at least two contributions, the grain and the grain boundary. In some ionic crystals, the space charge regions formed between grains and grain boundaries may also play an important

role (Vollman and Waser, 1994). The measurements of conductivity by the dc four-probe method were bulk values, i.e., including both grains and grain boundaries. The distribution of resistance from grains and grain boundaries in sintered materials may be separated using impedance spectroscopy (IS). However, the corresponding conductivities from grains and grain boundaries were impossible to measure because of the uncertainty of their geometric sizes. Therefore the conductance, the reciprocal of resistance, rather than the conductivity, is used to evaluate the effects of grain and grain boundaries on transport properties.

The ac impedance of $Sr_{0.88}Y_{0.08}TiO_{3-\delta}$ was measured in a range of temperatures, and a typical plot measured at 650^{o}C is shown in Fig. 7.22 (a). As can be seen, the grain has small resistance and negligible capacitance while the grain boundary has large resistance and capacitance at 650^{o}C. This difference could not be distinguished for the samples reduced in forming gas because of the high conductivity for both grains and grain boundaries. An equivalent circuit is shown is Fig. 7.22 (b). Fig. 7.23 shows the conductance of grain and grain boundary extracted from impedance measurements as a function of temperature. The conductance from grain boundaries varies significantly while the conductance from grains is relatively constant, suggesting that the conduction of grain boundaries is more sensitive to the temperature change than that of grains. The conductance difference between grain and grain boundary decreased with increasing temperature. Thus the effect of grain boundaries on electronic transport was less significant at high temperature. As mentioned before, the grain boundary has band bending, and the corresponding conductances of grain and grain boundary are illustrated

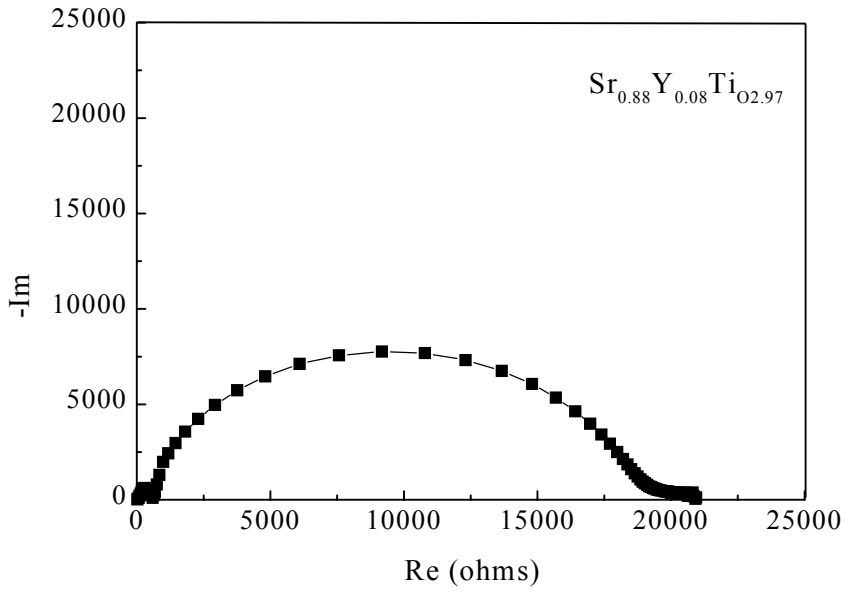

Fig. 7.22. (a) The ac complex impedance plot for $Sr_{0.88}Y_{0.08}TiO_{2.968}$ at 650°C, (b) The equivalent circuit that gives rise to the complex impedance plot

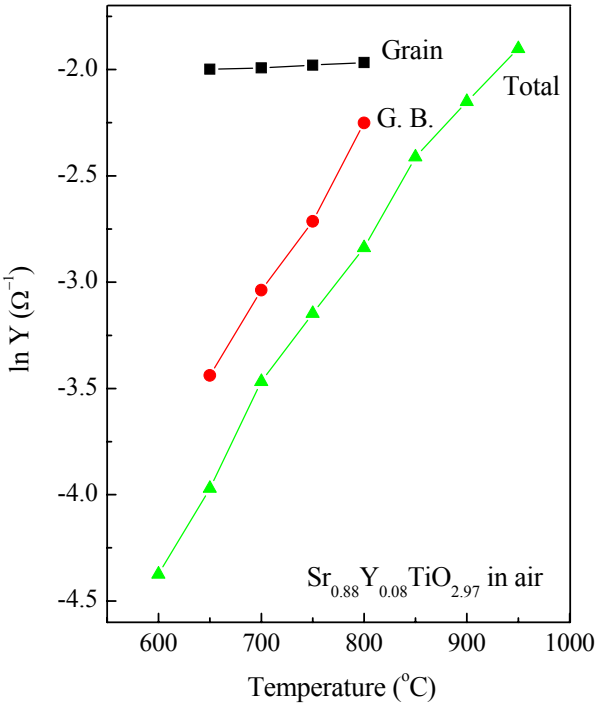

Fig. 7.23. Conductance contribution from grains and grain boundaries as a function of temperature for $Sr_{0.88}Y_{0.08}TiO_{2.968}$

in Fig. 7.24. A grain $_{boundary}$ in a $SrTiO_3$ becomes electrically active as a result of charge trapping by gap states localized between two adjacent grains. Such interface states are possibly created by the crystallographic mismatch between the adjacent grains, thereby leading to dangling bonds or other interfacial defects. A second possible origin of these states are yttrium or impurity atoms trapped at the interface and acting as donor levels. The effects of grain boundaries may be understood better by comparing the conductivity between single crystal and polycrystalline materials. Attempts to grow a single crystal of the composition $Sr_{0.88}Y_{0.08}TiO_{3-\delta}$ by floating-zone method was unsuccessful.

7.4.3. Dependence of Electrical Conductivity on Cation-Cation Ratio

The electrical properties are known to be very sensitive to the lattice defects created in particular by any deviation from unity of the ratio of Sr and Ti concentrations. For example, under certain conditions, a change of this ratio by only 0.1% may change the electrical conductivity by a factor of as much as 10 (Chan et al., 1981). In order to evaluate the dependence of conductivity on cation-cation ratio, a series of samples with composition $Sr_xY_{0.08}TiO_{3-\delta}$ ($0.75 \leq x \leq 0.92$) were prepared. Fig. 7.25 shows the measured conductivity in equilibrium with oxygen partial pressures between 10^{-14} to 10^{-19} atm for different compositions at 800^{o}C. The conductivity extracted from Fig. 7.25 at oxygen partial pressure of 10^{-19} atm was plotted as a function of composition deviation in Fig. 7.26. $Sr_xY_{0.08}TiO_3$ with x = 0.92 is the stoichiometric composition and x = 0.88 represents charge neutrality when all ions are in their normal valence states. The conductivity improved by increasing the Sr deficiency up to x = 0.86.

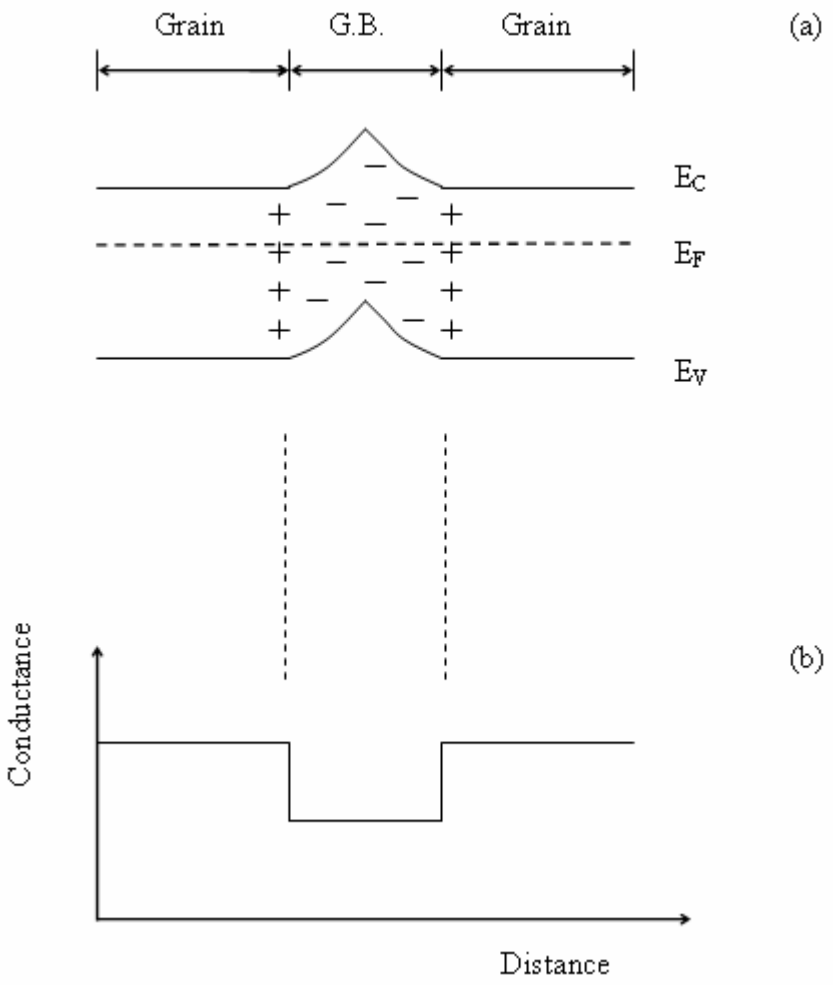

Fig. 7.24. (a) Illustration of band bending in grain boundary, and (b) corresponding conductance

Assuming the extra charge from Y^{3+} is balanced by V_{Sr}'' as discussed before, the composition of highest conductivity was found to be $Sr_{0.86}Y_{0.08}TiO_{3-\delta}$ that is off the ideally charge-balanced composition $Sr_{0.88}Y_{0.08}TiO_3$. The corresponding conductivity under reducing conditions at 800°C increased from 64 S/cm to 82 S/cm.

Ruddlesdon and Popper (1958) first noted that the Sr-Ti-O system forms a series of $xSrO\text{-}yTiO_2$ compounds, and specifically identified Sr_2TiO_4 and $Sr_3Ti_2O_7$. These compounds appear as varying numbers of SrO layers interleaved within perovskite layers, leaving the oxygen sublattice intact. Eror and Smyth (1978) have proposed that La-doped $SrTiO_3$ with unit cation/anion ratio may form a layer structure in a similar way to one of the Ruddlesdon and Popper phases. La as dopant induces the adsorption of oxygen that reacts to form an SrO layer and leaves Sr vacancies in the host lattice to compensate for the donor. The compensation of the donor becomes electronic, and consequently the electrical conductivity increases sharply when the excess oxygen is removed under reduction. The SrO and the associated Sr vacancies form layers of different composition on specific crystal planes without altering the perovskite lattice. This is supported by the work of Odekirk et al. (1982) who found evidence of Sr vacancies in La-doped $SrTiO_3$ using low temperature conductivity measurements, and by Tilley (1977) who observed by electron microscopy that excess SrO was accommodated in $SrTiO_3$ by the formation of a lamellar structure. In this study, agreement was achieved for the conductivity of SYT with Sr-site deficiency between measurement and calculation. However, the conductivity of SYT with unit A/B ratio, $Sr_{0.92}Y_{0.08}TiO_{3-\delta}$, was only half

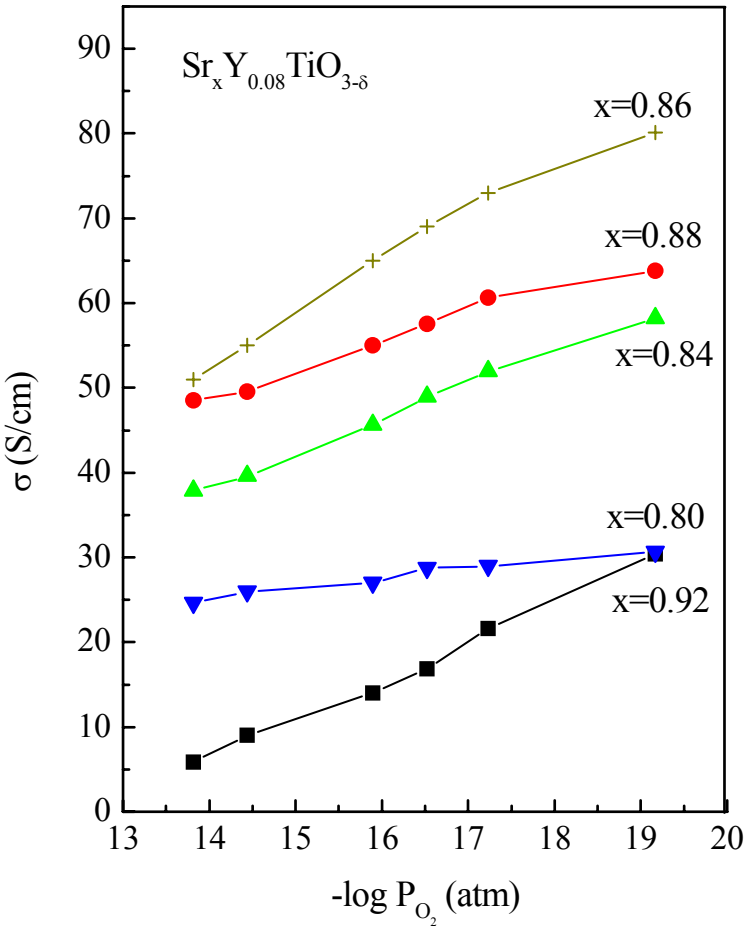

Fig. 7.25. Dependence of conductivity on composition $Sr_xY_{0.08}TiO_{3-\delta}$ ($0.80 \leq x \leq 0.92$) over a range of oxygen partial pressures at 800°C

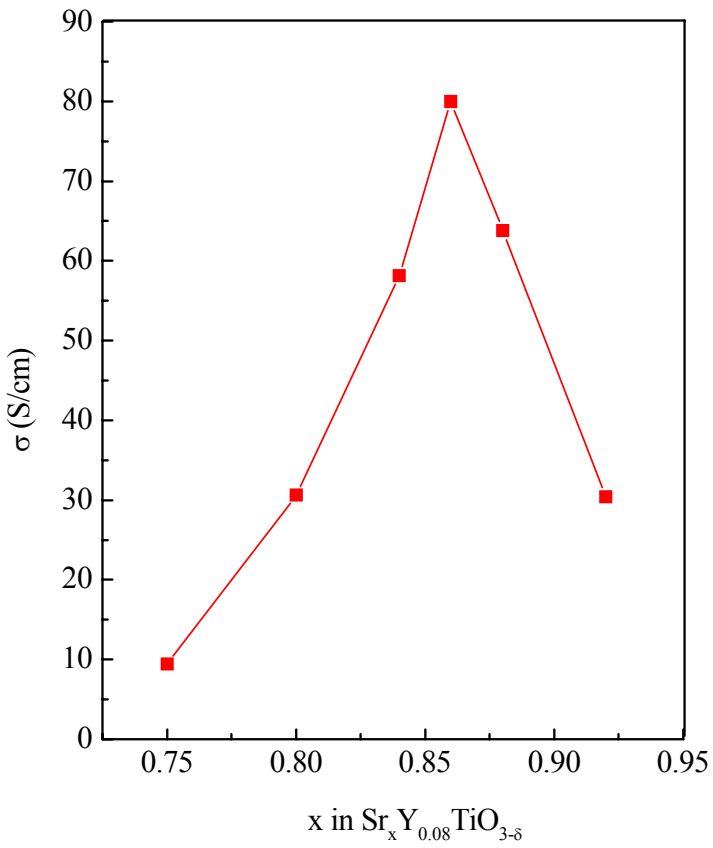

Fig. 7.26. Variation of conductivity with composition for $Sr_xY_{0.08}TiO_{3-\delta}$ at 800^{o}C and oxygen partial pressure of 10^{-19} atm

value of the conductivity of $Sr_{0.88}Y_{0.08}TiO_{3-\delta}$ with Sr vacancies under reducing conditions. For Y-doped $SrTiO_3$, conductivity increased when increasing Sr deficiency intentionally, indicating that the excess oxygen adsorbed to form SrO layers could not be completely removed by reduction. From studies of high resistivity materials, Aksenova et al. (1986) concluded that excess SrO prevented such reduction.

It is well known that A-site deficiency in titanate perovskites results in self doping at the titanium site, and consequently increases the electrical conductivity (Bazuev et al., 1983; Gong et al., 1991; Kim et al., 1994). The existence of A-site vacancies may weaken the bond strength of TiO_6 octahedra adjacent to the cation vacancies. When the material containing a large number of A-site vacancies is fired at elevated temperatures, oxygen vacancies plus electrons can be thermally generated. For Y-doped $SrTiO_3$, the defect compensation gets more complicated with Sr-site vacancies. As mentioned previously, charge carriers in Y-doped $SrTiO_3$ are mainly induced by reduction and are saturated by Y-doping level. Based on the considerations above, the A-site deficiencies may lead to a shift in the composition with highest conductivity from the ideal charge balanced $Sr_{0.88}Y_{0.08}TiO_{3-\delta}$, to the slightly lower $Sr_{0.86}Y_{0.08}TiO_{3-\delta}$.

CHAPTER 8

ACCEPTOR-DOPED STRONTIUM TITANATES

8.1. Acceptor-Doped $SrTiO_3$

Good performance of electrode materials requires fast compositional equilibrium upon the removal or addition of electroactive species at the electrolyte interface during charge or discharge. Polarization causes loss of the chemical energy converted into electrical energy in favor of the formation of heat. The problem is particularly significant for the development of fuel cells with high power density and high efficiency. It has been often shown that additions to perovskite oxides are crucial to promoting catalytic activity and high conductivity. However, reports on co-doped $SrTiO_3$ are rare and little is known about the defect chemistry or transport mechanism of these materials. In this chapter, the effect on conductivity of acceptor doping the titanium site are presented. The ionic conductivity with 5 mol% acceptor doping was estimated from the total electrical conductivity versus oxygen partial pressure plot.

As presented in Fig. 7.7, normally pure $SrTiO_3$ shows a p-n transition from acceptor impurities present, i.e., p-type semiconductor at high oxygen partial pressures and n-type semiconductor at low oxygen partial pressures. However, if one of the host cations is replaced with a cation of lower valence, and the host cation does not compensate by increasing its valence, oxygen ion vacancies can form so as to maintain electrical

neutrality of the crystal. The oxygen ion vacancies can facilitate the migration of oxygen ions as in the case of stabilized zirconia. To test this, acceptor-doped $SrTiO_3$ with composition $SrTi_{1-x}Ga_xO_{3-\delta}$ and $SrTi_{1-x}Co_xO_{3-\delta}$ were sintered in air. Fig. 8.1 shows the equilibrium conductivity at different oxygen partial pressures at 800°C, together with the results for undoped $SrTiO_3$. A p-n transition was found for all three compositions with different conductivity minima.

The introduction of acceptor dopants into $SrTiO_3$, such as gallium with fixed oxidation state, can be written as:

$$2SrO + Ga_2O_3 = 2Sr_{Sr} + 2Ga'_{Ti} + 5O_O + V_O^{\bullet\bullet} \tag{8.1}$$

Based on this equation it is assumed that the electroneutrality can be approximated by

$$2[V_O^{\bullet\bullet}] = [Ga'_{Ti}] = constant \tag{8.2}$$

As can be seen, oxygen vacancy concentration depends on the valence state and doping-level of the acceptor. More oxygen vacancies are generated by an acceptor with a lower oxidation state. Since the oxygen vacancy concentration is fixed extrinsically by the dopant concentration for a given acceptor, the oxygen conductivity is independent of oxygen partial pressure. However, the concentration of p-type electronic defects, and thus the conductivity, increases with increasing oxygen partial pressure, while the concentration, and thus the conductivity, of n-type defects increases with decreasing oxygen partial pressure. Thus, pure ionic conductivity occurs at intermediate oxygen pressures, where the contributions of both n-type and p-type conductivity are small.

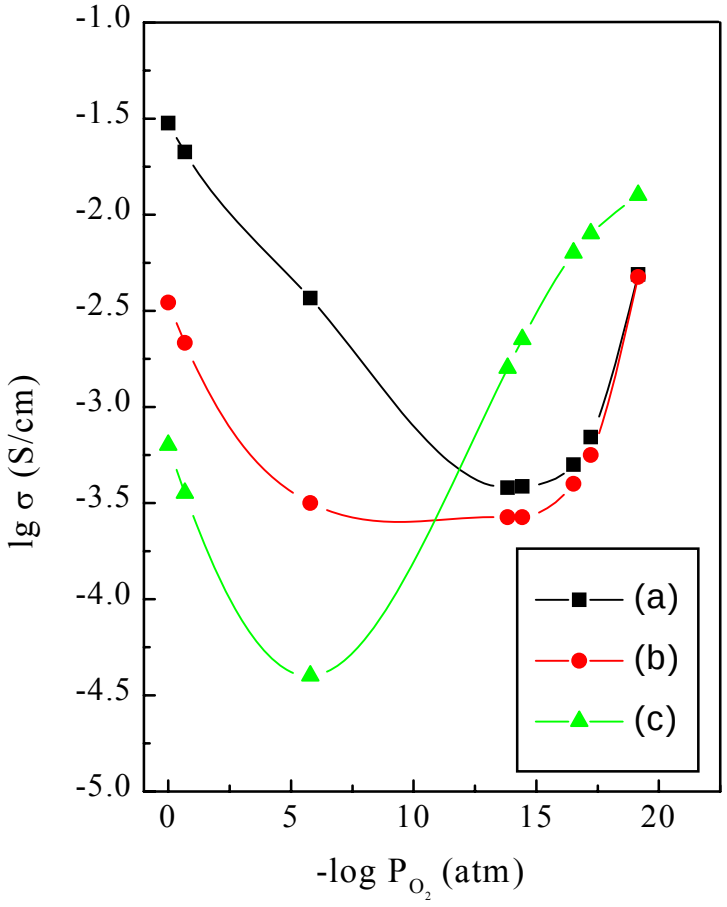

Fig. 8.1. Dependence of conductivity on oxygen partial pressure at 800^{o}C for (a) $SrTi_{0.95}Co_{0.05}O_{3-\delta}$, (b) $SrTi_{0.95}Ga_{0.05}O_{3-\delta}$, (c) $SrTiO_{3-\delta}$

Oxygen vacancies can also be induced by reduction or self-doping according to:

$$TiO_2 = 2Ti'_{Ti} + V_O^{\bullet\bullet} + \frac{1}{2}O_2(g) \qquad (8.3)$$

However, the concentration of oxygen vacancies generated is low, and the electrons induced have a more significant contribution to conductivity due to their much higher mobility. As discussed in Chapter 7, this leads to a pressure dependence of conductivity as a function of $P_{O_2}^{-1/6}$.

Therefore, one can expect that in the acceptor dominated region, oxygen vacancy concentration and resulting conductivity is independent of oxygen partial pressure while in the reduction dominated region, the slope of electron concentration or resulting conductivity versus oxygen partial pressure is independent of acceptor concentration.

Unlike gallium, cobalt has multiple oxidation states. Depending on the oxygen partial pressure, the oxidation state of cobalt can be 2, 3 or 4. Therefore, in comparison with Ga-doped $SrTiO_3$, a small amount of mixed valent cobalt at high oxygen partial pressure may lead to a significant increase in conductivity in Co-doped $SrTiO_3$ (Fig. 8.1).

At intermediate oxygen partial pressures, the conductivity curves show a flat region of essentially ionic conductivity that is due to oxygen vacancies and is independent of oxygen partial pressure according to Eq. 8.2. For the same doping level, the ionic conductivity only depends on the oxidation state of the acceptor. Consistent conductivity minima were observed for gallium and cobalt doped $SrTiO_3$, and if predominantly ionic, would indicate a similar oxygen vacancy concentration n and the same trivalent oxidation

state for cobalt as for gallium under the experimental conditions. The minimum conductivity increased from 3 x 10^{-5} S/cm for undoped $SrTiO_3$ to 3 x 10^{-4} S/cm for 5 mol% acceptor-doped $SrTiO_3$ at 800°C due to the acceptor doping. The ionic conductivity is expected to increase further with increasing temperature or acceptor-doping level. Fig. 8.2 shows the effect of temperature on the plots of log σ versus log P_{O_2} for Ga-doped $SrTiO_3$. For a fixed acceptor-doped level, the concentration of oxygen vacancies is constant, and the increase in the conductivity minimum is due to the increase of ionic mobility with temperature. Since the number of electrons generated by reduction also increases with temperature, the p-type region extended with decreasing temperature. The region of linearity in the p-type region increased in width with decreasing temperature as the p-n transition shifted to lower oxygen partial pressure (Fig. 8.2).

As anticipated, at low oxygen partial pressures, log conductivity tends to obey a –1/6 dependence of log oxygen partial pressure regardless of the type of acceptor, attributed to n-type conductivity. The electrons induced by reduction dominate the conductivity, and similar slopes were observed for gallium and cobalt doped $SrTiO_3$ as seen in Fig. 8.1.

8.2. Acceptor and Donor Co-doped $SrTiO_3$

As demonstrated previously, both donors such as yttrium or acceptors such as cobalt can modify electronic and ionic conductivity. It was anticipated that donor and acceptor co-doping could improve both electronic and ionic conductivities because these two types of conduction are generally independent. On the other hand, the changes in electronic structure would in turn also modify the catalytic performance of the resultant materials by a proper choice of the B-site cations.

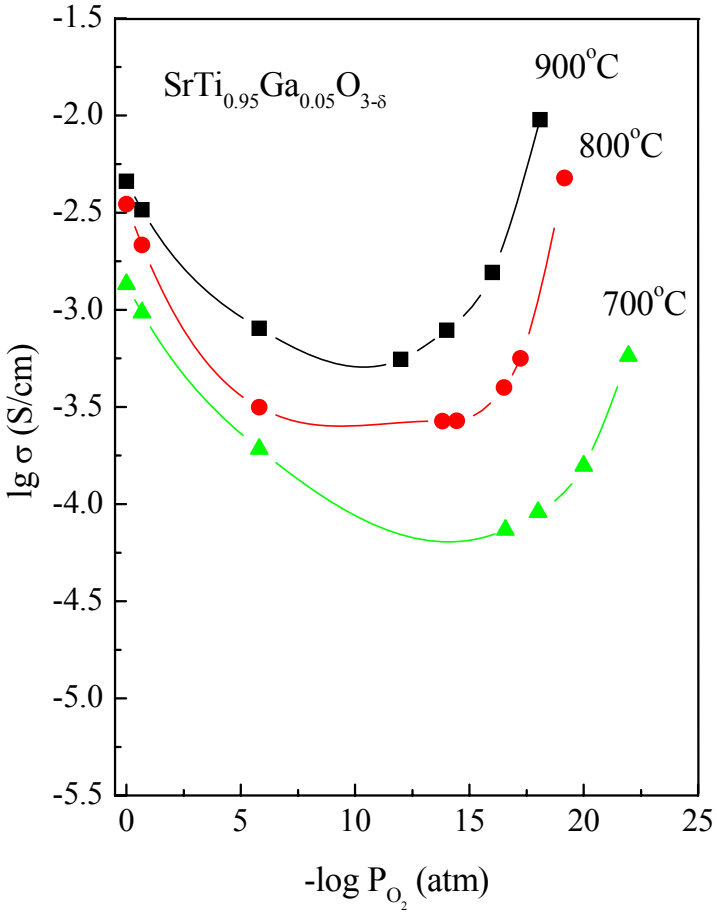

Fig. 8.2. Effects of temperatures on plots of conductivity versus oxygen partial pressure for Ga-doped $SrTiO_3$

A series of compositions, $Sr_{1-1.5x}Y_xTi_{0.95}Co_{0.05}O_{3-\delta}$ ($0.08 \le x \le 0.12$) were sintered in air at 1400°C for 10 hours. Following regrinding, the samples were pressed into rods (6 x 15 mm) and sintered in forming gas at 1400°C for 5 hours. The conductivities were measured by the dc four-probe method over a range of oxygen partial pressure at 800°C (Fig. 8.3.). Yttrium doping levels significantly influenced the conductivities while conductivities were almost independent of oxygen partial pressure. Fig. 8.4 shows the dependence of conductivity on yttrium content in $Sr_{1-1.5x}Y_xTi_{0.95}Co_{0.05}O_{3-\delta}$ at 800°C and an oxygen partial pressure of 10^{-19} atm, in comparison with the composition $Sr_{1-1.5x}Y_xTiO_{3-\delta}$. Although the profiles of conductivity versus yttrium content are similar for both systems, the effects of cobalt in SYT are apparent. The peak value of conductivity of cobalt-doped SYT dropped and shifted along the x-axis compared with that of SYT.

The distribution of electrons in thermal equilibrium is described by the Fermi-Dirac function (Kittel, 1976). The concentration of electrons in the conduction band is given by

$$n = N_c[1 + \exp\{(E_c - E_F)/kT\}]^{-1} \tag{8.4}$$

where E_c and E_F are the energies of conduction-band edge and Fermi levels, respectively, and N_c the effective density of states in the band. As most of the oxides are non-degenerate semiconductors, i.e., $E_c - E_F \gg kT$, a Boltzmann-like form may replace the Fermi-Dirac equation:

$$n = N_c \exp\{-(E_c - E_F)/kT\} \tag{8.5}$$

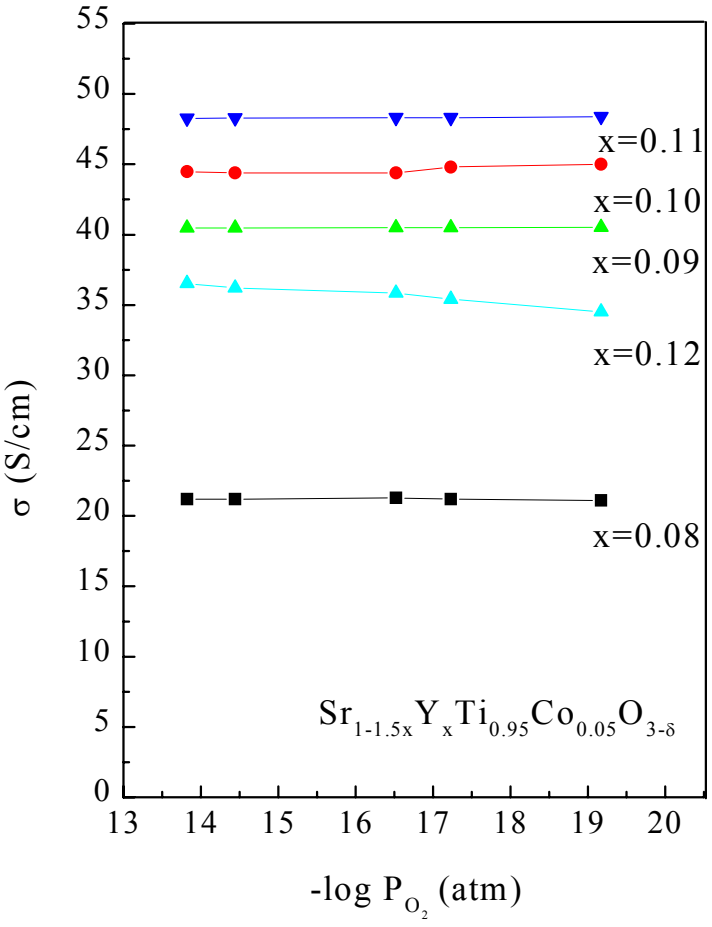

Fig. 8.3. Dependence of conductivity on oxygen partial pressure for yttrium and cobalt codoped $SrTiO_3$ at 800°C.

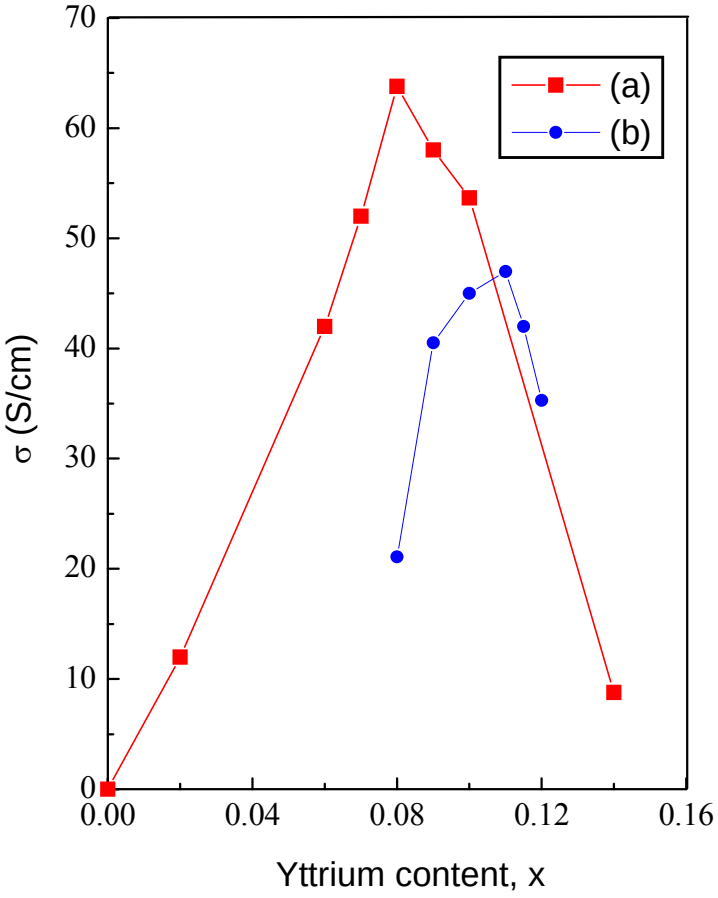

Fig. 8.4. Comparison of conductivity as a function of yttrium content between (a) $Sr_{1-1.5x}Y_xTiO_{3-\delta}$ and (b) $Sr_{1-1.5x}Y_xTi_{0.95}Co_{0.05}O_{3-\delta}$ at 800°C at oxygen partial pressure of 10^{-19} atm

A similar treatment for the hole concentration, p, gives

$$p = N_v \exp\{-(E_F - E_v)/kT\} \tag{8.6}$$

A general condition may therefore be written for electrons and holes simultaneously present in equilibrium

$$np = N_c N_v \exp(-E_g/kT) \tag{8.7}$$

where E_g (= $E_c - E_v$) is the band gap.

For a donor and acceptor co-doped system, the conductivity is a result of interaction between electronic defects generated by the donor and the acceptor. As pointed out in Chapter 7, extra electrons are generated by reduction and saturated by the Y-doping level:

$$O_O = \frac{1}{2}O_2 + V_O^{\bullet\bullet} + 2e' \tag{8.8}$$

When an acceptor such as Co^{3+} is added to Y-doped $SrTiO_3$, positively charged electron holes are generated in the valence band

$$Co_{Ti} = Co'_{Ti} + h^{\bullet} \tag{8.9}$$

Therefore, for donor and acceptor co-doped $SrTiO_3$, part of the electrons generated by the donor may be neutralized by electron holes generated by the acceptor:

$$null = e' + h^{\bullet} \tag{8.10}$$

In this way, the electron concentration decreases while the hole concentration

increases to satisfy the condition of Eq. (8.7). The decrease in electron concentration most likely results in decreased conductivity for donor and acceptor co-doped $SrTiO_3$ as observed in Fig. 8.4.

For fixed yttrium-doping levels, the electron and hole compensation in donor and acceptor co-doped systems becomes more significant with increasing hole concentration, for example, either by increasing the acceptor-doping level or decreasing the acceptor oxidation-state from 3+ to 2+. This was confirmed for the compositions $Sr_{0.85}Y_{0.10}Ti_{1-x}Co_xO_{3-\delta}$ (x = 0, 0.05, 0.10) in the range of oxygen partial pressure of 10^{-14} to 10^{-19} atm at 800^{o}C as shown in Fig. 8.5.

The charge neutralization of yttrium by addition of acceptors may also promote the dissolution of more yttrium in $SrTiO_3$. As can be seen in Fig. 8.4, the peak value of conductivity for $Sr_{1-1.5x}Y_xTi_{0.95}Co_{0.05}O_{3-\delta}$ shifted to a higher content of yttrium, indicating an increase in yttrium solid solubility in cobalt-doped $SrTiO_3$. This was confirmed by x-ray diffraction as shown in Fig. 8.6. Impurity peaks could not be identified for $Sr_{0.85}Y_{0.10}Ti_{0.95}Co_{0.05}O_{3-\delta}$. Doping acceptor can simultaneously enhance the solubility of the donor. This is in accord with a previous study on the influence of an acceptor (gallium) on the solubility of a donor (lithium) in germanium (Reiss et al., 1956). The intrinsic solubility of lithium at room temperature is about $10^{20}/m^3$. By addition of gallium, the solubility may be increased by a factor of almost 10^6.

For Co-doped SYT, $Sr_{0.88}Y_{0.08}Ti_{0.95}Co_{0.05}O_{3-\delta}$, the lattice parameter was determined to be 3.9030(3) Å that is between 3.9054(2) Å for $SrTiO_3$ and 3.9013(3) Å for

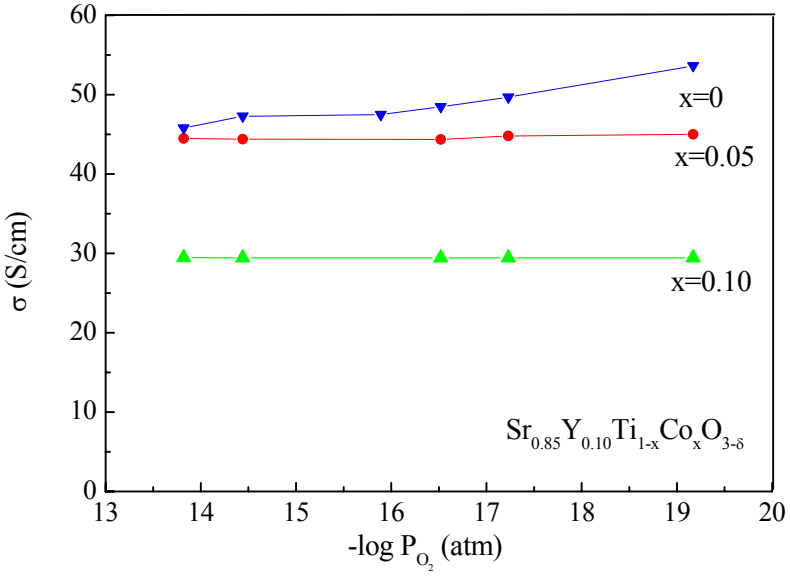

Fig. 8.5. Effects of acceptor-doping level on conductivity for $Sr_{0.85}Y_{0.10}TiO_{3-\delta}$ at 800°C

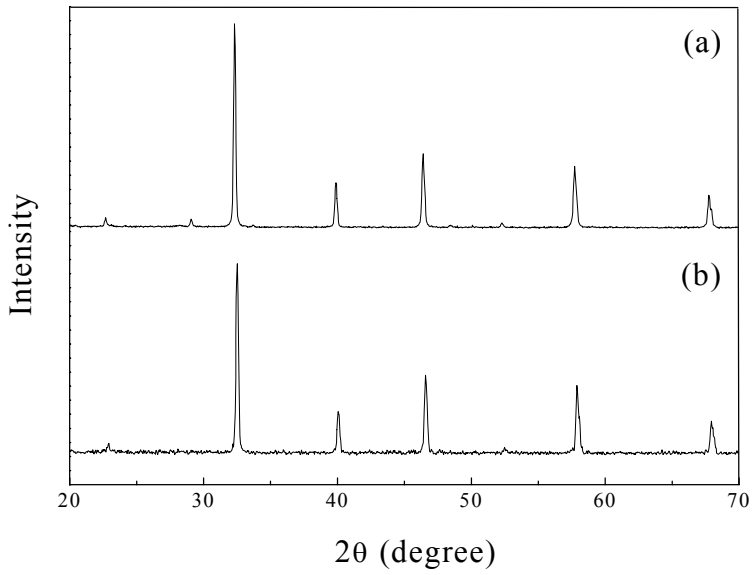

Fig. 8.6. X-ray diffraction spectrums for (a) $Sr_{0.85}Y_{0.10}TiO_{3-\delta}$ and (b) $Sr_{0.85}Y_{0.10}Ti_{0.95}Co_{0.}05O3_{-\delta}$

$Sr_{0.88}Y_{0.08}TiO_{3-\delta}$. The dissolution of 5 mol% cobalt in SYT is nominally accompanied by the generation of 2.5 mol% oxygen vacancies according to Eq. 8.2. Thermogravimetric measurement revealed that the concentration of oxygen vacancies increased from 1 mol% in $Sr_{0.88}Y_{0.08}TiO_{2.97}$ to 2 mol% in $Sr_{0.88}Y_{0.08}Ti_{0.95}Co_{0.05}O_{2.94}$. The difference between the measured value of 2 mol% and the theoretical calculation of 2.5 mol% is most likely due to the presence of Co^{4+}. In contrast with the decrease of electronic conductivity in donor and acceptor co-doped $SrTiO_3$, the ionic conductivity is expected to increase because of the increase of oxygen vacancy concentration. This co-doped system deserves further investigation to verify the degree of ionic conductivity.

For $Sr_{0.85}Y_{0.10}Ti_{0.95}Co_{0.05}O_{3-\delta}$, a semiconductor to metal transition was found during reduction-oxidation cycling as shown in Fig. 8.7. The conductivity of $Sr_{0.85}Y_{0.10}Ti_{0.95}Co_{0.05}O_{3-\delta}$ in oxidizing or weakly reducing environments increased with increasing temperature as shown in Fig. 8.8 (a), indicating semiconducting behavior. The activation energy for conduction in an argon atmosphere is estimated to be 1.3 eV. The conductivity of $Sr_{0.85}Y_{0.10}Ti_{0.95}Co_{0.05}O_{3-\delta}$ at oxygen partial pressures of 10^{-14} to 10^{-19} atm decreased with increasing temperature as seen in Fig. 8.8 (b), indicating metallic behavior. This suggested that a semiconductor to metal transition occurred between oxygen partial pressures of 10^{-6} to 10^{-14} atm. Unfortunately, the conductivity data in this range of oxygen partial pressures are not easily obtainable due to experimental limitations. The semiconductor/metal transition was confirmed for other cobalt and yttrium co-doped systems as shown in Fig. 8.9. On the other hand, the composition $Sr_{0.88}Y_{0.08}TiO_{3-\delta}$ was a semiconductor throughout the oxygen pressure range as discussed in Chapter 7. It is hypothesized that the presence of low spin Co^{3+} in SYT is responsible

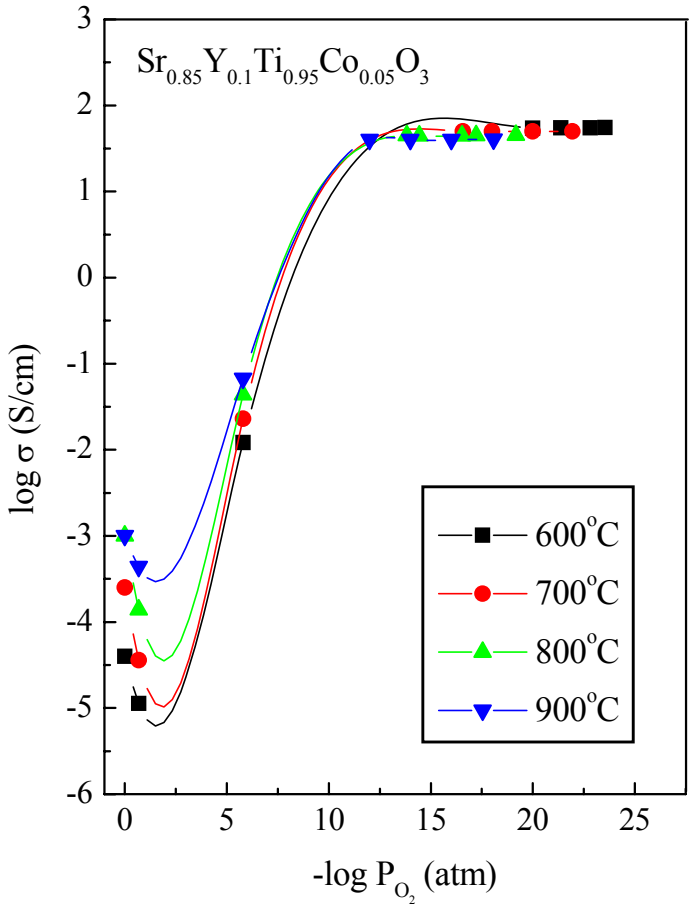

Fig. 8.7. Semiconductor to metal transition with changing oxygen partial pressure for Co-doped SYT

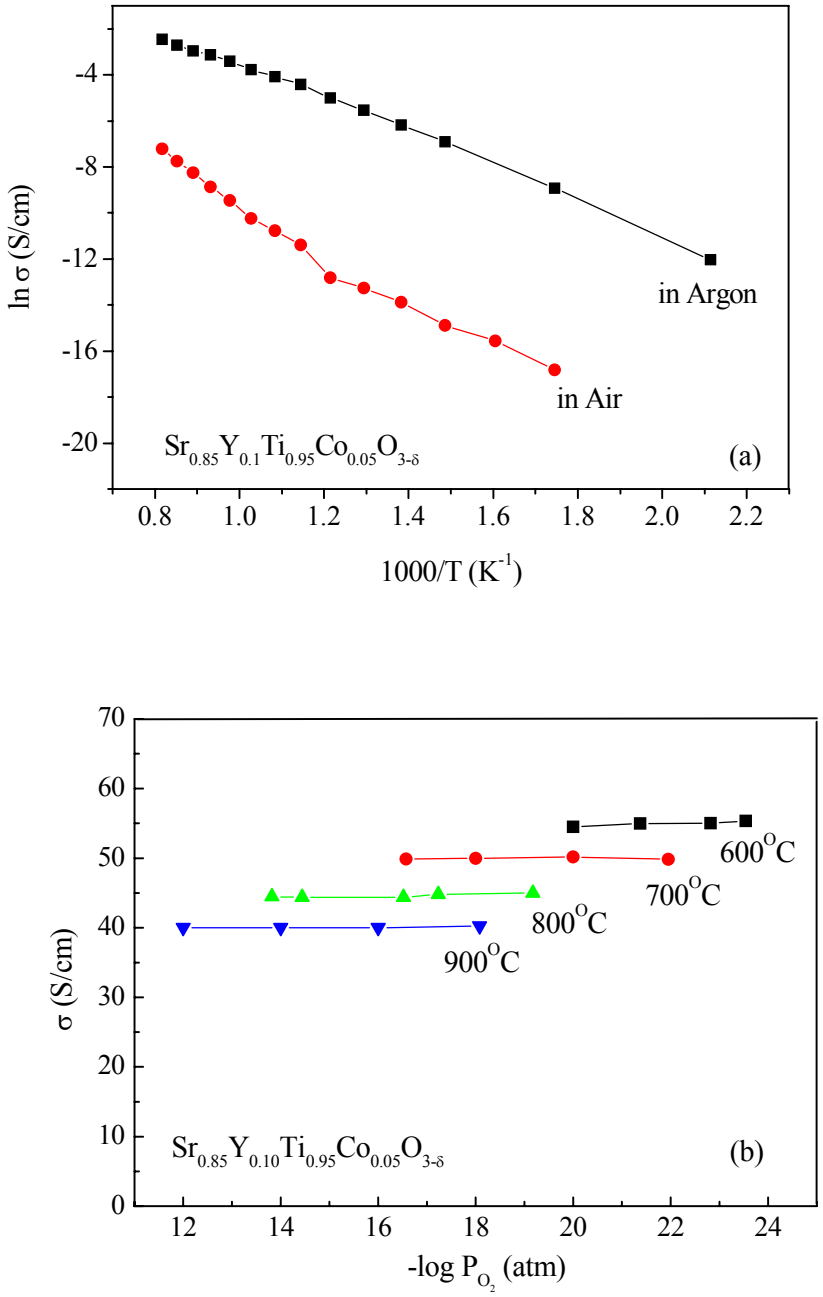

Fig. 8.8. (a) semiconducting behavior in the region of high oxygen partial pressure, (b) metallic behavior in the region of low oxygen partial pressure

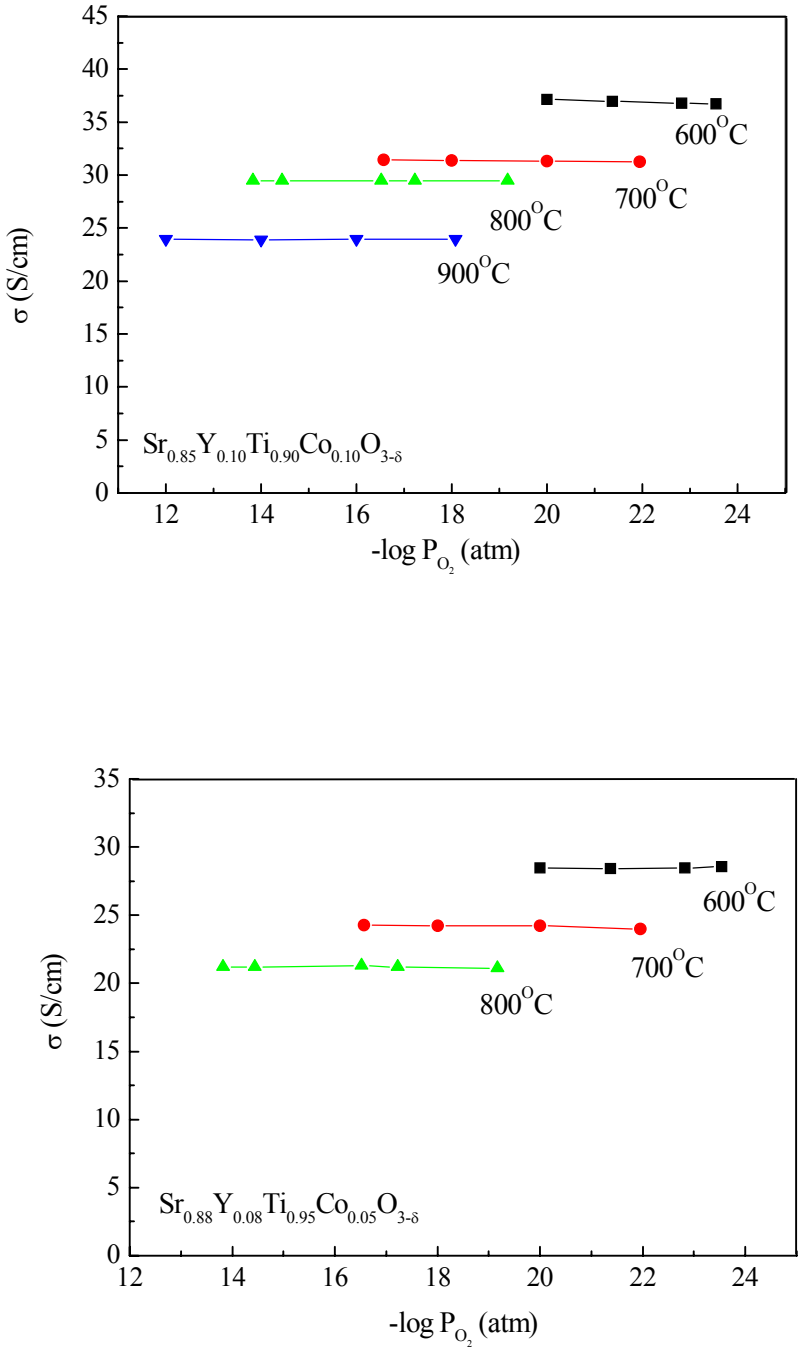

Fig. 8.9. Metallic behavior for cobalt and yttrium codoped $SrTiO_3$ under strongly reducing atmospheres

for this complicated electronic transition. This demonstrates that the electrical properties of SYT are significantly influenced by 5 mol% doping on the B-site.

Co^{3+} has the diamagnetic low-spin $3d^6$ configuration. An ion with this electronic configuration in octahedral coordination could have a full t_{2g} band and be non-metallic. It is known that the compound $LaCoO_3$, which has the perovskite structure with Co^{3+} occupying the octahedral site, is indeed non-metallic at low temperatures. However, it appears that the gap between the top of the t_{2g} and the bottom of the e_g bands is very small, and above room temperature $LaCoO_3$ undergoes a transition to metallic form (Goodenough, 1971). As the temperature increases, lattice expansion reduces the t_{2g}-e_g splitting, and facilitates the thermal excitation of carriers into the e_g band. Populating this more antibonding level will itself increase the lattice spacing, and thus the gap will disappear. Similar processes may occur in Co-doped SYT in strongly reducing environments where Co^{3+} exists, initiating the onset of a semiconductor/metal transition.

Cobalt-doping is of particular interest here because the most active catalysts are those that contain cobalt (Voorhoeve, 1977). Transition metal oxides have long been used as catalysts. It is well known that the A ions in perovskites are in general catalytically inactive. The catalytic activity of perovskites depends mainly on the B ions, and the activity sequence is similar to those of single B oxides. Nakamura et al. (1980) have studied the catalytic oxidation of propane, methane and CO on several perovskites of the type $(La_{1-x}A_x)MO_3$ (A = Ca, Sr, Ba, Ce; M = Cr, Mn, Fe, Co, Ni) prepared by co-precipitation. The general trend of catalytic activity was found to be in the order Co > Mn > Ni > Fe > Cr, and strontium was the most effective corresponding A-ion in enhancing the activity. The same authors also found that among the

cobaltites, $La_{0.8}Sr_{0.2}CoO_3$ was the most active and its activity was comparable to or higher than those of Pt, Pd and Ni catalysts. A similar order of activities in other oxidation-reduction reactions over transition metal oxides and perovskites was confirmed by other researchers (Bockris and Otagawa, 1984; Arai et al., 1986; McCarty and Wise, 1990). Two types of catalytic processes have been proposed for perovskite-type catalysts by Voorhoeve (1977): intrafacial and suprafacial catalysis. Suprafacial reactions are those for which the reaction between adsorbed species on the surface is much faster than reactions involving lattice oxygen. They are often low-temperature processes. On the other hand, the intrafacial reactions are those in which the removal of oxygen from the lattice or the reverse process, that is, reduction-oxidation of the catalyst, is an important process. The latter is considered here to apply to oxidation of fuel at the anode in an SOFC. To get a good anode capable of direct methane oxidation, the material must have an electron acceptor properly coordinated with oxygen at active centers. The more conducting the material is, both electronically and ionically, the better the activity, as long as the active centers are not lost.

In order to evaluate the effect on conductivity of B-site doping in SYT, a number of oxides with the composition $Sr_{0.85}Y_{0.10}Ti_{0.95}M_{0.05}O_{3-\delta}$ (M = V, Mn, Fe, Co, Ni, Cu, Zn, Mo, Mg, Zr, Al, Ga) were surveyed in a range of oxygen partial pressure from 10^{-14} to 10^{-19} atm at 800°C (Fig. 8.10. a). In cases of M = Cu, Ga, Mn, Co, the samples were sintered in air at 1400°C for 10 h to avoid volatilization loss under reducing conditions, and then reduced in forming gas at 1400°C for 5 h before the conductivity measurements were performed. All other samples were sintered in forming gas directly. In all the cases,

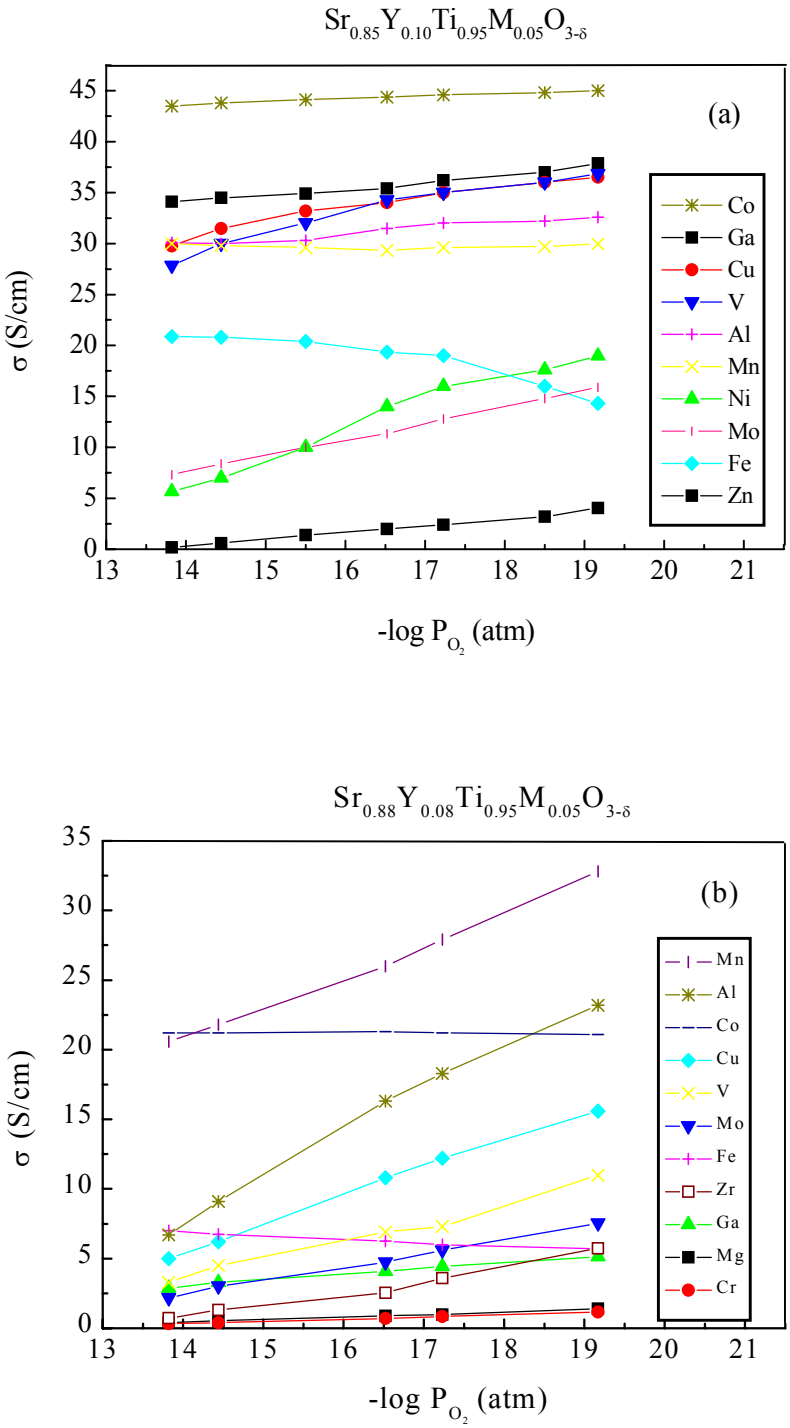

Fig. 8.10. Effects of acceptor doping on conductivity at 800°C in a range of oxygen partial pressures for (a) $Sr_{0.85}Y_{0.10}Ti_{0.95}M_{0.05}O_{3-\delta}$, (b) $Sr_{0.88}Y_{0.08}Ti_{0.95}M_{0.05}O_{3-\delta}$

the conductivities were lower with 5 mol% replacement of Ti in $Sr_{0.85}Y_{0.10}TiO_{3-\delta}$, with the effects being least deleterious for Co. Similar experiments were conducted for the composition $Sr_{0.88}Y_{0.08}Ti_{0.95}M_{0.05}O_{3-\delta}$ (M = V, Cr, Mn, Fe, Co, Cu, Mo, Mg, Zr, Al)

(Fig. 8.10. b). As discussed in Chapter 7, the conductivities of 10% yttrium doped samples were in general higher than that of 8% yttrium doped samples. The general trend of the effects of 3d transition metals on conductivity was plotted in Fig. 8.11. In both cases, conductivities varied with a zigzag pattern as a function of the first transition metal series.

It has been seen that the addition of cobalt to SYT brought about metallic behavior under strongly reducing conditions. Fig. 8.11 shows the variation of the effect of B-site doping on conductivity among different dopants. It is not clear why a zigzag pattern appears. A possible explanation is the dependence of charge carriers on the transition metals. Electrons are generated by oxygen loss from the lattice according to Eq. 8.8. Because electrical properties in perovskites are primarily dependent on the B-O interaction, the electrons induced from reduction will consequently depend on how easy it is to break the B-O bond. Therefore, we may expect that the fraction of electrons generated by the dopant metal, M, is proportional to the reciprocal of the M-O bond strength. We define ΔH_o for MO_x as one-Xth the enthalpy of formation for MO_x which normalizes the number of metal-oxygen bonds per mole of each oxide. ΔH_o may be taken as an indication of the metal-oxygen bond strength in the oxide, averaged over all the metal-oxygen bonds present. In this way, the values of ΔH_o are not seriously affected by the valence-state of the oxides. Fig. 8.12 shows a comparison between the trends of

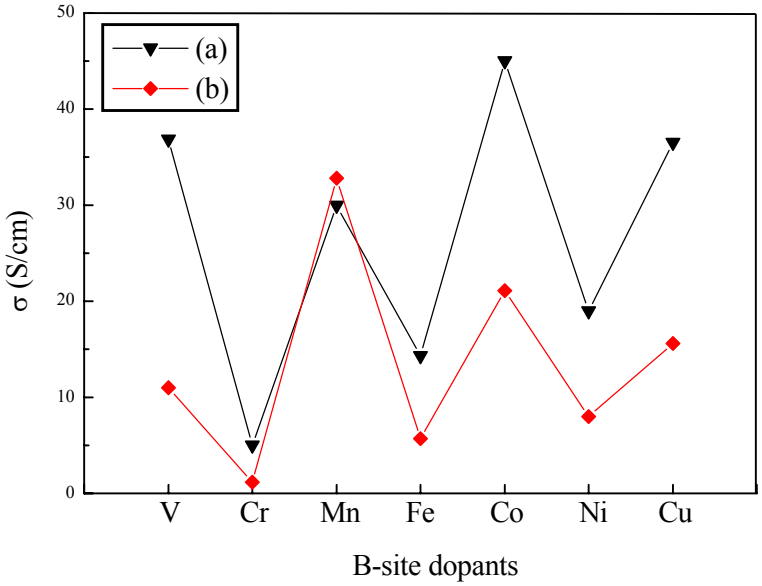

Fig. 8.11. Trend of conductivity among various acceptor dopants in the 3d transition series for (a) $Sr_{0.85}Y_{0.10}Ti_{0.95}M_{0.05}O_{3-\delta}$ (b) $Sr_{0.88}Y_{0.08}Ti_{0.95}M_{0.05}O_{3-\delta}$

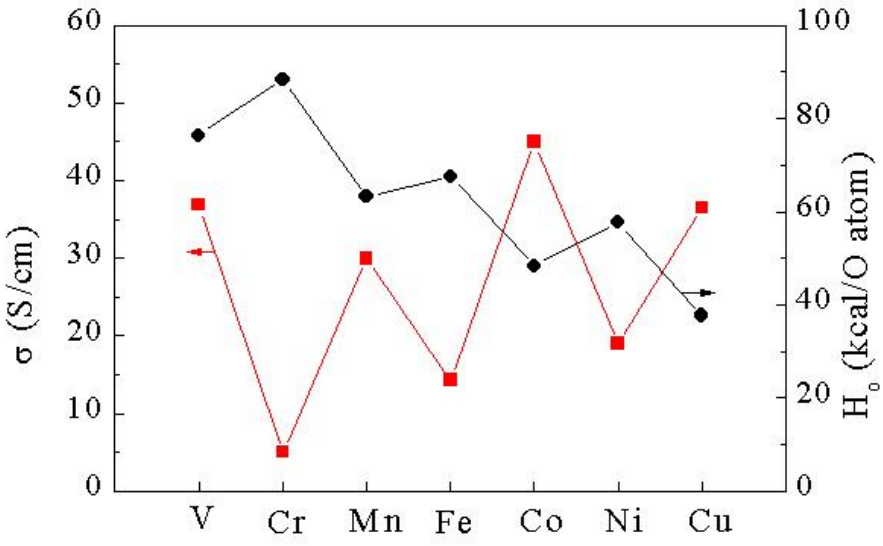

Fig. 8.12. Comparison between conductivity of $Sr_{0.85}Y_{0.10}Ti_{0.95}M_{0.05}O_{3-\delta}$ and M-O bond strength for V_2O_5, Cr_2O_3, Mn_2O_3, Fe_2O_3, CoO, NiO, and CuO

conductivities of $Sr_{0.}85Y0_{.10}Ti_{0.95}M_{0.05}O_{3-\delta}$ (M = V, Mn, Fe, Co, Ni, Cu, Zn) and ΔH_o along the first transition series. The values of ΔH_o were calculated from corresponding binary oxides (David, 1992). As expected, a good agreement between the conductivity and reciprocal M-O bond strength can be seen. Therefore, the zigzag pattern probably reflects that the less stable an M-O bond is, the more easily the oxygen is lost at evaluated temperatures to form electronic defects for conduction. A similar interpretation was used by Kremenić et al. (1985) to explain the twin-peak pattern of catalytic activity for $LaMO_3$ (M = Cr, Mn, Fe, Co, Ni).

CHAPTER 9

OXIDATION-REDUCTION BEHAVIOR

9.1. Redox Behavior of $Sr_{0.88}Y_{0.08}TiO_{3-\delta}$

The rate of oxidation and reduction of $Sr_{0.88}Y_{0.08}TiO_{3-\delta}$ has been studied by measuring the change in the electrical conductivity as a function of time as the specimen was annealed in air and 7% H_2 (Fig. 9.1). The samples were initially reduced in forming gas at 1400°C to obtain a reference conductivity under reducing conditions before the oxidation-reduction studies. The electrical conductivity changed rapidly with changing atmospheres either from forming gas to air (oxidation) or vice versa (reduction). One of the noticeable features is the parabolic time dependence of the change in electrical conductivity for both oxidation and reduction processes. Another observation is that conductivity was reversible on oxidation and reduction. However, the rate of reduction is much slower than that of oxidation, indicating that the incorporation of oxygen into lattice is much easier than the release of oxygen from lattice.

The oxidation-reduction reactions take place according to Eq. (9.1)

$$O_O \xleftrightarrow{oxidation-reduction} 2e' + V_O^{\bullet\bullet} + \frac{1}{2}O_2(g) \qquad (9.1)$$

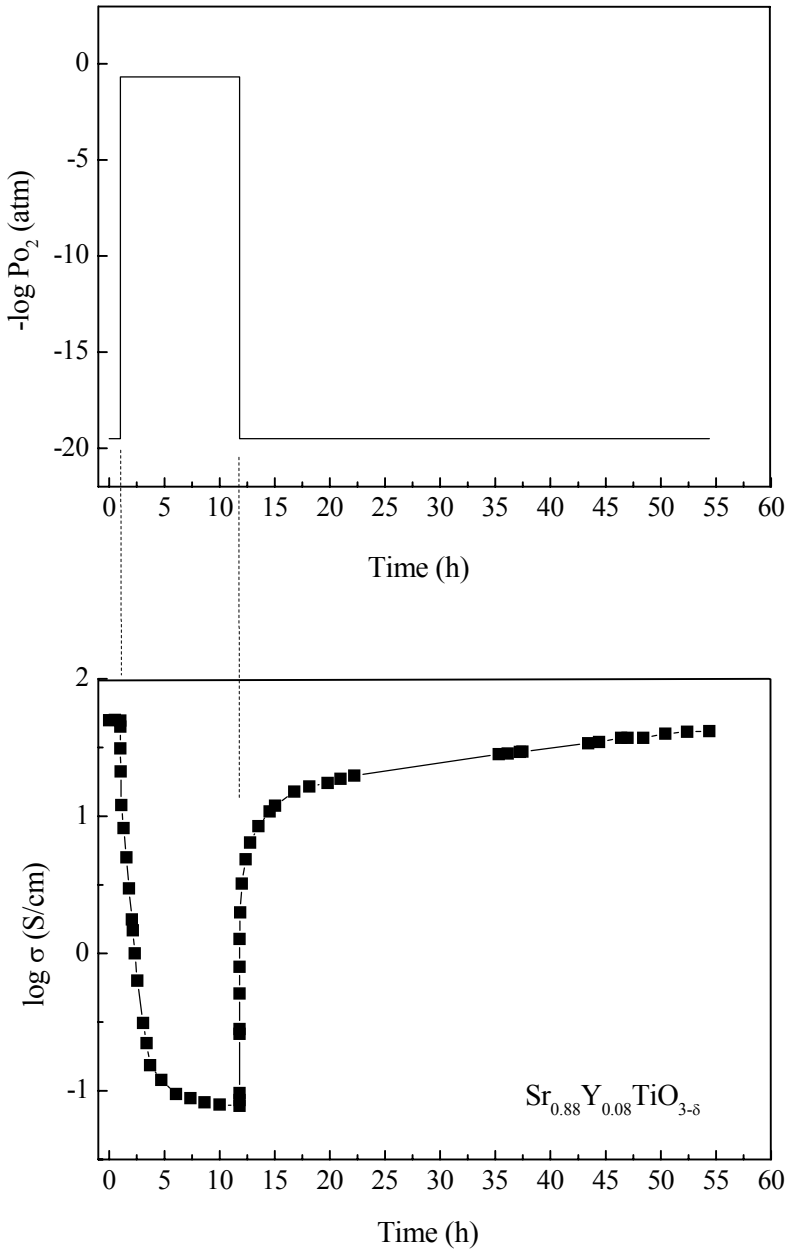

Fig. 9.1. Change of electrical conductivity for $Sr_{0.88}Y_{0.08}TiO_{3-\delta}$ at 800°C after a sudden oxygen partial pressure change

To be a useful material for fuel cell anodes, the change of electrical conductivity must be either rapid upon oxidation-reduction or kinetically hindered, especially for oxidation. The reduction of $Sr_{0.88}Y_{0.08}TiO_{3-\delta}$ involves the release of oxygen from lattice, and results in the formation of electrons and oxygen vacancies. The opposite reaction occurs during the oxidation process. The extent of reduction or oxidation, α, is defined as

$$\alpha = \frac{\Delta W_t - \Delta W_o}{\Delta W_\infty - \Delta W_o} \tag{9.2}$$

where ΔW is the weight loss, or oxygen deviation from stoichiometry, in relation to the stoichiometric composition, and t, o, and ∞ correspond to arbitrary time, initial state, and the final state, respectively (Smyth, 1989). Since the oxygen deviation is proportional to the electron concentration (Eq. 9.1), one can express Eq. 9.2 in terms of conductivity as

$$\alpha = \frac{\sigma_t - \sigma_o}{\sigma_\infty - \sigma_o} \tag{9.3}$$

assuming the electron mobility is independent of concentration. As can be seen, the degree of reduction is a time dependent parameter.

Two processes in series have been proposed for the oxidation and reduction reactions, the gas-solid interface reaction and the bulk diffusion of relevant species, one of which is rate controlling (Kung, 1989; Philibert, 1988). As can be seen in Fig. 9.1, the conductivity of $Sr_{0.88}Y_{0.08}TiO_{3-\delta}$ changes rapidly at first, and reaches a plateau after some time. This behavior is typical for diffusion controlled processes, indicating a fast surface reaction at 800^{o}C for both oxidation and reduction. The composition changes

must proceed by mass transport via diffusion from the gas-solid interface into the bulk (reduction) or from the bulk toward the gas-solid interface (oxidation). The kinetics of these oxidation-reduction processes depends therefore on the rate of diffusion or mobility of the oxygen vacancies. For the reduction process, the core of the $Sr_{0.88}Y_{0.08}TiO_{3-\delta}$ is reduced by diffusion of oxygen vacancies and reductant across the oxide/reduced oxide interface whose area decreases with time. The distance of this interface from the surface of the specimen increases with time. Therefore, the rate of reduction or the conductivity decreases with time.

As pointed out in Section 7.4, when temperature is changed, conductivity shows an effect due to the grain boundaries. For most oxides with a close-packed oxygen sublattice, oxygen diffusion at the grain boundaries appears to be rapid relative to diffusion within the grains. As a result, when oxygen partial pressure is changed, a stoichiometry change at the grain boundaries preferentially occurs (Kingery, 1974). The grain boundaries may act as fast conduction paths during reduction or as blocking layers during oxidation, via a conduction mechanism that is more or less independent of the grain behavior.

9.2. Redox Behavior of Acceptor and Donor Co-doped SrTiO3

To evaluate the effects of acceptor addition at titanium-sites on the oxidation-reduction behavior, a number of samples with the composition $Sr_{0.85}Y_{0.10}Ti_{0.95}M_{0.05}O_{3-\delta}$ (M = V, Mn, Fr, Co, Ni, Cu, Ga, Al,) were studied by either electrical conductivity measurements or thermogravimetric analysis. The samples were equilibrated in 7% H_2 at 1400^{o}C for 10 hours.

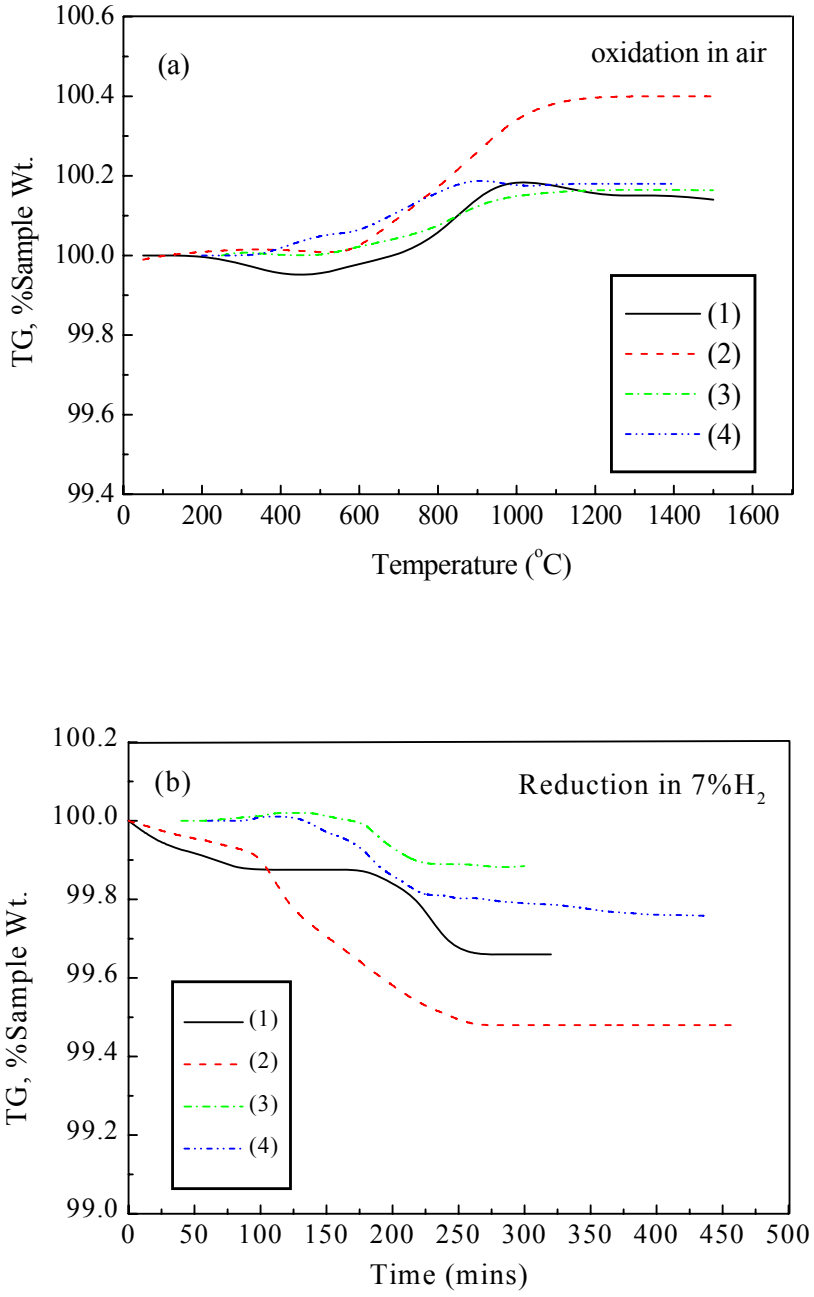

Fig. 9.2. Plots of thermogravimetric analysis during (a) oxidation process and (b) reduction process for (1) $Sr_{0.88}Y_{0.08}TiO_{3-\delta}$, (2) $Sr_{0.85}Y_{0.10}Ti_{0.95}Co_{0.05}O_{3-\delta}$, (3) $Sr_{0.85}Y_{0.10}Ti_{0.95}Ga_{0.05}O_{3-\delta}$, (4) $Sr_{0.85}Y_{0.10}Ti_{0.95}Cu_{0.05}O_{3-\delta}$

Fig. 9.2 shows the weight change for selected compositions during an oxidation-reduction cycle at a heating rate of 5°C/minute. The onset temperature, i.e., the starting temperature for observed change of weight, the weight change, and the degree of reduction are summarized in Table 9.1. For all the cases, the onset temperature for reduction is higher than that for oxidation, indicating the activation energy for reduction is higher than that for oxidation. This is in accord with the conductivity measurement in Section 9.1 where the reduction process and the conductivity took much longer to recover than the oxidation process at the same temperature.

Because the oxidation and reduction is limited by oxygen vacancy diffusion through the oxide, and assuming diffusion occurs by the motion of isolated oxygen vacancies, any dopant that enhances the oxygen vacancy concentration should increase the oxidation and reduction rate. Correspondingly, the faster the oxygen diffusion is, the higher the degree of reduction for oxidized materials. The degree of reduction for $Sr_{0.85}Y_{0.10}Ti_{0.95}M_{0.05}O_{3-\delta}$ (M = Co, Cu, Ga, Al,) was indeed enhanced compared with that of $Sr_{0.85}Y_{0.10}TiO_{3-\delta}$. However, this was not observed for manganese or vanadium doped samples.

These results were consistent with the results of conductivity measurements. Fig. 9.3 shows the change of electrical conductivity during reduction in 7% H_2 at 800°C for $Sr_{0.85}Y_{0.10}Ti_{0.95}M_{0.05}O_{3-\delta}$ (M =Mn, Co), together with the results for $Sr_{0.85}Y_{0.10}TiO_{3-\delta}$. Samples sintered in forming gas were equilibrated in air at 1400°C for 5 h before the conductivity measurement. The degree of reduction for $Sr_{0.85}Y_{0.10}TiO_{3-\delta}$, $Sr_{0.85}Y_{0.10}Ti_{0.95}Co_{0.05}O_{3-\delta}$ and $Sr_{0.85}Y_{0.10}Ti_{0.95}Mn_{0.05}O_{3-\delta}$ after a period of 24 h was 11.7, 17.3, and 2.1% , respectively.

Table 9.1. Results of thermogravimetric analysis (Oxidation was carried out at a constant heating rate of 5°C/min up to 1500°C. Reduction was carried out at 800°C in 7% H_2 for 5 h.)

Composition	Redox Condition	Onset Temperature (°C)	Weight Change (%)	Degree of Reduction (%)
$Sr_{0.88}Y_{0.08}TiO_{2.97}$	Oxidation	450	0.29	
	Reduction	900	0.19	66
$Sr_{0.85}Y_{0.1}Ti_{0.95}Co_{0.05}O_{3-\delta}$	Oxidation	550	0.40	
	Reduction	750	0.39	97
$Sr_{0.85}Y_{0.1}Ti_{0.95}Al_{0.05}O_{3-\delta}$	Oxidation	480	0.09	
	Reduction	850	0.09	100
$Sr_{0.85}Y_{0.1}Ti_{0.95}V_{0.05}O_{3-\delta}$	Oxidation	420	0.94	
	Reduction	550	0.52	55
$Sr_{0.85}Y_{0.1}Ti_{0.95}Cu_{0.05}O_{3-\delta}$	Oxidation	350	0.30	
	Reduction	670	0.30	100
$Sr_{0.85}Y_{0.1}Ti_{0.95}Ga_{0.05}O_{3-\delta}$	Oxidation	520	0.17	
	Reduction	720	0.16	94
$Sr_{0.85}Y_{0.1}Ti_{0.95}Mn_{0.05}O_{3-\delta}$	Oxidation	460	0.16	
	Reduction	620	0.06	38
$Sr_{0.85}Y_{0.1}Ti_{0.95}Ni_{0.05}O_{3-\delta}$	Oxidation	600	0.53	
	Reduction			
$Sr_{0.85}Y_{0.1}Ti_{0.95}Fe_{0.05}O_{3-\delta}$	Oxidation	550	0.39	
	Reduction			

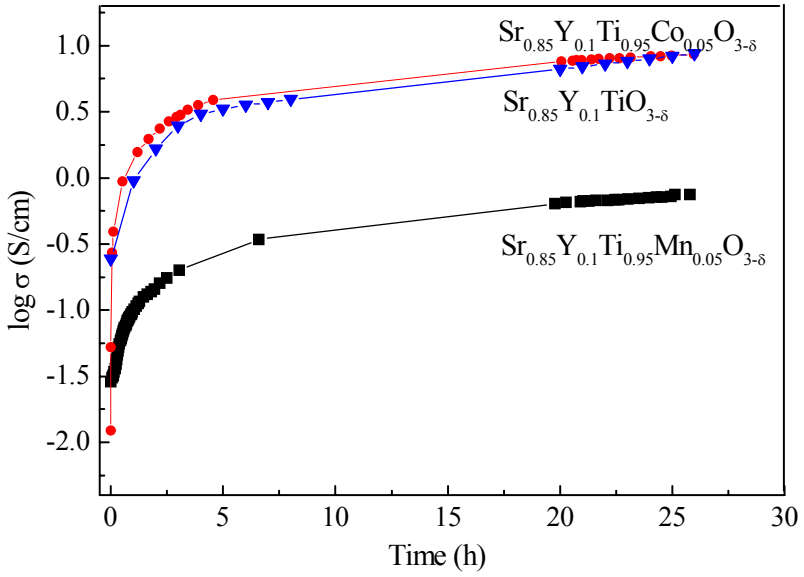

Fig. 9.3. Electrical conductivity as a function of time during reduction in 7% H_2 at 800°C

Another significant feature for acceptor and donor co-doped $SrTiO_3$ is their resistance to oxidation. Fig. 9.4 presents a comparison of conductivity change upon oxidation and reduction between $Sr_{0.85}Y_{0.1}TiO_{3-\delta}$ and $Sr_{0.85}Y_{0.1}Ti_{0.95}M_{0.05}O_{3-\delta}$ (M = Co, Mn) at 800°C. The change of conductivity for $Sr_{0.85}Y_{0.1}Ti_{0.95}M_{0.05}O_{3-\delta}$ (M = Co, Mn) is much less than that for $Sr_{0.85}Y_{0.1}TiO_{3-\delta}$ when oxygen partial pressure was changed from about 10^{-20} atm (in 7% H_2 at 800°C) to 0.21 atm (in air). Typically, for the composition containing cobalt, the conductivity dropped only 5 S/cm over a period of 6 hours. The conductivity of $Sr_{0.85}Y_{0.1}Ti_{0.95}Co_{0.05}O_{3-\delta}$ was still as high as 17.5 S/cm after oxidizing for 24 hours at 800°C. The oxidation resistance of electrical conductivity for

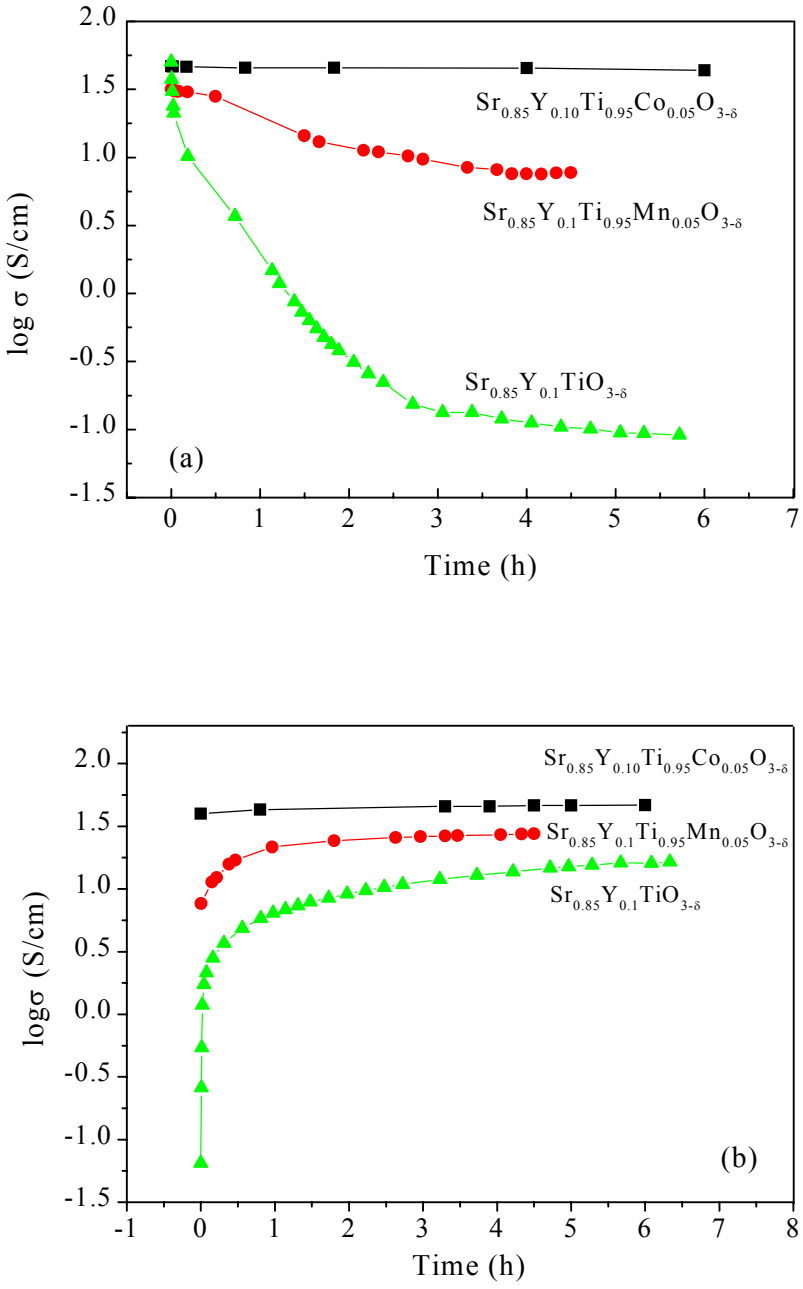

Fig. 9.4. Change of conductivity at 800°C after a sudden oxygen partial pressure change: (a) oxidation in air, (b) reduction in 7% H_2

$Sr_{0.85}Y_{0.1}Ti_{0.95}M_{0.}05O3_{-\delta}$ (M = Co, Mn) may be due to the existence of mixed valence states of Co^{3+}-Co^{4+} and Mn^{3+}-Mn^{4+}. It is well known that compounds containing these elements with mixed valence states have good electrical conductivity. To eliminate the effects of variable oxidation states, more work may be required to understand the mechanism of oxidation resistance by using dopants with fixed valence state.

9.3. Effects of Materials Processing on Redox Behavior

9.3.1. Effects of Atmosphere and Temperature

For practical applications, the anode material may be co-fired with the electrolyte and cathode materials at a temperature of about 1400°C. Air is preferred as the firing atmosphere from considerations of cost and chemical stability of cathode materials. A crude investigation was made to answer some concerns related to the practical fabrication of fuel cells using doped $SrTiO_3$ anodes. These concerns include the effects of firing conditions (atmospheres and temperatures) on reduction and the effects of porosity on oxidation and reduction. In the discussion here, the as-prepared samples refer to rod-shaped materials that were sintered in 7% H_2 for 10 h.

As pointed out previously, air-fired samples exhibited a low reduction rate in 7% H_2 at 800°C. An enhanced degree of reduction was expected for the samples fired in a mildly reducing atmosphere such as argon. Two as-prepared samples with the composition $Sr_{0.85}Y_{0.1}Ti_{0.95}Co_{0.05}O_{3-\delta}$ were individually fired in argon and air at 1400°C for 4 h. Fig. 9.5 shows the change of conductivity versus time in 7% H_2 at 950°C. The rate of reduction for $Sr_{0.85}Y_{0.1}Ti_{0.95}Co_{0.05}O_{3-\delta}$ fired in argon is greater than for that fired in

air. However, the slight difference indicates that firing in mildly reducing atmospheres does not strongly favor the reduction.

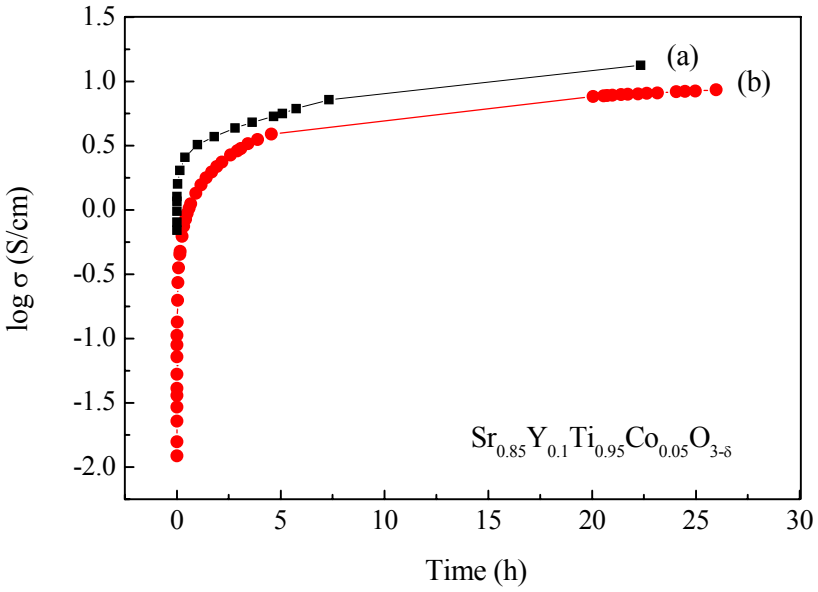

Fig. 9.5. Change of conductivity versus time in 7% H_2 at 950°C for $Sr_{0.85}Y_{0.10}Ti_{0.95}Co_{0.05}O_{3-\delta}$ at 1400°C fired (a) in Ar, (b) in air

Alternatively, the reduction of doped $SrTiO_3$ fired in air may be accelerated by stronger reducing agents. A comparison between 7% H_2 and pure H_2 was made for the reduction of $Sr_{0.88}Y_{0.08}Ti_{0.95}Mn_{0.05}O_{3-\delta}$ at 950°C (Fig. 9.6). The conductivity after a reduction period of 2 h in pure H_2 is 31.6 S/cm, while the conductivity is only 7.5 S/cm in 7% H_2. Compared with a conductivity of 30.1 S/cm for a fully reduced sample at 800°C, a high degree of reduction was achieved by using pure H_2 as the reducing agent.

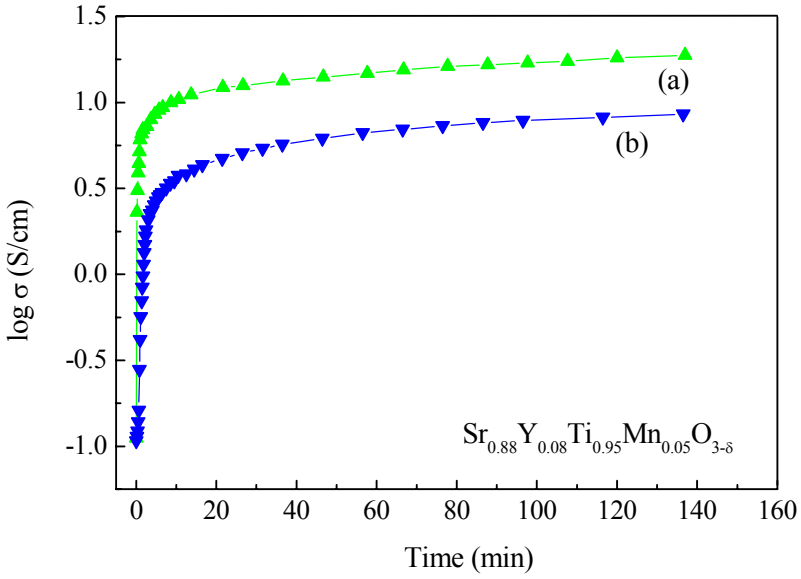

Fig. 9.6. Comparison of conductivity change in (a) H_2 and (b) 7% H_2 at 950°C for $Sr_{0.88}Y_{0.08}Ti_{0.95}Mn_{0.05}O_{3-\delta}$ fired in air at 1400°C

The effects of firing temperatures on the subsequent reduction process were also examined in this study. Four as-prepared samples with the same composition, $Sr_{0.85}Y_{0.1}Ti_{0.95}Mn_{0.05}O_{3-\delta}$, were fired at different temperatures in air for 4 h, and then followed by reduction in 7% H_2 at 800°C. The recovery of conductivity for samples fired at lower temperatures is much easier than for those fired at high temperatures as shown in Fig. 9.7. It was observed that the sample fired at 1200°C showed the same recovery of conductivity as samples oxidized at lower temperatures, but at higher temperatures, the samples were more resistant to reduction. Because the rate of diffusion increases with increasing temperature, the degree of both the oxidation and reduction increase with increasing temperature. In order to achieve a high degree of reduction for air-fired

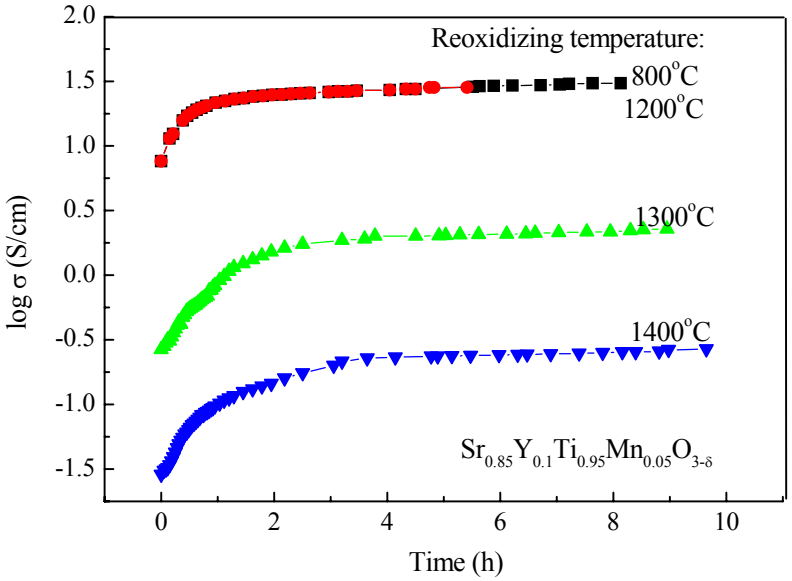

Fig. 9.7. Effects of firing temperatures on the reduction of $Sr_{0.85}Y_{0.10}Ti_{0.95}Mn_{0.05}O_{3-\delta}$ in 7% H_2 at 800°C

oxides, one must restrict the temperature of the oxidizing heat treatment or increase the reduction temperature (Fig. 9.7). On the other hand, the temperature for co-firing of cell components is fixed by ceramic properties and the temperature for subsequent reduction of the anode are also limited by the fuel cell specific design. Some compromise is required in the temperature for materials processing.

9.3.2. Effects of Porosity

Porous anodes are used in fuel cells to allow gas access to the reaction sites without significant diffusion limitation. In order to evaluate the effect of porosity on conductivity, porous samples with compositions $Sr_{0.85}Y_{0.10}Ti_{0.95}Co_{0.05}O_{3-\delta}$ and $Sr_{0.88}Y_{0.08}TiO_{3-\delta}$ were made by adding 20 wt% carbon black as a fugitive phase and annealing the samples in air

at 1400°C for 4 h. The relative density is estimated to be 72.8% and 69.5%, respectively.

Fig. 9.8 shows the change of conductivity of $Sr_{0.85}Y_{0.10}Ti_{0.95}Co_{0.05}O_{3-\delta}$ in the range of oxygen partial pressures of 10^{-14} to 10^{-19} atm at 800°C. A significant drop in conductivity was observed for the porous sample compared to the dense one. Juretscheke et al. have proposed a mathematical model to interpret the relationship of porosity and conductivity of ceramic materials (1956). Assuming that spherical pores are homogeneously distributed in dense materials, the relationship between relative conductivity and the porosity can be expressed as:

$$\sigma / \sigma^{o} = (1-\varepsilon)/(1+0.5\varepsilon) \qquad (9.4)$$

where the porosity $\varepsilon = 1-\rho/\rho^{o}$, ρ and ρ^{o} is the actual and theoretical density, respectively. The experimentally determined conductivity and porosity for $Sr_{0.85}Y_{0.10}Ti_{0.95}Co_{0.05}O_{3-\delta}$ are in accord with that predicted by Eq. 9.4.

Since the gas penetrates the materials via the pores so that diffusion lengths are greatly diminished, the oxidation and reduction rates are expected to be enhanced. This was confirmed by a comparison of conductivity change between a dense sample and a porous one with the composition $Sr_{0.88}Y_{0.08}TiO_{3-\delta}$ as shown in Fig. 9.9. Typically, a rapid reduction was observed for the porous sample rather than the long period of reduction of the dense one, which is favored for the anode reduction *in situ*.

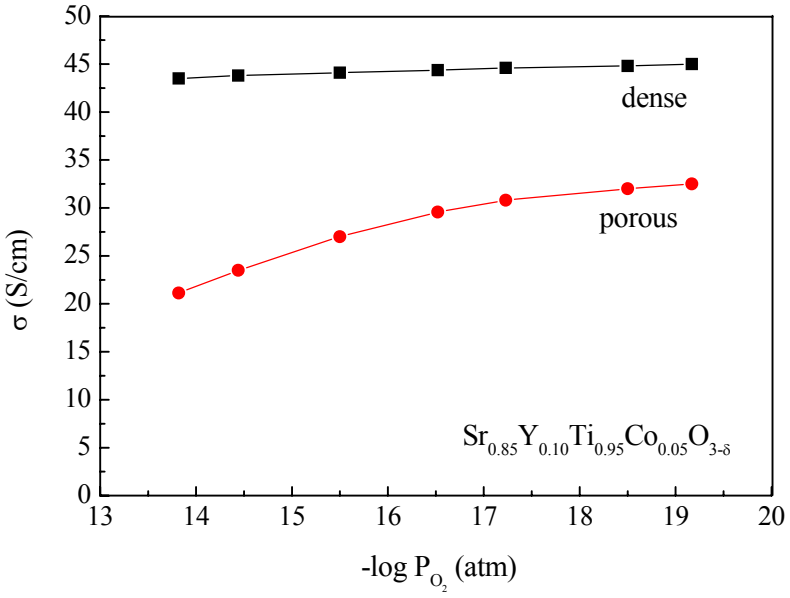

Fig. 9.8. Influence of porosity on electrical conductivity for $Sr_{0.85}Y_{0.10}Ti_{0.95}Co_{0.05}O_{3-\delta}$ at 800°C

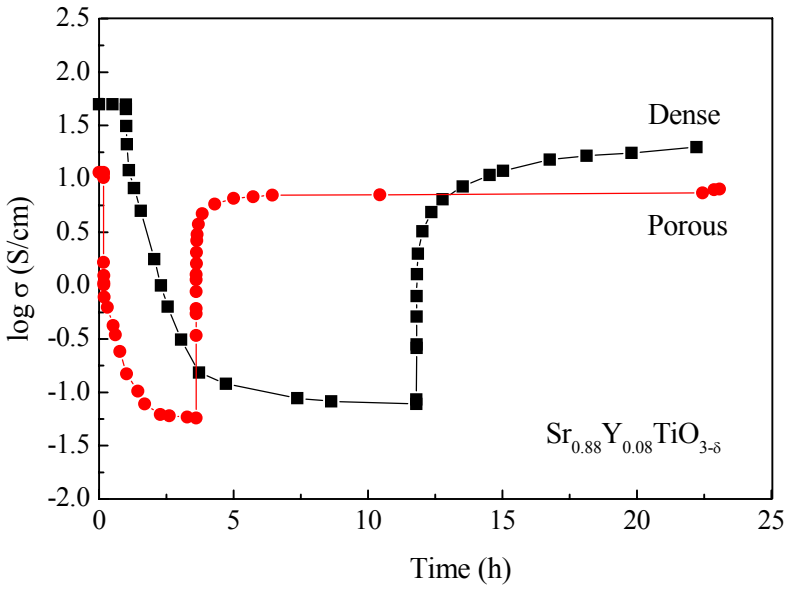

Fig. 9.9. Comparison of conductivity between dense and porous samples of $Sr_{0.88}Y_{0.08}TiO_{3-\delta}$ during oxidation-reduction processes at 800°C

9.4. Compatibility with Electrolytes

Since the SOFC membrane is a layered structure operating at elevated temperatures for long duration, chemical compatibility and thermal expansion compatibility of adjacent layers is essential.

Linear thermal expansion coefficients (TEC) of sintered samples (20 mm in length and 5 mm in diameter) were measured over the temperature range 25 to 1100^{o}C by mechanical dilatometry. Thermal expansion plots for several representative compositions are shown in Fig. 9.10, together with the thermal expansion of the electrolyte materials $Zr_{0.84}Y_{0.16}O_{1.92}$ and $La_{0.8}Sr_{0.2}Ga_{0.8}Mg_{0.2}O_{3-\delta}$ reported by Männer et al. (1991) and Stevenson et al. (1997). The TECs of doped $SrTiO_3$ change linearly with temperature and are close to those of the electrolyte materials. Average TEC values for all the compositions are summarized in Table 9.2. Since the longitudinal thermal stress, σ_x, is a product of thermal expansion coefficient, α, and Young's modulus, E, as given by

$$\sigma_x = -\alpha TE \tag{9.5}$$

where T is temperature (Timoshenko and Goodier, 1970), the difference of Young's modulus also has to be considered to avoid thermal stress failure.

In order to assess the possible reactions between yttrium-doped $SrTiO_3$ with YSZ or LSGM at high temperatures, powder mixtures of $Sr_{0.88}Y_{0.08}TiO_{3-\delta}$ / $Zr_{0.84}Y_{0.16}O_{2-\delta}$ (TZ-8Y, Tosoh Corp.) and $Sr_{0.88}Y_{0.08}TiO_{3-\delta}$ / $La_{0.8}Sr_{0.2}Ga_{0.8}Mg_{0.2}O_{3-\delta}$ (Praxair) were pressed into pellets and sintered at 1400^{o}C for 10 h. Fig. 9.11 shows the XRD spectrum for the

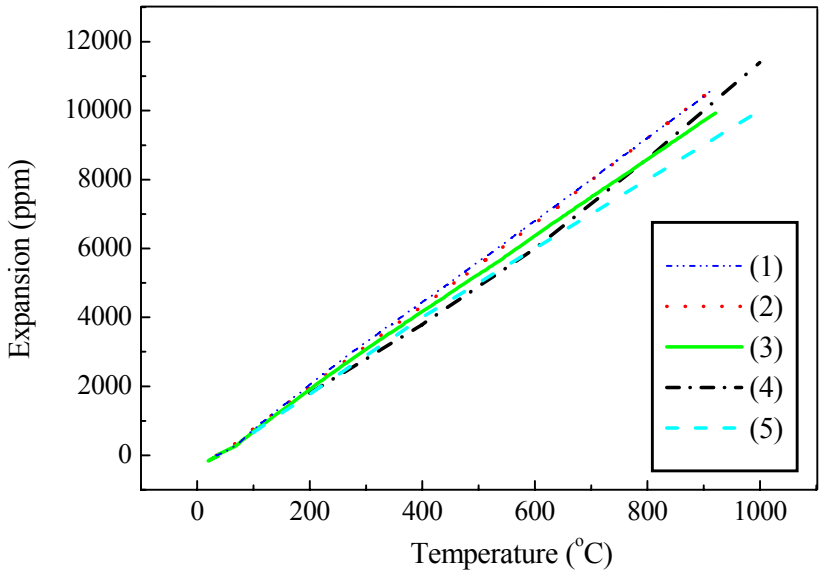

Fig. 9.10. Thermal expansion plots for (1) $Sr_{0.88}Y_{0.08}TiO_{3-\delta}$, (2) $Sr_{0.85}Y_{0.10}Ti_{0.95}Co_{0.05}O_{3-\delta}$, (3) $Sr_{0.85}Y_{0.10}Ti_{0.95}Al_{0.05}O_{3-\delta}$, (4) $La_{0.8}Sr_{0.2}Ga_{0.8}Mg_{0.2}O_{3-\delta}$, (5) $Zr_{0.84}Y_{0.16}O_{2-\delta}$

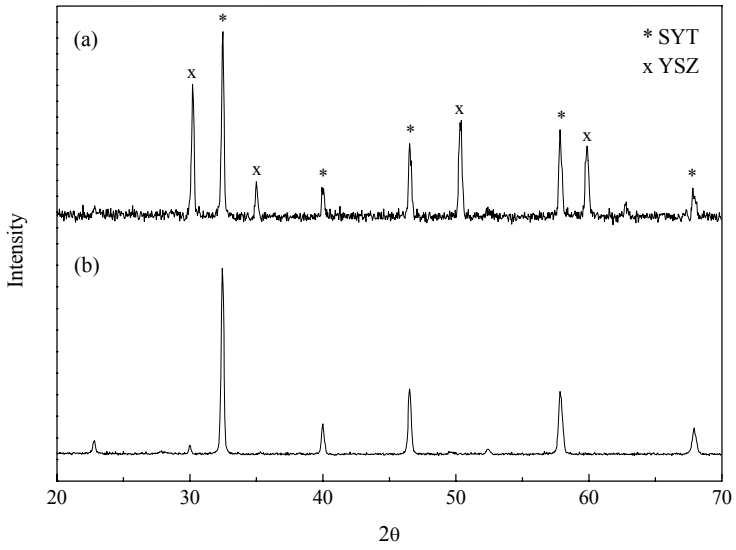

Fig. 9.11. X-ray spectrums for the sintered mixtures (a) $Sr_{0.88}Y_{0.08}TiO_{3-\delta}$ + $Zr_{0.84}Y_{0.16}O_{2-\delta}$, (b) $Sr_{0.88}Y_{0.08}TiO_{3-\delta}$ + $La_{0.8}Sr_{0.2}Ga_{0.8}Mg_{0.2}O_{3-\delta}$

Table 9.2. Average thermal expansion coefficients of doped $SrTiO_3$ and electrolyte materials from 25 to 1100°C

Composition	TEC (x 10^6/°C)
$Sr_{0.88}Y_{0.08}TiO_{3-\delta}$	12.0
$Sr_{0.85}Y_{0.10}Ti_{0.95}Al_{0.05}O_{3-\delta}$	11.2
$Sr_{0.85}Y_{0.10}Ti_{0.95}Co_{0.05}O_{3-\delta}$	12.0
$Zr_{0.84}Y_{0.16}O_{1.92}$	10.8
$La_{0.8}Sr_{0.2}Ga_{0.8}Mg_{0.2}O_{3-\delta}$	11.3

reacted samples. Peak overlaps were observed between $Sr_{0.88}Y_{0.08}TiO_{3-\delta}$ and $La_{0.8}Sr_{0.2}Ga_{0.8}Mg_{0.2}O_{3-\delta}$ because of the same lattice parameters of the two oxides. No new phases were detected for both cases under the experimental conditions. However, this examination could not determine the level of interfacial diffusion between the two phases and the resulting effects on conductivity. The addition of component elements in electrolytes, such as Ga, Mg, and Zr, results in a decrease of conductivity of $Sr_{0.85}Y_{0.10}TiO_{3-\delta}$ as shown in Fig. 9.12.

9.5. Fuel Cell Performance

An electrolyte disc (10 mm in diameter and 0.5 mm in thickness) was prepared by sintering pressed YSZ powder at 1400°C for 10 h. A doped-$SrTiO_3$-glycol slurry was then painted on one side of the YSZ disc to make a half cell and annealed at 1200°C in air for 2 h followed by a reduction of the anode at 1400°C in 7% H_2 for 5 h. Pt paste (Engelhard) was applied on both sides of the cell as current collector and/or cathode.

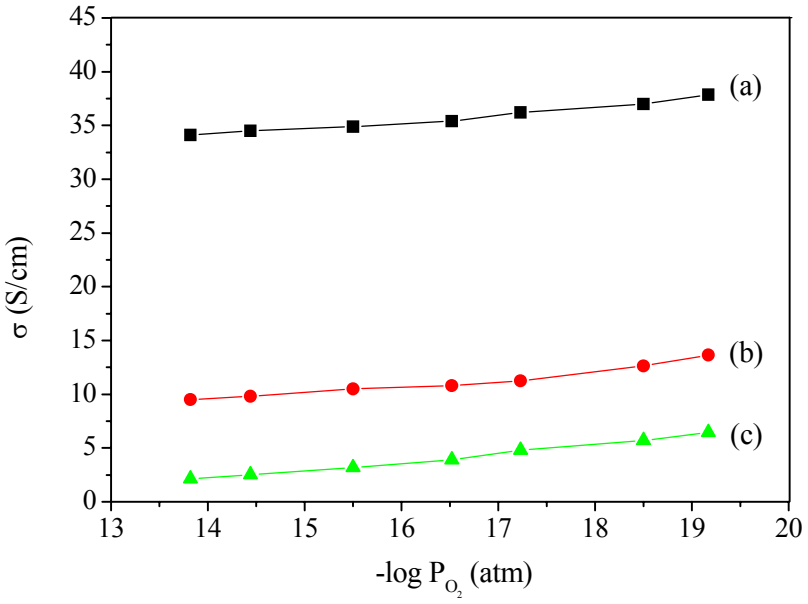

Fig. 9.12. Effect of component elements in electrolytes on conductivity of $Sr_{0.85}Y_{0.10}TiO_{3-\delta}$ at 800°C, containing 5% (a) Ga, (b)Zr, (c) Mg on the B-site

The active electrode area of both the anode and cathode was 0.35 cm^2. The single cell was sealed to an alumina tube with Aremco cement. A type K thermocouple was positioned close to the electrolyte. Gaseous H_2 saturated with water vapor at room temperature was used as fuel for the anode, and air was used as the oxidant at the cathode. The cell test setup is schematically shown in Fig. 9.13.

Fig. 9.14 shows results of voltage (V) versus current density (J) measurements for the SOFC with anode composition (a) $Sr_{0.85}Y_{0.10}Ti_{0.95}Ga_{0.05}O_{3-\delta}$ and (b) $Sr_{0.85}Y_{0.10}Ti_{0.95}Co_{0.05}O_{3-\delta}$. Stable cell potentials with a slight degradation were observed for a period of 24 h. Both current density and maximum power density increased with increasing temperature of operation. The cells with doped $SrTiO_3$ as anodes

gave poor power density (max. 58 mW/cm^2 at 900^{o}C) although the standard open circuit potential was observed.

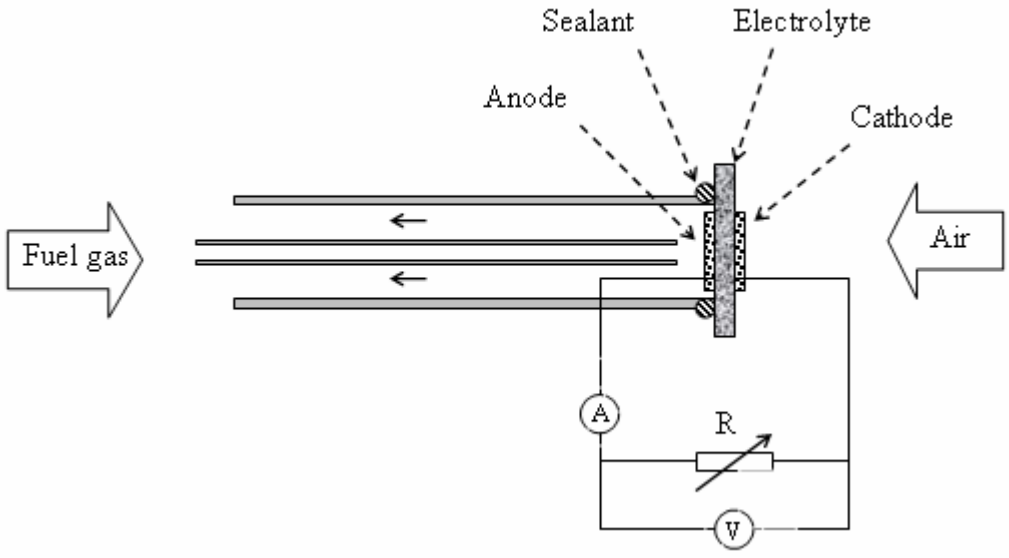

Fig. 9.13. Schematic of fuel cell test apparatus

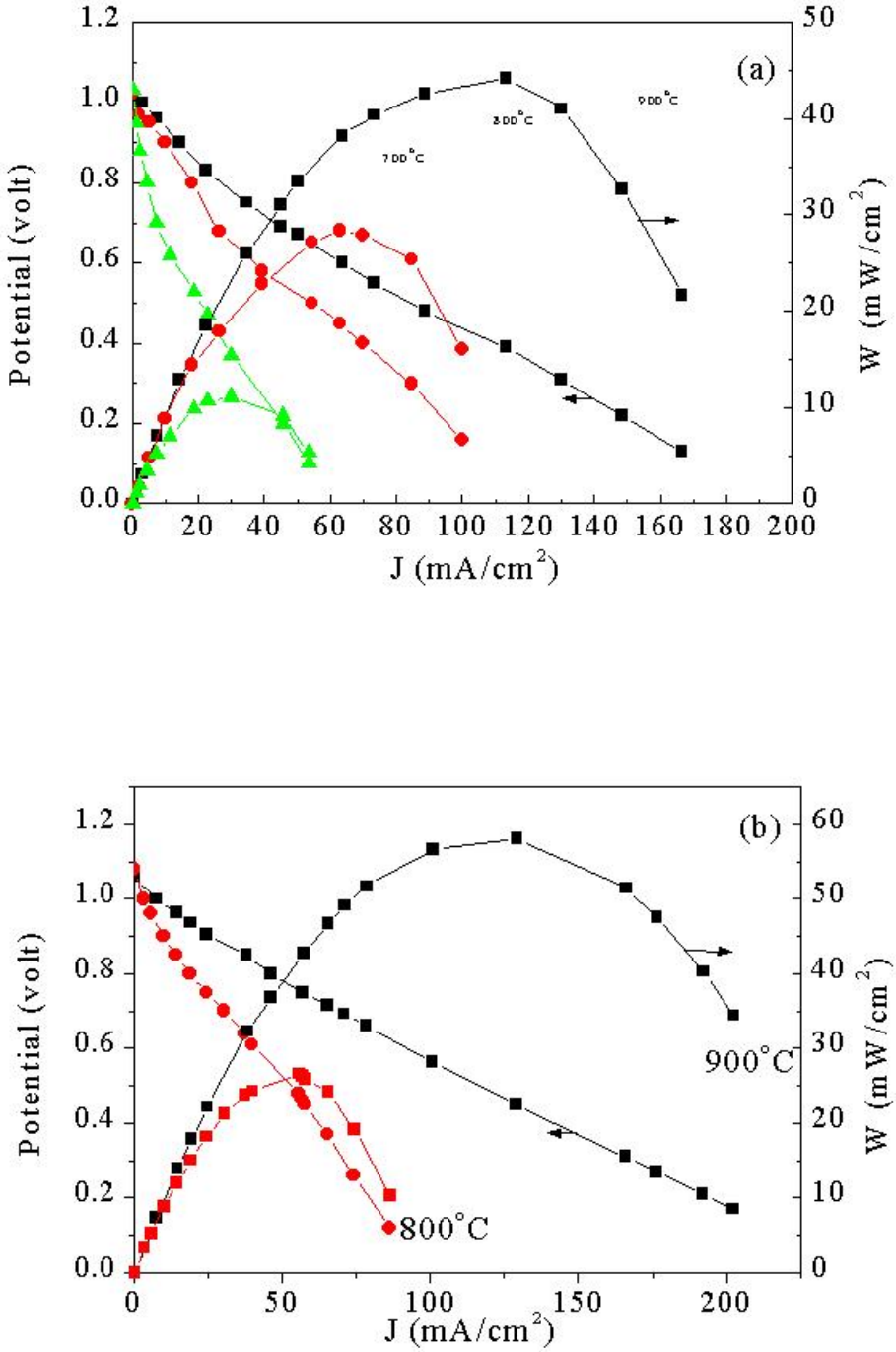

Fig. 9.14. Voltage and power density versus current for anodes with composition (a) $Sr_{0.85}Y_{0.10}Ti_{0.95}Ga_{0.05}O_{3-\delta}$, (b) $Sr_{0.85}Y_{0.10}Ti_{0.95}Co_{0.05}O_{3-\delta}$

The efficiency of an SOFC depends mainly on its ohmic resistance and electrode polarization but can be minimized by material modification and cell fabrication. The resistance of the total cell was observed to be 780 to 1000 Ω at operating temperatures, which is much higher than that expected from the anode and the electrolyte. Upon examination of the ceramic membrane after the fuel cell tests, it was observed that the coated anode separated from electrolyte. The poor power density observed in this study could be due to the high contact resistance between anode and electrolyte. If this is the case, the electrochemical performance of doped $SrTiO_3$ as anodes in fuel cells was not well characterized. The ohmic resistance could be reduced by decreasing the thickness of electrolyte and electrodes, as has been demonstrated by lamination of slip-cast tapes and screen printed or sprayed electrodes (Wang et al., 1999; Primdahl et al., 1999). These researchers have reported a power density up to 900 mW/cm^2 at 800^oC. Attempts to fabricate anode-supported cells with thin film electrolytes made by electrophoretic deposition (EPD) were unsuccessful due to the presence of pinholes or warping of the electrolyte. Reducing the resistance to less than 10 Ω by reducing the thickness of the membrane and improving interface contact is expected to render a performance comparable to industrial standards.

CHAPTER 10

SUMMARY AND CONCLUSIONS

10.1. Summary

A large number of perovskite oxides were synthesized by the solid state method to evaluate their suitability as anode materials. Their performance were characterized in terms of phase stability, electrical conductivity, oxidation-reduction behavior, effects of dopants and stoichiometry, thermal expansion, chemical compatibility, and performance in fuel cells.

Electrical conductivities of $LaNi_{1-x}M_xO_3$ perovskites (M = Ti, V, Nb, Mo, W) were found to be 1 S/cm or less at $Po_2 = 10^{-20}$ atm and 800°C. All of these oxides are stable over a wide oxygen partial pressure range (10^{-20} – 1 atm), and are p-type semiconductors. In contrast, $La_{1-x}Sr_xVO_{3-*}$ (x = 0.2, 0.3) showed n-type behavior with high electrical conductivities up to 120 S/cm at $Po_2 = 10^{-20}$ atm and 800°C. Unfortunately, strontium doped $LaVO_3$ is only stable under SOFC fuel inlet conditions, and once oxidized, the perovskite can not be readily restored by reduction.

The electrical conductivity of $SrTiO_3$ was enhanced by replacement of strontium with rare earth elements. The conductivities of $Sr_{1-1.5x}R_xTiO_{3-\delta}$ (R = La, Nd, Sm, Gd, Yb, Y) generally increase with decreasing ionic radius of the rare earths. An unusual increase of electrical conductivity was found for yttrium-doped $SrTiO_3$.

The compounds $Sr_{1-1.5x}Y_xTiO_{3-\delta}$ with x up to 8 at. % were observed to be single phase by x-ray diffraction. The lattice parameters of $Sr_{1-1.5x}Y_xTiO_{3-\delta}$ decrease linearly with increased yttrium content up to 8 at. % and tend to be constant with further increases in yttrium content. The lattice parameters of reduced samples are slightly larger than those of the oxidized samples.

The electrical conductivities of $Sr_{1-1.5x}Y_xTiO_{3-\delta}$ increase with increasing yttrium level and reach a maximum value of 64 S/cm with x = 0.08 at 800°C. The conductivities were controlled by the level of reduction that was affected by both the oxygen partial pressure of the reducing atmosphere and the saturation level of the dopant. This was confirmed by thermogravimetric measurements.

The oxide $Sr_{0.88}Y_{0.08}TiO_{3-\delta}$ is a semiconductor as observed by both conductivity and thermopower measurements. The electrical conductivity measurements also revealed that $Sr_{1-1.5x}Y_xTiO_{3-\delta}$ oxides have a transition from p to n-type with varying oxygen partial pressure. When the oxygen pressure is greater than 10^{-2} atm, p-type behavior is observed, which is not found for the A-site stoichiometric titanates with donor-doping.

The electrical $_{\text{conductivities}}$ of $Sr_{1-1.5x}Y_xTiO_{3-\delta}$ are furthermore highly sensitive to minor changes in cation-cation ratio. The conductivity changed from 64 S/cm for $Sr_{0.88}Y_{0.08}TiO_{3-\delta}$ to a maximum of 82 S/cm for $Sr_{0.86}Y_{0.08}TiO_{3-\delta}$ at 800°C and oxygen partial pressure of 10^{-19} atm.

SEM examination showed that the average grain size of $Sr_{1-1.5x}Y_xTiO_{3-\delta}$ ($0.02 \leq x \leq 0.08$) is 3-6 μm, significantly smaller than that of undoped $SrTiO_3$. Measurements by impedance spectroscopy (IS) revealed that the grain boundaries of the oxidized

$Sr_{0.88}Y_{0.08}TiO_{3-\delta}$ have little effect on the conductivity at temperatures above 800°C. The influence of grain boundaries of reduced $Sr_{0.88}Y_{0.08}TiO_{3-\delta}$ on conductivity could not be distinguished from grain conductivity by IS in the temperature range of 25 to 900°C. Preparation of single crystal $Sr_{0.88}Y_{0.08}TiO_{3-\delta}$ was unsuccessful.

The replacement of titanium by acceptors (V, Cr, Mn, Fe, Co, Ni, Cu, Zn, Mo, Al, and Ga) leads to a decrease of conductivity of $Sr_{1-1.5x}Y_xTiO_{3-\delta}$. The degree of the decrease depends strongly on the type of dopant. Of the 5 mol% acceptor-doped compositions, the system $Sr_{0.85}Y_{0.10}Ti_{0.95}Co_{0.05}O_{3-\delta}$ had the highest conductivity of 45 S/cm at 800°C and oxygen partial pressure of 10^{-19} atm, which dropped to 33 S/cm for a sample with 30% porosity.

The conductivity of $Sr_{0.88}Y_{0.08}TiO_{3-\delta}$ is reversibly recovered from oxidized samples by reduction at 800°C. However, the reduction rate is about four times slower than the oxidation rate. Thermogravimetric studies indicate that the reduction process starts at a higher temperature than the oxidation.

The oxidation behavior of yttrium-doped $SrTiO_3$ can be significantly influenced by the addition of cobalt or manganese at Ti-sites, presenting a high resistance to oxidation. The samples oxidized at temperatures below 1200°C could be easily reduced in 7% H_2 at 800°C.

The ionic conductivity of $SrTiO_3$ doped with 5 mol% acceptor at Ti-sites was estimated from the total conductivity as a function of oxygen partial pressure at different temperatures. The ionic conductivity of both $SrTi_{0.95}Ga_{0.05}O_{3-\delta}$ and $SrTi_{0.95}Co_{0.05}O_{3-\delta}$ at 800°C is about 3×10^{-4} S/cm, that is, one order of magnitude higher than that of undoped

$SrTiO_3$. The ionic conductivity of $SrTi_{0.95}Ga_{0.05}O_{3-\delta}$ increases from 6 x 10^{-5} to 6 x 10^{-4} S/cm with increasing temperature from 700 to 900°C.

No phase change was observed for mixtures of $Sr_{0.88}Y_{0.08}TiO_{3-\delta}$ with YSZ or LSGM fired at 1400°C for 10 h. This suggests a possible chemical compatibility between the yttrium-doped $SrTiO_3$ and the electrolytes. However, the effects of interfacial diffusion on conductivity have not been assessed.

The thermal expansion coefficients (TEC) of doped-$SrTiO_3$ were determined to be compatible with those of YSZ and LSGM.

An attempt was made to test single cells with doped-$SrTiO_3$ anodes by I-V measurements. The poor power output is most likely due to the poor adhesion of cell components.

As demonstrated in this study, the yttrium doped-$SrTiO_3$ meets the requirements of SOFC anodes to a high degree in terms of electrical conductivity, phase stability, oxidation-resistance, thermal expansion, and reversible change of conductivity upon oxidation-reduction. Of all the systems studied here, the $Sr_{0.85}Y_{0.10}Ti_{0.95}Co_{0.05}O_{3-\delta}$ composition appears to have the highest potential as an anode for SOFCs.

10.2. Conclusions

As observed in this work, the phenomena of electrical transport in doped-$SrTiO_3$ are diverse. Consequently, $SrTiO_3$-based perovskites are excellent candidates for further fundamental studies. It is well known that the conductivity of $SrTiO_3$ could be improved by doping of rare-earth elements. Why the conductivity increases as the dopant

decreases from lanthanum to ytterbium is not clearly understood, nor is the marked effect of yttrium relative to other rare earths. Furthermore, it is of interest to know why co-doping of lanthanum and yttrium in $SrTiO_3$ leads to a conductivity decrease relative to the singly doped oxide.

It was observed that both cobalt and yttrium doped $SrTiO_3$ are semiconductors in the range of oxygen partial pressure of 1 to 10^{-19} atm. However, the conduction of cobalt and yttrium co-doped $SrTiO_3$ had different behavior when changing oxygen partial pressures, i.e., a metal in the range of oxygen partial pressure of 10^{-14} to 10^{-19} atm and a insulator in the range of oxygen partial pressure of 1 to 10^{-6} atm. Therefore, a metal to insulator transition must occur at a given oxygen partial pressure between 10^{-6} to 10^{-14} atm. This may be confirmed by different characterization methods such as thermal power measurements.

As discussed in this study, doped-$SrTiO_3$ has many advantages as a potential anode. However, in order to determine its suitability for fuel cell applications, further measurements need to be performed. For example, the interfacial diffusion between doped $SrTiO_3$ and YSZ or LSGM at the sintering temperature, typically, above 1300^{o}C needs to be determined. It is known that interfacial diffusion can be limited by using low temperature processing methods or by applying a suitable diffusion barrier onto the electrolyte surface.

The exact value of oxygen ionic conductivity in yttrium and acceptor co-doped $SrTiO_3$ has not been determined in this study. For the investigation of low ionic conductivity with high electronic conduction background in doped $SrTiO_3$, oxygen permeability measurements may be required.

In addition, it will be necessary to evaluate the mechanical properties in order to determine if the material is suitable as the substrate to support the cell. Other studies are required to determine the catalytic ability to oxidize or reform CH_4. Finally, suitable techniques for cell fabrication have to be investigated to optimize fuel cell performance.

REFERENCES

Aksenova, L.A., Y.P. Kostikov, A.I. Leonov, B.A. Rotenberg, and V.S. Strykanov, Zhurnal Prikladnoi 59, 252 (1986).

Alvarez, I., J. Solid State Chem. 125, 47 (1996).

Anderson, H.U., Solid State Ionics 52, 33 (1992).

Anderson, H.U., L.W. Tai, C.C. Che, M.M. Nasrallah, and W. Huebner, SOFC IV 1995, p.375.

Appel, J., Solid State Phys. 21, 193 (1968).

Arai, H., T. Yamada, K. Eguchi and T. Seiyama, Appl. Catal. 26, 265 (1986).

Azad, A.M., S. Larose and S.A. Akbar, J. Matls. Science 29, 4135 (1994).

Balachandran, U. and N.G. Eror, in Extended Abstracts 158th Meeting of the Electrochem. Soc., Vol. 80-2, p.914 (1980).

Balachandran, U. and N.G. Eror, Commun. Amer. Ceram. Soc. 64, C75 (1981).

Balachandran, U. and N.G. Eror, J. Electrochem. Soc. 129, 1021 (1982).

Bale, C. W., A. D. Pelton and W. T. Thompson, F*A*C*T 2.1 – User Manual, Ecole Polytechnique de Montreal / Royal Military College, Canada, July 1996 (http://www.crct.polymtl.ca)

Battle, P.D., J.E. Bennett, J. Sloan, R.J.D. Tilley, and J.F. Vente, J. Solid State Chem. 149, 360 (2000).

Bazuev, G.V. and G.P. Shveikin, Zh. Fiz. Khim. 54, 282 (1980).

Bazuev, G.V., O.V. Makarova, and G.P. Shveikin, Izvestiya Akademii Nauk SSSR, Neorganicheskie Materialy 19, 108 (1983).

Bednorze, J.G. and K.A. Muller, Phys. Rev. Lett. 52, 2289 (1984).

Blanc, J. and D.L. Staebler, Phys. Rev. B 4, 3548 (1971).

Bockris, J.O'M. and T. Otagawa, J. Electrochem. Soc. 131, 290 (1984).

Bouwma, J. K.J. Devries, and A.J. Burggraaf, Phys. Stat. Sol. (a) 35, 281 (1976).

Brouwer, G., Philips Res. Rept. 9, 366 (1954).

Browall, K.W., O. Muller, and R.H. Doreonous, Mater. Res. Bull. 11, 1475 (1976).

Brugnoni, C., U. Ducati, and M. Scagliotti, *Solid Sate Inoics* 76, 177 (1995).

Burn, I. And S. Neirman, J. Mat. Sci. 17, 3510 (1982).

Carter, D.L. and A. Okaya, Phys. Rev. 118, 1486 (1960).

Carter, S., A. Selcuk, R.J. Chater, J. Kajda, J.A. Kilner, and B.C.H. Steel, Solid State Ionics 53-56, 597 (1992).

Chan, N.H. and D.M. Smyth, J. Electrochem. Soc., 123, 1584 (1976).

Chan, N.H., R.K. Sharma, and D.M. Smyth, J. Electrochem. Soc. 128, 1762

(1981).

Chiang, Y.M., and T. Takagi, J. Am. Ceram. Soc. 73, 3278 (1990).

Chiang, Y.M., D.P. Birnie, and W.D. Kingery, in Physical Ceramics, John Wiley & Sons, New York (1997).

Choi, G.M., H.L. Tuller and D. Goldschmidt, Phys. Rev. B 34, 6972 (1986).

Choi, G.M. and H.L. Tuller, J. Am. Ceram. Soc. 71, 201 (1988).

Cox, P.A., in The Electronic Structure and Chemistry of Solids, Oxford University Press, Oxford (1987).

Cox, P.A., in Transition Metal Oxides, Clarendon Press, Oxford (1992).

Crawford, J. and P. Jacobs, J. Solid State Chem. 144, 423 (1999).

Daniels, J. and K.H. Härdtl, Philips Res. Repts 31, 489 (1976).

David, R.L., editor-in-chief, in CRC Handbook of Chemistry and Physics, 73rd edition, 1992-1993.

Day, P., in Mixed-Valence Compounds, ed. D.B. Brown, D. Reidel Publishing, Dordrecht, Holland (1979).

Dees, D.W., T.D. Claar, T.E. Easler, D.C. Fee, and F.C. Mrazek, J. Electrochm. Soc., 134, 2141 (1987).

Denk, I., W. Münch, and J. Maier, J. Am. Ceram. Soc. 78, 3265 (1995).

Dieckmann, R., J. Phys. Chem. Solids 59, 507 (1998).

Dougier, P. and A. Casalot, J. Solid State Chem. 2, 396 (1970).

Duncan, A.B.F., in Chemical applications of Spectroscopy, Vol. IX, ed. W. West, Wiley Interscience, New York (1956).

Eguchi, K., T. Setoguchi, M. Sawano, S. Tamura and H. Arai, in Proc. 2nd Intern. Symp. on SOFCs, 1991, Athens, Greece, eds. F. Groz, P. Zegers, S. C. Singhal, and O. Yamamoto, Commission of the European Communities, Luxembourg, 1991, p.603. Eguchi, K., T. Setoguchi, K. Okamoto, and H. Arai, in Proc. 3rd Intern. Symp. on SOFCs, 1993, Honolulu, HI, eds. S. C. Singhal, and H. Iwahara, Electrochem. Soc., Pennington, NJ, 1993, p.494.

Elangovan, S. and A. Khandkar, in Proc.1st Intern. Symp. on Ionic and Mixed Conducting Ceramics, Oct. 16-17, 1991, Phoenix, AZ, Ramanarayanan, T. A. and Tuller, H. L. (eds), Electrochemical Society, Pennington, NJ, p.122 (1991).

Eylem, C., G.S. Szabo, B.H. Chen, B. Eichhorn, J.L. Peng, R. Greene, L.S. Riba, and S. Nahm, Chem. Mater. 4, 1038 (1992).

Emin, D., in The Hall Effect and Its Applications, ed. C.L. Chien and C.R. Westgate, Plenum, New York (1980).

Emin, D., Phys. Today, June 1982, p.34.

Eror, N.G. and D.M. Smyth, in The Chemistry of Extended Defects in Non-Metallic Solids, p. 62, eds. L. Eyring and M. O'Keefe, North-Holland Pub., Amsterdam (1970).

Eror, N.G. and D.M. Smyth, J. Solid State Chem. 24, 235 (1978).

Eror, N.G. and U. Balachandran, J. Solid State Chem. 40, 85 (1981).

Eror, N.G. and U. Balachandran, J. Solid State Chem. 42, 227 (1982).

Fagg, D. P., S.M. Fray, and J.T. Irvine, Solid State Ionics 72, 235-239 (1994).

Faughnan, B.W. and Z. Kiss, J. Phys. Rev. Lett. 21, 1331 (1968).

Fleig, J. and J. Maier, Proc. 3rd Intl. Symp. on Electrochem. Impedance Spectroscopy, Belgium, May 1995.

Frederikse, H.P.R., W.R. Thurber, and W.R. Hosler, Phys. Rev. 134, A442 (1964).

Frederikse, H.P.R. and W.R. Hosler, Phys. Rev. 161, 822 (1967).

Fujimori, A., A.E. Bocquet, K. Morikawa, K. Kobayashi, T. Saitoh, Y. Tokura, I. Hase, and M. Onoda, J. Phys. Chem. Solids 57, 1379 (1996).

Fujimoto, M. and W.D. Kingery, J. Am. Ceram. Soc. 68, 169 (1985).

Galasso, F. S., Structure, Properties and Preparation of Perovskite-Type Compounds, Pergamon Press, London (1969).

Gandy, H.W., Phys. Rev., 113, 795 (1959).

Ganguly, P., N.Y. Vasanthacharya, and C.R.N. Rao, J. Solid State Chem. 54, 400 (1984).

Gao, Wei and N.M. Sammes, in An Introduction to Electronic and Ionic Materials,

World Scientific Publishing, Singapore, 1999, p.340.

Gaskell, D.R., in Introduction to Metallurgical Thermodynamics, 2nd ed., Hemisphere Publishing, New York (1981).

Geller, S., Acta Crystallogr. 10, 243 (1957).

Gerblinger, J. and H. Meixner, Sens. Actuators B 4, 99 (1991).

Gervais, F., B. Cales, and P. Odier, Mater. Res. Bull. 22, 1629 (1987).

Glatz, W., E. Batawi, M. Janousek, W. Krausler, R. Zach, and G. Zobl, in Proc. 6th Intern. Symp. on SOFCs, 1999, Honolulu, HI, eds. S. C. Singhal, and M. Dokiya, Electrochem. Soc., Pennington, NJ, 1999, p.783.

Gong, W., H. Yun, Y.B. Ning, J.E. Greedan, W.R. Datars, and C.V. Stager, J. Solid State Chem. 90, 320 (1991).

Goodenough, J.B., J. Appl. Phys., 37, 1415 (1967a).

Goodenough, J.B., Mat. Res. Bull. 2, 37 (1967b).

Goodenough, J.B., J. Appl. Phys., 39, 403 (1968).

Goodenough, J.B. and J.M. Longo, Landolt-Bornstein Tablellen, New Series, III/4a, Springer Verlag, Berlin (1970).

Goodenough, J.B., Prog. Solid State Chem. 5, 145 (1971).

Goodenough, J.B., in Solid State Chemistry, ed. C.N.R. Rao, Marcel Dekker, New

York, p.215 (1974).

Greedan, J.E. and D.A. MacLean, Inst. Phys. Conf. Ser. No. 37, 249 (1978).

Greedan, J.E., J. Less-Comm. Met. 111, 335 (1985).

Hayes, W. and A.M. Stoneham, in Defects and Defect Processes in Nonmetallic Solids, John Wiley & Sons, New York (1985).

Heikes, R.H. and R.W. Ure, in Thermoelectricity, Interscience, New York (1961).

Hench, L.L. and D.B. Dove, in Physics of electronic ceramics, M. Dekker, New York (1971).

Hennings, D. and K.H. Hardtl, Phys. Stat. Sol. (a) 3, 465 (1970).

Hennings, D., Mat. Res. Bull. 6, 329 (1971).

Heyne, L., in Fast Ion Transport in Solids, ed. W. van Gool, North-Holland, Amsterdam (1973).

Heyne, L., in Solid Electrolyte, ed. S. Geller, Springer-Verlag, Heidelberg (1977).

Hoffman, A., Z. Physik. Chem. B28, 65 (1935).

Hoffmann, R., in Solids and Surfaces: A Chemist's View of Bonding in Extended Structures, VCH Publisher, New York (1988).

Honegger, K., R. Kruschwitz, M. Keller, and G.M. Christie, in Proc. 6th Intern. Symp. on SOFCs, 1999, Honolulu, HI, eds. S. C. Singhal, and M. Dokiya, Electrochem.

Soc., Pennington, NJ, 1999, p.127.

Hou, P.Y., K. Huang, and W.T. Bakker, in Proc. 6th Intern.Symp. on SOFCs, 1999, Honolulu, HI, eds. S. C. Singhal, and M. Dokiya, Electrochem. Soc., Pennington, NJ, 1999, p.127.

Howard, S.A., J.K. Yau, and H.U. Anderson, J. Appl. Phys. 65, 1492 (1989).

Huebner, W., D.M. Reed, and H.U. Anderson, in Proc. 6th Intern. Symp. SOFCs, 1999, Honolulu, HI, eds. S. C. Singhal, and M. Dokiya, Electrochem. Soc., Pennington, NJ, 1999, p.503.

Hüfner, S., Z. Phys. B 61, 135 (1985).

Hulm, J.K., M. Ashkin, D.W. Deis, and C.K. Jones, in Progress in Low Temperature Physics, ed. C.J. Gorter, North-Holland Publishing, Amsterdam (1970).

Imada, M., A. Fujimori, and Y. Tokura, Rev. Mod. Phys. 70, 1039 (1998).

Inoue, T., T. Setoguchi, K. Eguchi, and H. Arai, Solid State Ionics 35, 285 (1989).

Isenberg, A.O., Abstract of the 1982 Fuel Cell Seminar, Newport Beach, CA, Nov. 14-18, 154 (1982).

Ishigaki, T., S. Yabauchi, K. Kishio, J. Mizusaki, and K. Fuek, Solid State Chem. 73, 179 (1988).

Iwahara, H., T. Esaka, and T. Mangahara, J. Appl. Electrochem. 18, 173 (1988).

Jacobson, N.S. and W.L. Worrell, in Proc. High Temp. Mater., 2, 217 (1983).

Johnson, D.W., L.E. Cross, and F.A. Hummel, J. Appl. Phys. 41, 2828 (1970).

Kahn, M., J. Am. Ceram. Soc. 54, 452 (1971).

Katz, S., J. J. Croat and J. V. Laukonis, Ind. Eng. Chem. Prod. Res. Dev. 14, 274 (1975)

Kawada, T., N. Sakai, H. Yokokawa, M. Dokiya, M. Mori, and T. Iwata, J. Electrochem. Soc. 137, 3042 (1990a).

Kawada, T., N. Sakai, H. Yokokawa, M. Dokiya, M. Mori, and T. Iwata, Solid State Ionics, 40-41, 402 (1990b).

Khan, M.S. and M.S. Islam, J. Phys. Chem. B 102, 3099 (1998).

Kharton, V.V., E.N. Naumovich, A.A. Vecher, and A.V. Nikolaev, J. Solid State Chem. 120, 128 (1995).

Kim, K.H., K.H. Yoon, and J.S. Choi, J. Phys. Chem. Solids 40, 1061 (1985).

Kim, I.S., T. Nakamura, Y. Inaguma, and M. Itoh, J. Solid State Chem. 113, 281 (1994).

Kilner, J.A., P. Barrow, and R.J. Brook, J. Power Sources 3, 67 (1978).

Kilner, J.A., in Solid State Chemistry, 1982, eds. R. Metselaar, H.J.M. Heijingers, and J. Schoonman, Elsevier Science Ltd, Amsterdam (1983).

Kingery, W.D., J. Am. Ceram. Soc. 57, 1 (1974).

Kingery, W.D., H.K. Bowen, and D.R. Uhlmann, in Introduction to Ceramics, 2nd ed., John Wiley & Sons, New York, (1976).

Kittel, C.K., in Introduction to Solid State Physics, 5th ed. Wiley, New York (1976).

Kofstad, P., in Nonstiochiometry, Diffusion and Electrical Conductivity in Binary Metal Oxides, Robert E. Krieger Publishing, Florida (1983)

Komornicki, S., J.C. Grenier, J. Ravez, and P. Hagenmuller, Mat. Sci. Eng. B 10, 95 (1991).

Kremenić, G., J.M.L. Nieto, J.M.D. Tascón and L. G. Tejuca, J. Chem. Soc., Faraday Trans. 1 81, 939 (1985).

Kröger, F.A. and H.J. Vink, in Solid State Physics, eds. F. Seitz and D. Turnbull, Academic Press, New York (1956).

Kröger, F.A. and H.J. Vink, J. Phys. Chem. Solids 5, 208 (1958).

Lee, C., D. Destry, and J.L. Brebner, Phys. Rev. B 11, 2299 (1975).

Lee, C.H., H.Y. Lee and S.M. Oh, Solid State Ionics 98,39 (1997).

Levin, E.M., C.R. Robbins, and H.F. McMurdie, in Phase Diagrams for Ceramists, Am. Ceram. Soc., Columbus (1964), Fig. 297, 298. 1969 Supplement, Fig. 2334.

Liou, S.S. and W.L. Worrell, J. Appl. Physics A 49, 25 (1989).

Liu, G. and J. E. Greedan, J. Solid State Chem. 110, 274 (1994).

Long, S.A. and R.N. Blumenthal, J. Amer. Ceram. Soc. 54, 515 91971).

Macdonald, J.R., in Impedance Spectroscopy: Emphasizing Solid Materials and Systems, John Wiley and Sons, New York (1987).

Macdonald, J.R., in Superionic Conductors, eds. G.D. Maham and W.L. Roth, Plenum Press, New York (1976).

Maeno, Y., S. Awaji, H. Matsumoto, and T. Fujita, Physica B 165-166, 1185 (1990).

Maier, J., J. Phys. Chem. Solids 46, 309 (1985).

Markin, T. L., B. J. Bones, and R. M. Dell, in Conf. on Solid Electrolyte Fuel Cells, eds. Mahan, R. M. and Roth, W. L. (Plenum Press, New York, 1976) p. 15.

McCarty, J.G. and H. Wise, Catal. Today 8, 231 (1990).

Megaw. H.D., Proc. Phys. Soc. (London) 58, 133 (1946).

Metcalfe, I. S., P.H. Middleton, P. Petrolekas, and B.C.H. Steel, Solid State Ionics 57, 259 (1992).

Meyer, G.M., N.J. Nelmes, and J. Hutton, Ferroelectrics 21, 461 (1978).

Minh, N.Q., J. Am. Ceram. Soc., 76, 563 (1993).

Minh, N.Q. and T. Takahashi, in .Science and Technology of Ceramic Fuel Cells, Elsevier, Amsterdam, 1995.

Minh, N.Q., in Proc. 6th Intern. Symp. on SOFCs, 1999, Honolulu, HI, eds. S. C.

Singhal, and M. Dokiya, Electrochem. Soc., Pennington, NJ, 1999, p.127.

Mizusaki, J., Solid State Ionics 52, 79 (1992).

Mizusaki, J., H. Tagawa, T. Saito, K. Kamitani, T. Yamamura, K. Hirano, S. Ehara, T. Takagi, T. Hikita, M. Ippommatsu, S. Nakagawa, and K. Hashimoto, J. Electrochem. Soc., 141, 2129 (1994).

Mogensen, M. and J. J. Bentzen, in Proc. 1st Intern. Symp. on SOFCs, The Electrochem. Soc., Inc., 89-11, 99 (1989a).

Mogensen ,M. and J.J. Bentzen, in Proc. 1st Intern. Symp. SOFC, Oct. 16-18, 1989, Hollywwod, FL, Singhal, S. C. (ed.), Electrochem. Soc., Pennington, NJ, 1989b, p. 99.

Mogensen, M., in Proc. 2nd Intern. Symp. on SOFCs, 1991, Athens, Greece, eds. F. Groz, P. Zegers, S. C. Singhal, and O. Yamamoto, Commission of the European Communities, Luxembourg, 1991, p.577.

Mogesen ,M., T. Lindegaard, U.R. Hansen, and G. Mogesen, in "Ionic and Mixed Conducting Ceramics", Eds. Ramanarayanan, T. A., Proc. Vol. 94-12, (Electrochem. Soc., NJ, 1994) p. 448

Mogensen, M. and S. Skaarup, Solid State Ionics 86-8, 1151 (1996).

Mohapatra, S.K. and S. Wagner, J. Appl. Phys. 50, 5001 (1979).

Moos, R., A. Gnudi, and K.H. Härdtl, J. Appl. Phys. 78, 5042 (1995).

Moos, R. and K.H. Härdtl, J. Appl. Phys. 80, 393 (1996).

Mori, H., in Proc. 6th Intern. Symp. on SOFCs, 1999, Honolulu, HI, eds. S. C. Singhal, and M. Dokiya, Electrochem. Soc., Pennington, NJ, 1999, p.52.

Mott, N. F., rev. mod. Phys. 40, 673 (1968).

Moulson, A.J. and J.M. Herbert, in Electroceramics, Chapman and Hall, London (1990).

Müller, K.A., W. Berlinger, and R.S. Rubins, Phys. Rev. 186, 361 (1969).

Murray, E.P. and S.A. Barnett, in Proc. 6th Intern. Symp. on SOFCs, 1999, Honolulu, HI, eds. S. C. Singhal, and M. Dokiya, Electrochem. Soc., Pennington, NJ, 1999, p.1001.

Nakamura, T., Petzow, G. Petzow and L. J. Gauckler, Mat. Res. Bull. 14, 649 (1979).

Nakamura, T., M. Misono, T. Uchijima and Y. Yoneda, Nippon Kagaku Kaishi, 1679, (1980).

Nassau, K. and A.E. Miller, J. Crystal Growth 91, 373 (1988).

Noll, F., W. Münch, I. Denk, and J. Maier, Solid State Ionics 86-88, 711 (1996).

Nowotny, J., in The CRC Handbook of Solid State Electrochemistry, eds. P.J. Gellings and H.J.M. Bouwmeester, CRC press, Boca Raton (1997).

Odekirk, B., U. Balchandran, N.G. Eoro, and J.S. Blakemore, Mater. Res. Bull. 17, 199 (1982).

Ogumi, Z., T. Ioroi, Y. Uchimoto, Z. Takehara, T. Ogawa, and K. Toyama, J. Am. Ceram. Soc., 78, 593 (1995).

Osberg, P.A. and T. Norby, in 7th SOFC workshop, Theory and Measurement of Microscale Processes in Solid Oxide Fuel Cells, p. 47, KFA-ISR Forschungszentrum Jülich GmhH, D-52425 Jülich Germany (1995).

Paladino, A.E., Bull. Amer. Ceram. Soc. 48, 476 (1965).

Park, J.H. and R.N. Blumenthal, J. Electrochem. Soc. 136, 2868 (1989).

Park, S., J.M. Vohs, and R.J. Gorte, Nature 404, 265 (2000).

Patrakeev, M.V., I.A. Leonidov, V.L. Kozhevnikov, V.I. Tsidilkovskii, A.K. Demin, and A.V. Nokolaev, Solid State Ionics 66, 61 (1993).

Patterson, J.W., J. Electrochem. Soc. 118, 1033 (1971).

Peng, C.J. and H.Y. Lu, J. Am. Ceram. Soc. 71, C-44 (1988).

Phillips, C.S.G. and R.J.P. Williams, in Inorganic Chemistry, Oxford University Press, Oxford (1965).

Porat, O., C. Heremans, and H.L. Tuller, Solid State Ionics 94, 75-83 (1997).

Primdahl, S., M.J. Jrgensen, C. Bagger, and B. Kindl, in Proc. 6th Intern. Symp. on SOFCs, 1999, Honolulu, HI, eds. S. C. Singhal, and M. Dokiya, Electrochem. Soc., Pennington, NJ, 1999, p.793.

Raccah, P.M. and J.B. Goodenough, Phys. Rev. 155, 932 (1967).

Reiss, H., C.S. Fuller, and F.J. Morin, Bell Syst. Tech. J. 35, 535 (1956).

Riess, I., Proc. 2nd Intern. Symp. on Ionic and Mixed Conducting Ceramics, Vol. 94-12, p.302, eds. T.A. Ramanarayanan, W.L. Worrell, and H.L. Tuller, The Electrochem. Soc., Pennington, NJ (1994).

Riess, I., in The CRC Handbook of Solid State Electrochemistry, eds. P.J. Gellings and H.J.M. Bouwmeester, CRC press, Boca Raton (1997).

Robin, M.B. and P. Day, in Advances in Inorganic Chemistry and Radiochemistry, Vol.10, eds. H.J. Emeléus and A.G. Sharpe, Academic Press, New York (1967).

Ruddlesden, S.N. and P. Popper, Acta Cryst. 11, 54 (1958).

Sayer, S., R. Chen, R. Fletcher, and A. Mansingh, J. Phys. C 8, 2059 (1975).

Schäfer, W., A. Koch, U Herold-Schmidt, and D. Stolten, Solid State Ionics 86-88, 1235 (1996).

Schmalzried, H., in Progress in Solid State Chemistry, V.2, ed. H. Reiss, Pergamon Press, Oxford (1965).

Schooley, J.F., W.R. Hosler, and M.L. Cohen, Phys. Rev. Lett. 12, 474 (1964).

Schouler, E. J. L. Solid State Ionics 9 & 10, 945 (1982).

Setoguchi, T., K. Okamoto, K. Eguchi, and H. Arai, J. Electrochem. Soc., 139, 2875 (1992).

Shannon, R.D., Acta Cryst. A 32, 751 (1976).

Shirasaki, S., H. Yamamura, H. Haneda, K. Kakegawa, and J. Moori, J. Chem. Phys.

73, 4640 (1980).

Singhal, S.C., in Proc. 6th Intern. Symp. on SOFCs, 1999, Honolulu, HI, eds. S. C. Singhal, and M. Dokiya, Electrochem. Soc., Pennington, NJ, 1999, p.39.

Slater, P. R., D.P. Fagg, and J.T. Irvine, J. Mater. Chem. 7 (12), 2495-2498 (1997).

Sleight, A.W., in High-Temperature Superconducting Materials, eds. W.E. Hatfield and J.H. Miller, p.1 (1988).

Smyth, D.M., J. Solid State Chem. 16, 73 (1976).

Smyth, D.M., J. Solid State Chem. 20, 359 (1977).

Smyth, D.M., in Advances in Ceramics, Proc. Supercond. Symp., The Am.Ceram. Soc. (1988).

Sridhar, S. and U.B. Pal, Powder Technology, 88, 173 (1996).

Staebler, D.L., J. Solid State Chem. 12, 177 (1975).

Steele, B. C., I. Kelly, H. Middleton, and R. Rudkin, Solid State Ionics 28-30, 1547 (1988).

Steele, B.C.H., in High Temperature Solid Ionic Conductors, ed. T. Takahashi, World Scientific, singapore (1989).

Steele, B. C. H., Mater. Sci. Eng., B13, 79-87 (1992).

Steele, B.C.H., Phil. Trans. R. Soc. Lond. A 354, 1695 (1996).

Steinsvik, S., T. Norby, and P. Kofstad, Electroceramics IV, Vol. II, p. 691,eds. R. Waser, S. Hoffmann, D. Bonnenberg, and C. Hoffmann, Augustinus Buchhandlung, Aachen, Germany (1994).

Stöver, D., U. Diekmann, U. Flesch, H. Kabs, W.J. Quadakers, F. Tietz, and I.C. Vinke, in Proc. 6th Intern. Symp. on SOFCs, 1999, Honolulu, HI, eds. S. C. Singhal, and M. Dokiya, Electrochem. Soc., Pennington, NJ, 1999, p.812. Suzuki, M., H. Sasaki, S. Otpshi, and M. Ippomatsu, in Proc. 2nd Intern. Symp. on SOFC, eds. F. Gross, P. Zegers, S.C. Singhal, and O. Yamamoto, (CEC, Luxemburg, 1991) p. 585.

Subramanian, M. A., J. Solid State Chem. 31, 329 (1980).

Sunstrom IV, J.E., S.M. Kauzlarich, and P. Klavins, Chem. Mater. 4, 346 (1992).

Swalin, R.A., in Thermodynamics of solids, 2d ed. A Wiley-Interscience publication, New York (1972)

Swanson, H. and Fuyat, Natl. Bur. Stand. (U.S.), Circ. 539, 344 (1954).

Taguchi, Y, Y. Tokura, T. Arima, and F. Inaba, Phys. Rev. B 48, 511 (1993).

Takahashi, T. and H. Iwahara, Energy Conversion 11, 105 (1971).

Takahashi, T., in Physics of Electrolytes Vol 2, ed. Hladik, J., Academic Press, London, 1972, p. 989.

Takegahara, K., J. Electron Spectroscopy and Related Phenomena 66, 303 (1994).

Tamura, H., H. Yoneyama, and Y. Matsumoto, in Electrodes of Conductive Metallic

Oxides, ed. S. Trasatti, Elsevier Scientific Publishing, Amsterdam (1980).

Tannenberger, H. and H. Siegert, Adv. Chem. 90, 281 (1969).

Tedmon, C.S., H.S. Spacil, and S.P. Mitoff, J. Electrochem. Soc. 116, 1170 (1969).

Teraoka, Y., H. Zhang, K. Okamoto, and N. Yamazoe, Mat. Res. Bull. 23, 51 (1988).

Teraoka, Y., H. Zhang, K. Okamoto, and N. Yamazoe, Mat. Res. Bull. 5, 1 (1998).

Thampi, K.R., A.J. McEvoy, and J. van Herle, J. Electrochem. Soc. 142, 506 (1995).

Tien, T.Y. and F.A. Hummel, Trans. Brit. Ceram. Soc. 66, 233 (1967).

Tilley, R.J.D., J. Solid State Chem. 21, 293 (1977).

Tofield, B.C. and W.R. Scott, J. Solid State Chem. 10, 183 (1974).

Tokura, Y, Taguchi, Y, Y, Okada, T. Arima, K. Kumagai, and Y. Iye, Phys. Rev. Lett. 70, 2126 (1993).

Tsai, T. and S.A. Barnett, Solid State Ionics 98,191 (1997).

Tsuda, N., K. Nasu, A. Yanase, and K. Siratori, in Electronic Conduction in Oxides, Springer-Verlag, New York (1991).

Tufte, O.N. and P.W. Chapman, Phys. Rev. 155, 796 (1967).

Tuller, H.L. and A.S. Nowick, J. Electrochem. Soc. 122, 255 (1975).

Tuller, H.L., in Nonstiochiometric Oxides, ed., O.T. Sørensen, Academic Press, New York (1981).

Tuller, H.L., J. Phys. Chem. Sol. 55, 1393 (1994).

Tuller, H.L., Solid State Ionics 94, 63 (1997).

Uematsu, K., O. Sakurai, N. Mizutani, and M. Kato, J. Mat. Sci. 19, 3671 (1984).

van Berkel, F.P.F., F.H. van Heuveln, and J.P.P. Huijsmans, in Proc. 3rd Intern. Symp. on SOFC, eds. S.C. Singhal, and H. Iwahara, Vol. 93-4 (Electrochemical Soc., New York, 1993) p. 744.

van Heuveln, F.H., F.P.F. van Berkel, and J.P.P. Huijsmans, in Proc. 14th Risø Intern. Symp. On Materials Science: High Temperature Electrochemical Behaviour of Fast Ion and Mixed Conductors, eds. F.W. Poulsen, J.J. Bentszen, T. Jacobsen, E. Skou and M.J.L. Østergard, Risø National Laboratory, Roskilde, Denmark, p. 53 (1993).

Vest, R.W. and J.M. Honing, in Electrical Conductivity in Ceramics and Glass, ed. N.M. Tallan, Marcel Dekker, New York (1974).

Visco, S.J., C.P. Jacobson, and C.D. Jonghe, in Proc. 6th Intern. Symposium on SOFCs, 1999, Honolulu, HI, eds. S. C. Singhal, and M. Dokiya, Electrochem. Soc., Pennington, NJ, 1999, p.127.

Verwey, E.J.W., P.W. Haaijamn, F.C. Romeijn, and G.W. van Oosterhout, Philips Res. Rept. 5, 173 (1950).

Voorhoeve, R. J. H., J. P. Remeika, L. E. Trimble, A. S. Cooper, F. J. Disalvo, and P. K. Gallagher, J. Solid State Chem. 14, 395-406 (1975).

Voorhoeve, R. J. H., in Advanced Materials in Catalysis, eds. J.J. Burton and R. L.

Garten, Academic Press, New York (1977).

Voorhoeve, R. J. H., D. W. Johnson, J. P. Remeika and P. K. Gallagher, Science 195, 827 (1977).

Wagner, C., Proc. Intern.Comm. Electrochem. Thermodyn. Kinet., 7, 361 (1957).

Walters, L.C. and R.E. Grace, J. Phys. Chem. Solids 28, 245 (1967a).

Walters, L.C. and R.E. Grace, J. Phys. Chem. Solids 28, 239 (1967b).

Wang, C., W.L. Worrell, S. Park, J.M. Vohs, and R.J. Gorte, in Proc. 6th Intern. Symp. on SOFCs, 1999, Honolulu, HI, eds. S. C. Singhal, and M. Dokiya, Electrochem. Soc., Pennington, NJ, 1999, p.851.

Waser, R., T. Baiatu, and K.H. Härdtl, J. Am. Ceram. Soc. 73, 1645 (1990).

Waser, R., J. Am. Ceram. Soc. 74, 1934 (1991).

Webb, J.B., M. Sayer, and A. Mansingh, Can. J. Phys. 55, 1725 (1977).

Weise, E.K. and I.A. Lesk, J. Chem. Phys. 21, 801 (1953).

West, A.R., in Solid State Chemistry and its Applications, John Wiley & Sons, Chichester (1987).

Wildenhöner, R., T. Kloidt, W. Mallener, and U. Stimming (ed.), in Proc. 4th Intern. Symp. on SOFC, The Electrochem. Soc., New Jersey, Vol. 97-18, 851 (1997).

Worrell, W., Solid State Ionic 52, 147 (1992).

Xue, L.A., Y. Chen, and R.J. Brook, Mat. Sci. Eng. B 1, 193 (1988).

Yamada, H. and G.R. Miller, J. Solid State Chem. 6, 169 (1973).

Yan, M.F., Mater. Sci. Eng. 48, 53 (1981).

Yang, W.D., J. Mat. Sci. 34, 3533 (1999).

Yokokawa, H., N. Sakai, T. Kawada and M. Dokiya, Solid State Ionics 52, 43 (1992).

Zaanen, J., G.A. Sawatzky, and J.W. Allen, Phys. Rev. Lett. 55, 418 (1985).

Zhang, Y., Y. Ma, J. Liang, and G. Rao, Mod.Phys. Lett. B 12, 155 (1998).

Zhi, J., A. Chen, Y. Zhi, P.M. Vilarinho, and J. Baptista, J. Am. Ceram. Soc. 82, 1345 (1999).